

Combined Author Index

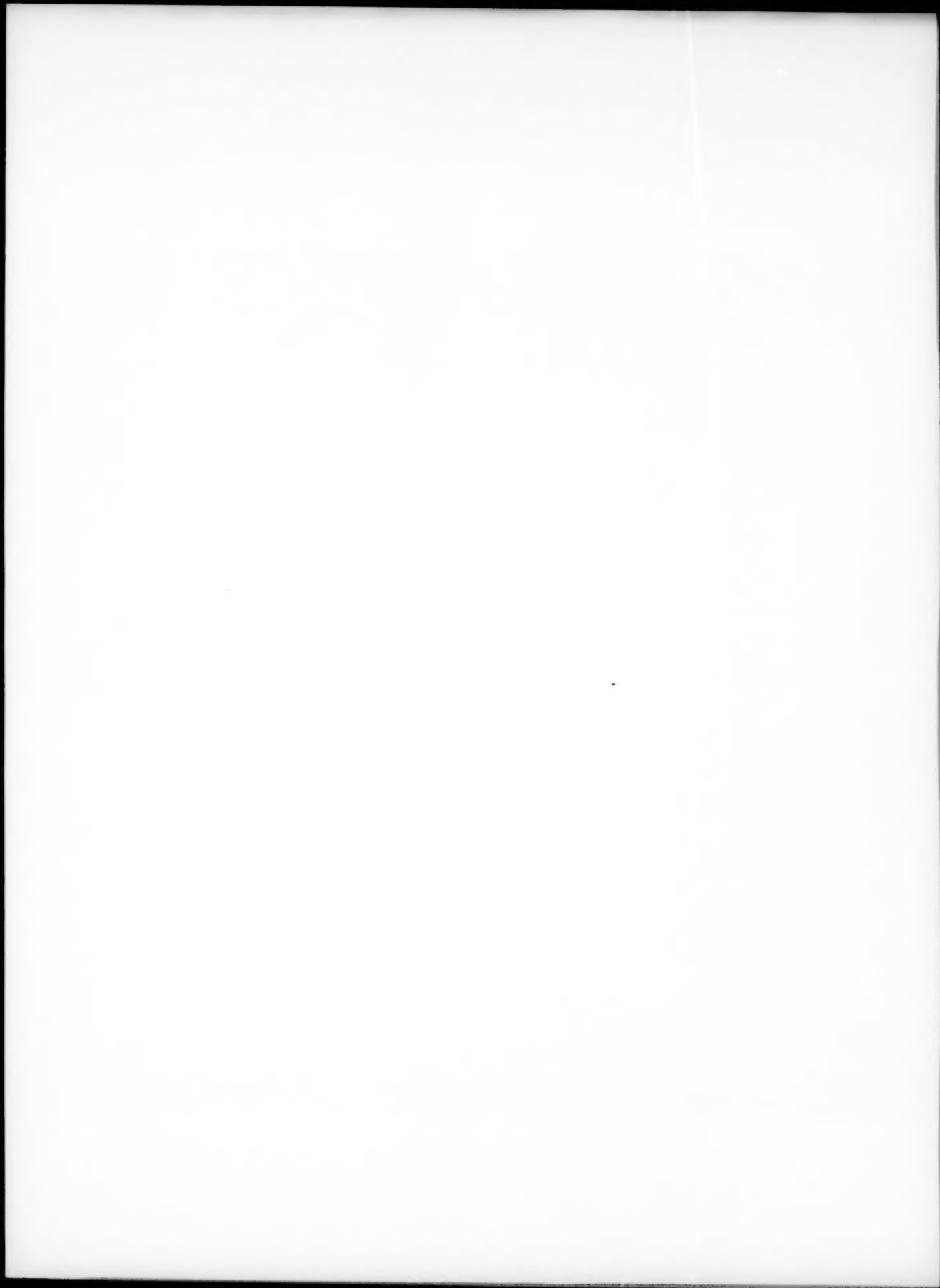
- Aaronson, H.I. 973-983A
1187-1210A
1223-1235A
Abd El-Latif, M.H. 2291-2303A
Abe, F. 1255-1262A
3187-3199A
Abe, T. 3737-3744A
Abriata, J.P. 2343-2349A
Acosta, G.F.A. 541-560B
561-573B
Acseirad, O. 3863-3866A
Adams, B.L. 1981-1989A
1991-1998A
Agarwal, S. 3032-3038A
Ågren, J. 2799-2802A
3693-3700A
Ahlaczi, H. 2127-2141A
Ahn, S. 493-502A
Ahokainen, T. 839-845B
Ajersch, F. 161-170B
171-178B
Akai, N. 993-998B
Akamatsu, S. 1815-1828A
Akhonin, S.V. 235-245B
Akiyama, T. 993-998B
Alexandrescu, B. 717-718A
Alexandrou, A.N. 1187-1202B
Alexiadis, A. 949-956B
Alexopoulos, N.D. 301-308A
3079-3089A
Allard, L.F. 1055-1065A
1113-1124A
Allen, S. 631-640A
641-653A
Allison, J.E. 2407-2418A
Almesallmy, M. 3113-3127A
Alpas, A.T. 2393-2400A
Altenhof, W.J. 2393-2400A
Amadou, T. 3499-3513A
Amaral Fortes, M. 3091-3101A
Anacleto, N. 609-615B
Angella, G. 2993-3001A
Anglada, M. 2503-2510A
Antonsson, T. 2869-2879A
Antony, M.M. 679-693A
Apelian, D. 381-392B
1187-1202B
2174-2180A
Appel, F. 3563-3570A
Araoka, A. 2161-2170A
Ardell, A.J. 3063-3069A
Armstrong, R.W. 2675-2079A
Armstrong, W.D. 1403-1406A
Armborg, L. 2981-2991A
Asai, T. 847-855B
Asaki, Z. 651-661B
Asthana, R. 911-923A
Atkinson, H.V. 899-910A
Aune, R.E. 3673-3680A
Auras, R. 1579-1590A
Azari, H.N. 949-952A
1839-1851A
Aziz, M.J. 2803-2807A
Babu, P.E.J. 1029-1039B
Baeslack, W.A., III 1273-1280A
Bakke, P. 1905-1909A
Balasubramaniam, R. 1789-1798A
Balch, D.K. 1159-1165A
Baligidad, R.G. 1789-1798A
Ballal, N.B. 65-74B
Bampton, C. 947-949A
Ban, C. 2487-2494A
Banchik, A.D. 2343-2349A
Banerjee, R. 2143-2152A
Banerjee, S. 205-216A
Bannur, S. 1403-1406A
Barat, P. 3319-3322A
Barker, D.R. 3015-3018A
Barr, P.V. 1059-1070B
Barranco, V. 2185-2187A
Barreto, J. De J. 957-966B
Barreto-Sandoval, J.D.J. 247-257B
Bassim, M.N. 2725-2728A
Basumallick, A. 1123-1128B
Baum, M.M. 381-392B
Bazan, G. 2587-2607A
Beaman, J.J. 101-113B
Becker, R. 2625-2631A
Becker, R.M. 381-392B
Beckermann, C. 1915A
Beitelman, L. 1129-1137B
Belak, J. 2587-2607A
Belassel, M. 2361-2369A
Bellon, P. 1105-1111A
Beltran-Sanchez, L. 2471-2485A
Bencze, L. 867-876B
Benson, D. 2575-2586A
Berbon, P.B. 3855-3861A
Besson, J. 1039-1053A
Beyerlein, I.J. 3763-3774A
Beynon, J.H. 2993-3001A
Bhattacharjee, D. 121-130A
Bhattacharya, B. 71-81A
Bhattacharya, D.K. 599-605A
Bhowmik, S. 865-877A
Bhuvaneshwar, N. 1799-1806A
Biallas, G. 321-331A
Binet, C. 3833-3841A
Bingert, J.F. 1487-1499A
3445-3454A
217-226A
Biro, E. 755-759B
Blackburn, S. 761-768B
3149-3154A
2267-2278A
Boehert, C.J. 785-803B
Bojarevics, V. 217-226A
Boomer, D.R. 1410-1414A
Bouchard, R. 1655-1661A
Bouzay, E. 3775-3786A
Bowen, P. 1007-1016A
1393-1401A
Bowles, A.L. 1905-1909A
Braham, C. 3499-3513A
Brass, A.-M. 1449-1464A
Brass, A.M. 457-464A
Bratberg, J. 3649-3663A
Brecht, Y. 1211-1221A
Briant, C.L. 1745-1755A
3032-3038A
2587-2607A
1107-1112B
3563-3570A
785-796A
839-848A
3015-3018A
15-23A
Buchanan, R.A. 2351-2360A
Buchheit, T.E. 1963-1967A
Budai, J.D. 1691-1701A
Burt, H. 293-300A
Cabibbo, M. 1097-1103A
Cabrera, J.M. 2617-2624A
Cady, C.M. 2511-2515A
Cai, X. 3201-3210A
Campanella, T. 1425-1435A
Campbell, J. 2063-2071A
2893-2902A
Camporredondo, S.J.E. 541-560B
561-573B
2127-2141A
Candan, E. 2575-2586A
Cao, B.Y. 2729-2739A
309-319A
2853-2859A
Cao, H. 439-456A
Cao, J.-W. 1425-1435A
Cao, R. 617-623B
Cao, X. 1011-1013B
Carkin, G. 3024-3029A
Carneiro, T. 25-35A
Carreño-Morelli, E. 2223-2228A
Castaing, J. 541-560B
Castillejos, E.A.H. 561-573B
Catalina, A.V. 1525-1538A
Caturia, M. 2587-2607A
Cazamias, J.U. 2663-2673A
Cendrowicz, A.M. 755-759B
761-768B
1999-2011A
Cerreta, E. 2557-2566A
2767-2781A
Cesari, E. 761-770A
Chaki, T.K. 865-877A
Chan, C.H. 3177-3186A
Chan, K.S. 589-597A
3409-3422A
3721-3735A
1381-1391A
Chandrawat, H.N. 1359-1368A
Chang, C.-P. 1129-1137B
Chang, F.-C. 1853-1860A
Chang, K.Y. 2533-2536A
Chang, S.-Y. 2153-2160A
Chao, C.-G. 3201-3210A
Charbon, C. 3319-3322A
Chatterjee, S.K. 3681-3691A
Chatterjee, U.K. 3319-3322A
Chattopadhyay, S.K. 339-350B
Chattopadhyay, K. 1123-1128B
Chattoraj, I. 3477-3487A
Chaturvedi, M.C. 37-43A
Chawla, K.K. 53-61A
Chawla, N. 733-740A
Chen, C.D. 3477-3487A
Chen, G.Z. 223-233B
Chen, H.-K. 55-63B
Chen, J.H. 439-456A
1765-1778A
1725-1734A
Chen, K.H. 839-848A
Chen, L. 2313-2321A
Chen, L.-Q. 952-957A
Chen, L.H. 2279-2286A
Chen, M.W. 1203-1207B
Chen, Q. 2511-2515A
3423-3430A
1465-1469A
2533-2536A
741-749A
2557-2566A
2073-2085A
Chen, T.J. 3032-3038A
Chen, Y.-L. 1281-1288A
Chène, J. 457-464A
Cheng, C.-W. 1501-1515A
Chi, D.Z. 3053-3061A
Chiang, J.T. 3817-3821A
Chikhradze, N.M. 1125-1131A
Chin, T.-S. 2533-2536A
Cho, J.-H. 1075-1086A
Cho, J.-Y. 3399-3408A
Choi, B. 3431-3438A
Choi, C.-H. 115-120B
Choi, J.-H. 719-724A
Choi, J.K. 1663-1668A
Choi, Y.S. 513-524A
Chou, K.-C. 715-720B
Christensen, A.N. 929-936B
Chua, S.J. 3053-3061A
Chumbley, L.S. 3377-3386A
Chuzhoy, L. 1745-1755A
Çimenoglu, H. 2127-2141A
Cirre, J. 755-759B
761-768B
3543-3550A
Claessens, S. 2747-2755A
Cleland, D.J. 3563-3570A
Clemens, H. 3211-3220A
Cochrane, R.F. 523-540B
Cockcroft, S.L. 3843-3854A
1055-1065A
Coffey, D.W. 2143-2152A
Collins, P.C. 2587-2607A
Colvin, J.D. 1703-1713A
Conlon, K.T. 771-783A
Connolly, T. 2681-2696A
Conrad, H. 83-91A
Cotes, S.M. 93-102A
Cotrana, E. 179-181B
Cramb, A.W. 2487-2494A
Cui, J. 3631-3633A
Cui, Y. 959A
1097-1106B
1829-1837A
Dahle, A.K. 2881-2891A
3531-3541A
2305-2311A
Dahmen, U. 1905-1909A
3681-3691A
1087-1095A
1369-1379A
Dargusch, M.S. 7-14A
Das, K. 121-130A
Das, S. 965-972A
599-605A
De, P.K. 1945-1952A
DeCarlo, F. 3461-3468A
Decker, B.J. 259-268B
Decterov, S.A. 493-507B
877-889B
2223-2228A
Deeb, C. 3863-3866A
Delplanck, J.-L. 449-460B
Demedices-Garcia, L. 797-811A
Demonet, X. 813-823A
Deschamps, A. 1437-1448A
Desimoni, J. 103-110A
Dey, G.K. 189-203A
205-216A
Dhanjal, S.K. 1059-1070B
Dhindaw, B.K. 1167-1176A
2869-2879A
Díaz-Cruz, M. 85-99B
247-257B
449-460B
Dickerson, P. 2247-2255A
Dickerson, R. 2247-2255A
Dille, J. 3863-3866A
Ding, P. 2757-2766A
Ding, X.D. 1725-1734A
Dinnis, C.M. 3531-3541A
Dippenaar, R. 3701-3706A
Döbrich, K.M. 1953-1961A
Dolan, M.D. 675-684B
Domgini, J.F. 949-956B
Dong, H. 2487-2494A
Dong, W. 331-338B
Donlon, W. 2407-2418A
Dorn, L. 865-877A
Dorogoy, A. 3787-3795A
Dour, G. 879-889A
Dracup, B. 2305-2311A
Dragnevski, K.I. 3211-3220A
Du Terrail, Y. 743-754B
Du, J. 2111-2114A
Du, Y. 1613-1628A
Duggan, B.J. 3423-3430A
Dunand, D.C. 287-292A
1159-1165A
Dunlap, J. 785-796A
Dunlop, G.L. 1905-1909A
Dunn, D.N. 1935-1943A
DuPont, J.N. 143-152B
1133-1140A
Duran-Valencia, C. 957-966B
Durand, F. 743-754B
Dutta, P. 339-350B
Dye, D. 1703-1713A
Eckert, J. 1591-1601A
3489-3498A
3605-3612A
Edmonds, D.V. 2757-2766A
Edwards, M.J. 2587-2607A
2625-2631A
El-Dasher, B.S. 1969-1979A
1981-1989A
El-Latif, M.H.A. 45-52A
El-Madhou, Y. 2725-2728A
Elert, M.L. 2647-2650A
Elliott, A.J. 3221-3231A
Eilner, M. 63-70A
Elmadagli, M. 2393-2400A
Ely, K.J. 1273-1280A
Emura, S. 2161-2170A
2971-2979A
Enomoto, M. 1263-1272A
1927-1933A
2719-2723A
Entel, P. 461-469B
Eriksson, R. 2903-2915A
Eskin, D. 1325-1335A
Eskin, D.G. 3551-3561A
1051-1058B
Etsell, T.H.

| | | | | | | | |
|-----------------------|------------|--------------------|------------|-------------------|------------|-------------------|------------|
| Evangelista, E. | 293-300A | Girard, S.X. | 949-952A | Hayakawa, M. | 1311-1316A | Inal, K. | 2361-2369A |
| Evans, J.W. | 400-404B | Glavicic, M.G. | 679-693A | Hayasaka, M. | 993-998B | Indacochea, J.E. | 153-160B |
| Fagin, P.N. | 679-693A | Gleeson, B. | 3377-3386A | Hayes, P.C. | 203-215B | Inoue, H. | 3469-3476A |
| Fahey, N.P. | 3015-3018A | Glendinning, S.G. | 2587-2607A | Hayes, R.W. | 633-642B | Inoue, T. | 665-677A |
| Faivre, G. | 197-202B | Glicksman, M.E. | 435-438A | Haynes, J.A. | 3855-3861A | Inui, H. | 2229-2238A |
| Fang, Z.Z. | 1815-1828A | Glynn, M.L. | 2279-2286A | He, G. | 3581-3593A | Irisarri, A.M. | 2503-2510A |
| Fautrelle, Y. | 1881-1888A | Goerner, H. | 2981-2991A | He, L.M. | 1591-1601A | Ishida, A. | 111-119A |
| Feliu, S., Jr. | 743-754B | Goetz, R.L. | 655-663A | | 3605-3612A | Ishida, K. | 1243-1253A |
| Ferreira, I.L. | 2039-2050A | Goff, T.A. | 679-693A | | 891-897A | Ishii, K. | 1641-1654A |
| Ferreira, P.J. | 2185-2187A | Goldstein, J.I. | 3015-3018A | | 1113-1124A | Ishikawa, N. | 517-522B |
| Field, R.D. | 285-297B | Golkovski, M.G. | 1681-1690A | He, X.-M. | 3581-3593A | Ishimaru, T. | 993-998B |
| Fielden, D.E. | 3091-3101A | Gong, W. | 3455-3460A | He, Y. | 2783-2788A | Ishimatsu, N. | 1927-1933A |
| | 3445-3454A | Gonzalez, D.L.P.R. | 1613-1628A | Heaney, D.F. | 2747-2755A | Itagaki, K. | 3029-3032A |
| | 15-23A | González, J.A. | 561-573B | Hecker, S.S. | 3833-3841A | Ito, G. | 1041-1049B |
| Fine, M.E. | 3334-3339A | Goods, S.H. | 439-448B | | 2203-2205A | Ivanchenko, V.G. | 2383-2392A |
| Finot, E. | 2323-2329A | Gopalan, V. | 2351-2360A | Hector, L.G., Jr. | 2207-2222A | Ivanov, D.S. | 235-245B |
| Fitzner, K. | 3515-3521A | Gordo, E. | 2287-2290A | Heiberg, G. | 3032-3038A | Ivasishin, O.M. | 2587-2607A |
| Fletcher, H.A. | 1071-1085B | Goryczka, T. | 223-233B | Heintz, O. | 2981-2991A | Iza-Mendia, A. | 235-245B |
| Floran, R.J. | 1223-1235A | Gottstein, G. | 761-770A | Hemker, K.J. | 3515-3521A | Jacqueson, M. | 93-102A |
| | 1021-1028B | Gouret, N. | 1203-1207B | Henao, H.M. | 2279-2286A | Jak, E. | 3289-3305A |
| | 3641-3648A | Gourgues, A.F. | 879-889A | Henrie, B.L. | 1041-1049B | | 203-215B |
| Flores, E. | 1097-1103A | Gourlay, C.M. | 1039-1053A | Henry, S. | 3745-3751A | | 633-642B |
| Fonda, R.W. | 1487-1499A | Graat, P.C.J. | 2881-2891A | Heo, Y.-U. | 2495-2501A | Jamshidi, E. | 825-828B |
| Forest, S. | 797-811A | Grabke, H.J. | 3387-3398A | Herlach, D.M. | 355-356A | Janek, R.P. | 2351-2360A |
| | 813-823A | Grange, M. | 751-759A | | 607-612A | Jang, J. | 3331-3333A |
| Fortunier, R. | 879-889A | Grant, P.S. | 2087-2102A | Herman, H. | 1067-1073A | Jang, Y. | 3431-3438A |
| Fotedar, R.K. | 189-203A | Gray, G.T. | 1113-1122B | Hermida, J.D. | 1945-1952A | Janovec, J. | 751-759A |
| Frangopol, D.M. | 1471-1476A | Gray, G.T., III | 2557-2566A | Herrera, G.M.A. | 313-330B | Javaherdashti, R. | 2051-2056A |
| Fraser, H.L. | 2143-2152A | Greer, A.L. | 1999-2011A | Hétu, J.-F. | 541-560B | Javernick, D.A. | 2445-2454A |
| Fray, D.J. | 223-233B | | 2617-2624A | | 161-170B | Jena, P.K. | 1107-1112B |
| Fredriksson, H. | 2869-2879A | | 607-612A | Hibbins, S. | 171-178B | Jiang, L. | 785-796A |
| Frey, N.D. | 679-693A | | 1067-1073A | Hillert, M. | 3843-3854A | | 839-848A |
| Frick, C.P. | 2013-2025A | Gregori, F. | 2633-2646A | | 351-352A | Jiang, X. | 179-181B |
| Friddy, J. | 1969-1979A | Gregorutti, R. | 103-110A | | 3693-3700A | Jiang, Z.-M. | 2783-2788A |
| Frisk, K. | 3649-3663A | Griffiths, W.D. | 721-733B | Hilpert, K. | 867-876B | Jiao, T. | 3439-3444A |
| Froes, F.H. | 1899-1903A | Grillon, F. | 797-811A | Hines, J.A. | 299-311B | Jiles, D.C. | 599-605A |
| | 3009-3012A | Grinfeld, M.A. | 2651-2661A | Hirohashi, M. | 2757-2766A | Jin, H. | 997-1006A |
| Fruehan, R.J. | 617-623B | Gröbner, J. | 3349-3362A | Hirsch, T.K. | 3523-3530A | Jin, O. | 131-138A |
| | 643-650B | Gruen, G.-U. | 2495-2501A | Hixson, R.S. | 2617-2624A | Jin, Z. | 1613-1628A |
| | 829-838B | Gruzieski, J.E. | 3233-3250A | Hodgson, P.D. | 2331-2341A | Jo, S.-K. | 115-120B |
| | 1011-1013B | Gu, Y.F. | 3329-3331A | Hoffman, F. | 865-877A | | 1087-1095B |
| Fu, N.X. | 625-631B | Guillemet, A.F. | 83-91A | Hogg, S.C. | 899-910A | Johnston, R.F. | 675-684B |
| Fuchsmann, A. | 1211-1221A | Guillon, F. | 1449-1464A | Höglund, L. | 3693-3700A | Jolly, M.R. | 755-759B |
| Fujii, A. | 2229-2238A | Gullett, P. | 321-331A | Holte, S. | 1113-1122B | | 761-768B |
| Fujii, H. | 583-588A | Guo, G. | 1203-1207B | Holian, B.L. | 2609-2615A | Jones, J.W. | 2407-2418A |
| | 2861-2867A | Guo, H. | 1237-1242A | | 2719-2723A | Joo, H.D. | 1663-1668A |
| Fukaura, K. | 1289-1300A | Guo, X. | 517-522B | | 2741-2745A | Jung, I.-H. | 259-268B |
| Fukui, T. | 3275-3288A | Gupta, G. | 717-718A | Holloway, P.C. | 1051-1058B | | 493-507B |
| Fukumoto, S. | 217-226A | Gupta, O.P. | 985-996A | Hong, C.P. | 1555-1563A | | 877-889B |
| | 3165-3176A | Gupta, V.K. | 1381-1391A | Hong, J.H. | 2027-2037A | Jung, K.-Y. | 1969-1979A |
| Fukunaka, Y. | 651-661B | Guruswamy, S. | 2963-2970A | Hong, S.I. | 695-705A | Kad, B. | 2587-2607A |
| Fundenberger, J.J. | 3775-3786A | Guthrie, R.I.L. | 417-437B | Hongo, H. | 1757-1764A | Kad, B.K. | 2633-2646A |
| Furuya, Y. | 1715-1723A | Gutiérrez, I. | 93-102A | Horiguchi, K. | 3797-3802A | Kadau, D. | 2719-2723A |
| | 3737-3744A | Gutiérrez, M.E.P. | 541-560B | Horita, Z. | 1735-1744A | Kadau, K. | 2719-2723A |
| Gagliano, M.S. | 2323-2329A | | 561-573B | Horstemeyer, M.F. | 321-331A | Kagawa, Y. | 2853-2859A |
| Gail, K. | 321-331A | Ha, J. | 1757-1764A | Hort, N. | 1167-1176A | Kaibyshev, R. | 2383-2392A |
| | 2013-2025A | Haarberg, G.M. | 398-400B | Hosford, W.F. | 2191-2192A | Kainer, K.U. | 1167-1176A |
| Gallermeault, M. | 351-361B | Hadji, L. | 2181-2185A | Howard, I.C. | 1087-1095A | Kainuma, R. | 1243-1253A |
| Gan, J.-Y. | 2533-2536A | Hagiwara, M. | 2161-2170A | Hsu, C.-H. | 471-480A | | 1641-1654A |
| Gandin, C.-A. | 1915A | | 2971-2979A | Hsu, C.-Y. | 1465-1469A | Kalantar, D. | 2633-2646A |
| | 2981-2991A | | 3605-3612A | Hsu, H.-C. | 55-63B | Kalantar, D.H. | 2587-2607A |
| Ganesh, V.V. | 53-61A | Hahn, J.D. | 1105-1111A | Hu, H. | 3018-3024A | Kamath, H.C. | 575-585B |
| Gangloff, R.P. | 849-864A | Hakik, M. | 2247-2255A | Hua, M.-J. | 1203-1207B | Kampe, S.L. | 1603-1611A |
| Gao, Y.X. | 3275-3288A | Hallam, C.P. | 721-733B | Huang, B. | 1281-1288A | | 1861-1867A |
| Garcia, A. | 285-297B | Hammerberg, J.E. | 2741-2745A | Huang, C.A. | 1613-1628A | | 1869-1879A |
| Garcia-Cordovilla, C. | 2503-2510A | Han, B.Q. | 947-949A | Huang, J. | 1351-1357A | | 2821-2828A |
| Garcia-Demedices, L. | 85-99B | | 1343-1350A | Huang, J.C. | 3363-3375A | Kaneno, Y. | 3469-3476A |
| Garcia-Romero, A. | 2503-2510A | Han, L. | 1139-1150B | | 555-562A | Kang, C.G. | 769-776B |
| Gardin, P. | 949-956B | Han, S. | 465-469A | | 2455-2469A | | 2419-2426A |
| Garduño-Esquivel, J. | 373-380B | Hanamura, T. | 665-677A | | 3803-3815A | Kang, S.-B. | 279-286A |
| Garnier, S. | 1655-1661A | Hänninen, H. | 2103-2109A | Huang, J.G. | 15-23A | Kang, Y.-B. | 259-268B |
| Garratt-Reed, A.J. | 1223-1235A | Hansen, B.L. | 2401-2406A | Huang, J.Y. | 15-23A | Kankaanpää, T. | 839-845B |
| Gay, B. | 3543-3550A | Hansson, R. | 3745-3751A | Huang, P. | 1301-1309A | Kao, P.-W. | 1359-1368A |
| Gebelin, J.-C. | 755-759B | Hao, H. | 398-400B | Huang, P.G. | 857-866B | Kapinus, V.A. | 381-392B |
| | 761-768B | Hao, Y. | 633-642B | Huang, S.-C. | 3221-3231A | Kapranos, P. | 899-910A |
| Genc, A. | 2143-2152A | Hao, Y. | 3843-3854A | Hufnagel, T.C. | 3439-3444A | Kaplay, G. | 393-398B |
| Gerber, A.G. | 351-361B | Hara, T. | 2073-2085A | Hull, J.R. | 1129-1137B | | 471-486B |
| German, R.M. | 257-263A | Harada, H. | 2935-2949A | Hull, R. | 1935-1943A | Karaman, I. | 247-256A |
| | 3833-3841A | | 587-597B | Humphreys, E.S. | 1223-1235A | | 2935-2949A |
| Germann, T.C. | 2609-2615A | | 1779-1787A | Hur, S.-M. | 719-724A | Karma, A. | 1815-1828A |
| | 2719-2723A | | 1911-1914A | | 3103-3112A | Kaschner, G.C. | 3763-3774A |
| | 2741-2745A | | 3329-3331A | Hutchins, J.D. | 1223-1235A | Kashani-Nejad, S. | 405-406B |
| Ghonem, H. | 3113-3127A | Harada, Y. | 535-542A | Hutchinson, C.R. | 1211-1221A | | 406-408B |
| Ghosh, A.K. | 2187-2190A | Harding, R.A. | 785-803B | | 1237-1242A | Kashiwaya, Y. | 517-522B |
| | 2439-2444A | | 2893-2902A | Hwang, B. | 2371-2382A | Katada, Y. | 1477-1486A |
| Ghosh, J. | 3319-3322A | Harris, R. | 405-406B | Hwang, D.-Y. | 825-837A | Katgerman, L. | 1325-1335A |
| Ghosh, K.S. | 3681-3691A | | 406-408B | Ice, G.E. | 1963-1967A | | 2917-2926A |
| Ghosh, P.K. | 2439-2444A | Hartwig, K.T. | 247-256A | Ilincic, F. | 161-170B | | 3551-3561A |
| Giard, S.X. | 1839-1851A | | 2935-2949A | | 171-178B | Kath, D. | 867-876B |
| Gibala, R. | 2239-2245A | Hashimoto, T. | 2229-2238A | Ilyushechkin, A. | 203-215B | Kauerauf, B. | 239-246A |
| Giogliotti, M.F.X. | 3221-3231A | Hassan, H.A. | 45-52A | Im, J.-T. | 247-256A | Kaufman, M.J. | 1669-1679A |
| Girard, A. | 3289-3305A | | 2291-2303A | Im, Y.-R. | 2027-2037A | Kaukler, W.F. | 1525-1538A |

| | | | | | |
|-----------------------|------------|------------|-------------------|------------|------------|
| Kayanuma, Y. | 817-824B | 2587-2607A | Levin, R. | 3787-3795A | 3843-3854A |
| Ke, L. | 153-160B | 2663-2673A | Levit, V.I. | 1669-1679A | 2174-2180A |
| Kecskes, L.J. | 1125-1131A | 825-828B | Lewandowski, J.J. | 45-52A | 3038-3043A |
| | 3439-3444A | 1351-1357A | | 2291-2303A | 227-238A |
| Kelly, S.M. | 1861-1867A | 15-23A | Li, C. | 1151-1172B | 1237-1242A |
| | 1869-1879A | 3187-3199A | Li, D. | 849-864A | 131-138A |
| | 2821-2828A | 891-895B | Li, L. | 1565-1577A | 2617-2624A |
| Keppens, V. | 3149-3154A | 189-203A | Li, S.-H. | 2511-2515A | 3129-3139A |
| Kernan, B. | 631-640A | 205-216A | Li, W. | 2153-2160A | 3334-3339A |
| Kerr, J.J. | 643-650B | 1017-1027A | Li, Y. | 2511-2515A | 1281-1288A |
| Kesloglu, K. | 3665-3672A | 1407-1410A | | 617-623B | 3665-3672A |
| Kevorkian, V. | 707-715A | 257-263A | Li, Y.-Y. | 1565-1577A | 2609-2615A |
| Khalifa, W. | 3233-3250A | 3091-3101A | Liaw, P.K. | 2783-2788A | 1603-1611A |
| Khanna, R. | 75-83B | 1789-1798A | | 15-23A | 2821-2828A |
| Khatak, H.S. | 1799-1806A | 1039-1053A | | 785-796A | 2223-2228A |
| Khoshandam, B. | 825-828B | 1113-1124A | | 839-848A | 1915A |
| Kim, C. | 465-469A | 103-110A | | 3334-3339A | 3745-3751A |
| Kim, C.K. | 481-492A | 1735-1744A | | 2103-2109A | 797-811A |
| | 2057-2061A | 2675-2079A | Liimatainen, J. | 2829-2835A | 813-823A |
| Kim, D. | 3063-3069A | 381-392B | Lim, S. | 2837-2843A | 947-949A |
| Kim, G.Y. | 3581-3593A | 523-540B | Lim, S.K. | 2057-2061A | 247-256A |
| Kim, H.-W. | 279-286A | 1991-1998A | Lin, C.-F. | 1501-1515A | 239-246A |
| Kim, I.S. | 1477-1486A | 1963-1967A | Lin, C.-I. | 55-63B | 153-162A |
| Kim, J.-S. | 1087-1095B | 2799-2802A | Lin, C.-K. | 3018-3024A | 1735-1744A |
| Kim, J.-T. | 115-120B | 2587-2607A | Lin, S.-J. | 2533-2536A | 583-588A |
| Kim, N.J. | 493-502A | 2567-2573A | Lin, Y. | 1173-1185B | 2257-2266A |
| | 1029-1038A | 2729-2739A | | 3251-3263A | 1311-1316A |
| | 1629-1632A | 2881-2891A | | 3265-3273A | 1715-1723A |
| | 3455-3460A | 573-581A | | 3595-3603A | 3737-3744A |
| | 3753-3761A | 947-949A | | 3633-3635A | 471-486B |
| Kim, S. | 465-469A | 1173-1185B | Lindley, T.C. | 3275-3288A | 333-339A |
| | 1017-1027A | 1343-1350A | Liou, F.W. | 1139-1150B | 1517-1524A |
| | 1407-1410A | 3251-3263A | Lippold, J.C. | 1273-1280A | 400-404B |
| | 1745-1755A | 3265-3273A | Liu, C.-Y. | 1501-1515A | 805-809B |
| | 2027-2037A | 3595-3603A | Liu, C.S. | 356-362A | 3763-3774A |
| | 2829-2835A | 3633-3635A | Liu, G. | 1725-1734A | 959A |
| | 2829-2835A | 3307-3317A | Liu, J. | 1881-1888A | 1097-1106B |
| | 2837-2843A | 919-928B | Liu, L. | 2111-2114A | 1829-1837A |
| | 2837-2843A | 2361-2369A | Liu, R.P. | 607-612A | 321-331A |
| | 3149-3154A | 3149-3154A | | 1067-1073A | 3149-3154A |
| | 3431-3438A | 2247-2255A | Liu, S. | 909-917B | 3595-3603A |
| Kim, S.-H. | 115-120B | 2829-2835A | Liu, W. | 356-362A | 3633-3635A |
| | 1087-1095B | 2837-2843A | | 1133-1140A | 1317-1324A |
| Kim, S.-J. | 2027-2037A | 2371-2382A | | 1963-1967A | 2587-2607A |
| | 2371-2382A | 719-724A | Liu, W.C. | 265-277A | 2625-2631A |
| Kim, S.U. | 1663-1668A | 3103-3112A | | 3613-3629A | 2951-2961A |
| Kim, Y.-J. | 3377-3386A | 3331-3333A | Liu, X.J. | 1243-1253A | 1539-1553A |
| Kim, Y.C. | 493-502A | 719-724A | | 1641-1654A | 743-754B |
| | 1029-1038A | 3103-3112A | Liu, Y. | 2511-2515A | 75-83B |
| Kimura, M. | 1311-1316A | 3753-3761A | Liu, Z.-K. | 2313-2321A | 3319-3322A |
| King, W.T. | 3221-3231A | 355-356A | Lloyd, D.J. | 997-1006A | 101-113B |
| Kinoshita, C. | 2257-2266A | 2027-2037A | | 1839-1851A | 103-110A |
| Kinoshita, H. | 333-339A | 2371-2382A | Locci, I.E. | 1632-1635A | 1655-1661A |
| Kirby, B.C. | 2809-2819A | 493-502A | Lomdahl, P.S. | 2609-2615A | 1655-1661A |
| Klarstrom, D.L. | 15-23A | 1017-1027A | | 2719-2723A | 891-897A |
| | 785-796A | 1407-1410A | Long, A.E. | 2172-2174A | 3581-3593A |
| | 839-848A | 3431-3438A | Loomans, M.E. | 3053-3061A | 2587-2607A |
| Knipling, K.E. | 2821-2828A | 3455-3460A | López, B. | 93-102A | 2575-2586A |
| Knott, J.F. | 121-130A | 909-917B | Lopez, H.F. | 2517-2523A | 2587-2607A |
| Kobayashi, K. | 1311-1316A | 3071-3077A | Lopez-Ramirez, S. | 957-966B | 2633-2646A |
| Kobayashi, M. | 625-631B | 3753-3761A | Lorenz, A. | 631-640A | 2729-2739A |
| Kobayashi, T. | 1779-1787A | 3455-3460A | | 641-653A | 2893-2902A |
| | 1911-1914A | 115-120B | Lorenz, K.T. | 2587-2607A | 2351-2360A |
| Kocaele, D. | 999-1009B | 695-705A | | 2625-2631A | 1021-1028B |
| Kocaele, Y. | 999-1009B | 1853-1860A | Lorenz, U. | 3563-3570A | 3641-3648A |
| Koizumi, Y. | 1779-1787A | 3275-3288A | Löser, W. | 1591-1601A | 879-889A |
| | 1911-1914A | 139-151A | Lu, S. | 2861-2867A | 911-923A |
| Kokawa, H. | 331-338B | 481-492A | Lu, X.G. | 3673-3680A | 1393-1401A |
| Kolman, D.G. | 3445-3454A | 493-502A | Lu, Y. | 2757-2766A | 3461-3468A |
| Kondo, T. | 3003-3008A | 525-534A | Lui, T.S. | 952-957A | 2445-2454A |
| Kong, J.S. | 1471-1476A | 719-724A | Lum, I. | 217-226A | 3363-3375A |
| Koo, Y.M. | 1663-1668A | 1029-1038A | Lundin, C.D. | 3631-3633A | 3015-3018A |
| Kool, W.H. | 2917-2926A | 2027-2037A | Luo, H. | 1889-1898A | 973-983A |
| Koss, D.A. | 1317-1324A | 2371-2382A | | 2789-2797A | 3141-3148A |
| Kotula, P.G. | 2351-2360A | 3103-3112A | Luo, J. | 1007-1016A | 269-275B |
| Kouzei, M. | 287-292A | 3455-3460A | Luo, Z.P. | 247-256A | 2663-2673A |
| Koyama, K. | 891-895B | 3753-3761A | Lvov, G. | 1669-1679A | 3349-3362A |
| Kramb, R.C. | 679-693A | 471-480A | MHamdi, M. | 2903-2915A | 3855-3861A |
| Krauss, G. | 153-162A | 1477-1486A | Ma, D. | 735-742B | 3763-3774A |
| Krawiec, H. | 3515-3521A | 1501-1515A | MacKay, R.A. | 2313-2321A | 3024-3029A |
| Krendelsberger, N. | 1613-1628A | 891-897A | Madan, M. | 805-809B | 487-492B |
| Kreth, M. | 2719-2723A | 1055-1065A | Madsen, I.C. | 929-936B | 2267-2278A |
| Krill, C.E., III | 1953-1961A | 1113-1124A | Maeda, M. | 181-182B | 599-605A |
| Kroupa, A. | 751-759A | 3581-3593A | | 487-492B | 3387-3398A |
| Ksiazek, M. | 911-923A | 1017-1027A | | 817-824B | 909-917B |
| Kubis, A.J. | 1935-1943A | 1407-1410A | Magadi, G. | 2927-2934A | 1735-1744A |
| Kudoh, M. | 333-339A | 3331-3333A | Maresh, S. | 3763-3774A | 2853-2859A |
| Kuhlmann-Wilsdorf, D. | 5-54B | 719-724A | Maier, H.J. | 321-331A | 2903-2915A |
| | 369-418A | 3103-3112A | | 2013-2025A | 2725-2728A |
| Kulkarni, A. | 1945-1952A | 217-221B | | 2935-2949A | 573-581A |
| Kumar, A. | 1123-1128B | 3833-3841A | | 523-540B | 947-949A |
| Kumar, M. | 2567-2573A | 2803-2807A | Majder, D.M. | 3275-3288A | 1343-1350A |

| | | | | | | | |
|---------------------|------------|----------------------|------------|--------------------------|------------|----------------------|------------|
| Mohanty, O.N. | 985-996A | Ortega, A.M. | 2013-2025A | Rao, K.B.S. | 3129-3139A | Schultz, L. | 1591-1601A |
| Mondal, D.P. | 1369-1379A | Osborne, J.M. | 197-202B | Rao, P.K. | 65-74B | Schuster, D. | 3489-3498A |
| Monzen, R. | 3003-3008A | Ostrovski, O. | 609-615B | Rapp, R.A. | 133-141B | Schuster, J.C. | 3307-3317A |
| Moon, K.I. | 1853-1860A | Otte, M.O. | 3531-3541A | | 182-186B | Schvezov, C. | 1613-1628A |
| Mooney, J.F. | 1325-1335A | Paciawski, K. | 1071-1085B | | 509-515B | Schwartz, A.J. | 1579-1590A |
| Morales, R.D. | 85-99B | Pai, B.C. | 1029-1039B | Rappaz, M. | 2495-2501A | | 2567-2573A |
| | 247-257B | Palafox-Ramos, J. | 247-257B | | 3201-3210A | | 2663-2673A |
| | 449-460B | | 449-460B | | 3543-3550A | Schwartz, D.S. | 2267-2278A |
| Morawiec, A. | 3775-3786A | Palmiere, E.J. | 1087-1095A | Rashid, A.K.M.B. | 2063-2071A | Scrymgeour, D.A. | 2287-2290A |
| Morishita, M. | 891-895B | Pan, F. | 2757-2766A | Rau, C. | 1953-1961A | Scully, J.R. | 849-864A |
| Morita, K. | 277-284B | Pan, Q.Y. | 1187-1202B | Ravelo, R. | 2609-2615A | Sediako, D. | 3843-3854A |
| Morris, J.G. | 265-277A | Pantelakis, S.G. | 301-308A | | 2741-2745A | Seetharaman, S. | 461-469B |
| | 3613-3629A | | 3079-3089A | Raviart, J.L. | 2087-2102A | | 3673-3680A |
| Morris, J.W., Jr. | 2305-2311A | Papaelias, M.P. | 965-972A | Ravikumar, B. | 1123-1128B | Semiatin, S.L. | 235-245B |
| Morrison, R. | 101-113B | Parisot, R. | 797-811A | Rawn, C.J. | 785-796A | | 855-863A |
| Moss, J.A. | 381-392B | | 813-823A | Ray, R.K. | 71-81A | | 679-693A |
| Motohashi, Y. | 2383-2392A | Park, C. | 1017-1027A | Ray, S. | 865-877A | | 1141-1149A |
| Motta, M.S. | 1107-1112B | | 1407-1410A | | 1381-1391A | | 2187-2190A |
| Mudali, U.K. | 1799-1806A | Park, J.H. | 269-275B | Rayment, T. | 1113-1122B | | 2809-2819A |
| Mukai, K. | 471-486B | Park, J.I. | 481-492A | Reed, P.A.S. | 771-783A | | 2993-3001A |
| Mukherjee, P. | 3319-3322A | Park, J.K. | 3071-3077A | Reed, R.C. | 1703-1713A | | 3015-3018A |
| Mukherjee, S. | 613-621A | Park, K.-T. | 825-837A | Reguly, A. | 153-162A | Sen, S. | 1525-1538A |
| | 623-629A | Pantankar, S.N. | 1899-1903A | Remington, B.A. | 2587-2607A | Sengupta, A.K. | 205-216A |
| | 1123-1128B | | 3009-3012A | | 2625-2631A | Sengupta, J. | 523-540B |
| Mullis, A.M. | 3211-3220A | Paul, H. | 3775-3786A | | 2633-2646A | Sha, W. | 2172-2174A |
| Mun, S.-H. | 355-356A | Peascoe, R.A. | 785-796A | Ren, X.C. | 1765-1778A | | 2747-2755A |
| Mungole, M.N. | 1789-1798A | Peikrishvili, A.B. | 1125-1131A | Renk, T.J. | 2803-2807A | | 3012-3015A |
| Murakumo, T. | 1911-1914A | Pelton, A.D. | 259-268B | Rex, S. | 239-246A | Shabrov, M.N. | 1745-1755A |
| Murayama, Y. | 503-511A | | 493-507B | Reynolds, W.T. | 1187-1210A | Shan, Z.-W. | 1281-1288A |
| Murdeswar, N.M. | 1273-1280A | | 877-889B | Reynolds, W.T., Jr. | 1223-1235A | Shankar, P. | 1799-1806A |
| Murray-Chiasson, A. | 999-1009B | | 897-907B | Ricker, R.E. | 2427-2437A | Shankar, S. | 2174-2180A |
| Murry, J.M. | 3015-3018A | Peng, L. | 3323-3328A | Riddle, Y.W. | 341-350A | | 3038-3043A |
| Musin, F. | 2383-2392A | Peng, Z.F. | 2171-2172A | | 3038-3043A | Shankar, V. | 3129-3139A |
| Nagai, K. | 665-677A | Penhoud, P. | 2223-2228A | Ringer, S.P. | 973-983A | Sharif, M.A.R. | 623-629A |
| | 3399-3408A | Peralta, P. | 2247-2255A | Rittel, D. | 3787-3795A | Sharma, J. | 2675-2079A |
| Nagesh, C.R.V.S. | 65-74B | Pereira, L.C. | 3863-3866A | Rivarola, J.B. | 439-448B | Shekhter, A. | 973-983A |
| Nakagawa, Y. | 3469-3476A | Pereloma, E.V. | 973-983A | Rivera-Díaz-Del-Castillo | | Sheldine, G.J. | 101-113B |
| Nakano, J. | 1237-1242A | | 2331-2341A | P.E.J. | 425-433A | Shen, P. | 583-588A |
| Nakata, K. | 227-238A | Pérez-Revenga, M.L. | 2039-2050A | Ro, Y. | 1779-1787A | Shen, T. | 2729-2739A |
| Nam, S.W. | 2161-2170A | | 2185-2187A | | 3329-3331A | Shen, W. | 163-187A |
| Napolitano, R.E. | 1539-1553A | Pericleous, K. | 785-803B | Robertson, J. | 247-256A | Sherman, D.H. | 1745-1755A |
| Nathani, H. | 3024-3029A | Peter, W.H. | 15-23A | Rocha, A.D.S. | 3523-3530A | Shibata, H. | 179-181B |
| Needleman, A. | 1745-1755A | Petterson, K. | 1905-1909A | Rodriguez, P. | 2697-2705A | Shifflet, G.J. | 1935-1943A |
| Nelson, T.W. | 3461-3468A | Peyton, A.J. | 965-972A | Rohrer, G.S. | 1981-1989A | Shikata, S. | 891-895B |
| Nenonen, P. | 2103-2109A | Phanikumar, G. | 339-350B | Rollett, A.D. | 513-524A | Shim, S.-C. | 1087-1095B |
| Nesterenko, V.F. | 2575-2586A | Phatak, K.M. | 1139-1150B | | 1675-1086A | Shimada, M. | 2257-2266A |
| Neuschütz, D. | 983-991B | Phelan, D. | 3701-3706A | | 1969-1979A | Shimpo, T. | 277-284B |
| Newby, M. | 2115-2125A | Phillion, A. | 1237-1242A | Romero Serrano, J.A. | 957-966B | Shin, D.H. | 825-837A |
| Ng, B.-C. | 1151-1158A | Philkowski, A. | 3775-3786A | Romig, A.D., Jr. | 1021-1028B | Shin, K.S. | 1629-1632A |
| Ng, C. | 351-361B | Piehler, H.R. | 513-524A | | 3641-3648A | Shin, N.S. | 1663-1668A |
| Ng, K.W. | 405-406B | Pillai, U.T.S. | 1029-1039B | Rong, L.-J. | 2783-2788A | Shindo, Y. | 3797-3802A |
| | 406-408B | Pineau, A. | 797-811A | Roviglione, A.N. | 313-330B | Shiue, R.K. | 3177-3186A |
| Nguyen, F. | 813-823A | | 813-823A | Rowley, D. | 2587-2607A | Shome, M. | 985-996A |
| Ni, J. | 1565-1577A | | 1039-1053A | Ruiz, M.D.C. | 439-448B | Shun, T.-T. | 1465-1469A |
| Nicolaou, P.D. | 655-663A | Pirzada, M.D.S. | 1899-1903A | Russell, A.M. | 695-705A | | 2533-2536A |
| | 1141-1149A | Plapp, M. | 1815-1828A | Rutherford, R.W. | 2617-2624A | Siciliano, F. | 3024-3029A |
| Nicolas, M. | 2187-2190A | Polidoro, P. | 1151-1158A | Ryu, J.H. | 481-492A | Sidhom, H. | 3499-3513A |
| Nielsen, Ø. | 1437-1448A | Pollaine, S.M. | 2587-2607A | Ryu, W.-S. | 3331-3333A | Sietsma, J. | 425-433A |
| Nogi, K. | 2903-2915A | Pollock, T.M. | 2557-2566A | Sachs, E. | 631-640A | | 1889-1898A |
| | 583-588A | | 3221-3231A | Sade, M. | 641-653A | | 2789-2797A |
| Nogita, K. | 2861-2867A | Pons, J. | 761-770A | Saha, D. | 83-91A | Sikka, V.K. | 1281-1288A |
| Nogueira, P.F. | 959A | Poole, W.J. | 3363-3375A | | 381-392B | Simchi, A. | 937-948B |
| Noolu, N.J. | 829-838B | Poiths, R.M. | 2993-3001A | Sahajwalla, V. | 2174-2180A | Singer, R.F. | 939-946A |
| Nunes, A.C., Jr. | 1273-1280A | Pownceby, M.I. | 929-936B | Sakamoto, H. | 75-83B | | 1337-1342A |
| Oates, W.A. | 777-783B | Prabhu, N. | 189-203A | Saldívar-García, A.J. | 2229-2238A | Singh Raman, R.K. | 2525-2531A |
| Oehring, M. | 867-876B | | 205-216A | Salishchev, G.A. | 2517-2523A | Singh, A.K. | 925-938A |
| Ogasawara, T. | 3563-3570A | Prado, J.M. | 1097-1103A | Samuel, F.H. | 2809-2819A | Singh, S.B. | 1381-1391A |
| Okawa, M. | 847-855B | Prasanna Kumar, T.S. | 575-585B | Sánchez-Pérez, R. | 3233-3250A | Singheiser, L. | 867-876B |
| Oh, J.C. | 331-338B | Purdy, G.R. | 1187-1210A | | 85-99B | Sinha, V. | 3141-3148A |
| | 139-151A | | 1223-1235A | Sanders, T.H., Jr. | 449-460B | Sivaramakrishnan, S. | 967-982B |
| Oh, K.H. | 525-534A | Quintero, A. | 1237-1242A | Sano, N. | 341-350A | Slane, J.A. | 2239-2245A |
| Oh, M.S. | 1075-1086A | Quiroga, A. | 3581-3593A | | 1263-1272A | Smith, G.D.W. | 1223-1235A |
| Oh, Y.-J. | 3071-3077A | Racz, A. | 3543-3550A | Sanoso, F. | 3113-3127A | Smuk, O. | 2103-2109A |
| Ohishi, K. | 825-837A | Radmilovic, V. | 2305-2311A | Santamaria, R. | 761-770A | Sobczak, N. | 911-923A |
| Ohmi, T. | 2951-2961A | Radziwill, W. | 911-923A | Santos, C.A. | 285-297B | Soboyejo, A.B.O. | 163-187A |
| Ohnuma, I. | 333-339A | Rafflenbeul, L. | 631-640A | Sasaki, Y. | 517-522B | Soboyejo, W.O. | 163-187A |
| | 1243-1253A | Raffinfor, W.M. | 2993-3001A | Sato, M. | 111-119A | Sohn, H.S. | 651-661B |
| | 1641-1654A | Raj, B. | 1799-1806A | Sato, T. | 3029-3032A | Sohn, H.Y. | 121-131B |
| Oho, K. | 3029-3032A | Raj, D.D. | 867-876B | Sato, Y.S. | 331-338B | | 651-661B |
| Ohira, T. | 3469-3476A | Raj, I.E. | 1471-1476A | Savithri, S. | 1029-1039B | Sohn, K. | 465-469A |
| Ohtera, I. | 535-542A | Raj, S.V. | 1632-1635A | Savran, V.I. | 3551-3561A | Soler, M. | 1655-1661A |
| Ohuchi, T. | 471-486B | Ramesh, K.T. | 2279-2286A | Sawada, K. | 1255-1262A | Son, J. | 3431-3438A |
| Oishi, T. | 651-661B | | 3439-3444A | Sawaguchi, T. | 111-119A | Song, H.S. | 269-275B |
| Okabe, T.H. | 817-824B | Ramírez, M. | 363-372B | Sawla, S. | 1369-1379A | Song, J.M. | 952-957A |
| Okada, I. | 1779-1787A | | 373-380B | Saylor, D.M. | 1969-1979A | Sota, R. | 3029-3032A |
| Okamoto, N.L. | 2229-2238A | Ramos, F.D. | 3523-3530A | Scarlett, N.V.Y. | 1981-1989A | Spigarelli, S. | 293-300A |
| Okazaki, K. | 3323-3328A | Ramos, J.P. | 85-99B | Schacherl, R.E. | 929-936B | | 2963-2970A |
| Okazaki, M. | 535-542A | Ramos-Banderas, A. | 449-460B | Schmid-Fetzer, R. | 3387-3398A | N. | 599-605A |
| Olive, J.M. | 3515-3521A | Ranjan, M. | 3707-3720A | Schneider, J.A. | 3349-3362A | Srivastava, P.K. | 599-605A |
| Olivier, E. | 879-889A | Rao, C.S. | 65-74B | Schneider, M. | 777-783B | Stan, M. | 2267-2278A |
| Oltra, R. | 3515-3521A | | | Schneider, M.S. | 2587-2607A | Stangeland, A. | 2903-2915A |
| Ono, K. | 1289-1300A | | | | 2633-2646A | Starink, M.J. | 771-783A |

| | | | | | | | |
|-------------------|------------|--------------------|------------|----------------------|------------|-------------------|------------|
| Stauffer, A.C. | 1317-1324A | Thomas, M. | 1151-1172B | Wark, J.S. | 2587-2607A | Yao, H.T. | 1351-1357A |
| Stefanescu, D.M. | 613-621A | Thompson, M.O. | 2087-2102A | Warner, N.A. | 663-674B | Yao, Z.M. | 356-362A |
| | 623-629A | Tian, H. | 2803-2807A | Was, G.S. | 717-718A | Yasuda, K. | 2257-2266A |
| | 1525-1538A | Timokhina, I.B. | 3334-3339A | Watanabe, C. | 3003-3008A | Yeh, J.-W. | 1465-1469A |
| Stevenson, R. | 2471-2485A | Tin, S. | 2331-2341A | Watanabe, M. | 355-356A | | 2533-2536A |
| StJohn, D.H. | 1151-1158A | Tinoco, J. | 3221-3231A | Watanabe, S. | 1517-1524A | Yeh, M.S. | 3817-3821A |
| | 1097-1106B | Tischler, J.Z. | 2869-2879A | Watanabe, T. | 1757-1764A | Yin, F. | 665-677A |
| | 1929-1837A | Tiwari, R. | 1963-1967A | Watkinson, A.P. | 1517-1524A | Yin, Z. | 1203-1207B |
| Stobbs, W.M. | 733-740A | Tomé, C.N. | 2927-2934A | Weakley-Bollin, S.C. | 1059-1070B | Ying, D.Y. | 2115-2125A |
| Stölken, J.S. | 2587-2607A | Tong, M. | 3763-3774A | Weaver, D.S. | 2407-2418A | Yokobori, T., Jr. | 1757-1764A |
| Stoudt, M.R. | 2427-2437A | Tong, S.-X. | 1565-1577A | Weber, S.V. | 679-693A | Yokoi, D. | 1289-1300A |
| Stout, M. | 2767-2781A | Totermeier, T.C. | 217-221B | Wei, F. | 2587-2607A | Yokoyama, Y. | 15-23A |
| Strizak, J.P. | 965-972A | Trapaga, G. | 1807-1814A | Wei, F.G. | 503-511A | | 1289-1300A |
| Strohaecker, T.R. | 3334-3339A | Trivedi, R. | 363-372B | | 587-597B | Yoo, C.-S. | 2057-2061A |
| | 153-162A | Tsai, C.-H. | 373-380B | Wei, X. | 3155-3163A | Yoo, M.S. | 1629-1632A |
| | 3523-3530A | Tsujii, N. | 909-917B | Weitzer, F. | 2111-2114A | Yoon, C.S. | 2057-2061A |
| Sturel, T. | 1039-1053A | Tsukamoto, S. | 2533-2536A | Wells, M.A. | 1613-1628A | Yoshikawa, N. | 847-855B |
| Sturz, L. | 239-246A | Tsuzaki, K. | 1289-1300A | | 523-540B | Yoshikawa, T. | 277-284B |
| Su, Y.-F. | 1055-1065A | | 331-338B | Wessén, M. | 3843-3854A | Youn, S.W. | 769-776B |
| | 1113-1124A | | 587-597B | Westerhoff, F. | 309-319A | | 2419-2426A |
| Subramanian, R. | 1945-1952A | Tu, G.C. | 3155-3163A | White, C.T. | 2719-2723A | Yu, F. | 2487-2494A |
| Suh, D.-W. | 3399-3408A | Turchi, P.E.A. | 1351-1357A | Whitehouse, A.F. | 2647-2650A | Yuan, Q. | 685-702B |
| Suk, M.-O. | 1087-1095B | Turner, R.E. | 2305-2311A | Wickins, M. | 695-705A | | 703-714B |
| Sun, J. | 1301-1309A | Tuset, J.K. | 3015-3018A | Wilkinson, D.S. | 785-803B | | 967-982B |
| | 1725-1734A | Tyber, J. | 398-400B | | 949-952A | Yuan, Z. | 1613-1628A |
| Sun, P.-L. | 2073-2085A | Tyson, W.R. | 2013-2025A | Williams, D.B. | 1839-1851A | Yue, S. | 3823-3832A |
| Sundararajan, T. | 1359-1368A | Ueda, S. | 1410-1414A | Williams, J.C. | 355-356A | Yun, E. | 525-534A |
| Suri, P. | 3187-3199A | Umakoshi, Y. | 181-182B | Williamson, R.L. | 3141-3148A | | 1029-1038A |
| Sutcliffe, M.P.F. | 257-263A | Umazawa, O. | 2845-2852A | Willis, M. | 101-113B | Zahrah, T.F. | 3455-3460A |
| Suwas, S. | 919-928B | Unocic, R.R. | 543-553A | Wilshire, B. | 563-571A | Zarandi, F. | 1603-1611A |
| Suyitno | 925-938A | Usta, M. | 143-152B | | 563-571A | Zeman, G. | 3823-3832A |
| | 1325-1335A | Valdez, M. | 435-438A | Wilson, E.A. | 1691-1701A | Zeng, D. | 2821-2828A |
| | 2917-2926A | Valle, R. | 179-181B | Wolf, D.E. | 352-355A | Zeng, D. | 2111-2114A |
| | 3551-3561A | | 3289-3305A | Wolfer, W.G. | 2719-2723A | Zerilli, F.J. | 2547-2555A |
| Suzuki, A. | 1927-1933A | Valsan, M. | 3307-3317A | Wolverton, C. | 2239-2245A | Zhang, C. | 1263-1272A |
| Suzuki, K. | 333-339A | van der Zwaag, S. | 3129-3139A | | 2407-2418A | | 1927-1933A |
| Svoboda, M. | 751-759A | | 425-433A | Wright, R.N. | 435-438A | Zhang, D.L. | 2115-2125A |
| Swank, W.D. | 1807-1814A | | 741-749A | | 1807-1814A | Zhang, F. | 3015-3018A |
| Swinbourne, D.R. | 197-202B | | 1889-1898A | Wright, T.W. | 2651-2661A | Zhang, G.J. | 1725-1734A |
| Sylvén, E. | 1745-1755A | Van Ooij, W.J. | 2789-2797A | Wu, F. | 1105-1111A | Zhang, J. | 439-456A |
| Szewczyk, S.T. | 1125-1131A | Vander Sande, J.B. | 3707-3720A | Wu, N.Q. | 1281-1288A | | 939-946A |
| Tabuchi, M. | 1757-1764A | Vandyoussefi, M. | 3091-3101A | Wu, S.H. | 2455-2469A | | 1337-1342A |
| Takahashi, H. | 333-339A | | 607-612A | Wu, S.K. | 3177-3186A | Zhang, J.X. | 1911-1914A |
| Takaku, Y. | 1243-1253A | Vanka, S.P. | 1067-1073A | Wu, X. | 133-141B | Zhang, L.-Q. | 217-221B |
| Takasugi, T. | 3469-3476A | | 685-702B | | 1477-1486A | Zhang, P. | 1203-1207B |
| Takeuchi, E. | 1311-1316A | | 703-714B | Wu, Y. | 257-263A | Zhang, Y. | 133-141B |
| Talonen, J. | 2401-2406A | Vargas-Zamora, A. | 967-982B | Wynne, B.P. | 2993-3001A | | 182-186B |
| Tamagawa, T. | 625-631B | Vasudevan, V.K. | 247-257B | Xia, J.L. | 839-845B | | 509-515B |
| Tan, B.H. | 952-957A | Veyssiére, P. | 3707-3720A | Xiao, L. | 2845-2852A | | 1565-1577A |
| Tan, P. | 983-991B | Vidal-Sétf, M.-H. | 2223-2228A | | 3477-3487A | Zhang, Y.M. | 857-866B |
| Tanaka, K. | 2229-2238A | | 3289-3305A | Xing, L. | 153-160B | Zhang, Z. | 947-949A |
| Tanaka, M. | 625-631B | Vignal, V. | 3307-3317A | Xiong, Y. | 2111-2114A | Zhang, Z.F. | 3489-3498A |
| Taneike, M. | 1255-1262A | Vite-Martinez, P. | 3515-3521A | Xu, B. | 2511-2515A | Zhao, Y.M. | 3613-3629A |
| Tang, A. | 2757-2766A | Vivet, S. | 957-966B | Xu, H. | 1613-1628A | Zhao, Z. | 2487-2494A |
| Tanguy, D. | 2609-2615A | Vizcaino, P. | 1449-1464A | Xu, K. | 715-720B | Zheng, Y.G. | 356-362A |
| Taniguchi, S. | 847-855B | Voller, V.R. | 2343-2349A | Xu, S. | 1410-1414A | Zhigilei, L.V. | 2587-2607A |
| Tao, D.P. | 419-424A | Vyrostkova, A. | 285-297B | Xu, Y.B. | 2575-2586A | Zhong, X. | 715-720B |
| Taylor, J.A. | 1097-1106B | Waite, P. | 751-759A | Xun, Y. | 573-581A | Zhou, F. | 947-949A |
| | 1829-1837A | Waldner, P. | 999-1009B | Yaakobi, B. | 2587-2607A | Zhou, H. | 1779-1787A |
| | 3531-3541A | Walter, P. | 897-907B | Yamaguchi, K. | 1311-1316A | Zhou, Y. | 217-226A |
| Teague, J. | 2767-2781A | Wang, C.P. | 2223-2228A | Yamaguchi, M. | 2229-2238A | | 1173-1185B |
| Teklu, A. | 3149-3154A | | 1243-1253A | Yamaguchi, S. | 487-492B | | 3165-3176A |
| Teng, H.-Y. | 471-480A | Wang, G. | 1641-1654A | Yamashita, T. | 1263-1272A | | 3251-3263A |
| Teng, L.D. | 3673-3680A | | 15-23A | Yan, D.-S. | 2783-2788A | | 3265-3273A |
| Terada, Y. | 3029-3032A | Wang, G.Z. | 857-866B | Yan, S. | 197-202B | | 3595-3603A |
| Tewari, A. | 1789-1798A | | 439-456A | Yang, A. | 2111-2114A | Zhu, J. | 3633-3635A |
| Tewari, R. | 189-203A | Wang, H. | 1765-1778A | Yang, B. | 15-23A | Zhu, M.F. | 2313-2321A |
| | 205-216A | Wang, J. | 839-848A | Yang, F. | 3323-3328A | Zhu, S. | 1555-1563A |
| | 3707-3720A | Wang, Q.G. | 279-286A | Yang, J. | 1681-1690A | Zimmermann, G. | 2853-2859A |
| Tewari, S.N. | 1632-1635A | Wang, T. | 2707-2718A | Yang, K. | 2747-2755A | Zou, W. | 239-246A |
| | 2927-2934A | Wang, Y.N. | 2313-2321A | Yang, K.L. | 3803-3815A | Zurob, H.S. | 217-221B |
| Thakur, S.K. | 1167-1176A | | 555-562A | Yang, S.J. | 2161-2170A | Zybin, S.V. | 1237-1242A |
| Thomas, B.G. | 685-702B | | 2455-2469A | | 2971-2979A | | 2647-2650A |
| | 703-714B | | 3803-3815A | | 1963-1967A | | |
| | 967-982B | Wang, Z.-C. | 217-221B | | | | |



Combined Subject Index

- Abrasion resistance**
Correlation of Microstructure and Abrasive and Sliding Wear Resistance of (TiC,SiC)/Ti-6Al-4V Surface Composites Fabricated by High-Energy Electron-Beam Irradiation. 139-151A
Mechanical Properties of Al-60 Pct SiCp Composites Alloyed with Mg. 2127-2141A
- Abrasive wear**
Correlation of Microstructure and Abrasive and Sliding Wear Resistance of (TiC,SiC)/Ti-6Al-4V Surface Composites Fabricated by High-Energy Electron-Beam Irradiation. 139-151A
Solid Particle Erosion of Al Alloy and Al-Alloy Composites: Effect of Heat Treatment and Angle of Impingement. 1369-1379A
- Absolute zero**
Standard Gibbs Energy of Formation of Mg48Zn52 Determined by Solution Calorimetry and Measurement of Heat Capacity from Near Absolute Zero Kelvin. 891-895B
- Absorption**
Hydrogen Absorption of Incoherent TiC Particles in Iron from Environment at High Temperatures. 3155-3163A
- Accident prevention**
Numerical Analysis of Metal Transfer in Gas Metal Arc Welding under Modified Pulsed Current Conditions. 857-866B
- Acetone**
Response of Primary Dendrite Spacing to Varying Temperature Gradient during Directional Solidification. 735-742B
- Acicular structure**
Effect of Simulated Thermal Cycles on the Microstructure of the Heat-Affected Zone in HSLA-80 and HSLA-100 Steel Plates. The Microstructural Response of Delta-Stabilized Plutonium to Pulsed Laser Welding. 985-996A
2445-2454A
- Acid leaching**
Thermodynamic Study of the Effect of Calcium on Removal of Phosphorus from Silicon by Acid Leaching Treatment. 277-284B
- Activation energy**
Recrystallization Behavior of a Heavily Cold-Rolled Ni₃Al (B,Zr) Alloy. 71-81A
The influence of chemical equilibrium on fluid-solid reaction rates and the falsification of activation energy. 121-131B
Kinetics of Chlorination of Tantalum Pentoxide in Mixture with Sucrose Carbon by Chlorine Gas. 439-448B
Precise Determination of the Activation Energy for Desorption of Hydrogen in Two Ti-Added Steels by a Single Thermal-Desorption Spectrum. 587-597B
Reduction of Cobalt Oxide With Methane. 825-828B
Temperature-Dependent Variability in Lifetime Prediction of Thermally Activated Systems. 1471-1476A
Characterization of the Nucleation and Growth Behavior of Copper Precipitates in Low-Carbon Steels. 2323-2329A
Coarsening of Al₃Sc precipitates in an Al-0.28 Wt pct Sc alloy. 3003-3008A
Ductility Exhaustion Mechanisms in Thermally Exposed Thin Sheets of a Near- β Titanium Alloy. 3113-3127A
Effects of Temperature and Strain Rate on Tensile Properties and Activation Energy for Dynamic Strain Aging in Alloy 625. 3129-3139A
- Activity (chemical)**
A Comparison of the Molecular Interaction Volume Model with the Subregular Solution Model in Multicomponent Liquid Alloys. 419-424A
- Adhesion**
Effect of Surface Modification of High-Density Polyethylene by Direct Current and Radio Frequency Glow Discharge on Wetting and Adhesion Characteristics. 865-877A
- Adhesive bonding**
Effect of Surface Modification of High-Density Polyethylene by Direct Current and Radio Frequency Glow Discharge on Wetting and Adhesion Characteristics. 865-877A
- Adhesive joints**
Effect of Surface Modification of High-Density Polyethylene by Direct Current and Radio Frequency Glow Discharge on Wetting and Adhesion Characteristics. 865-877A
- Adhesive strength**
Effect of Thermal Spray on the Microstructure and Adhesive Strength of High Velocity Oxy-Fuel-Sprayed Ni-Cr Coatings on 9Cr-1Mo Steel. 3187-3199A
- Adiabatic flow**
Effects of Martensite Morphology and Tempering on Dynamic Deformation Behavior of Dual-Phase Steels. 2371-2382A
Dynamic Deformation Behavior and Ballistic Impact Properties of Ti-6Al-4V Alloy Having Equiaxed and Bimodal Microstructures. 3103-3112A
On the Isotropy of the Dynamic Mechanical and Failure Properties of Swaged Tungsten Heavy Alloys. 3787-3795A
Fracture Behavior of Thick-Section Weldment in Fe-12Cr-12Ni-10Mn-0.24N Stainless Steel at Liquid Helium Temperature. 3797-3802A
- Adsorption**
Communication: Grain Boundary Engineering of Ferritic-Martensitic Alloy T91. 717-718A
- Aerospace**
Analysis of Diffusive Cellular Patterns in Directional Solidification of Bulk Samples. 239-246A
Communication: Resonant Vibration Behavior of an Al-3.8Cu-0.8Li-0.3Mg Alloy. 952-957A
Effect of Mg₂Si Particles on the Elevated Temperature Tensile Properties of Squeeze-Cast Mg-Al Alloys. 1629-1632A
- Age hardening**
Modeling the Age-Hardening Behavior of Al-Si-Cu Alloys. 2407-2418A
- Agglomerates**
Correlation of Microstructure with Hardness and Wear Resistance in (TiC,SiC)/Stainless Steel Surface Composites Fabricated by High-Energy Electron-Beam Irradiation. 1029-1038A
- Agglomeration**
The Role of Particle Size on the Laser Sintering of Iron Powder. 937-948B
Effect of Clustering of Precipitates on Grain Growth. 1097-1103A
Tensile behavior of friction-stir-welded A356-T6/Al 6061-T651 Bi-alloy plate. 2837-2843A
- Aging**
Evolution of Secondary Phases in Cr-V Low-Alloy Steels during Aging. 751-759A
Communication: Resonant Vibration Behavior of an Al-3.8Cu-0.8Li-0.3Mg Alloy. 952-957A
Effect of Aging and Deformation on the Microstructure and Properties of Fe-Ni-Ti Maraging Steel. 973-983A
Precipitate Microstructures and Resulting Properties of Al-Zn-Mg Metal Inert Gas-Weld Heat-Affected Zones. 1437-1448A
Validation of Predicted Precipitate Compositions in Al-Si-Ge. Microstructure and mechanical properties of a 2000 MPa Co-free maraging steel after aging at 753 K. 2305-2311A
Tensile properties and microstructure of Haynes 25 alloy after aging at elevated temperatures for extended times. 2747-2755A
Communication: Evaluation of aging precipitation kinetics and potential in aluminum alloys using indiscriminately integrated peak areas in calorimetry curves. 2767-2781A
Characterization of Retrogression and Reaging Behavior of 8090 Al-Li-Cu-Mg-Zr Alloy. 3012-3015A
Communication: Room-Temperature Cleavage Fracture of FeMnAlC Steels. 3681-3691A
3863-3866A
- Aging (artificial)**
Communication: Discussion of "Precipitation of Austenite Particles at Grain Boundaries during Aging of Fe-Mn-Ni Steel". 352-355A
Communication: Authors' Reply. 355-356A
Cu Precipitation in a Prestrained Fe-1.5 Wt Pct Cu Alloy during Isothermal Aging. 1263-1272A
Quality Assessment of Artificially Aged A357 Aluminum Alloy Cast Ingots by Introducing Approximate Expressions of the Quality Index QD. 3079-3089A
- Aircraft components**
Communication: Casting of Aluminum-Based Wrought Alloys Using Controlled Diffusion Solidification. 2174-2180A
- Aircraft components, Mechanical properties**
A New Quality Index for Characterizing Aluminum Cast Alloys with Regard to Aircraft Structure Design Requirements. 301-308A
- Aircraft industry**
Studies of Lattice Imperfections in Deformed Aluminum-Based Lithium Alloys by X-Ray Diffraction. 3319-3322A
- Alloy powders**
Preparation of Cu-Ni Alloys through a New Chemical Route. 1107-1112B
Mechanochemical Processing of Nanocrystalline Ti-6Al-4V Alloy. 1899-1903A
- Alloy steels**
Characterization of the peritectic reaction in medium-alloy steel through microsegregation and heat-of-transformation studies. Role of Carbon and Alloying Elements in the Formation of Bainitic Ferrite. 2869-2879A
3693-3700A
- Alloy systems**
Defect Structures and Room Temperature Mechanical Properties of C15 Laves Phases in Zr-Nb-Cr and Zr-Hf-Cr Alloy Systems. 3469-3476A
- Alloying additive**
Carbides in high-speed steels containing silicon. 2757-2766A
Communication: A thousandfold creep strengthening by Ca addition in die-cast AM50 magnesium alloy. 3029-3032A
Communication: Eutectic solidification of aluminum-silicon alloys. 3038-3043A
- Alloying effects**
Effect of the Presence of Alloying Elements in Interstitial-Free and Low-Carbon Steels on Their Surface Composition after Annealing in Reducing Atmospheres (Dew Point = -30 °C). Mechanical Properties of Al-60 Pct SiCp Composites Alloyed with Mg. 2127-2141A
Carbides in high-speed steels containing silicon. The Influence of Strontium on Porosity Formation in Al-Si Alloys. 2757-2766A
3531-3541A
- Alloying elements**
Phase Equilibrium and Distribution of Minor Elements between Ni-S Melt and Al₂O₃-CaO-MgO Slag at 1873 K. 1041-1049B
Communication: Eutectic solidification of aluminum-silicon alloys. 3038-3043A
Communication: Tensile Properties of Chromium Alloyed with Silver. 3329-3331A
- Alpha iron**
Characterization of Three-Dimensional Grain Structure in Polycrystalline Iron by Serial Sectioning. 1927-1933A

| | | |
|--|------------|--------------------------|
| Alpha particles | | |
| Coarsening behavior of an alpha-beta titanium alloy. | 2809-2819A | 769-776B 909-917B |
| Alternating current | | |
| Simulation of Flow Control in the Meniscus of a Continuous Casting Mold with Opposing Alternating Current Magnetic Fields | 1129-1137B | 919-928B 999-1009B |
| Aluminates | | |
| Application of the Generalized Method of Cells Principle to Particulate-Reinforced Metal Matrix Composites | 1029-1039B | 1029-1039B |
| Effects of Simultaneous Displacive and Ionizing Radiations and of Electric Field on Radiation Damage in Ionic Crystals. | 2257-2266A | 1097-1106B |
| Aluminides | | |
| The Development and Experimental Validation of a Numerical Model of an Induction Skull Melting Furnace. | 785-803B | 1173-1185B |
| Nickel-Aluminides/Steel Clad Pipe Fabricated by Reactive Centrifugal Casting Method from Liquid Aluminum and Solid Nickel. | 1517-1524A | 1187-1202B 1325-1335A |
| Microstructural Evolution in Iron Aluminide Fe-28Al-2C after High-Temperature Hydrogen Treatment. | 1789-1798A | 1359-1368A |
| Influence of Microstructure on Tensile and Creep Properties of a New Castable TiAl-Based Alloy. | 2087-2102A | 1369-1379A |
| Communication: Determination of γ Phase Lattice Parameter Based on the Chemical Concentration of Its Sublattices in Ni-Base Superalloys. | 2171-2172A | 1381-1391A |
| Mechanisms of Hf Dopant Incorporation during the Early Stage of Chemical Vapor Deposition Aluminide Coating Growth under Continuous Doping Conditions | 3581-3593A | 1393-1401A |
| Aluminides, Coatings | | |
| Effects of Preheating on Morphological Development of a Chemical Vapor Deposition Aluminide Coating Formed on Single-Crystal Ni-Based Superalloy. | 891-897A | 1403-1406A 1407-1410A |
| Aluminides, Composite materials | | |
| Fabrication of Carbide-Particle-Reinforced Titanium Aluminide-Matrix Composites by Laser-Engineered Net Shaping. | 1133-1140A | 1425-1435A |
| Aluminides, Mechanical properties | | |
| Study on Notch Fracture of TiAl Alloys at Room Temperature. | 439-456A | 1437-1448A |
| Aluminides, Microstructure | | |
| Recrystallization Behavior of a Heavily Cold-Rolled Ni ₃ Al (B,Zr) Alloy. | 71-81A | 1487-1499A 1525-1538A |
| Aluminides, Phase transformations | | |
| Dynamic Phase Transformation during Superplastic Deformation of Nb/Nb ₃ Al In-Situ Composite. | 503-511A | 1555-1563A |
| Aluminizing | | |
| Effects of Preheating on Morphological Development of a Chemical Vapor Deposition Aluminide Coating Formed on Single-Crystal Ni-Based Superalloy. | 891-897A | 1691-1701A |
| Mechanisms of Hf Dopant Incorporation during the Early Stage of Chemical Vapor Deposition Aluminide Coating Growth under Continuous Doping Conditions | 3581-3593A | 1725-1734A |
| Aluminous refractories | | |
| On Different Modifications of the Capillary Model of Penetration of Inert Liquid Metals into Porous Refractories and their Connection to the Pore Size Distribution of the Refractories. | 471-486B | 1799-1806A 1829-1837A |
| Aluminum | | |
| Experimental Study of Phase Equilibria in the Al-Fe-Zn-O System in Air. | 633-642B | 1839-1851A |
| Reaction Sequences in the Formation of Silico-Ferrites of Calcium and Aluminum in Iron Ore Sinter. | 929-936B | 1853-1860A |
| Communication: The Pressure of Al ₂ O ₃ and Al in Equilibrium with an Al ₂ O ₃ -Al ₄ C ₃ (Saturated) Slag at 1950°C to 2020°C. | 1011-1013B | 1953-1961A |
| A Thermodynamic Description of the Al-Mn-Si System over the Entire Composition and Temperature Ranges. | 1613-1628A | 1969-1979A |
| Modeling of Lattice Parameter in the Ni-Al System. | 2313-2321A | 2115-2125A |
| The Behavior and Effect of Rare Earth CeO ₂ on In-Situ TiC/Al Composite. | 2511-2515A | 2127-2141A |
| Molecular-dynamics study of mechanical deformation in nanocrystalline aluminum. | 2719-2723A | 2153-2160A |
| Nonequilibrium molecular dynamics simulations of metallic friction at Ta/Al and Cu/Ag interfaces. | 2741-2745A | 2172-2174A |
| Communication: Diffusion coefficients for modeling the heat treatment of Ti-6Al-4V. | 3015-3018A | 2172-2180A |
| Variability of Large-Crack Fatigue-Crack-Growth Thresholds in Structural Alloys | 3721-3735A | 2191-2192A |
| Aluminum, Composite materials | | |
| Reactive Wetting of SiO ₂ Substrates by Molten Al. | 583-588A | 2291-2303A 2305-2311A |
| Aluminum base alloys | | |
| Analytical, Numerical, and Experimental Analysis of Inverse Macroregression during Upward Unidirectional Solidification of Al-Cu Alloys. | 285-297B | 2383-2392A 2407-2418A |
| Determination of Interfacial Heat-Transfer Boundary Conditions in an Aluminum Low-Pressure Permanent Mold Test Casting. | 299-311B | 2419-2426A |
| Surface-Oriented Melt/Substrate Heat-Transfer Model in Aluminum Strip Casting. | 351-361B | 2439-2444A |
| Communication: Discussion of "Thermodynamics of Liquid Al-Na Alloys Determined by Using CaF ₂ Solid Electrolyte". | 393-398B | 2471-2485A |
| Communication: Authors' Reply. | 398-400B | 2487-2494A |
| Fluid Flows in Metallurgy: Friend or Foe? | 417-437B | 2495-2501A |
| On the Development of a Three-Dimensional Transient Thermal Model to Predict Ingot Cooling Behavior during the Start-Up Phase of the Direct Chill-Casting Process for an AA5182 Aluminum Alloy Ingot. | 523-540B | 2503-2510A 2625-2631A |
| Estimation of Multiple Heat-Flux Components at the Metal/Mold Interface in Bar and Plate Aluminum Alloy Castings. | 575-585B | 2707-2718A |
| Mechanism and Rate of Reaction of Al ₂ O ₃ , Al, and CO Vapors with Carbon. | 617-623B | 2725-2728A 2829-2835A |
| A Model of the Interfacial Heat Transfer Coefficient for the Aluminum Gravity Die-Casting Process. | 721-733B | 2837-2843A 2881-2891A |
| Fabrication of Foamable Precursors by Powder Compression | | |
| and Induction Heating Process. | | |
| Diffusion-Coefficient Measurements in Liquid Metallic Alloys | | |
| The Effect of Surface Deformation on Lubrication and Oxide-Scale Fracture in Cold Metal Rolling | | |
| Study of Inclusion Re-Entrainment in a Filter Bed | | |
| Application of the Generalized Method of Cells Principle to Particulate-Reinforced Metal Matrix Composites | | |
| Modification-Related Porosity Formation in Hypoeutectic Aluminum-Silicon Alloys | | |
| A Numerical Study of Oxidation Behavior during Reactive Atomization and Deposition | | |
| Yield Behavior of Commercial Al-Si Alloys in the Semisolid State | | |
| Contraction of Aluminum Alloys during and after Solidification. | | |
| Effect of Deformation Route on Microstructural Development in Aluminum Processed by Equal Channel Angular Extrusion. | | |
| Solid Particle Erosion of Al Alloy and Al-Alloy Composites: Effect of Heat Treatment and Angle of Impingement. | | |
| Creep Behavior of a Rotating Functionally Graded Composite Disc Operating under Thermal Gradient. | | |
| Fracture Toughness of Selectively Reinforced Al2124 Alloy: Precrack Tip in the Composite Side. | | |
| Communication: Observed Dependencies of the Large Thermal-Compressive Response of a NiTi Shape-Memory Alloy Fiber Aluminum Metal Matrix Composite on Maximum Tensile Strain Imposed during a Preceding Room-Temperature Tensile Process. | | |
| Communication: Effect of Microstructure on Tensile Behavior of Thixoformed 357-T5 Semisolid Al Alloy. | | |
| The Solidification Characteristics of Fe-Rich Intermetallics in Al-11.5Si-0.4Mg Cast Alloys. | | |
| Precipitate Microstructures and Resulting Properties of Al-Zn-Mg Metal Inert Gas-Weld Heat-Affected Zones. | | |
| Microstructural Evolution in the Heat-Affected Zone of a Friction Stir Weld. | | |
| Interaction of Porosity with a Planar Solid/Liquid Interface. | | |
| Modeling of Irregular Eutectic Microstructures in Solidification of Al-Si Alloys. | | |
| Theoretical and Practical Implications of Creep Curve Shape Analyses for 2124 and 2419. | | |
| The Influences of Multiscale-Sized Second-Phase Particles on Ductility of Aged Aluminum Alloys. | | |
| Intermetallic Diffusion Coatings for Enhanced Hot-Salt Oxidation Resistance of Nitrogen-Containing Austenitic Stainless Steels. | | |
| Eutectic Grains in Unmodified and Strontium-Modified Hypoeutectic Aluminum-Silicon Alloys. | | |
| Effect of Thermomechanical Treatment on the Evolution of Rolling and Recrystallization Textures in Twin-Belt Cast AA5754 Aluminum Alloy. | | |
| A Study on the Microstructural Evolution of Al-25 Al. Pct V-12.5 Al. pct M (M = Cu, Ni, Mn) Powders by Planetary Ball Milling. | | |
| Quantitative Characterization of the Three-Dimensional Microstructure of Polycrystalline Al-Sn using X-Ray Microtomography. | | |
| Statistically Representative Three-Dimensional Microstructures Based on Orthogonal Observation Sections. | | |
| Solid-State Reactions during Heating Mechanically Milled Al/TiO ₂ Composite Powders. | | |
| Mechanical Properties of Al-60 Pct SiCp Composites Alloyed with Mg. | | |
| Effects of Carbon Fiber/Al Interface on Mechanical Properties of Carbon-Fiber-Reinforced Aluminum-Matrix Composites. | | |
| Communication: Quantification of Overaging Hardening Kinetics of Aluminum Alloys. | | |
| Communication: Casting of Aluminum-Based Wrought Alloys Using Controlled Diffusion Solidification. | | |
| Communication: A Brick-Wall Model for Calculating Young's Modulus of a Particulate Composite. | | |
| Effects of Changes in Test Temperature on Fatigue Crack Propagation of Al6090/SiCp-Al 6013 Laminated Metal Composites. | | |
| Validation of Predicted Precipitate Compositions in Al-Si-Ge. | | |
| Superplastic Behavior and Microstructure Evolution in a Commercial Al-Mg-Sc Alloy Subjected to Intense Plastic Straining. | | |
| Modeling the Age-Hardening Behavior of Al-Si-Cu Alloys. | | |
| Evaluation of Mechanical Properties of Porous 6061 Alloys Fabricated by the Powder Compression and Induction Heating Process. | | |
| Control of Residual Stresses Affecting Fatigue Life of Pulsed Current Gas-Metal-Arc Weld of High-Strength Aluminum Alloy. | | |
| A Quantitative Dendrite Growth Model and Analysis of Stability Concepts. | | |
| Effect of Low-Frequency Electromagnetic Casting on the Castability, Microstructure, and Tensile Properties of Direct-Chill Cast Al-Zn-Mg-Cu Alloy. | | |
| Influence of Convection on Feathering Grain Formation in Aluminum Alloys. | | |
| Study of the Porosity Produced in an Aluminum Alloy Matrix Composite Due to a T6 Heat Treatment. | | |
| High-pressure, laser-driven deformation of an aluminum alloy. | | |
| Plastic deformation behavior of aluminum casting alloys A356/357. | | |
| The effect of grain size on low-cycle fatigue behavior of Al-2024 polycrystalline alloy. | | |
| Tensile behavior of friction-stir-welded Al 6061-T651. | | |
| Tensile behavior of friction-stir-welded A356-T6/Al 6061-T651 Bi-alloy plate. | | |
| Segregation band formation in Al-Si die castings. | | |
| Effects of the entrained surface film on the reliability of castings. | | |

- Development of thermal strain in the coherent mushy zone during solidification of aluminum alloys. 2903-2915A
- Finite element method simulation of mushy zone behavior during direct-chill casting of an Al-4.5 pct Cu alloy. 2917-2926A
- Experimental and modeling studies of the thermal conditions and magnesium, iron, and copper content on the morphology of the aluminum silicon eutectic in hypoeutectic aluminum silicon alloys. 2981-2991A
- Coarsening of Al₃Sc precipitates in an Al-0.28 Wt pct Sc alloy. Communication: Evaluation of aging precipitation kinetics and potential in aluminum alloys using indiscriminately integrated peak areas in calorimetry curves. 3003-3008A
- Communication: Texture characterization of autogenous Nd:YAG laser welds in AA5182-O and AA6111-T4 aluminum alloys. 3012-3015A
- Communication: Eutectic solidification of aluminum-silicon alloys. 3032-3038A
- Quality Assessment of Artificially Aged A357 Aluminum Alloy Cast Ingots by Introducing Approximate Expressions of the Quality Index QD. 3038-3043A
- Nucleation of Solid Aluminum on Inclusion Particles Injected into Al-Si-Fe Alloys. 3079-3089A
- On the Influence of In-Situ Reactions on Grain Size during Reactive Atomization and Deposition. 3233-3250A
- An Analytical Model for the Oxide Size in Al Alloys Synthesized by Reactive Atomization and Deposition. 3251-3263A
- A Through-Process Model of an A356 Brake Caliper for Fatigue Life Prediction. 3265-3273A
- Tensile and Fatigue Behavior of Al-Based Metal Matrix Composites Reinforced with Continuous Carbon or Alumina Fibers: Part I. Quasi-Unidirectional Composites. 3275-3288A
- Tensile and Fatigue Behavior of Al-Based Metal Matrix Composites Reinforced with Continuous Carbon or Alumina Fibers: Part II. Quasi-Unidirectional Composite Cross-Ply Laminates. 3289-3305A
- Studies of Lattice Imperfections in Deformed Aluminum-Based Lithium Alloys by X-Ray Diffraction. 3307-3317A
- Microindentation of Aluminum. 3319-3322A
- Thermodynamic Aspects of the Constitution, Grain Refining, and Solidification Enthalpies of Al-Ce-Si Alloys. 3323-3328A
- Formability and Strength of Friction-Stir-Welded Aluminum Sheets. 3349-3362A
- The Influence of Strontium on Porosity Formation in Al-Si Alloys. 3461-3468A
- Effects of Alloy Composition and Casting Speed on Structure Formation and Hot Tearing during Direct-Chill Casting of Al-Cu Alloys. 3531-3541A
- Quantitative Analysis of Texture Evolution of Cold-Rolled Direct-Chill-Cast and Continuous-Cast AA5052 and AA5182 Aluminum Alloys during Isothermal Annealing. 3551-3561A
- Communication: The Transient to Steady-State Transition during the Spray-Rolling Process. 3613-3629A
- Characterization of Retrogression and Reaging Behavior of 8090 Al-Li-Cu-Mg-Zr Alloy. 3633-3635A
- Variability of Large-Crack Fatigue-Crack-Growth Thresholds in Structural Alloys. 3681-3691A
- Microstructure Characterization and Creep Deformation of an Al-10 Wt Pct Ti-2 Wt Pct Cu Nanocomposite. 3721-3735A
- 3855-3861A
- Aluminum base alloys, Binary systems**
- Correction to Metallurgical and Materials Transactions A, November 2003, vol. 34A, pp. 2690-2693: "Authors Reply" to Discussion of "Eutectic Solidification of Al-Si Alloys". 959A
- Erratum: A Solutal Interaction mechanism for the Columnar-to-Equiaxed Transition in Alloy Solidification. 1915A
- Aluminum base alloys, Composite materials**
- Quantifying Thermomechanical Fatigue of Light-Metal-Matrix Composites by Mechanical Spectroscopy. 25-35A
- Damage Evolution during Thermal Fatigue in Fiber-Reinforced Light-Metal-Matrix Composites. 37-43A
- Effects of Lamination and Changes in Layer Thickness on Fatigue-Crack Propagation of Lightweight Laminated Metal Composites. 45-52A
- Effect of Reinforcement-Particle-Orientation Anisotropy on the Tensile and Fatigue Behavior of Metal-Matrix Composites. 53-61A
- Effect of Temperature and Strain Rate on the Compressive Flow of Aluminum Composites Containing Submicron Alumina Particles. 287-292A
- Aluminum base alloys, Crystal growth**
- The Effect of Heat Treatment on Mg₂Si Coarsening in Aluminum 6105 Alloy. 435-438A
- Undercooling and Solidification of Al-50 At. Pct Si Alloy by Electromagnetic Levitation. 607-612A
- Aluminum base alloys, Crystal lattices**
- Advancing Towards Constitutive Equations for the Metal Industry via the LEDS Theory. 5-54B
- Advancing Towards Constitutive Equations for the Metal Industry via the LEDS Theory. 369-418A
- Aluminum base alloys, Mechanical properties**
- Characterizing Small Fatigue Cracks in Metallic Alloys. 7-14A
- A New Quality Index for Characterizing Aluminum Cast Alloys with Regard to Aircraft Structure Design Requirements. 301-308A
- Communication: Mechanical Behavior of a Cryomilled Nanostructured Al-7.5 pct Mg Alloy. 947-949A
- Communication: Resonant Vibration Behavior of an Al-3.8Cu-0.8Li-0.3Mg Alloy. 952-957A
- The Tensile Response of a Fine-Grained AA5754 Alloy Produced by Asymmetric Rolling and Annealing. 997-1006A
- Fracture Behavior of Thixoformed 357-T5 Al Alloys. 1017-1027A
- Aluminum base alloys, Microstructure**
- Quantitative Analysis of Texture Evolution in Cold-Rolled, Continuous-Cast AA 5xxx-Series Aluminum Alloys. 265-277A
- Microstructure Transformation from Lamellar to Equiaxed Microduplex through Equal-Channel Angular Pressing in an Al-33 Pct Cu Eutectic Alloy. 279-286A
- Microstructural Characterization of Secondary-Phase Particles in a Hot-Deformed Al-Cu-Mg-Zr Alloy. 293-300A
- A Study of Coarsening, Recrystallization, and Morphology of Microstructure in Al-Sc-(Zr)-(Mg) Alloys. 341-350A
- Formation of Mesoscale Roughening in 6022-T4 Al Sheets Deformed in Plane-Strain Tension. 513-524A
- A Single-Grain Approach Applied to the Modeling of Recrystallization Kinetics for Cold-Rolled Single-Phase Metals. 741-749A
- High-Strain-Rate Superplastic Behavior of Equal-Channel Angular-Pressed 5083 Al-0.2 Wt Pct Sc. 825-837A
- Communication: Effect of Thermomechanical Processing on Grain Structure Development in a Twin-Belt Strip Cast Automotive Aluminum Alloy. 949-952A
- Aluminum base alloys, Physical properties**
- Semi-Solid Rapid Compression Testing of Spray-Formed Hypereutectic Al-Si Alloys. 899-910A
- The Effect of Temperature, Matrix Alloying and Substrate Coatings on Wettability and Shear Strength of Al/Al₂O₃ Couples. 911-923A
- Aluminum base alloys, Powder technology**
- Hot Explosive Compaction of Aluminum-Nickel Composites. 1125-1131A
- Aluminum base alloys, Structural hardening**
- Dispersion Strengthening in a Hypereutectic Al-Si Alloy Prepared by Extrusion of Rapidly Solidified Powder. 333-339A
- Aluminum base alloys, Welding**
- Material Flow Patterns and Cavity Model in Friction-Stir Welding of Aluminum Alloys. 153-160B
- Electrode Pitting in Resistance Spot Welding of Aluminum Alloy 5182. 217-226A
- Aluminum bronzes**
- Microstructural modification of as-cast NiAl bronze by friction stir processing. 2951-2961A
- Aluminum compounds, Powder technology**
- Hot Explosive Compaction of Aluminum-Nickel Composites. 1125-1131A
- Aluminum killed steels**
- Experimental Determination of the Carbon Solubility Limit in Ferritic Steels. 1655-1661A
- Aluminum oxide**
- Amphoteric Behavior of Alumina in Viscous Flow and Structure of CaO-SiO₂-(MgO)-Al₂O₃ Slags. 269-275B
- Application of the Generalized Method of Cells Principle to Particulate-Reinforced Metal Matrix Composites. 1029-1039B
- Effects of Simultaneous Displacive and Ionizing Radiations and of Electric Field on Radiation Damage in Ionic Crystals. 2257-2266A
- Study of the Porosity Produced in an Aluminum Alloy Matrix Composite Due to a T6 Heat Treatment. 2503-2510A
- Tensile and Fatigue Behavior of Al-Based Metal Matrix Composites Reinforced with Continuous Carbon or Alumina Fibers: Part I. Quasi-Unidirectional Composites. 3289-3305A
- Tensile and Fatigue Behavior of Al-Based Metal Matrix Composites Reinforced with Continuous Carbon or Alumina Fibers: Part II. Quasi-Unidirectional Composite Cross-Ply Laminates. 3307-3317A
- Aluminum oxide, Coatings**
- Effects of Preoxidation on the Nucleation and Growth Behavior of Chemically Vapor-Deposited α -Al₂O₃ on a Single-Crystal Ni-Based Superalloy. 1113-1124A
- Aluminum oxide, Composite materials**
- Damage Evolution during Thermal Fatigue in Fiber-Reinforced Light-Metal-Matrix Composites. 37-43A
- Effect of Temperature and Strain Rate on the Compressive Flow of Aluminum Composites Containing Submicron Alumina Particles. 287-292A
- Aluminum oxide, Crystal growth**
- Effects of an α -Al₂O₃ Thin Film on the Oxidation Behavior of a Single-Crystal Ni-Based Superalloy. 1055-1065A
- Aluminum oxide, Reactions (chemical)**
- Communication: The Solubility of Titanium Dioxide in Cryolite-Alumina Melts at 1300 K. 182-186B
- Aluminum oxides**
- Communication: The Pressure of Al₂O and Al in Equilibrium with a Al₂O₃-Al₄C₃ (Saturated) Slag at 1950°C to 2020°C. 1011-1013B
- Aluminum silicates**
- Salt Roasting of Suncor Oil Sands Fly Ash. 1051-1058B
- Amorphous alloys**
- Two-Layered Zr-Base Amorphous Alloy/Metal Surface Composites Fabricated by High Energy Electron-Beam Irradiation. 3455-3460A
- Amorphous structure**
- A Study on the Microstructural Evolution of Al-25 At. Pct V-12.5 At. pct M (M = Cu, Ni, Mn) Powders by Planetary Ball Milling. 1853-1860A
- Anelasticity**
- Experimental and Theoretical Evidence for Carbon-Vacancy Binding in Austenite. 2239-2245A
- Anisotropy**
- The Influence of Texture, Strain Rate, Temperature, and Chemistry on the Mechanical Behavior of Hafnium. 1999-2011A
- Effects of Carbon Fiber/Al Interface on Mechanical Properties of Carbon-Fiber-Reinforced Aluminum-Matrix Composites. 2153-2160A
- A Quantitative Dendrite Growth Model and Analysis of Stability Concepts. 2471-2485A
- Shear localization-martensitic transformation interactions in Fe-Cr-Ni monocrystal. 2575-2586A
- A Micromechanical Analysis of the Yielding Behavior of Individ-

| | | | |
|---|------------|---|------------|
| ual Widmanstätten Colonies of an $\alpha + \beta$ Titanium Alloy | 3409-3422A | Self-Consistent Modeling and X-Ray Diffraction Analysis. | 2361-2369A |
| Neutron Diffraction Study of Texture Development during Hot Working of Different Gamma-Titanium Aluminide Alloys | 3563-3570A | Shear localization-martensitic transformation interactions in Fe-Cr-Ni monocrystal. | 2575-2586A |
| Inclusion-Controlled Fatigue Properties of 1800 MPA-Class Spring Steels | 3737-3744A | Study of the Ni41.3Ti38.7Nb20 wide transformation hysteresis shape-memory alloy. | 2783-2788A |
| On the Isotropy of the Dynamic Mechanical and Failure Properties of Swaged Tungsten Heavy Alloys | 3787-3795A | A novel observation of strain-induced ferrite-to-austenite retransformation after intercritical deformation of C-Mn steel. | 2789-2797A |
| Texture Evolution and Mechanical Anisotropy in Dual-Phase TiAl-Based Alloy Loaded at 700 °C to 1000 °C | 3803-3815A | Characterization of the peritectic reaction in medium-alloy steel through microsegregation and heat-of-transformation studies. | 2869-2879A |
| Annealing | | Communication: Effect of texture and microstructure on resistance to cracking of high-strength hot-rolled Nb-Ti microalloyed steels. | 3024-3029A |
| Grain-Size Effect on Shape-Memory Behavior of $\text{Ti}_{49}\text{Ni}_{49.7}\text{Zr}_{15.4}$ Thin Films. | 111-119A | Austenite Formation during Intercritical Annealing | 3363-3375A |
| The Tensile Response of a Fine-Grained AA5754 Alloy Produced by Asymmetric Rolling and Annealing. | 997-1006A | Effect of Initial Grain Size of Austenite on Hot-Deformed Structure of Ni-30Fe Alloy | 3399-3408A |
| Communication: Persistence of Superficial Contamination of Rolled Steel during Successive Treatments up to the Formation of a Galvanneal Coating. | 2185-2187A | Effect of Different Cr Contents on Tensile and Corrosion Behaviors of 0.13 Pct N-Containing CD4MCU Cast Duplex Stainless Steels | 3431-3438A |
| Oxide Dispersion Strengthening of Nickel Electrodeposits for Microsystem Applications. | 2351-2360A | Role of Carbon and Alloying Elements in the Formation of Bainitic Ferrite | 3693-3700A |
| Crystallographic textures in rolled and annealed Fe-Ga and Fe-Al alloys. | 2963-2970A | Austenitic stainless steels | |
| Microindentation of Aluminum | 3323-3328A | Fatigue Fracture Mechanism Maps for a Type 304 Stainless Steel. | 1311-1316A |
| Austenite Formation during Intercritical Annealing | 3363-3375A | Microstructural Banding and Failure of a Stainless Steel. | 1317-1324A |
| Antiphase boundaries | | The Effects of Strain Rate and Welding Current Mode on the Dynamic Impact Behavior of Plasma-Arc-Welded 304L Stainless Steel Weldments | 1501-1515A |
| Interfacial Segregation and Influence of Antiphase Boundaries on Rattling in a γ/γ' Alloy. | 733-740A | Experimental and Numerical Study on the Relationship between Creep Crack Growth Properties and Fracture Mechanisms. | 1757-1764A |
| Arc spraying | | Intermetallic Diffusion Coatings for Enhanced Hot-Salt Oxidation Resistance of Nitrogen-Containing Austenitic Stainless Steels. | 1799-1806A |
| Phase Transformations and Control of Residual Stresses in Thick Spray-Formed Steel Shells | 1113-1122B | Residual Stresses in High Velocity Oxy-Fuel Metallic Coatings. New Stereology for the Recovery of Grain-Boundary Plane Distributions in the Crystal Frame. | 1807-1814A |
| Armor, Mechanical properties | | Experimental and Theoretical Evidence for Carbon-Vacancy Binding in Austenite. | 1991-1998A |
| Communications: Ultra-High-Speed Exploding Properties of Ti-6Al-4V Alloy Having Equiaxed and Bimodal Microstructures. | 719-724A | Damping Properties of Austenitic Stainless Steels Containing Strain-Induced Martensite. | 2239-2245A |
| Assemblies | | The influence of explosive-driven 'Taylor-wave' shock prestraining on the structure/property behavior of 304 stainless steel. | 2401-2406A |
| Tensile Test Behavior of the Eutectic Sn-Ag Solder Joint in Ball Grid Array Assemblies | 3817-3821A | Marangoni convection in weld pool in CO ₂ -Ar-shielded gas thermal arc welding. | 2617-2624A |
| Asymmetry | | Microstructure Development during High Velocity Deformation Communication: The Observation and Identification of the Oxide Film on the Creep Cavity Wall of Type 316L Stainless Steel | 2861-2867A |
| Local Electromechanical Response at a Single Ferroelectric Domain Wall in Lithium Niobate. | 2287-2290A | Communication: Comparisons of Experimental Measurements and a Theoretical Model for Specimen Self-Heating during Fatigue of Type 316 LN Stainless Steel | 3091-3101A |
| Atomic force microscopy | | The Microstructural, Mechanical, and Fracture Properties of Austenitic Stainless Steel Alloyed with Gallium | 3331-3333A |
| Atomic force microscopy studies of fracture surfaces of composition B energetic materials. | 2675-2079A | Local Electrochemical Studies after Heat Treatment of Stainless Steel: Role of Induced Metallurgical and Surface Modifications on Pitting Triggering | 3334-3339A |
| Atomic structure | | Communication: Ferrite Number as a Function of the Larson-Miller Parameter for Austenitic Stainless Weld Metals after Creep Testing | 3445-3454A |
| Defect Structures and Room Temperature Mechanical Properties of C15 Laves Phases in Zr-Nb-Cr and Zr-Hf-Cr Alloy Systems | 3469-3476A | Fracture Behavior of Thick-Section Weldment in Fe-12Cr-12Ni-10Mn-0.24N Stainless Steel at Liquid Helium Temperature | 3515-3521A |
| Atomizing | | Austenitic stainless steels, Composite materials | 3631-3633A |
| A Numerical Study of Oxidation Behavior during Reactive Atomization and Deposition | 1173-1185B | Correlation of Microstructure with Hardness and Wear Resistance in (Ti,C)/Stainless Steel Surface Composites Fabricated by High-Energy Electron-Beam Irradiation. | 3797-3802A |
| On the Influence of In-Situ Reactions on Grain Size during Reactive Atomization and Deposition | 3251-3263A | Austenitic stainless steels, Mechanical properties | |
| An Analytical Model for the Oxide Size in Al Alloys Synthesized by Reactive Atomization and Deposition | 3265-3273A | Effects of Partial Recrystallization on High-Cycle Fatigue Deformation and Crack Generation of a Nitrogen-Strengthened 32Mn-7Cr Austenitic Steel at Liquid-Nitrogen Temperature. | 1029-1038A |
| Communication: The Transient to Steady-State Transition during the Spray-Rolling Process | 3633-3635A | Mechanisms of Strain Accumulation and Damage Development during Creep of Prestrained 316 Stainless Steels. | 543-553A |
| Ausforming | | Austenitic stainless steels, Phase transformations | 563-571A |
| Gigacycle Fatigue Properties of a Modified-Ausformed Si-Mn Steel and Effects of Microstructure. | 1715-1723A | Ferromagnetic Properties of Deformation-Induced Martensite Transformation in AISI 304 Stainless Steel. | 599-605A |
| Austempering | | Austenitizing | |
| Study of the Austempering Transformation Kinetics in Compacted Graphite Cast Irons. | 103-110A | Quench Embrittlement of Hardened 5160 Steel as a Function of Austenitizing Temperature. | 153-162A |
| Austenite | | Characterization of the Nucleation and Growth Behavior of Copper Precipitates in Low-Carbon Steels. | 2323-2329A |
| Study of the Austempering Transformation Kinetics in Compacted Graphite Cast Irons. | 103-110A | Hydrogen Absorption of Incoherent TiC Particles in Iron from Environment at High Temperatures | 3155-3163A |
| From Flake to Nodular: A New Theory of Morphological Modification in Gray Cast Iron. | 313-330B | Automotive components | |
| A Model for Ferrite/Pearlite Band Formation and Prevention in Steels. | 425-433A | Deformation and Damage Mechanisms of Zinc Coatings on Hot-Dip Galvanized Steel Sheets: Part II. Damage Modes. | 813-823A |
| Measurement and Modeling of the Electromagnetic Response to Phase Transformation in Steels. | 965-972A | Metal Vapor Treatment for Enhancing the Dissolution of Platinum Group Metals from Automotive Catalyst Scrap | 817-824B |
| Effect of Aging and Deformation on the Microstructure and Properties of Fe-Ni-Ti Maraging Steel. | 973-983A | Communication: Casting of Aluminum-Based Wrought Alloys Using Controlled Diffusion Solidification. | 2174-2180A |
| Effect of Simulated Thermal Cycles on the Microstructure of the Heat-Affected Zone in HSLA-80 and HSLA-100 Steel Plates. | 985-996A | A Through-Process Model of an A356 Brake Caliper for Fatigue Life Prediction | 3275-3288A |
| Phase Transformations and Control of Residual Stresses in Thick Spray-Formed Steel Shells | 1113-1122B | Formability and Strength of Friction-Stir-Welded Aluminum Sheets | 3461-3468A |
| Coupled-Solute Drag Effects on Ferrite Formation in Fe-C-X Systems. | 1187-1210A | Automotive components, Welding | |
| The Diffusional Formation of Ferrite from Austenite in Fe-C-Ni Alloys. | 1211-1221A | Electrode Pitting in Resistance Spot Welding of Aluminum Alloy 5182. | 217-226A |
| Molybdenum Accumulation at Ferrite/Austenite Interfaces during Isothermal Transformation of an Fe-0.24 Pct C-0.93 Pct Mo Alloy. | 1223-1235A | Automotive industry | |
| Studies of the Influence of Alloying Elements on the Growth of Ferrite from Austenite under Decarburization Conditions: Fe-C-Ni Alloys. | 1237-1242A | Determination of Interfacial Heat-Transfer Boundary Conditions | |
| Fine Carbide-Strengthened 3Cr-3WVTa Bainitic Steel. | 1281-1288A | | |
| Monte Carlo-Method Simulation of the Deformation-Induced Ferrite Transformation in the Fe-C System. | 1565-1577A | | |
| An Effect of a Strong Magnetic Field on the Phase Transformation in Plain Carbon Steels. | 1663-1668A | | |
| A Metallurgical Interpretation of the Static Recrystallization Kinetics of an Intercritically Deformed C-Mn Steel. | 1889-1898A | | |
| Microstructures of a Powder Metallurgy-Hot-Isostatically Pressed Super Duplex Stainless Steel Forming in Industrial Heat Treatments. | 2103-2109A | | |
| Experimental and Theoretical Evidence for Carbon-Vacancy Binding in Austenite. | 2239-2245A | | |
| Second-Order Stresses and Strains in Heterogeneous Steels: | | | |

- in an Aluminum Low-Pressure Permanent Mold Test Casting. Deformation and Damage Mechanisms of Zinc Coatings on Hot-Dip Galvanized Steel Sheets: Part I. Deformation Modes. Effect of Mg₂Si Particles on the Elevated Temperature Tensile Properties of Squeeze-Cast Mg-Al Alloys. 299-311B
- Axial stress**
Effect of Temperature and Strain Rate on the Compressive Flow of Aluminum Composites Containing Submicron Alumina Particles. 287-292A
Characterization and Modeling of Quenching-Induced Residual Stresses in the Nickel-Based Superalloy IN718. 1703-1713A
Experimental and Numerical Study on the Relationship between Creep Crack Growth Properties and Fracture Mechanisms. 1757-1764A
Deformation and Failure of Zr57Nb5Al10Cu15.4Ni12.6/W Particle Composites Under Quasi-Static and Dynamic Compression. 3439-3444A
- Bacterial corrosion**
Modeling Microbiologically Influenced Corrosion of N-80 Carbon Steel by Fuzzy Calculus. 2051-2056A
- Bainite**
Coupled-Solute Drag Effects on Ferrite Formation in Fe-C-X Systems. 1187-1210A
Fine Carbide-Strengthened 3Cr-3WV Ta Bainitic Steel. 1281-1288A
Effect of Microstructure on the Stability of Retained Austenite in Transformation-Induced-Plasticity Steels. 2331-2341A
Communication: Effect of texture and microstructure on resistance to cracking of high-strength hot-rolled Nb-Ti microalloyed steels. 3024-3029A
- Bainitic transformations**
Phase Transformations and Control of Residual Stresses in Thick Spray-Formed Steel Shells. 1113-1122B
Microstructural modification of as-cast NiAl bronze by friction stir processing. 2951-2961A
- Ball milling**
Cr-Mo Solid Solutions Forced by High-Energy Ball Milling. 1105-1111A
A Study on the Microstructural Evolution of Al-25 At. Pct V-12.5 At. pct M (M = Cu, Ni, Mn) Powders by Planetary Ball Milling. 1853-1860A
Mechanochemical Processing of Nanocrystalline Ti-6Al-4V Alloy. 1899-1903A
- Ballistic impact tests**
Communications: Ultra-High-Speed Exploding Properties of Ti-6Al-4V Alloy Having Equiaxed and Bimodal Microstructures. Dynamic Deformation Behavior and Ballistic Impact Properties of Ti-6Al-4V Alloy Having Equiaxed and Bimodal Microstructures. 719-724A
3103-3112A
- Banded structure**
A Model for Ferrite/Pearlite Band Formation and Prevention in Steels. 425-433A
Formation of Mesoscale Roughening in 6022-T4 Al Sheets Deformed in Plane-Strain Tension. 513-524A
Characterization of Plastic Flow and Resulting Microtextures in a Friction Stir Weld. 777-783B
Microstructural Banding and Failure of a Stainless Steel. 1317-1324A
Segregation band formation in Al-Si die castings. 2881-2891A
- Base metal**
The Effects of Strain Rate and Welding Current Mode on the Dynamic Impact Behavior of Plasma-Arc-Welded 304L Stainless Steel Weldments. 1501-1515A
Effects of Alloying Elements on Fracture Toughness in the Transition Temperature Region of Base Metals and Simulated Heat-Affected Zones of Mn-Mo-Ni Low-Alloy Steels. 2027-2037A
Communication: Texture characterization of autogenous Nd:YAG laser welds in AA5182-O and AA6111-T4 aluminum alloys. 3032-3038A
- Bauschinger effect**
Microindentation of Aluminum. 3323-3328A
- BCC metals**
Dislocation mechanics-based constitutive equations. 2547-2555A
- Bearing steels**
Cu Precipitation in a Prestrained Fe-1.5 Wt Pct Cu Alloy during Isothermal Aging. 1263-1272A
- Bend properties**
Residual Stress-Affected Diffusion during Plasma Nitriding of Tool Steels. 3523-3530A
- Bend tests**
Effects of Temperature and Shot Peening on S-N Behavior of a PM Ni-Base Superalloy UDIMET 720. 1007-1016A
Mechanical Properties of Al-60 Pct SiCp Composites Alloyed with Mg. 2127-2141A
A Semiautomated Electron Backscatter Diffraction Technique for Extracting Reliable Twin Statistics. 3745-3751A
- Bending**
Failure in Internally Pressurized Bent Tubes. 1151-1158A
- Bicrystals, Directional solidification**
Effect of Grain-Boundary Characteristics on Castability of Nickel-Base Superalloys. 939-946A
- Bifurcations**
Effects of Changes in Test Temperature on Fatigue Crack Propagation of Al6090/SiCp-Al 6013 Laminated Metal Composites. 2291-2303A
- Billet casting**
Thermomechanical Finite-Element Model of Shell Behavior in Continuous Casting of Steel. 1151-1172B
Finite element method simulation of mushy zone behavior during direct-chill casting of an Al-4.5 pct Cu alloy. 2917-2926A
Development and Validation of a Thermal Model of the Direct Chill Casting of AZ31 Magnesium Billets. 3843-3854A
- Billets**
Inclusion-Controlled Fatigue Properties of 1800 MPA-Class Spring Steels. 3737-3744A
- Binary alloys**
Experimental and modeling studies of the thermal conditions and magnesium, iron, and copper content on the morphology of the aluminum silicon eutectic in hypoeutectic aluminum silicon alloys. 2981-2991A
Coarsening Behavior of Ni₃Ga Precipitates in Ni-Ga Alloys: Dependence of Microstructure and Kinetics on Volume Fraction. 3063-3069A
Effects of Alloy Composition and Casting Speed on Structure Formation and Hot Tearing during Direct-Chill Casting of Al-Cu Alloys. 3551-3561A
- Binary systems**
Calculation of Physicochemical Properties in a Ternary System with Miscibility Gap. 715-720B
Coupled-Solute Drag Effects on Ferrite Formation in Fe-C-X Systems. 1187-1210A
Monte Carlo-Method Simulation of the Deformation-Induced Ferrite Transformation in the Fe-C System. 1565-1577A
Experimental Investigation and Thermodynamic Calculation of the Phase Equilibria in the Cu-Sn and Cu-Sn-Mn Systems. 1641-1654A
Phase Stability and Phase Transformations in Plutonium and Plutonium-Gallium Alloys. 2267-2278A
Modeling of Lattice Parameter in the Ni-Al System. 2313-2321A
- Binary systems, Crystal growth**
Correction to Metallurgical and Materials Transactions A, November 2003, vol. 34A, pp. 2690-2693: "Authors Reply" to Discussion of "Eutectic Solidification of Al-Si Alloys" 959A
- Binary systems, Microstructure**
Erratum: A Solutal Interaction mechanism for the Columnar-to-Equiaxed Transition in Alloy Solidification. 1915A
- Binary systems, Phase transformations**
Fcc/Hcp Martensitic Transformation in the Fe-Mn System: Part II. Driving Force and Thermodynamics of the Nucleation Process. 83-91A
- Binary systems, Phases (state of matter)**
A Comparison of the Molecular Interaction Volume Model with the Subregular Solution Model in Multicomponent Liquid Alloys. 419-424A
- Binding energy**
Hydrogen Trap States in Ultrahigh-Strength AERMET 100 Steel. 849-864A
Experimental and Theoretical Evidence for Carbon-Vacancy Binding in Austenite. 2239-2245A
Hydrogen Absorption of Incoherent TiC Particles in Iron from Environment at High Temperatures. 3155-3163A
- Biography**
A Tribute to Terence E. Mitchell. 2203-2205A
- Bismuth, Binary systems**
A Comparison of the Molecular Interaction Volume Model with the Subregular Solution Model in Multicomponent Liquid Alloys. 419-424A
- Blast furnace slags, Reduction (chemical)**
Influence of Chemical Compositions of Slag and Graphite on the Phenomena Occurring in the Graphite/Slag Interfacial Region. 75-83B
- Blast furnaces**
Fluid Flows in Metallurgy - Friend or Foe? 417-437B
Blast Furnace Burden Softening and Melting Phenomena: Part I. Pellet Bulk Interaction Observation. 829-838B
- Body centered cubic lattice**
Experimental Investigation and Thermodynamic Calculation of the Phase Equilibria in the Cu-Sn and Cu-Sn-Mn Systems. 1641-1654A
Single-Crystal Elastic Constants of Fe-15Ni-15Cr Alloy. 3149-3154A
Thermodynamic Investigations of Cr₃C₂ and Reassessment of the Cr-C System. 3673-3680A
Application of a Substructure-Based Hardening Model to Copper under Loading Path Changes. 3763-3774A
- Body centered cubic lattices**
Communication: Formation of Simple Crystal Structures in Cu-Co-Ni-Cr-Al-Fe-Ti-V Alloys with Multiprincipal Metallic Elements. 2533-2536A
- Bonding strength**
The Effect of Temperature, Matrix Alloying and Substrate Coatings on Wettability and Shear Strength of Al/Al₂O₃ Couples. 911-923A
The Influence of a Martensitic Phase Transformation on Stress Development in Thermal Barrier Coating Systems. 2279-2286A
Tensile and Fatigue Behavior of Al-Based Metal Matrix Composites Reinforced with Continuous Carbon or Alumina Fibers: Part I. Quasi-Unidirectional Composites. 3289-3305A
- Borides**
Comparison of Microstructural Evolution in Laser-Deposited and Arc-Melted In-Situ Ti-TiB Composites. 2143-2152A
- Boron**
Effect of Boron on the Low-Cycle Fatigue Behavior and Deformation Structure of INCONEL 718 at 650°C. 3477-3487A
- Boron, Composite materials**
Damage Evolution during Thermal Fatigue in Fiber-Reinforced Light-Metal-Matrix Composites. 37-43A
- Boundary conditions**
Numerical Analysis of Metal Transfer in Gas Metal Arc Welding under Modified Pulsed Current Conditions. 857-866B
A Semiautomated Electron Backscatter Diffraction Technique

- for Extracting Reliable Twin Statistics
Development and Validation of a Thermal Model of the Direct
Chill Casting of AZ31 Magnesium Billets 3745-3751A
- Boundary value problems**
Morphology of fractured domains in brittle fracture. 3843-3854A
- Bowing**
Communication: Quantification of Overaging Hardening Kinet-
ics of Aluminum Alloys. 2651-2661A
- Brakes**
A Through-Process Model of an A356 Brake Caliper for
Fatigue Life Prediction 2172-2174A
- Brasses**
A Tribute to Terence E. Mitchell. 3275-3288A
- Brasses, Crystal lattices**
Advancing Towards Constitutive Equations for the Metal Indus-
try via the LEDS Theory. 2203-2205A
Advancing Towards Constitutive Equations for the Metal Indus-
try via the LEDS Theory. 5-54B
369-418A
- Brasses, Microstructure**
Determination of Volume Fractions of Texture Components
with Standard Distributions in Euler Space. 1075-1086A
- Bridges (structures), Design**
Communications: Ultra-High-Speed Exploding Properties of Ti-
6Al-4V Alloy Having Equiaxed and Bimodal Microstructures. 719-724A
- Briquets**
Additions to Generate Foam in Stainless Steelmaking. 643-650B
- Brittle fracture**
Shape Memory Properties of Ni-Ti Based Melt-Spun Ribbons.
Morphology of fractured domains in brittle fracture. 761-770A
Ductility Exhaustion Mechanisms in Thermally Exposed Thin
Sheets of a Near- β Titanium Alloy 2651-2661A
Two-Layered Zr-Based Amorphous Alloy/Metal Surface Com-
posites Fabricated by High Energy Electron-Beam Irradiation 3113-3127A
Fatigue and Fracture Behavior of Bulk Metallic Glass 3455-3460A
Effect of Sn on Microstructure and Mechanical Properties of Ti-
Base Dendrite/Ultrafine-Structured Multicomponent Alloys 3489-3498A
3605-3612A
- Brittleness**
Effects of Carbon Fiber/Al Interface on Mechanical Properties
of Carbon-Fiber-Reinforced Aluminum-Matrix Composites.
Superplastic Behavior and Microstructure Evolution in a Com-
mercial Al-Mg-Sc Alloy Subjected to Intense Plastic Strain-
ing. 2153-2160A
Tensile and Fatigue Behavior of Al-Based Metal Matrix Com-
posites Reinforced with Continuous Carbon or Alumina
Fibers: Part I. Quasi-Unidirectional Composites 2383-2392A
3289-3305A
- Broaching**
Effect of Broaching on High-Temperature Fatigue Behavior in
Notched Specimens of INCONEL 718. 771-783A
- Bubbles**
Spot Turbulence, Breakup, and Coalescence of Bubbles
Released from a Porous Plug Injector into a Gas-Stirred
Ladle 949-956B
- Bulging**
Analysis of Thin-Slab Casting by the Compact-Strip Process:
Part II. Effect of Operating and Design Parameters on Solidi-
fication and Bulging. 561-573B
- Bulk density**
Zinc Recovery from Spent ZnO Catalyst by Carbon in the Pres-
ence of Calcium Carbonate. 55-63B
- Bulk sampling**
Reaction Sequences in the Formation of Silico-Ferrites of Cal-
cium and Aluminum in Iron Ore Sinter 929-936B
- Buoyancy**
Physical and Mathematical Determination of the Influence of
Input Temperature Changes on the Molten Steel Flow Char-
acteristics in Slab Tundishes 957-966B
- Burgers vector**
Variability of Large-Crack Fatigue-Crack-Growth Thresholds in
Structural Alloys 3721-3735A
- Byproducts**
Continuous Oxygen Steelmaking with Copper-, Tin-, and Zinc-
Contaminated Scrap. 663-674B
- Cadmium**
Grain size dependence of the activation parameters for plastic
deformation: influence of crystal structure, slip system, and
rate-controlling dislocation mechanism. 2697-2705A
- Cadmium, Binary systems**
A Comparison of the Molecular Interaction Volume Model with
the Subregular Solution Model in Multicomponent Liquid
Alloys. 419-424A
- Calcium**
Reaction Sequences in the Formation of Silico-Ferrites of Cal-
cium and Aluminum in Iron Ore Sinter 929-936B
Communication: A thousandfold creep strengthening by Ca
addition in die-cast AM50 magnesium alloy. 3029-3032A
- Calcium compounds**
Amphoteric Behavior of Alumina in Viscous Flow and Structure
of CaO-SiO₂ (-MgO)-Al₂O₃ Slags. 269-275B
- Calculus**
Modeling Microbiologically Influenced Corrosion of N-80 Car-
bon Steel by Fuzzy Calculus. 2051-2056A
- Calipers**
A Through-Process Model of an A356 Brake Caliper for
Fatigue Life Prediction 3275-3288A
- Calorimetry**
Calorimetric Determination of the 5 Hydride Dissolution
Enthalpy in ZIRCALOY-4. 2343-2349A
- Carbides**
Evolution of Secondary Phases in Cr-V Low-Alloy Steels dur-
ing Aging. 751-759A
Oxide Defects in a Vacuum Investment-Cast Ni-Based Turbine
Blade. 2063-2071A
Carbides in high-speed steels containing silicon. 2757-2766A
- Carbon**
Coupled-Solute Drag Effects on Ferrite Formation in Fe-C-X
Systems. 1187-1210A
Effect of Carbon Concentration on Precipitation Behavior of
M23C6 Carbides and MX Carbonitrides in Martensitic 9Cr
Steel during Heat Treatment. 1255-1262A
Monte Carlo-Method Simulation of the Deformation-Induced
Ferrite Transformation in the Fe-C System. 1565-1577A
Experimental Determination of the Carbon Solubility Limit in
Ferritic Steels. 1655-1661A
Experimental and Theoretical Evidence for Carbon-Vacancy
Binding in Austenite. 2239-2245A
An Experimental and Theoretical Analysis of the Phase Equi-
libria in the Fe-Cr-VC System 3649-3663A
Role of Carbon and Alloying Elements in the Formation of Bai-
nitic Ferrite 3693-3700A
- Carbon fibers**
Effects of Carbon Fiber/Al Interface on Mechanical Properties
of Carbon-Fiber-Reinforced Aluminum-Matrix Composites.
Tensile and Fatigue Behavior of Al-Based Metal Matrix Com-
posites Reinforced with Continuous Carbon or Alumina
Fibers: Part I. Quasi-Unidirectional Composites 3289-3305A
Tensile and Fatigue Behavior of Al-Based Metal Matrix Com-
posites Reinforced with Continuous Carbon or Alumina
Fibers: Part II. Quasi-Unidirectional Composite Cross-Ply
Laminates 3307-3317A
- Carbon fibers, Composite materials**
Some Studies on the Thermal-Expansion Behavior of C-Fiber,
SiC_p and In-Situ Mg₂Si-Reinforced AZ31 Mg Alloy-Based
Hybrid Composites. 1167-1176A
- Carbon manganese steels**
A Metallurgical Interpretation of the Static Recrystallization
Kinetics of an Intercritically Deformed C-Mn Steel. 1889-1896A
A novel observation of strain-induced ferrite-to-austenite
rettransformation after intercritical deformation of C-Mn steel. 2789-2797A
- Carbon steels**
An Effect of a Strong Magnetic Field on the Phase Transforma-
tion in Plain Carbon Steels. 1663-1668A
Effect of Ternary Additions on the Structure and Properties of
Coatings Produced by a High Aluminum Galvanizing Bath 3707-3720A
- Carbon steels, Joining**
Effect of Surface Modification of High-Density Polyethylene by
Direct Current and Radio Frequency Glow Discharge on
Wetting and Adhesion Characteristics. 865-877A
- Carbon steels, Metal working**
Failure in Internally Pressurized Bent Tubes. 1151-1158A
- Carbon steels, Phase transformations**
Measurement and Modeling of the Electromagnetic Response
to Phase Transformation in Steels. 965-972A
- Carbon-carbon composites**
Time-dependent deformation in an enhanced SiC/SiC compos-
ite. 2853-2859A
- Carbonitrides**
Effect of Carbon Concentration on Precipitation Behavior of
M23C6 Carbides and MX Carbonitrides in Martensitic 9Cr
Steel during Heat Treatment. 1255-1262A
- Carbonization**
Nanoparticle Recovery Using a Fume Collector Comprised of
Carbonized Refuse-Derived Fuel 993-998B
- Carbothermic reactions**
Solid-State Reduction of Chromium Oxide by Methane-Con-
taining Gas. 609-615B
Mechanism and Rate of Reaction of Al₂O₃, Al, and CO Vapors
with Carbon. 617-623B
Communication: The Pressure of Al₂O₃ and Al in Equilibrium
with a Al₂O₃-Al₄C₃ (Saturated) Slag at 1950°C to 2020°C 1011-1013B
- Case depth**
Solute diffusion in liquid nickel measured by pulsed ion beam
melting. 2803-2807A
- Casing (material)**
Fracture Behavior of Thick-Section Weldment in Fe-12Cr-12Ni-
10Mn-0.24N Stainless Steel at Liquid Helium Temperature 3797-3802A
- Cast alloys**
Modeling the Age-Hardening Behavior of Al-Si-Cu Alloys. 2407-2418A
The Role of Microstructure in Localized Corrosion of Magne-
sium Alloys. 2525-2531A
Determination of Isothermal Transformation Diagrams for
Sigma-Phase Formation in Cast Duplex Stainless Steels
CD3Mn and CD3MWCuN 3377-3386A
Quantitative Analysis of Texture Evolution of Cold-Rolled
Direct-Chill-Cast and Continuous-Cast AA5052 and AA5182
Aluminum Alloys during Isothermal Annealing 3613-3629A
- Castability**
Effect of Grain-Boundary Characteristics on Castability of
Nickel-Base Superalloys. 939-946A
Effect of Zr and B on Castability of Ni-Based Superalloy IN792. 1337-1342A
Effect of Low-Frequency Electromagnetic Casting on the
Castability, Microstructure, and Tensile Properties of Direct-

- Chill Cast Al-Zn-Mg-Cu Alloy. 2487-2494A
- Casting alloys**
- The Solidification Characteristics of Fe-Rich Intermetallics in Al-11.5Si-0.4Mg Cast Alloys. 1425-1435A
- Communication: Casting of Aluminum-Based Wrought Alloys Using Controlled Diffusion Solidification. 2174-2180A
- Plastic deformation behavior of aluminum casting alloys A356/357. 2707-2718A
- Casting defects**
- Communication: Casting of Aluminum-Based Wrought Alloys Using Controlled Diffusion Solidification. 2174-2180A
- Castings**
- Estimation of Multiple Heat-Flux Components at the Metal/Mold Interface in Bar and Plate Aluminum Alloy Castings. 575-585B
- Modification-Related Porosity Formation in Hypoeutectic Aluminum-Silicon Alloys. 1097-1106B
- Effects of the entrained surface film on the reliability of castings. 2893-2902A
- Directional Solidification of Large Superalloy Castings with Radiation and Liquid-Metal Cooling: A Comparative Assessment. 3221-3231A
- A Through-Process Model of an A356 Brake Caliper for Fatigue Life Prediction. 3275-3288A
- The Influence of Strontium on Porosity Formation in Al-Si Alloys. 3531-3541A
- Cavitation**
- Damage Evolution during Thermal Fatigue in Fiber-Reinforced Light-Metal-Matrix Composites. 37-43A
- Electrode Pitting in Resistance Spot Welding of Aluminum Alloy 5182. 217-226A
- Influence of Stress State on Cavitation during Hot Working of Ti-6Al-4V. 655-663A
- A Hybrid Micromechanical-Macroscopic Model for the Analysis of the Tensile Behavior of Cavitating Materials. 1141-1149A
- Communication: The Dependence of Cavity-Growth Rate on Stress Triaxiality. 2187-2190A
- Superplastic Behavior and Microstructure Evolution in a Commercial Al-Mg-Sc Alloy Subjected to Intense Plastic Straining. 2383-2392A
- Communication: The Observation and Identification of the Oxide Film on the Creep Cavity Wall of Type 316L Stainless Steel. 3331-3333A
- Cavitation erosion**
- Communication: Cavitation Erosion Characteristics of a NiTi Alloy. 356-362A
- Cellular automata**
- A Quantitative Dendrite Growth Model and Analysis of Stability Concepts. 2471-2485A
- Cellular structure, Directional solidification**
- Analysis of Diffusive Cellular Patterns in Directional Solidification of Bulk Samples. 239-246A
- Cementite**
- An Effect of a Strong Magnetic Field on the Phase Transformation in Plain Carbon Steels. 1663-1668A
- Role of Carbon and Alloying Elements in the Formation of Bainitic Ferrite. 3693-3700A
- Centrifugal casting**
- Correlation of Microstructure and Thermal-Fatigue Properties of Centrifugally Cast High-Speed Steel Rolls. 481-492A
- Nickel-Aluminides/Steel Clad Pipe Fabricated by Reactive Centrifugal Casting Method from Liquid Aluminum and Solid Nickel. 1517-1524A
- Ceramics, Composite materials**
- Quantifying Thermomechanical Fatigue of Light-Metal-Matrix Composites by Mechanical Spectroscopy. 25-35A
- Cerium oxide**
- The Behavior and Effect of Rare Earth CeO₂ on In-Situ TiC/Al Composite. 2511-2515A
- Charpy impact test**
- Quality Assessment of Artificially Aged A357 Aluminum Alloy Cast Ingots by Introducing Approximate Expressions of the Quality Index QD. 3079-3089A
- Chemical bonds**
- Partial Atomic Volume and Partial Molar Enthalpy of Formation of the 3d Metals in the Palladium-Based Solid Solutions. 63-70A
- Chemical equilibrium**
- The influence of chemical equilibrium on fluid-solid reaction rates and the falsification of activation energy. 121-131B
- Chemical vapor deposition**
- Effects of Preheating on Morphological Development of a Chemical Vapor Deposition Aluminide Coating Formed on Single-Crystal Ni-Based Superalloy. 891-897A
- Effects of an α -Al₂O₃ Thin Film on the Oxidation Behavior of a Single-Crystal Ni-Based Superalloy. 1055-1065A
- Effects of Preoxidation on the Nucleation and Growth Behavior of Chemically Vapor-Deposited α -Al₂O₃ on a Single-Crystal Ni-Based Superalloy. 1113-1124A
- Mechanisms of Hf Dopant Incorporation during the Early Stage of Chemical Vapor Deposition Aluminide Coating Growth under Continuous Doping Conditions. 3581-3593A
- Chill casting**
- A Model of the Interfacial Heat Transfer Coefficient for the Aluminum Gravity Die-Casting Process. 721-733B
- Effect of Low-Frequency Electromagnetic Casting on the Castability, Microstructure, and Tensile Properties of Direct-Chill Cast Al-Zn-Mg-Cu Alloy. 2487-2494A
- Chlorides**
- Kinetics of Gold(III) Chloride Complex Reduction Using Sulfur(IV). 1071-1085B
- Chloridizing**
- Salt Roasting of Suncor Oil Sands Fly Ash. 1051-1058B
- Chlorination**
- Rare Earth Extraction from Bastnaesite Concentrate by Stepwise Carbochlorination-Chemical Vapor Transport-Oxidation. 217-221B
- Kinetics of Chlorination of Tantalum Pentoxide in Mixture with Sucrose Carbon by Chlorine Gas. 439-448B
- Chromium**
- Direct Electrolytic Preparation of Chromium Powder. 223-233B
- Characterization of the peritectic reaction in medium-alloy steel through microsegregation and heat-of-transformation studies. 2869-2879A
- Effect of Different Cr Contents on Tensile and Corrosion Behaviors of 0.13 Pct N-Containing CD4MCU Cast Duplex Stainless Steels. 3431-3438A
- An Experimental and Theoretical Analysis of the Phase Equilibria in the Fe-Cr-VC System. 3649-3663A
- Chromium, Composite materials**
- Creep Behavior of Copper-Chromium In-Situ Composite. 695-705A
- Chromium, Thermal properties**
- Partial Atomic Volume and Partial Molar Enthalpy of Formation of the 3d Metals in the Palladium-Based Solid Solutions. 63-70A
- Chromium base alloys**
- Communication: Tensile Properties of Chromium Alloyed with Silver. 3329-3331A
- Chromium base alloys, Crystal lattices**
- Cr-Mo Solid Solutions Forced by High-Energy Ball Milling. 1105-1111A
- Chromium carbides**
- Thermodynamic Investigations of Cr₃C₂ and Reassessment of the Cr-C System. 3673-3680A
- Chromium molybdenum steels**
- Effect of Thermal Spray on the Microstructure and Adhesive Strength of High Velocity Oxy-Fuel-Sprayed Ni-Cr Coatings on 9Cr-1Mo Steel. 3187-3199A
- Chromium molybdenum vanadium steels**
- Quantification of Hydrogen Diffusion and Trapping in 2.25Cr-1Mo and 3Cr-1Mo-V Steels with the Electrochemical Permeation Technique and Melt Extractions. 1449-1464A
- Chromium molybdenum vanadium steels, Coating**
- Process Efficiency Measurements in the Laser Engineered Net Shaping Process. 143-152B
- Chromium oxides**
- Solid-State Reduction of Chromium Oxide by Methane-Containing Gas. 609-615B
- Chromium steels**
- Effect of Carbon Concentration on Precipitation Behavior of M₂₃C₆ Carbides and MX Carbonitrides in Martensitic 9Cr Steel during Heat Treatment. 1255-1262A
- Chromium vanadium steels, Phases (state of matter)**
- Evolution of Secondary Phases in Cr-V Low-Alloy Steels during Aging. 751-759A
- Clad metals**
- Nickel-Aluminides/Steel Clad Pipe Fabricated by Reactive Centrifugal Casting Method from Liquid Aluminum and Solid Nickel. 1517-1524A
- Cleanliness**
- The Effect of Carbon in Slag on Steel Reoxidation and Carbon Analysis by X-Ray Photoelectron Spectroscopy in the CaO-SiO₂-Al₂O₃-MgO-MnO-FeO System. 1087-1095B
- Cleavage**
- Charpy-Impact-Toughness Prediction using an "Effective" Grain Size for Thermomechanically Controlled Rolled Microalloyed Steels. 121-130A
- Study on Notch Fracture of TiAl Alloys at Room Temperature. 439-456A
- Deformation and Damage Mechanisms of Zinc Coatings on Hot-Dip Galvanized Steel Sheets: Part II. Damage Modes. 813-823A
- Mechanisms and Modeling of Cleavage Fracture in Simulated Heat-Affected Zone Microstructures of a High-Strength Low Alloy Steel. 1039-1053A
- Dislocation Structure and Deformation in Iron Processed by Equal-Channel-Angular Pressing. 1343-1350A
- Effects of Loading Rate on Fracture Behavior of Low-Alloy Steel with Different Grain Sizes. 1765-1778A
- Effects of Martensite Morphology and Tempering on Dynamic Deformation Behavior of Dual-Phase Steels. 2371-2382A
- The Microstructural, Mechanical, and Fracture Properties of Austenitic Stainless Steel Alloyed with Gallium. 3445-3454A
- Communication: Room-Temperature Cleavage Fracture of FeMnAlC Steels. 3863-3866A
- Close packed lattices**
- Temperature Effects on the Lattice Constants and Crystal Structure of a Co-27Cr-5Mo Low-Carbon Alloy. 2517-2523A
- A Micromechanical Analysis of the Yielding Behavior of Individual Widmanstätten Colonies of an $\alpha + \beta$ Titanium Alloy. 3409-3422A
- Clustering**
- Effect of Clustering of Precipitates on Grain Growth. 1097-1103A
- Effects of Simultaneous Displacive and Ionizing Radiations and of Electric Field on Radiation Damage in Ionic Crystals. 2257-2266A
- Tensile behavior of friction-stir-welded Al 6061-T651. 2829-2835A
- Coagulation**
- Nickel Droplet Settling Behavior in an Electric Furnace. 839-845B
- Coalescing**
- Spot Turbulence, Breakup, and Coalescence of Bubbles Released from a Porous Plug Injector into a Gas-Stirred

- Ladle
Mechanism of Primary MC Carbide Decomposition in Ni-Base Superalloys. 949-956B
Coarsening Behavior of Ni₃Ga Precipitates in Ni-Ga Alloys: Dependence of Microstructure and Kinetics on Volume Fraction. 1669-1679A
3063-3069A
- Coarsening**
Study of the Ferrite Grain Coarsening behind the Transformation Front by Electron Backscattered Diffraction Techniques. 93-102A
A Study of Coarsening, Recrystallization, and Morphology of Microstructure in Al-Sc-(Zr)-(Mg) Alloys. 341-350A
The Effect of Heat Treatment on Mg₂Si Coarsening in Aluminum 6105 Alloy. 435-438A
Precipitate Microstructures and Resulting Properties of Al-Zn-Mg Metal Inert Gas-Weld Heat-Affected Zones. 1437-1448A
Mechanism of Primary MC Carbide Decomposition in Ni-Base Superalloys. 1669-1679A
Microstructural Evolution of Predeformed SiCp/ZA27 Composites during Partial Remelting. 2073-2085A
Communication: Quantification of Overaging Hardening Kinetics of Aluminum Alloys. 2172-2174A
Effect of microstructural length scales on spall behavior of copper. 2663-2673A
Microstructure and mechanical properties of a 2000 MPa Co-free maraging steel after aging at 753 K. 2747-2755A
Coarsening behavior of an alpha-beta titanium alloy. 2809-2819A
Tensile behavior of friction-stir-welded Al 6061-T651. 2829-2835A
Experimental and modeling studies of the thermal conditions and magnesium, iron, and copper content on the morphology of the aluminum silicon eutectic in hypoeutectic aluminum silicon alloys. 2981-2991A
Effect of strain reversal on the dynamic spheroidization of Ti-6Al-4V during hot deformation. 2993-3001A
Coarsening of Al₃Sc precipitates in an Al-0.28 wt pct Sc alloy. 3003-3008A
Communication: High-temperature fatigue crack growth behavior of 17-4 PH stainless steels. 3018-3024A
Coarsening Behavior of Ni₃Ga Precipitates in Ni-Ga Alloys: Dependence of Microstructure and Kinetics on Volume Fraction. 3063-3069A
On the Influence of In-Situ Reactions on Grain Size during Reactive Atomization and Deposition. 3251-3263A
- Cobalt**
Communication: A Brick-Wall Model for Calculating Young's Modulus of a Particulate Composite. 2191-2192A
- Cobalt base alloys**
Crystallization of Co100-xPtB10Si12 Amorphous Metallic Alloys. 2057-2061A
Temperature Effects on the Lattice Constants and Crystal Structure of a Co-27Cr-5Mo Low-Carbon Alloy. 2517-2523A
Tensile properties and microstructure of Haynes 25 alloy after aging at elevated temperatures for extended times. 2767-2781A
- Cobalt base alloys, Mechanical properties**
Thermal-Imaging Technologies for Detecting Damage during High-Cycle Fatigue. 15-23A
Low-Cycle Fatigue Behavior of UHMETAL Alloy. 785-796A
Temperature Evolution and Life Prediction in Fatigue of Superalloys. 839-848A
- Cobalt compounds**
Crystallization of Co100-xPtB10Si12 Amorphous Metallic Alloys. 2057-2061A
- Cobalt oxides**
Reduction of Cobalt Oxide With Methane. 825-828B
- Coercive force**
Ferromagnetic Properties of Deformation-Induced Martensite Transformation in AISI 304 Stainless Steel. 599-605A
Crystallization of Co100-xPtB10Si12 Amorphous Metallic Alloys. 2057-2061A
- Cohesion**
Effect of Zr and B on Castability of Ni-Based Superalloy IN792. 1337-1342A
- Cold isostatic pressing**
Copper-Zirconium Tungstate Composites Exhibiting Low and Negative Thermal Expansion Influenced by Reinforcement Phase Transformations. 1159-1165A
- Cold reduction**
Preparation of Cu-Ni Alloys through a New Chemical Route. 1107-1112B
- Cold rolling**
Recrystallization Behavior of a Heavily Cold-Rolled Ni₃Al (B,Zr) Alloy. 71-81A
Quantitative Analysis of Texture Evolution in Cold-Rolled, Continuous-Cast AA 5xxx-Series Aluminum Alloys. 265-277A
The Effect of Surface Deformation on Lubrication and Oxide-Scale Fracture in Cold Metal Rolling. 919-928B
The Tensile Response of a Fine-Grained AA5754 Alloy Produced by Asymmetric Rolling and Annealing. 997-1006A
Effect of Thermomechanical Treatment on the Evolution of Rolling and Recrystallization Textures in Twin-Belt Cast AA5754 Aluminum Alloy. 1839-1851A
Damping Properties of Austenitic Stainless Steels Containing Strain-Induced Martensite. 2401-2406A
Austenite Formation during Inter-critical Annealing. 3363-3375A
On Coils and Microbands Formed in an Interstitial-Free Steel during Cold Rolling at Low to Medium Reductions. 3423-3430A
Quantitative Analysis of Texture Evolution of Cold-Rolled Direct-Chill-Cast and Continuous-Cast AA5052 and AA5182 Aluminum Alloys during Isothermal Annealing. 3613-3629A
- Cold work tool steels**
Carbides in high-speed steels containing silicon. 2757-2766A
- Columnar structure**
- Microstructural Evolution in Laser-Deposited Multilayer Ti-6Al-4V Builds: Part I. Microstructural Characterization. 1861-1867A
Erratum: A Solutal Interaction mechanism for the Columnar-to-Equiaxed Transition in Alloy Solidification. 1915A
A Quantitative Dendrite Growth Model and Analysis of Stability Concepts. 2471-2485A
Influence of Convection on Feathery Grain Formation in Aluminum Alloys. 2495-2501A
Atomic force microscopy studies of fracture surfaces of composition B energetic materials. 2675-2079A
Communication: Texture characterization of autogenous Nd:YAG laser welds in AA5182-O and AA6111-T4 aluminum alloys. 3032-3038A
Directional Solidification of Large Superalloy Castings with Radiation and Liquid-Metal Cooling: A Comparative Assessment. 3221-3231A
A Novel Experiment for the Study of Substrate-Induced Nucleation in Metallic Alloys: Application to Zn-Al. 3543-3550A
- Compacted graphite iron, Phase transformations**
Study of the Austempering Transformation Kinetics in Compacted Graphite Cast Irons. 103-110A
- Composition effects**
Modeling of Lattice Parameter in the Ni-Al System. 2313-2321A
Experimental and modeling studies of the thermal conditions and magnesium, iron, and copper content on the morphology of the aluminum silicon eutectic in hypoeutectic aluminum silicon alloys. 2981-2991A
Defect Structures and Room Temperature Mechanical Properties of C15 Laves Phases in Zr-Nb-Cr and Zr-Hf-Cr Alloy Systems. 3469-3476A
Effects of Alloy Composition and Casting Speed on Structure Formation and Hot Tearing during Direct-Chill Casting of Al-Cu Alloys. 3551-3561A
- Compressing**
Fabrication of Foamable Precursors by Powder Compression and Induction Heating Process. 769-776B
Laser-induced shock compression of copper: orientation and pressure decay effects. 2633-2646A
Effect of low-temperature shock compression on the microstructure and strength of copper. 2729-2739A
Deformation and Failure of Zr57Nb5Al10Cu15.4Ni12.6/W Particle Composites Under Quasi-Static and Dynamic Compression. 3439-3444A
Application of a Substructure-Based Hardening Model to Copper under Loading Path Changes. 3763-3774A
- Compression tests**
Effect of Temperature and Strain Rate on the Compressive Flow of Aluminum Composites Containing Submicron Alumina Particles. 287-292A
Deformation and Recrystallization Behavior during Hot Working of a Coarse-Grain, Nickel-Base Superalloy Ingot Material. 679-693A
Semi-Solid Rapid Compression Testing of Spray-Formed Hypereutectic Al-Si Alloys. 899-910A
Yield Behavior of Commercial Al-Si Alloys in the Semisolid State. 1187-1202B
Mechanical Properties of Al-60 Pct SiCp Composites Alloyed with Mg. 2127-2141A
Evaluation of Mechanical Properties of Porous 6061 Alloys Fabricated by the Powder Compression and Induction Heating Process. 2419-2426A
Materials science under extreme conditions of pressure and strain rate. 2587-2607A
The influence of explosive-driven 'Taylor-wave' shock pre-straining on the structure/property behavior of 304 stainless steel. 2617-2624A
Plastic deformation behavior of aluminum casting alloys A356/357. 2707-2718A
Effect of low-temperature shock compression on the microstructure and strength of copper. 2729-2739A
Brass Type Shear Bands and their Influence on Texture Formation. 3775-3786A
On the Isotropy of the Dynamic Mechanical and Failure Properties of Swaged Tungsten Heavy Alloys. 3787-3795A
- Compressive properties**
Fracture Toughness of Selectively Reinforced Al2124 Alloy: Precrack Tip in the Composite Side. 1393-1401A
Residual Stresses in High Velocity Oxy-Fuel Metallic Coatings. 1807-1814A
Effect of Initial Grain Size of Austenite on Hot-Deformed Structure of Ni-30Fe Alloy. 3399-3408A
Residual Stress-Affected Diffusion during Plasma Nitriding of Tool Steels. 3523-3530A
- Compressive strength**
The Effect of Temperature and Extrusion Speed on The Consolidation of Zirconium-Based Metallic Glass Powder Using Equal-Channel Angular Extrusion. 247-256A
Wear Resistance and High-Temperature Compression Strength of Fcc CuCoNiCrAl_{0.5}Fe Alloy with Boron Addition. 1465-1469A
Evaluation of Mechanical Properties of Porous 6061 Alloys Fabricated by the Powder Compression and Induction Heating Process. 2419-2426A
Effect of low-temperature shock compression on the microstructure and strength of copper. 2729-2739A
Microstructure evolution and mechanical behavior of bulk copper obtained by consolidation of micro- and nanopowders using equal-channel angular extrusion. 2935-2949A
Fatigue and Fracture Behavior of Bulk Metallic Glass. 3489-3498A
In-Situ Microfracture Observation of Strip-Cast Zr-Ti-Cu-Ni-Be Bulk Metallic Glass Alloys. 3753-3761A
- Computational fluid dynamics**
Study of Transient Flow and Particle Transport in Continuous

- Steel Caster Molds: Part I. Fluid Flow. 685-702B
 Study of Transient Flow and Particle Transport in Continuous Steel Caster Molds: Part II. Particle Transport. 703-714B
 Nickel Droplet Settling Behavior in an Electric Furnace. 839-845B
 Numerical Analysis of Metal Transfer in Gas Metal Arc Welding under Modified Pulsed Current Conditions. 857-866B
 Spot Turbulence, Breakup, and Coalescence of Bubbles Released from a Porous Plug Injector into a Gas-Stirred Ladle. 949-956B
 Physical and Mathematical Determination of the Influence of Input Temperature Changes on the Molten Steel Flow Characteristics in Slab Tundishes. 957-966B
 Computational and Experimental Study of Turbulent Flow in a 0.4-Scale Water Model of a Continuous Steel Caster. 967-982B
 Study of Inclusion Re-Entrainment in a Filter Bed. 999-1009B
 Simulation of Flow Control in the Meniscus of a Continuous Casting Mold with Opposing Alternating Current Magnetic Fields. 1129-1137B
 Modeling of Laser Cladding with Powder Injection. 1139-1150B
 Thermomechanical Finite-Element Model of Shell Behavior in Continuous Casting of Steel. 1151-1172B
 Influence of Convection on Feathery Grain Formation in Aluminum Alloys. 2495-2501A
 Marangoni convection in weld pool in CO₂-Ar-shielded gas thermal arc welding. 2861-2867A
 Effects of the entrained surface film on the reliability of castings. 2893-2902A
- Computer aided design**
 Fabrication of Carbide-Particle-Reinforced Titanium Aluminide-Matrix Composites by Laser-Engineered Net Shaping. 1133-1140A
- Computer aided testing**
 Evaluation of Mechanical Properties of Porous 6061 Alloys Fabricated by the Powder Compression and Induction Heating Process. 2419-2426A
- Computer control**
 Effects of the entrained surface film on the reliability of castings. 2893-2902A
 Continuous Cooling β -to- α Transformation Behaviors of Extra-Pure and Commercially Pure Ti. 3071-3077A
- Computer programs**
 Critical Thermodynamic Evaluation and Optimization of the FeO-Fe₂O₃-MgO-SiO₂ System. 877-889B
 Influence of Convection on Feathery Grain Formation in Aluminum Alloys. 2495-2501A
- Computer simulation**
 Determination of Interfacial Heat-Transfer Boundary Conditions in an Aluminum Low-Pressure Permanent Mold Test Casting. 299-311B
 Mathematical Simulation and Physical Modeling of Unsteady Fluid Flows in a Water Model of a Slab Mold. 449-460B
 Study of Transient Flow and Particle Transport in Continuous Steel Caster Molds: Part I. Fluid Flow. 685-702B
 Channel Segregation during Solidification and the Effects of an Alternating Traveling Magnetic Field. 743-754B
 Simulation of Die Filling for the Wax Injection Process: Part I. Models for Material Behavior. 755-759B
 Simulation of Die Filling for the Wax Injection Process: Part II. Numerical Simulation. 761-768B
 The Development and Experimental Validation of a Numerical Model of an Induction Skull Melting Furnace. 785-803B
 Communication: A Computational Assessment of Viscosity Measurement in Rotating Viscometers through Detailed Numerical Simulation. 805-809B
 Contraction of Aluminum Alloys during and after Solidification. Focused Ion-Beam Tomography. 1325-1335A
 Statistically Representative Three-Dimensional Microstructures Based on Orthogonal Observation Sections. 1935-1943A
 Validation of Predicted Precipitate Compositions in Al-Si-Ge. Grain-size dependence of the flow stress of Cu from millimeters to nanometers. 1969-1979A
 Gas nitriding of high vanadium steels - experiments and simulations. 2305-2311A
 Infrared Brazing Cu and Ti Using a 95Ag-5Al Braze Alloy. Grain Refinement Induced by Electromagnetic Stirring: A Dendrite Fragmentation Criterion. 2681-2696A
 2799-2802A
 3177-3186A
- Computer software**
 An Experimental and Theoretical Analysis of the Phase Equilibria in the Fe-Cr-VC System. 3201-3210A
 3649-3663A
- Concentration gradient**
 Gas nitriding of high vanadium steels - experiments and simulations. 2799-2802A
- Condensation**
 Condensation of Zinc Vapor on Solid Media in Zn (g)-CO-CO₂-Ar Mixtures. 625-631B
- Conduction**
 Mathematical Modeling of a Direct Current Electric Arc: Part I. Analysis of the Characteristics of a Direct Current Arc. 363-372B
- Conservation equations**
 A Quantitative Dendrite Growth Model and Analysis of Stability Concepts. 2471-2485A
- Consolidation**
 Preparation of Cu-Ni Alloys through a New Chemical Route. Microstructure evolution and mechanical behavior of bulk copper obtained by consolidation of micro- and nanopowders using equal-channel angular extrusion. 1107-1112B
 2935-2949A
- Constitution**
 Thermodynamic Aspects of the Constitution, Grain Refining, and Solidification Enthalpies of Al-Ce-Si Alloys. 3349-3362A
- Constitutive equations**
 Dislocation mechanics-based constitutive equations. 2547-2555A
 Development of thermal strain in the coherent mushy zone during solidification of aluminum alloys. 2903-2915A
- Constitutive relationships**
 Dislocation mechanics-based constitutive equations. 2547-2555A
 Dynamic deformation and damage in cast γ -TiAl during Taylor cylinder impact: experiments and model validation. 2557-2566A
 Morphology of fractured domains in brittle fracture. 2651-2661A
 Development of thermal strain in the coherent mushy zone during solidification of aluminum alloys. 2903-2915A
- Constraining**
 Deformation and Damage Mechanisms of Zinc Coatings on Hot-Dip Galvanized Steel Sheets: Part I. Deformation Modes. 797-811A
 Two-Layered Zr-Base Amorphous Alloy/Metal Surface Composites Fabricated by High Energy Electron-Beam Irradiation. 3455-3460A
- Contact angle**
 Influence of Chemical Compositions of Slag and Graphite on the Phenomena Occurring in the Graphite/Slag Interfacial Region. 75-83B
 Communication: The Contact Angle between Liquid Iron and a Single-Crystal Magnesium Oxide Substrate at 1873 K. 179-181B
 Reactive Wetting of SiO₂ Substrates by Molten Al. 583-588A
 The Effect of Temperature, Matrix Alloying and Substrate Coatings on Wettability and Shear Strength of Al/Al₂O₃ Couples. 911-923A
- Containers**
 Communication: Comparisons of Experimental Measurements and a Theoretical Model for Specimen Self-Heating during Fatigue of Type 316 LN Stainless Steel. 3334-3339A
- Contamination**
 Communication: Persistence of Superficial Contamination of Rolled Steel during Successive Treatments up to the Formation of a Galvanneal Coating. 2185-2187A
- Continuous annealing**
 Quantitative Analysis of Texture Evolution of Cold-Rolled Direct-Chill-Cast and Continuous-Cast AA5052 and AA5182 Aluminum Alloys during Isothermal Annealing. 3613-3629A
- Continuous casting**
 Study of Transient Flow and Particle Transport in Continuous Steel Caster Molds: Part I. Fluid Flow. 685-702B
 Study of Transient Flow and Particle Transport in Continuous Steel Caster Molds: Part II. Particle Transport. 703-714B
 Simulation of Flow Control in the Meniscus of a Continuous Casting Mold with Opposing Alternating Current Magnetic Fields. 1129-1137B
 Thermomechanical Finite-Element Model of Shell Behavior in Continuous Casting of Steel. 1151-1172B
 Failure Mode Analysis and a Mechanism for Hot-Ductility Improvement in the Nb-Microalloyed Steel. 3823-3832A
- Continuous casting machines**
 Fluid Flows in Metallurgy - Friend or Foe? 417-437B
 Computational and Experimental Study of Turbulent Flow in a 0.4-Scale Water Model of a Continuous Steel Caster. 967-982B
- Continuous coating**
 Simulation of Flow in a Continuous Galvanizing Bath: Part I. Thermal Effects of Ingot Addition. 161-170B
 Simulation of Flow in a Continuous Galvanizing Bath: Part II. Transient Aluminum Distribution Resulting from Ingot Addition. 171-178B
 Mechanisms of Hf Dopant Incorporation during the Early Stage of Chemical Vapor Deposition Aluminide Coating Growth under Continuous Doping Conditions. 3581-3593A
- Continuous fiber composites**
 Tensile and Fatigue Behavior of Al-Based Metal Matrix Composites Reinforced with Continuous Carbon or Alumina Fibers: Part I. Quasi-Unidirectional Composites. 3289-3305A
 Tensile and Fatigue Behavior of Al-Based Metal Matrix Composites Reinforced with Continuous Carbon or Alumina Fibers: Part II. Quasi-Unidirectional Composite Cross-Ply Laminates. 3307-3317A
- Continuous rolling**
 Quantitative Analysis of Texture Evolution of Cold-Rolled Direct-Chill-Cast and Continuous-Cast AA5052 and AA5182 Aluminum Alloys during Isothermal Annealing. 3613-3629A
- Contraction**
 Contraction of Aluminum Alloys during and after Solidification. 1325-1335A
- Control equipment**
 Simulation of Flow Control in the Meniscus of a Continuous Casting Mold with Opposing Alternating Current Magnetic Fields. 1129-1137B
- Control surfaces**
 The Selection of the Spray Deposition Rate during the Spray Rolling Process. 3595-3603A
- Controlled atmospheres**
 Studies of the Influence of Alloying Elements on the Growth of Ferrite from Austenite under Decarburization Conditions: Fe-C-Ni Alloys. 1237-1242A
- Controlled rolling**
 Effect of Microstructure on the Stability of Retained Austenite in Transformation-Induced-Plasticity Steels. 2331-2341A
 Inclusion-Controlled Fatigue Properties of 1800 MPA-Class Spring Steels. 3737-3744A
- Convection**
 Liquid Convection Effects on the Pushing-Engulfment Transition of Insoluble Particles by a Solidifying Interface: Part I. Analytical Calculation of the Lift Forces. 613-621A
 Liquid Convection Effects on the Pushing-Engulfment Transition of Insoluble Particles by a Solidifying Interface: Part II.

- Numerical Calculation of Drag and Lift Forces on a Particle in Parabolic Shear Flow. 623-629A
- Influence of Convection on Feathery Grain Formation in Aluminum Alloys. 2495-2501A
- Converters**
- The Solubility of Cr₂O₃ in Calcium Ferrite Slags at 1573 K. 197-202B
- Cooling**
- Development and Validation of a Thermal Model of the Direct Chill Casting of AZ31 Magnesium Billets 3843-3854A
- Cooling curves**
- Erratum: A Solutal Interaction mechanism for the Columnar-to-Equiaxed Transition in Alloy Solidification. 1915A
- Cooling rate**
- Microstructural Evolution in Laser-Deposited Multilayer Ti-6Al-4V Builds: Part II. Thermal Modeling. 1869-1879A
- Continuous Cooling β -to- α Transformation Behaviors of Extra-Pure and Commercially Pure Ti 3071-3077A
- Copper**
- Liquidus Temperatures in Calcium Ferrite Slags in Equilibrium with Molten Copper. 203-215B
- Computational Modeling of Laser Welding of Cu-Ni Dissimilar Couple. 339-350B
- Experimental Investigation and Thermodynamic Calculation of the Phase Equilibria in the Cu-Sn and Cu-Sn-Mn Systems. A Tribute to Terence E. Mitchell. 1641-1654A
- Characterization of Surface Deformation around Vickers Indents in Monocrystalline Materials. 2247-2255A
- Characterization of the Nucleation and Growth Behavior of Copper Precipitates in Low-Carbon Steels. 2323-2329A
- An Eulerian Finite-Element Model for Determination of Deformation State of a Copper Subjected to Orthogonal Cutting. 2393-2400A
- Laser-induced shock compression of copper: orientation and pressure decay effects. 2633-2646A
- Effect of microstructural length scales on spall behavior of copper. 2663-2673A
- Effect of low-temperature shock compression on the microstructure and strength of copper. 2729-2739A
- Nonequilibrium molecular dynamics simulations of metallic friction at Ta/Al and Cu/Ag interfaces. 2741-2745A
- Microstructure evolution and mechanical behavior of bulk copper obtained by consolidation of micro- and nanopowders using equal-channel angular extrusion. 2935-2949A
- Application of a Substructure-Based Hardening Model to Copper under Loading Path Changes. 3763-3774A
- Brass Type Shear Bands and their Influence on Texture Formation. 3775-3786A
- Copper, Coatings**
- Process Efficiency Measurements in the Laser Engineered Net Shaping Process. 143-152B
- Copper, Composite materials**
- Creep Behavior of Copper-Chromium In-Situ Composite. 695-705A
- Copper-Zirconium Tungstate Composites Exhibiting Low and Negative Thermal Expansion Influenced by Reinforcement Phase Transformations. 1159-1165A
- Copper, Corrosion**
- Electrode Pitting in Resistance Spot Welding of Aluminum Alloy 5182. 217-226A
- Copper, Mechanical properties**
- Correlation of the Microstructure and Mechanical Properties of Oxide-Dispersion-Strengthened Coppers Fabricated by Internal Oxidation. 493-502A
- Copper, Microstructure**
- Determination of Volume Fractions of Texture Components with Standard Distributions in Euler Space. 1075-1086A
- Copper base alloys**
- Preparation of Cu-Ni Alloys through a New Chemical Route: Formation of Core-Type Macroscopic Morphologies in Cu-Fe Base Alloys with Liquid Miscibility Gap. 1107-1122B
- Wear Resistance and High-Temperature Compression Strength of Fcc CuCoNiCrAl_{0.5}Fe Alloy with Boron Addition. 1243-1253A
- Communication: Formation of Simple Crystal Structures in Cu-Co-Ni-Cr-Al-Fe-Ti-V Alloys with Multiprincipal Metallic Elements. 1465-1469A
- The Solidification of Undercooled Melts via Twinned Dendritic Growth. 2533-2536A
- Variability of Large-Crack Fatigue-Crack-Growth Thresholds in Structural Alloys. 3211-3220A
- Copper base alloys, Anisotropy**
- Tensile Anisotropy in Cu-Ni-Mn-Sn-Al Alloys. 3721-3735A
- Copper base alloys, Crystal lattices**
- Advancing Towards Constitutive Equations for the Metal Industry via the LEDS Theory. 465-469A
- Advancing Towards Constitutive Equations for the Metal Industry via the LEDS Theory. 5-54B
- Copper mattes**
- The Solubility of Cr₂O₃ in Calcium Ferrite Slags at 1573 K. Kinetics of As, Sb, Bi and Pb Volatilization from Industrial Copper Matte during Ar + O₂ Bubbling. 369-418A
- Correlation analysis**
- Response of Primary Dendrite Spacing to Varying Temperature Gradient during Directional Solidification. 197-202B
- Analysis of intergranular impurity concentration and the effects on the ductility of copper-shaped charge jets. 651-661B
- Corrosion fatigue**
- Electrochemical Evaluation of a Corrosion Fatigue Failure Mechanism in a Duplex Stainless Steel. 735-742B
- Corrosion resistance**
- 2567-2573A
- 2427-2437A
- Communication: Casting of Aluminum-Based Wrought Alloys Using Controlled Diffusion Solidification. 2174-2180A
- Electrochemical Evaluation of a Corrosion Fatigue Failure Mechanism in a Duplex Stainless Steel. 2427-2437A
- The Role of Microstructure in Localized Corrosion of Magnesium Alloys. 2525-2531A
- Effect of Different Cr Contents on Tensile and Corrosion Behaviors of 0.13 Pct Ni-Containing CD4MCU Cast Duplex Stainless Steels. 3431-3438A
- Two-Layered Zr-Base Amorphous Alloy/Metal Surface Composites Fabricated by High Energy Electron-Beam Irradiation. 3455-3460A
- Local Electrochemical Studies after Heat Treatment of Stainless Steel: Role of Induced Metallurgical and Surface Modifications on Pitting Triggering. 3515-3521A
- Characterization of Retrogression and Reaging Behavior of 8090 Al-Li-Cu-Mg-Zr Alloy. 3681-3691A
- Effect of Ternary Additions on the Structure and Properties of Coatings Produced by a High Aluminum Galvanizing Bath. 3707-3720A
- Corrosion tests**
- Double Loop Electrochemical Potentiokinetic Reactivation Test Optimization in Checking of Duplex Stainless Steel Intergranular Corrosion Susceptibility. 3499-3513A
- Corundum**
- Experimental Study of Phase Equilibria in the Al-Fe-Zn-O System in Air. 633-642B
- Crack closure**
- Effects of Temperature and Shot Peening on S-N Behavior of a PM Ni-Base Superalloy UDIMET 720. 1007-1016A
- Crack initiation**
- Charpy-Impact-Toughness Prediction using an "Effective" Grain Size for Thermomechanically Controlled Rolled Microalloyed Steels. 121-130A
- Study on Notch Fracture of TiAl Alloys at Room Temperature. Correlation of Microstructure and Thermal-Fatigue Properties of Centrifugally Cast High-Speed Steel Rolls. 439-456A
- Damage Repair in CMSX-4 Alloy without Fatigue Life Reduction Penalty. 481-492A
- Effects of Partial Recrystallization on High-Cycle Fatigue Deformation and Crack Generation of a Nitrogen-Strengthened 32Mn-7Cr Austenitic Steel at Liquid-Nitrogen Temperature. 535-542A
- Effect of Broaching on High-Temperature Fatigue Behavior in Notched Specimens of INCONEL 718. 543-553A
- Fatigue of Cold-Work Tool Steels: Effect of Heat Treatment and Carbide Morphology on Fatigue Crack Formation, Life, and Fracture Surface Observations. 771-783A
- Fatigue Fracture Mechanism Maps for a Type 304 Stainless Steel. 1289-1300A
- Hydrogen-Involved Tensile and Cyclic Deformation Behavior of Low-Alloy Pressure Vessel Steel. 1311-1316A
- Effects of Loading Rate on Fracture Behavior of Low-Alloy Steel with Different Grain Sizes. 1477-1486A
- The Effect of Lamellar Morphology on Tensile and High-Cycle Fatigue Behavior of Orthorhombic Ti-22Al-27Nb Alloy. 1765-1778A
- Communication: Casting of Aluminum-Based Wrought Alloys Using Controlled Diffusion Solidification. 2161-2170A
- Electrochemical Evaluation of a Corrosion Fatigue Failure Mechanism in a Duplex Stainless Steel. 2174-2180A
- Tensile behavior of friction-stir-welded A356-T6/Al 6061-T651 Bi-alloy plate. 2427-2437A
- The Microstructural, Mechanical, and Fracture Properties of Austenitic Stainless Steel Alloyed with Gallium. 2837-2843A
- Crack opening displacement**
- Characterizing Small Fatigue Cracks in Metallic Alloys. 3445-3454A
- Crack propagation**
- Characterizing Small Fatigue Cracks in Metallic Alloys. 7-14A
- Thermal-Imaging Technologies for Detecting Damage during High-Cycle Fatigue. 7-14A
- Effects of Lamination and Changes in Layer Thickness on Fatigue-Crack Propagation of Lightweight Laminated Metal Composites. 15-23A
- Charpy-Impact-Toughness Prediction using an "Effective" Grain Size for Thermomechanically Controlled Rolled Microalloyed Steels. 45-52A
- Microstructural Effects on Fatigue and Dwell-Fatigue Crack Growth in α/β Ti-6Al-2Sn-4Zr-2Mo-0.1Si. 121-130A
- In-Situ Observations of Low-Cycle Fatigue Damage in Cast AM60B Magnesium in an Environmental Scanning Electron Microscope. 163-187A
- Communication: Cavitation Erosion Characteristics of a NiTi Alloy. 321-331A
- Study on Notch Fracture of TiAl Alloys at Room Temperature. Effects of Heat Treatment and Testing Temperature on Fracture Mechanics Behavior of Low-Si CA-15 Stainless Steel. 356-362A
- Damage Repair in CMSX-4 Alloy without Fatigue Life Reduction Penalty. 439-456A
- Effects of Partial Recrystallization on High-Cycle Fatigue Deformation and Crack Generation of a Nitrogen-Strengthened 32Mn-7Cr Austenitic Steel at Liquid-Nitrogen Temperature. 471-480A
- Effect of Broaching on High-Temperature Fatigue Behavior in Notched Specimens of INCONEL 718. 535-542A
- Low-Cycle Fatigue Behavior of ULTIMET Alloy. 543-553A
- Communication: Resonant Vibration Behavior of an Al-3.8Cu-0.8Li-0.3Mg Alloy. 771-783A
- Fracture Behavior of Thixoformed 357-T5 Al Alloys. 785-796A
- Fatigue of Cold-Work Tool Steels: Effect of Heat Treatment and Carbide Morphology on Fatigue Crack Formation, Life, and Fracture Surface Observations. 952-957A
- Fatigue Fracture Mechanism Maps for a Type 304 Stainless Steel. 1017-1027A
- 1289-1300A

- Steel.
Fracture Toughness of Selectively Reinforced Al2124 Alloy: Precrack Tip in the Composite Side.
Hydrogen-Involved Tensile and Cyclic Deformation Behavior of Low-Alloy Pressure Vessel Steel.
Experimental and Numerical Study on the Relationship between Creep Crack Growth Properties and Fracture Mechanisms.
Effects of Loading Rate on Fracture Behavior of Low-Alloy Steel with Different Grain Sizes.
The Effect of Lamellar Morphology on Tensile and High-Cycle Fatigue Behavior of Orthorhombic Ti-22Al-27Nb Alloy.
Effects of Changes in Test Temperature on Fatigue Crack Propagation of Al6090/SiCp-Al 6013 Laminated Metal Composites.
Atomic force microscopy studies of fracture surfaces of composition B energetic materials.
Communication: High-temperature fatigue crack growth behavior of 17-4 PH stainless steels.
The Microstructural, Mechanical, and Fracture Properties of Austenitic Stainless Steel Alloyed with Gallium.
Fatigue and Fracture Behavior of Bulk Metallic Glass.
Variability of Large-Crack Fatigue-Crack-Growth Thresholds in Structural Alloys.
In-Situ Microfracture Observation of Strip-Cast Zr-Ti-Cu-Ni-Be Bulk Metallic Glass Alloys.
Tensile Test Behavior of the Eutectic Sn-Ag Solder Joint in Ball Grid Array Assemblies.
- Cracking (fracturing)**
Fabrication of Carbide-Particle-Reinforced Titanium Aluminide-Matrix Composites by Laser-Engineered Net Shaping.
Dynamic deformation and damage in cast γ -TiAl during Taylor cylinder impact: experiments and model validation.
Plastic deformation behavior of aluminum casting alloys A356/357.
Time-dependent deformation in an enhanced SiC/SiC composite.
Finite element method simulation of mushy zone behavior during direct-chill casting of an Al-4.5 pct Cu alloy.
Dynamic Deformation Behavior and Ballistic Impact Properties of Ti-6Al-4V Alloy Having Equiaxed and Bimodal Microstructures.
Effects of Alloy Composition and Casting Speed on Structure Formation and Hot Tearing during Direct-Chill Casting of Al-Cu Alloys.
- Creep (materials)**
Microstructural Effects on Fatigue and Dwell-Fatigue Crack Growth in α/β Ti-6Al-2Sn-4Zr-2Mo-0.1Si.
Dynamic Phase Transformation during Superplastic Deformation of Nb/Nb₂Al In-Situ Composite.
Transition of Dominant Diffusion Process during Superplastic Deformation in AZ61 Magnesium Alloys.
Analysis of Thin-Slab Casting by the Compact-Strip Process: Part II. Effect of Operating and Design Parameters on Solidification and Bulging.
Mechanisms of Strain Accumulation and Damage Development during Creep of Prestrained 316 Stainless Steels.
Creep Behavior of a Rotating Functionally Graded Composite Disc Operating under Thermal Gradient.
Theoretical and Practical Implications of Creep Curve Shape Analyses for 2124 and 2419.
Experimental and Numerical Study on the Relationship between Creep Crack Growth Properties and Fracture Mechanisms.
Understanding the Contributions of Normal-Fatigue and Static Loading to the Dwell Fatigue in a Near-Alpha Titanium Alloy.
Texture Evolution and Mechanical Anisotropy in Dual-Phase TiAl-Based Alloy Loaded at 700 °C to 1000 °C.
Tensile Test Behavior of the Eutectic Sn-Ag Solder Joint in Ball Grid Array Assemblies.
- Creep life**
Time-dependent deformation in an enhanced SiC/SiC composite.
- Creep rate**
Communication: Grain Boundary Engineering of Ferritic-Martensitic Alloy T91.
The Effect of Silicon Content on the Microstructure and Creep Behavior in Die-Cast Magnesium AS Alloys.
Experimental and Theoretical Evidence for Carbon-Vacancy Binding in Austenite.
Communication: A thousandfold creep strengthening by Ca addition in die-cast AM50 magnesium alloy.
- Creep strength**
Deformation Behavior of Zr-Al-Nb Alloys II: Indentation Creep Studies.
Creep Behavior of Copper-Chromium In-Situ Composite.
Communication: Grain Boundary Engineering of Ferritic-Martensitic Alloy T91.
Communication: Strengthening by γ/γ' Interfacial Dislocation Networks in TMS-162-Toward a Fifth-Generation Single-Crystal Superalloy.
Influence of Microstructure on Tensile and Creep Properties of a New Castable TiAl-Based Alloy.
Communication: A thousandfold creep strengthening by Ca addition in die-cast AM50 magnesium alloy.
Microstructure Characterization and Creep Deformation of an Al-10 Wt Pct Ti-2 Wt Pct Cu Nanocomposite.
- Creep tests**
Creep Behavior of Copper-Chromium In-Situ Composite.
Influence of Microstructure on Tensile and Creep Properties of
- a New Castable TiAl-Based Alloy.
Communication: The Observation and Identification of the Oxide Film on the Creep Cavity Wall of Type 316L Stainless Steel.
Communication: Ferrite Number as a Function of the Larson-Miller Parameter for Austenitic Stainless Steel Metals after Creep Testing.
Critical temperature
Shape Memory Properties of Ni-Ti Based Melt-Spun Ribbons.
Study on Polychlorinated Dibenzop-dioxin/Furan Formation in Iron Ore Sintering Process.
Cross sections
Characterization of Plastic Flow and Resulting Microtextures in a Friction Stir Weld.
An Analytical Model for the Oxide Size in Al Alloys Synthesized by Reactive Atomization and Deposition.
Cross slip
Grain size dependence of the activation parameters for plastic deformation: influence of crystal structure, slip system, and rate-controlling dislocation mechanism.
Crushing
Metal Vapor Treatment for Enhancing the Dissolution of Platinum Group Metals from Automotive Catalyst Scrap.
Cryogenics
Study of the Ni41.3Ti38.7Nb20 wide transformation hysteresis shape-memory alloy.
Fracture Behavior of Thick-Section Weldment in Fe-12Cr-12Ni-10Mn-0.24N Stainless Steel at Liquid Helium Temperature.
Cryolite
Modeling the Dependence of Alumina Solubility on Temperature and Melt Composition in Cryolite-Based Melts.
Cryolite, Reactions (chemical)
Modeling of the Solubilities of NiO/NiAl₂O₄ and FeO/FeAl₂O₄ in Cryolite Melts at 1300 K.
Communication: The Solubility of Titanium Dioxide in Cryolite-Alumina Melts at 1300 K.
Crystal defects
Defect Structures in Cosputtered Thin Films of Transition Metal Disilicides with C11b, C40 and C54 Structures.
Local Electromechanical Response at a Single Ferroelectric Domain Wall in Lithium Niobate.
Characterization of the peritectic reaction in medium-alloy steel through microsegregation and heat-of-transformation studies.
Directional Solidification of Large Superalloy Castings with Radiation and Liquid-Metal Cooling: A Comparative Assessment.
Crystal lattices
Dislocation mechanics-based constitutive equations.
Crystal structure
Microreaction Mechanism in Reduction of Magnetite to Wustite.
Salt Roasting of Suncor Oil Sands Fly Ash.
The Three-Dimensional X-ray Crystal Microscope: A New Tool for Materials Characterization.
Defect Structures in Cosputtered Thin Films of Transition Metal Disilicides with C11b, C40 and C54 Structures.
Characterization of Surface Deformation around Vickers Indents in Monocrystalline Materials.
Temperature Effects on the Lattice Constants and Crystal Structure of a Co-27Cr-5Mo Low-Carbon Alloy.
Communication: Formation of Simple Crystal Structures in Cu-Co-Ni-Cr-Al-Fe-Ti-V Alloys with Multiprincipal Metallic Elements.
Dislocation structure behind a shock front in fcc perfect crystals: atomistic simulation results.
Laser-induced shock compression of copper: orientation and pressure decay effects.
Grain size dependence of the activation parameters for plastic deformation: influence of crystal structure, slip system, and rate-controlling dislocation mechanism.
In-Situ Microfracture Observation of Strip-Cast Zr-Ti-Cu-Ni-Be Bulk Metallic Glass Alloys.
Crystallites
Defect Structures in Cosputtered Thin Films of Transition Metal Disilicides with C11b, C40 and C54 Structures.
Crystallization
Shape Memory Properties of Ni-Ti Based Melt-Spun Ribbons.
Reaction Sequences in the Formation of Silico-Ferrites of Calcium and Aluminum in Iron Ore Sinter.
Salt Roasting of Suncor Oil Sands Fly Ash.
A Study on the Microstructural Evolution of Al-25 At. Pct V-12.5 At. pct M (M = Cu, Ni, Mn) Powders by Planetary Ball Milling.
Crystallization of Co100-xPtB10Si12 Amorphous Metallic Alloys.
Cube texture
Quantitative Analysis of Texture Evolution of Cold-Rolled Direct-Chill-Cast and Continuous-Cast AA5052 and AA5182 Aluminum Alloys during Isothermal Annealing.
Cubic lattice
Determination of Volume Fractions of Texture Components with Standard Distributions in Euler Space.
Curie temperature
Measurement and Modeling of the Electromagnetic Response to Phase Transformation in Steels.
Magnetic Contribution to the Interdiffusion Coefficients in Bcc (α) and Fcc (γ) Fe-Ni Alloys.

| | | | |
|---|------------|------------|------------|
| Current carriers | | | |
| A Tribute to Terence E. Mitchell. | 2203-2205A | | |
| Current density | | | |
| Mathematical Modeling of a Direct Current Electric Arc: Part I. | | | |
| Analysis of the Characteristics of a Direct Current Arc. | 363-372B | | |
| Numerical Analysis of Metal Transfer in Gas Metal Arc Welding under Modified Pulsed Current Conditions | 857-866B | | |
| Curvature | | | |
| A Quantitative Dendrite Growth Model and Analysis of Stability Concepts. | 2471-2485A | | |
| Effect of strain reversal on the dynamic spheroidization of Ti-6Al-4V during hot deformation. | 2993-3001A | | |
| Cutting | | | |
| An Eulerian Finite-Element Model for Determination of Deformation State of a Copper Subjected to Orthogonal Cutting. | 2393-2400A | | |
| Cyclic loads | | | |
| The effect of grain size on low-cycle fatigue behavior of Al-2024 polycrystalline alloy. | 2725-2728A | | |
| Fatigue and Fracture Behavior of Bulk Metallic Glass | 3489-3498A | | |
| Cylinder heads | | | |
| Determination of Interfacial Heat-Transfer Boundary Conditions in an Aluminum Low-Pressure Permanent Mold Test Casting. | 299-311B | | |
| Damage | | | |
| Damage Evolution during Thermal Fatigue in Fiber-Reinforced Light-Metal-Matrix Composites. | 37-43A | | |
| Mechanisms of Strain Accumulation and Damage Development during Creep of Prestrained 316 Stainless Steels. | 563-571A | | |
| Influence of Stress State on Cavitation during Hot Working of Ti-6Al-4V. | 655-663A | | |
| Deformation and Damage Mechanisms of Zinc Coatings on Hot-Dip Galvanized Steel Sheets: Part I. Deformation Modes. | 797-811A | | |
| On the Isotropy of the Dynamic Mechanical and Failure Properties of Swaged Tungsten Heavy Alloys | 3787-3795A | | |
| Damage tolerance | | | |
| A New Quality Index for Characterizing Aluminum Cast Alloys with Regard to Aircraft Structure Design Requirements. | 301-308A | | |
| Communication: Grain Boundary Engineering of Ferritic-Martensitic Alloy T91. | 717-718A | | |
| Damping capacity | | | |
| Communication: Resonant Vibration Behavior of an Al-3.8Cu-0.8Li-0.3Mg Alloy. | 952-957A | | |
| Damping Properties of Austenitic Stainless Steels Containing Strain-Induced Martensite. | 2401-2406A | | |
| Data bases | | | |
| Phase Stability and Phase Transformations in Plutonium and Plutonium-Gallium Alloys. | 2267-2278A | | |
| Debonding | | | |
| Quantifying Thermomechanical Fatigue of Light-Metal-Matrix Composites by Mechanical Spectroscopy. | 25-35A | | |
| Void Nucleation by Inclusion Cracking. | 1745-1755A | | |
| Debye temperature | | | |
| Single-Crystal Elastic Constants of Fe-15Ni-15Cr Alloy | 3149-3154A | | |
| Decarburizing | | | |
| Studies of the Influence of Alloying Elements on the Growth of Ferrite from Austenite under Decarburization Conditions: Fe-C-Ni Alloys. | 1237-1242A | | |
| Decision making | | | |
| Nanotechnology: Scientific Challenges and Societal Benefits and Risks | 1021-1028B | | |
| Nanotechnology: Scientific Challenges and Societal Benefits and Risks | 3641-3648A | | |
| Decomposition | | | |
| Double Loop Electrochemical Potentiokinetic Reactivation Test Optimization in Checking of Duplex Stainless Steel Intergranular Corrosion Susceptibility | 3499-3513A | | |
| Defects | | | |
| Correlation of Microstructure with the Hardness and Wear Resistance of (TiC,SiC)/Ti-6Al-4V Surface Composites Fabricated by High-Energy Electron-Beam Irradiation. | 525-534A | | |
| Oxide Defects in a Vacuum Investment-Cast Ni-Based Turbine Blade. | 2063-2071A | | |
| Defect Structures and Room Temperature Mechanical Properties of C15 Laves Phases in Zr-Nb-Cr and Zr-Hf-Cr Alloy Systems | 3469-3476A | | |
| Deflection | | | |
| Communication: Resonant Vibration Behavior of an Al-3.8Cu-0.8Li-0.3Mg Alloy. | 952-957A | | |
| Variability of Large-Crack Fatigue-Crack-Growth Thresholds in Structural Alloys | 3721-3735A | | |
| Deformation | | | |
| Dislocation Structure and Deformation in Iron Processed by Equal-Channel-Angular Pressing. | 1343-1350A | | |
| Co-Deformation Processing and Modeling of In-Situ Multiphase Composites. | 1603-1611A | | |
| Experimental Determination of the Carbon Solubility Limit in Ferritic Steels. | 1655-1661A | | |
| Effects of Martensite Morphology and Tempering on Dynamic Deformation Behavior of Dual-Phase Steels. | 2371-2382A | | |
| Dynamic deformation and damage in cast γ -TiAl during Taylor cylinder impact: experiments and model validation. | 2557-2566A | | |
| Molecular-dynamics study of mechanical deformation in nanocrystalline aluminum. | 2719-2723A | | |
| Nonequilibrium molecular dynamics simulations of metallic friction at Ta/Al and Cu/Ag interfaces. | 2741-2745A | | |
| A novel observation of strain-induced ferrite-to-austenite retransformation after intercritical deformation of C-Mn steel. | 2789-2797A | | |
| Effect of dissolved tungsten on the deformation of 70Ni-30Fe alloys. | | | 2821-2828A |
| Cyclic deformation behavior and dislocation structure of Ti-2 Al. Pct Al single crystals oriented for double prism slip. | | | 2845-2852A |
| Effect of strain reversal on the dynamic spheroidization of Ti-6Al-4V during hot deformation. | | | 2993-3001A |
| Communication: Effect of texture and microstructure on resistance to cracking of high-strength hot-rolled Nb-Ti microalloyed steels. | | | 3024-3029A |
| Continuous Cooling β -to- α Transformation Behaviors of Extra-Pure and Commercially Pure Ti | | | 3071-3077A |
| Microstructure Development during High Velocity Deformation Dynamic Deformation Behavior and Ballistic Impact Properties of Ti-6Al-4V Alloy Having Equiaxed and Bimodal Microstructures | | | 3091-3101A |
| Studies of Lattice Imperfections in Deformed Aluminum-Based Lithium Alloys by X-Ray Diffraction | | | 3103-3112A |
| Effect of Initial Grain Size of Austenite on Hot-Deformed Structure of Ni-30Fe Alloy | | | 3319-3322A |
| On Cells and Microbands Formed in an Interstitial-Free Steel during Cold Rolling at Low to Medium Reductions | | | 3399-3408A |
| Neutron Diffraction Study of Texture Development during Hot Working of Different Gamma-Titanium Aluminide Alloys | | | 3423-3430A |
| A Semiautomated Electron Backscatter Diffraction Technique for Extracting Reliable Twin Statistics | | | 3563-3570A |
| Brass Type Shear Bands and their Influence on Texture Formation | | | 3745-3751A |
| Texture Evolution and Mechanical Anisotropy in Dual-Phase Ti3Al-Based Alloy Loaded at 700 °C to 1000 °C | | | 3775-3786A |
| Failure Mode Analysis and a Mechanism for Hot-Ductility Improvement in the Nb-Microalloyed Steel | | | 3803-3815A |
| Microstructure Characterization and Creep Deformation of an Al-10 Wt Pct Ti-2 Wt Pct Cu Nanocomposite | | | 3823-3832A |
| Deformation effects | | | 3855-3861A |
| Study of the Ni41.3Ti38.7Nb20 wide transformation hysteresis shape-memory alloy. | | | 2783-2788A |
| Inclusion-Controlled Fatigue Properties of 1800 MPA-Class Spring Steels | | | 3737-3744A |
| Deformation mechanisms | | | |
| Advancing Towards Constitutive Equations for the Metal Industry via the LEDS Theory. | | 5-54B | |
| The Effect of Temperature and Extrusion Speed on The Consolidation of Zirconium-Based Metallic Glass Powder Using Equal-Channel Angular Extrusion. | | 247-256A | |
| Advancing Towards Constitutive Equations for the Metal Industry via the LEDS Theory. | | 369-418A | |
| Deformation and Damage Mechanisms of Zinc Coatings on Hot-Dip Galvanized Steel Sheets: Part I. Deformation Modes. | | 797-811A | |
| Deformation and Damage Mechanisms of Zinc Coatings on Hot-Dip Galvanized Steel Sheets: Part II. Damage Modes. | | 813-823A | |
| High-Strain-Rate Superplastic Behavior of Equal-Channel Angular-Pressed 5083 Al-0.2 Wt Pct Sc. | | 825-837A | |
| Materials science under extreme conditions of pressure and strain rate. | | 2587-2607A | |
| Laser-induced shock compression of copper: orientation and pressure decay effects. | | 2633-2646A | |
| A novel observation of strain-induced ferrite-to-austenite retransformation after intercritical deformation of C-Mn steel. | | 2789-2797A | |
| Microstructure evolution and mechanical behavior of bulk copper obtained by consolidation of micro- and nanopowders using equal-channel angular extrusion. | | 2935-2949A | |
| Effect of Boron on the Low-Cycle Fatigue Behavior and Deformation Structure of INCONEL 718 at 650°C | | 3477-3487A | |
| Fatigue and Fracture Behavior of Bulk Metallic Glass Inclusion-Controlled Fatigue Properties of 1800 MPA-Class Spring Steels | | 3489-3498A | |
| Deformation resistance | | | 3737-3744A |
| Communication: Resonant Vibration Behavior of an Al-3.8Cu-0.8Li-0.3Mg Alloy. | | 952-957A | |
| Degradation | | | |
| Damage Evolution during Thermal Fatigue in Fiber-Reinforced Light-Metal-Matrix Composites. | | 37-43A | |
| Hydrogen-Involved Tensile and Cyclic Deformation Behavior of Low-Alloy Pressure Vessel Steel. | | 1477-1486A | |
| A Comparison between Growth Morphology of "Eutectic" Cells/Dendrites and Single-Phase Cells/Dendrites. | | 1632-1635A | |
| Dehydration | | | |
| Communication: Preparation of MgOHCl by Controlled Dehydration of MgCl ₂ ·6H ₂ O. | | 405-406B | |
| Dehydrogenation | | | |
| Mechanochemical Processing of Nanocrystalline Ti-6Al-4V Alloy. | | 1899-1903A | |
| Delamination | | | |
| Study on Notch Fracture of TiAl Alloys at Room Temperature. | | 439-456A | |
| Dynamic Deformation Behavior and Ballistic Impact Properties of Ti-6Al-4V Alloy Having Equiaxed and Bimodal Microstructures | | 3103-3112A | |
| Dendritic structure | | | |
| Effect of Microstructure on Mechanical Properties of As-Cast Mg-Al Alloys. | | 309-319A | |
| In-Situ Observations of Low-Cycle Fatigue Damage in Cast AM60B Magnesium in an Environmental Scanning Electron Microscope. | | 321-331A | |
| Undercooling and Solidification of Al-50 At. Pct Si Alloy by Electromagnetic Levitation. | | 607-612A | |
| Response of Primary Dendrite Spacing to Varying Temperature Gradient during Directional Solidification. | | 735-742B | |
| Effect of Grain-Boundary Characteristics on Castability of Nickel-Base Superalloys. | | 939-946A | |
| Morphologies of Silicon Crystals Solidified on a Chill Plate. | | 1067-1073A | |
| Modeling of Irregular Eutectic Microstructures in Solidification | | | |

- of Al-Si Alloys.
A Comparison between Growth Morphology of "Eutectic" Cells/
Dendrites and Single-Phase Cells/Dendrites.
Erratum: A Solutal Interaction Mechanism for the Columnar-to-
Equiaxed Transition in Alloy Solidification. 1915A
Microstructural Evolution of Predeformed SiCp/ZA27 Compos-
ites during Partial Remelting. 2073-2085A
A Quantitative Dendrite Growth Model and Analysis of Stability
Concepts. 2471-2485A
Influence of Convection on Feathery Grain Formation in Alumi-
num Alloys. 2495-2501A
Plastic deformation behavior of aluminum casting alloys A356/
357. 2707-2718A
Experimental and modeling studies of the thermal conditions
and magnesium, iron, and copper content on the morphology
of the aluminum silicon eutectic in hypoeutectic aluminum sil-
icon alloys. 2981-2991A
The Solidification of Undercooled Melts via Twinned Dendritic
Growth. 3211-3220A
Directional Solidification of Large Superalloy Castings with
Radiation and Liquid-Metal Cooling: A Comparative Assess-
ment. 3221-3231A
Nucleation of Solid Aluminum on Inclusion Particles Injected
into Al-Si-Fe Alloys. 3233-3250A
A Through-Process Model of an A356 Brake Caliper for
Fatigue Life Prediction. 3275-3288A
Effect of Sn on Microstructure and Mechanical Properties of Ti-
Base Dendrite/Ultrafine-Structured Multicomponent Alloys. 3605-3612A
- Densification**
Simulation of the Sintering Densification and Shrinkage Behav-
ior of Powder-Injection-Molded 17-4 PH Stainless Steel. 257-263A
Densification of a Powder-Metal Skeleton by Transient Liquid-
Phase Infiltration. 631-640A
The Role of Particle Size on the Laser Sintering of Iron Powder
Hot Explosive Compaction of Aluminum-Nickel Composites.
Copper-Zirconium Tungstate Composites Exhibiting Low and
Negative Thermal Expansion Influenced by Reinforcement
Phase Transformations. 937-948B
Modeling of Distortion after Densification during Liquid-Phase
Sintering. 1125-1131A
1159-1165A
3833-3841A
- Density measurement**
Defect Structures and Room Temperature Mechanical Proper-
ties of C15 Laves Phases in Zr-Nb-Cr and Zr-Hf-Cr Alloy
Systems. 3469-3476A
- Density of states**
Standard Gibbs Energy of Formation of Mg48Zn52 Determined
by Solution Calorimetry and Measurement of Heat Capacity
from Near Absolute Zero Kelvin. 891-895B
- Deoxidizers**
A Thermodynamic Model for Deoxidation Equilibria in Steel. 493-507B
- Deoxidizing**
A Thermodynamic Model for Deoxidation Equilibria in Steel. 493-507B
- Depth profiling**
Solute diffusion in liquid nickel measured by pulsed ion beam
melting. 2803-2807A
- Desorption**
Precise Determination of the Activation Energy for Desorption
of Hydrogen in Two Ti-Added Steels by a Single Thermal-
Desorption Spectrum. 587-597B
Continuous Oxygen Steelmaking with Copper-, Tin-, and Zinc-
Contaminated Scrap. 663-674B
Hydrogen Trap States in Ultrahigh-Strength AERMET 100
Steel. 849-864A
- Desulfurizing**
Kinetics of As, Sb, Bi and Pb Volatilization from Industrial Cop-
per Matte during Ar + O₂ Bubbling. 651-661B
- Diamond pyramid hardness**
Dispersion Strengthening in a Hypereutectic Al-Si Alloy Pre-
pared by Extrusion of Rapidly Solidified Powder. 333-339A
- Diamonds**
Nanoscale view of shock-wave splitting in diamond. 2647-2650A
- Die casting**
A Model of the Interfacial Heat Transfer Coefficient for the Alu-
minum Gravity Die-Casting Process. 721-733B
- Die castings**
The Effect of Silicon Content on the Microstructure and Creep
Behavior in Die-Cast Magnesium AS Alloys. 1905-1909A
Segregation band formation in Al-Si die castings. 2881-2891A
- Die steels**
Fatigue of Cold-Work Tool Steels: Effect of Heat Treatment and
Carbide Morphology on Fatigue Crack Formation, Life, and
Fracture Surface Observations. 1289-1300A
- Die steels, Coating**
Process Efficiency Measurements in the Laser Engineered Net
Shaping Process. 143-152B
- Diesel engines**
Study of the Porosity Produced in an Aluminum Alloy Matrix
Composite Due to a T6 Heat Treatment. 2503-2510A
- Differential equations**
Calorimetric Determination of the 5 Hydride Dissolution
Enthalpy in ZIRCALOY-4. 2343-2349A
Dislocation mechanics-based constitutive equations. 2547-2555A
- Diffusion**
Thermodynamic Properties and Diffusion Thermodynamic Fac-
tors in B2-NiAl. 867-876B
Partial Diffusion Reactions and the Associated Volume
Changes in Thermally Exposed Au-Al Ball Bonds. 1273-1280A
- 1555-1563A
1632-1635A
1915A
2073-2085A
2471-2485A
2495-2501A
2707-2718A
2981-2991A
3211-3220A
3221-3231A
3233-3250A
3275-3288A
3605-3612A
257-263A
631-640A
937-948B
1125-1131A
1159-1165A
3833-3841A
3469-3476A
891-895B
493-507B
493-507B
2803-2807A
587-597B
663-674B
849-864A
651-661B
333-339A
2647-2650A
721-733B
1905-1909A
2881-2891A
1289-1300A
143-152B
2503-2510A
2343-2349A
2547-2555A
867-876B
1273-1280A
- Temperature-Dependent Variability in Lifetime Prediction of
Thermally Activated Systems. 1471-1476A
Magnetic Contribution to the Interdiffusion Coefficients in Bcc
(α) and Fcc (γ) Fe-Ni Alloys. 1681-1690A
Experimental and Theoretical Evidence for Carbon-Vacancy
Binding in Austenite. 2239-2245A
Characterization of the peritectic reaction in medium-alloy steel
through microsegregation and heat-of-transformation stud-
ies. 2869-2879A
Continuous Cooling β -to- α Transformation Behaviors of Extra-
Pure and Commercially Pure Ti. 3071-3077A
Ductility Exhaustion Mechanisms in Thermally Exposed Thin
Sheets of a Near- β Titanium Alloy. 3113-3127A
Microstructure Characterization and Creep Deformation of an
Al-10 Wt Pct Ti-2 Wt Pct Cu Nanocomposite. 3855-3861A
- Diffusion barriers**
Effects of Preoxidation on the Nucleation and Growth Behavior
of Chemically Vapor-Deposited α -Al₂O₃ on a Single-Crystal
Ni-Based Superalloy. 1113-1124A
- Diffusion coating**
Intermetallic Diffusion Coatings for Enhanced Hot-Salt Oxida-
tion Resistance of Nitrogen-Containing Austenitic Stainless
Steels. 1799-1806A
Effect of Thermal Spray on the Microstructure and Adhesive
Strength of High Velocity Oxy-Fuel-Sprayed Ni-Cr Coatings
on 9Cr-1Mo Steel. 3187-3199A
- Diffusion coefficient**
Diffusion-Coefficient Measurements in Liquid Metallic Alloys
Solute diffusion in liquid nickel measured by pulsed ion beam
melting. 909-917B
Coarsening of Al₃Sc precipitates in an Al-0.28 Wt pct Sc alloy.
Communication: Diffusion coefficients for modeling the heat
treatment of Ti-6Al-4V. 2803-2807A
3003-3008A
Coarsening Behavior of Ni₃Ga Precipitates in Ni-Ga Alloys:
Dependence of Microstructure and Kinetics on Volume Frac-
tion. 3015-3018A
3063-3069A
- Diffusion layers**
Effect of Thermal Spray on the Microstructure and Adhesive
Strength of High Velocity Oxy-Fuel-Sprayed Ni-Cr Coatings
on 9Cr-1Mo Steel. 3187-3199A
Residual Stress-Affected Diffusion during Plasma Nitriding of
Tool Steels. 3523-3530A
- Diffusion rate**
Multicomponent Diffusion in Molten Slags.
Characterization of the Nucleation and Growth Behavior of
Copper Precipitates in Low-Carbon Steels. 675-684B
2323-2329A
- Diffusivity**
Diffusion Models for Evaporation Losses during Electron-Beam
Melting of Alpha/Beta-Titanium Alloys. 235-245B
Mechanism and Rate of Reaction of Al₂O₃, Al, and CO Vapors
with Carbon. 617-623B
Freeze-Off Limits in Transient Liquid-Phase Infiltration.
Multicomponent Diffusion in Molten Slags. 641-653A
Communication: Grain Boundary Engineering of Ferritic-Mar-
tensitic Alloy T91. 675-684B
717-718A
Hydrogen Trap States in Ultrahigh-Strength AERMET 100
Steel. 849-864A
Alteration in Hydrogen Absorption by and Hydrogen Permea-
tion through a High-Strength Low-Alloy Steel due to Plasma
Source Ion Implantation of Nitrogen. 1123-1128B
Quantification of Hydrogen Diffusion and Trapping in 2.25Cr-
1Mo and 3Cr-1Mo-V Steels with the Electrochemical Permea-
tion Technique and Melt Extractions. 1449-1464A
A Study on the Microstructural Evolution of Al-25 At. Pct V-12.5
At. pct M (M = Cu, Ni, Mn) Powders by Planetary Ball Milling.
Communication: Diffusion coefficients for modeling the heat
treatment of Ti-6Al-4V. 1853-1860A
3015-3018A
- Dimensional stability**
Wear Behavior, Microstructure, and Dimensional Stability of
As-Cast Zinc-Aluminum/SiC (Metal Matrix Composites)
Alloys. 1579-1590A
- Dioxins**
Study on Polychlorinated Dibenzo-p-Dioxin/Furan Formation in
Iron Ore Sintering Process. 983-991B
- Direct chill casting**
On the Development of a Three-Dimensional Transient Ther-
mal Model to Predict Ingot Cooling Behavior during the Start-
Up Phase of the Direct Chill-Casting Process for an AA5182
Aluminum Alloy Ingot. 523-540B
Finite element method simulation of mushy zone behavior dur-
ing direct-chill casting of an Al-4.5 pct Cu alloy. 2917-2926A
Effects of Alloy Composition and Casting Speed on Structure
Formation and Hot Tearing during Direct-Chill Casting of Al-
Cu Alloys. 3551-3561A
Development and Validation of a Thermal Model of the Direct
Chill Casting of AZ31 Magnesium Billets. 3843-3854A
- Direct current**
Mathematical Modeling of a Direct Current Electric Arc: Part I.
Analysis of the Characteristics of a Direct Current Arc. 363-372B
Mathematical Modeling of a Direct Current Electric Arc: Part II.
Dimensionless Representation of a Direct Current Arc. 373-380B
Effect of Low-Frequency Electromagnetic Casting on the
Castability, Microstructure, and Tensile Properties of Direct-
Chill Cast Al-Zn-Mg-Cu Alloy. 2487-2494A
- Directional solidification**
Analytical, Numerical, and Experimental Analysis of Inverse
Macrosegregation during Upward Unidirectional Solidifica-
tion of Al-Cu Alloys. 285-297B
Response of Primary Dendrite Spacing to Varying Temperature

- Gradient during Directional Solidification. 735-742B
Effect of Zr and B on Castability of Ni-Based Superalloy IN792. 1337-1342A
Overstability of Lamellar Eutectic Growth below the Minimum-Undercooling Spacing. 1815-1828A
Characterization of the peritectic reaction in medium-alloy steel through microsegregation and heat-of-transformation studies. 2869-2879A
Mushy-zone Rayleigh number to describe macrosegregation and channel segregate formation during directional solidification of metallic alloys. 2927-2934A
Experimental and modeling studies of the thermal conditions and magnesium, iron, and copper content on the morphology of the aluminum silicon eutectic in hypoeutectic aluminum silicon alloys. 2981-2991A
Directional Solidification of Large Superalloy Castings with Radiation and Liquid-Metal Cooling: A Comparative Assessment. 3221-3231A
A Novel Experiment for the Study of Substrate-Induced Nucleation in Metallic Alloys: Application to Zn-Al. 3543-3550A
- Directionally solidified eutectics**
Diffusion-Coefficient Measurements in Liquid Metallic Alloys. 909-917B
A Comparison between Growth Morphology of "Eutectic" Cells/Dendrites and Single-Phase Cells/Dendrites. 1632-1635A
- Disilicides**
Defect Structures in Computerized Thin Films of Transition Metal Disilicides with C11b, C40 and C54 Structures. 2229-2238A
Monosilicide-Disilicide-Silicon Phase Equilibria in the Nickel-Platinum-Silicon and Nickel-Palladium-Silicon Systems. 3053-3061A
- Dislocation density**
Effect of Temperature and Strain Rate on the Compressive Flow of Aluminum Composites Containing Submicron Alumina Particles. 287-292A
Mechanisms of Strain Accumulation and Damage Development during Creep of Prestrained 316 Stainless Steels. 563-571A
Cr-Mo Solid Solutions Formed by High-Energy Ball Milling. 1105-1111A
The Effects of Strain Rate and Welding Current Mode on the Dynamic Impact Behavior of Plasma-Arc-Welded 304L Stainless Steel Weldments. 1501-1515A
Laser-induced shock compression of copper: orientation and pressure decay effects. 2633-2646A
Microindentation of Aluminum. 3323-3328A
On Cells and Microbands Formed in an Interstitial-Free Steel during Cold Rolling at Low to Medium Reductions. 3423-3430A
- Dislocation loops**
Effects of Simultaneous Displacive and Ionizing Radiations and of Electric Field on Radiation Damage in Ionic Crystals. 2257-2266A
Dislocation structure behind a shock front in fcc perfect crystals: atomistic simulation results. 2609-2615A
- Dislocation mobility**
Dislocation mechanics-based constitutive equations. 2547-2555A
Dislocation structure behind a shock front in fcc perfect crystals: atomistic simulation results. 2609-2615A
- Dislocation pinning**
Microstructural Characterization of Secondary-Phase Particles in a Hot-Deformed Al-Cu-Mg-Zr Alloy. 293-300A
Synthesis of Nanocrystalline Zn-22 Pct Al Using Cryomilling. 573-581A
- Dislocations**
Quantifying Thermomechanical Fatigue of Light-Metal-Matrix Composites by Mechanical Spectroscopy. 25-35A
Role of Temperature and Strain Rate on the Hydrogen-Induced Intergranular Rupture in Alloy 600. 457-464A
Tensile Anisotropy in Cu-Ni-Mn-Sn-Al Alloys. 465-469A
Dynamic Phase Transformation during Superplastic Deformation of Nb/Nb-Al In-Situ Composite. 503-511A
Effects of Partial Recrystallization on High-Cycle Fatigue Deformation and Crack Generation of a Nitrogen-Strengthened 32Mn-7Cr Austenitic Steel at Liquid-Nitrogen Temperature. 543-553A
Transition of Dominant Diffusion Process during Superplastic Deformation in AZ61 Magnesium Alloys. 555-562A
Fiber Texture and Substructural Features in the Caliber-Rolled Low-Carbon Steels. 665-677A
Creep Behavior of Copper-Chromium In-Situ Composite. 695-705A
Communication: Grain Boundary Engineering of Ferritic-Martensitic Alloy T91. 717-718A
High-Strain-Rate Superplastic Behavior of Equal-Channel Angular-Pressed 5083 Al-0.2 Wt Pct Sc. 825-837A
Cu Precipitation in a Prestrained Fe-1.5 Wt Pct Cu Alloy during Isothermal Aging. 1263-1272A
Dislocation Structure and Deformation in Iron Processed by Equal-Channel-Angular Pressing. 1343-1350A
Quantification of Hydrogen Diffusion and Trapping in 2.25Cr-1Mo and 3Cr-1Mo-V Steels with the Electrochemical Permeation Technique and Melt Extractions. 1449-1464A
Experimental Determination of the Carbon Solubility Limit in Ferritic Steels. 1655-1661A
Thermomechanical Fatigue Behavior of the Third-Generation, Single-Crystal Superalloy TMS-75: Deformation Structure. 1779-1787A
Communication: Strengthening by γ/γ' Interfacial Dislocation Networks in TMS-162-Toward a Fifth-Generation Single-Crystal Superalloy. 1911-1914A
Multiscale Structure and Properties of Cast and Deformation Processed Polycrystalline NiTi Shape-Memory Alloys. 2013-2025A
A Tribute to Terence E. Mitchell. 2203-2205A
Dislocations in Milled Galena (PbS). 2223-2228A
Grain size dependence of the activation parameters for plastic deformation: influence of crystal structure, slip system, and rate-controlling dislocation mechanism. 2697-2705A
Cyclic deformation behavior and dislocation structure of Ti-2 Al. Pct Al single crystals oriented for double prism slip. 2845-2852A
- Room-temperature tensile and high-cycle-fatigue strength of fine TiB particulate-reinforced Ti-22Al-27Nb composites. 2971-2979A
Microstructure Development during High Velocity Deformation Application of a Substructure-Based Hardening Model to Copper under Loading Path Changes. 3091-3101A
Texture Evolution and Mechanical Anisotropy in Dual-Phase Ti3Al-Based Alloy Loaded at 700 °C to 1000 °C. 3763-3774A
Microstructure Characterization and Creep Deformation of an Al-10 Wt Pct Ti-2 Wt Pct Cu Nanocomposite. 3803-3815A
3855-3861A
- Dispensing**
Comparison of Microstructural Evolution in Laser-Deposited and Arc-Melted In-Situ Ti-TiB Composites. 2143-2152A
- Dispersion**
Modification-Related Porosity Formation in Hypoeutectic Aluminum-Silicon Alloys. 1097-1106B
The Influence of Strontium on Porosity Formation in Al-Si Alloys. 3531-3541A
- Dispersion hardening**
Effect of Temperature and Strain Rate on the Compressive Flow of Aluminum Composites Containing Submicron Alumina Particles. 287-292A
Dispersion Strengthening in a Hypereutectic Al-Si Alloy Prepared by Extrusion of Rapidly Solidified Powder. 333-339A
- Dispersion hardening alloys, Mechanical properties**
Correlation of the Microstructure and Mechanical Properties of Oxide-Dispersion-Strengthened Coppers Fabricated by Internal Oxidation. 493-502A
- Dispersions**
A Study of Coarsening, Recrystallization, and Morphology of Microstructure in Al-Sc-(Zr)-(Mg) Alloys. 341-350A
Nickel Droplet Settling Behavior in an Electric Furnace. 839-845B
Spot Turbulence, Breakup, and Coalescence of Bubbles Released from a Porous Plug Injector into a Gas-Stirred Ladle. 949-956B
Validation of Predicted Precipitate Compositions in Al-Si-Ge. 2305-2311A
The Behavior and Effect of Rare Earth CeO₂ on In-Situ TiC/Al Composite. 2511-2515A
An Analytical Model for the Oxide Size in Al Alloys Synthesized by Reactive Atomization and Deposition. 3265-3273A
- Dissimilar metals**
Computational Modeling of Laser Welding of Cu-Ni Dissimilar Couple. 339-350B
Tensile behavior of friction-stir-welded A356-T6/Al 6061-T651 Bi-alloy plate. 2837-2843A
- Dissipation**
Communication: Comparisons of Experimental Measurements and a Theoretical Model for Specimen Self-Heating during Fatigue of Type 316 LN Stainless Steel. 3334-3339A
- Dissolution**
Communication: The Solubility of Titanium Dioxide in Cryolite-Alumina Melts at 1300 K. 182-186B
Kinetics of As, Sb, Bi and Pb Volatilization from Industrial Copper Matte during Ar + O₂ Bubbling. 651-661B
Metal Vapor Treatment for Enhancing the Dissolution of Platinum Group Metals from Automotive Catalyst Scrap. 817-824B
The Effect of Temperature, Matrix Alloying and Substrate Coatings on Wettability and Shear Strength of Al/Al₂O₃ Couples. 911-923A
Phase Equilibrium and Distribution of Minor Elements between Ni-S Melt and Al₂O₃-CaO-MgO Slag at 1873 K. 1041-1049B
The Effect of Carbon in Slag on Steel Reoxidation and Carbon Analysis by X-Ray Photoelectron Spectroscopy in the CaO-SiO₂-Al₂O₃-MgO-MnO-FeO System. 1087-1095B
Precipitate Microstructures and Resulting Properties of Al-Zn-Mg Metal Inert Gas-Weld Heat-Affected Zones. 1437-1448A
Calorimetric Determination of the 5 Hydride Dissolution Enthalpy in ZIRCALOY-4. 2343-2349A
Electrochemical Evaluation of a Corrosion Fatigue Failure Mechanism in a Duplex Stainless Steel. 2427-2437A
Effect of dissolved tungsten on the deformation of 70Ni-30Fe alloys. 2821-2828A
Infrared Brazing Cu and Ti Using a 95Ag-5Al Braze Alloy. 3177-3186A
The Nitriding Kinetics of Iron-Chromium Alloys; The Role of Excess Nitrogen: Experiments and Modelling. 3387-3398A
Characterization of Retrogression and Reaging Behavior of 8090 Al-Li-Cu-Mg-Zr Alloy. 3681-3691A
- Distortion**
Formation of Mesoscale Roughening in 6022-T4 Al Sheets Deformed in Plane-Strain Tension. 513-524A
Modeling of Distortion after Densification during Liquid-Phase Sintering. 3833-3841A
- Distribution functions**
Effects of the entrained surface film on the reliability of castings. 2893-2902A
- Domain wall**
Local Electromechanical Response at a Single Ferroelectric Domain Wall in Lithium Niobate. 2287-2290A
- Doping**
Effects of Prehafnizing on Morphological Development of a Chemical Vapor Deposition Aluminide Coating Formed on Single-Crystal Ni-Based Superalloy. 891-897A
Mechanisms of Hf Dopant Incorporation during the Early Stage of Chemical Vapor Deposition Aluminide Coating Growth under Continuous Doping Conditions. 3581-3593A
- Drag**
Role of Carbon and Alloying Elements in the Formation of Bainitic Ferrite. 3693-3700A
- Drag (hindrance)**
The Selection of the Spray Deposition Rate during the Spray

- Rolling Process 3595-3603A
- Droplets**
- Nickel Droplet Settling Behavior in an Electric Furnace 839-845B
- A Numerical Study of Oxidation Behavior during Reactive Atomization and Deposition 1173-1185B
- An Analytical Model for the Oxide Size in Al Alloys Synthesized by Reactive Atomization and Deposition 3265-3273A
- The Selection of the Spray Deposition Rate during the Spray Rolling Process 3595-3603A
- Dry friction**
- Nonequilibrium molecular dynamics simulations of metallic friction at Ta/Al and Cu/Ag interfaces. 2741-2745A
- Dual phase steels**
- Effects of Martensite Morphology and Tempering on Dynamic Deformation Behavior of Dual-Phase Steels. 2371-2382A
- Austenite Formation during Intercritical Annealing 3363-3375A
- Ductile brittle transition**
- Mechanisms and Modeling of Cleavage Fracture in Simulated Heat-Affected Zone Microstructures of a High-Strength Low Alloy Steel. 1039-1053A
- Effect of Sn on Microstructure and Mechanical Properties of Ti-Base Dendrite/Ultrafine-Structured Multicomponent Alloys 3605-3612A
- Ductile fracture**
- Effects of Martensite Morphology and Tempering on Dynamic Deformation Behavior of Dual-Phase Steels. 2371-2382A
- Effect of Sn on Microstructure and Mechanical Properties of Ti-Base Dendrite/Ultrafine-Structured Multicomponent Alloys 3605-3612A
- Ductility**
- A New Quality Index for Characterizing Aluminum Cast Alloys with Regard to Aircraft Structure Design Requirements. 301-308A
- Role of Temperature and Strain Rate on the Hydrogen-Induced Intergranular Rupture in Alloy 600. 457-464A
- Effect of Aging and Deformation on the Microstructure and Properties of Fe-Ni-Ti Maraging Steel. 973-983A
- A Hybrid Micromechanical-Macroscopic Model for the Analysis of the Tensile Behavior of Cavitating Materials. 1141-1149A
- Microstructural Banding and Failure of a Stainless Steel. 1317-1324A
- Dislocation Structure and Deformation in Iron Processed by Equal-Channel-Angular Pressing. 1343-1350A
- Hydrogen-Involved Tensile and Cyclic Deformation Behavior of Low-Alloy Pressure Vessel Steel. 1477-1486A
- Microstructure, Mechanical Properties, and Fracture Mechanism of As-Cast (Ti_{0.5}Cu_{0.25}Ni_{0.15}Sn_{0.05}Zr_{0.05})(100-x)Mo(x) Composites. 1591-1601A
- Effect of Mg₂Si Particles on the Elevated Temperature Tensile Properties of Squeeze-Cast Mg-Al Alloys. 1629-1632A
- The Influences of Multiscale-Sized Second-Phase Particles on Ductility of Aged Aluminum Alloys. 1725-1734A
- Achieving Enhanced Ductility in a Dilute Magnesium Alloy through Severe Plastic Deformation. 1735-1744A
- Experimental and Numerical Study on the Relationship between Creep Crack Growth Properties and Fracture Mechanisms. 1757-1764A
- Superplastic Behavior and Microstructure Evolution in a Commercial Al-Mg-Sc Alloy Subjected to Intense Plastic Straining. 2383-2392A
- Nonequilibrium molecular dynamics simulations of metallic friction at Ta/Al and Cu/Ag interfaces. 2741-2745A
- Tensile properties and microstructure of Haynes 25 alloy after aging at elevated temperatures for extended times. 2767-2781A
- Effect of dissolved tungsten on the deformation of 70Ni-30Fe alloys. 2821-2828A
- Tensile behavior of friction-stir-welded A356-T6/Al 6061-T651 Bi-alloy plate. 2837-2843A
- Microstructure evolution and mechanical behavior of bulk copper obtained by consolidation of micro- and nanopowders using equal-channel angular extrusion. 2935-2949A
- Quality Assessment of Artificially Aged A357 Aluminum Alloy Cast Ingots by Introducing Approximate Expressions of the Quality Index QD 3079-3089A
- Ductility Exhaustion Mechanisms in Thermally Exposed Thin Sheets of a Near- β Titanium Alloy 3113-3127A
- Effects of Temperature and Strain Rate on Tensile Properties and Activation Energy for Dynamic Strain Aging in Alloy 625 3129-3139A
- Communication: Tensile Properties of Chromium Alloyed with Silver 3329-3331A
- Two-Layered Zr-Base Amorphous Alloy/Metal Surface Composites Fabricated by High Energy Electron-Beam Irradiation Formability and Strength of Friction-Stir-Welded Aluminum Sheets 3455-3460A
- Characterization of Retrogression and Reaging Behavior of 8090 Al-Li-Cu-Mg-Zr Alloy 3461-3468A
- On the Isotropy of the Dynamic Mechanical and Failure Properties of Swaged Tungsten Heavy Alloys 3681-3691A
- Failure Mode Analysis and a Mechanism for Hot-Ductility Improvement in the Nb-Microalloyed Steel 3787-3795A
- Communication: Room-Temperature Cleavage Fracture of FeMnAlC Steels 3823-3832A
- 3863-3866A
- Ductility tests**
- Analysis of intergranular impurity concentration and the effects on the ductility of copper-shaped charge jets. 2567-2573A
- The Microstructural, Mechanical, and Fracture Properties of Austenitic Stainless Steel Alloyed with Gallium 3445-3454A
- Duplex stainless steels**
- Microstructures of a Powder Metallurgy--Hot-Isostatically Pressed Super Duplex Stainless Steel Forming in Industrial Heat Treatments. 2103-2109A
- Second-Order Stresses and Strains in Heterogeneous Steels: Self-Consistent Modeling and X-Ray Diffraction Analysis. 2361-2369A
- Electrochemical Evaluation of a Corrosion Fatigue Failure Mechanism in a Duplex Stainless Steel. 2427-2437A
- Determination of Isothermal Transformation Diagrams for Sigma-Phase Formation in Cast Duplex Stainless Steels 3377-3386A
- Effect of Different Cr Contents on Tensile and Corrosion Behaviors of 0.13 Pct N-Containing CD4MCU Cast Duplex Stainless Steels 3431-3438A
- Double Loop Electrochemical Potentiokinetic Reactivation Test Optimization in Checking of Duplex Stainless Steel Intergranular Corrosion Susceptibility 3499-3513A
- Dynamic mechanical properties**
- Effects of Martensite Morphology and Tempering on Dynamic Deformation Behavior of Dual-Phase Steels. 2371-2382A
- Dynamic deformation and damage in cast γ -TiAl during Taylor cylinder impact: experiments and model validation. 2557-2566A
- Dynamic Deformation Behavior and Ballistic Impact Properties of Ti-6Al-4V Alloy Having Equiaxed and Bimodal Microstructures 3103-3112A
- On the Isotropy of the Dynamic Mechanical and Failure Properties of Swaged Tungsten Heavy Alloys 3787-3795A
- Dynamic recrystallization**
- Deformation and Recrystallization Behavior during Hot Working of a Coarse-Grain, Nickel-Base Superalloy Ingot Material. 679-693A
- Effect of Initial Grain Size of Austenite on Hot-Deformed Structure of Ni-30Fe Alloy 3399-3408A
- Dynamic strain aging**
- Experimental and Theoretical Evidence for Carbon-Vacancy Binding in Austenite. 2239-2245A
- Grain size dependence of the activation parameters for plastic deformation: influence of crystal structure, slip system, and rate-controlling dislocation mechanism. 2697-2705A
- Effects of Temperature and Strain Rate on Tensile Properties and Activation Energy for Dynamic Strain Aging in Alloy 625 3129-3139A
- Dynamic tests**
- Effects of Martensite Morphology and Tempering on Dynamic Deformation Behavior of Dual-Phase Steels. 2371-2382A
- Dynamic systems**
- Nonequilibrium molecular dynamics simulations of metallic friction at Ta/Al and Cu/Ag interfaces. 2741-2745A
- Dynamics**
- Materials science under extreme conditions of pressure and strain rate. 2587-2607A
- Infrared Brazing Cu and Ti Using a 95Ag-5Al Braze Alloy 3177-3186A
- Edge dislocations**
- Synthesis of Nanocrystalline Zn-22 Pct Al Using Cryomilling. 573-581A
- Elastic anisotropy**
- Second-Order Stresses and Strains in Heterogeneous Steels: Self-Consistent Modeling and X-Ray Diffraction Analysis. 2361-2369A
- Single-Crystal Elastic Constants of Fe-15Ni-15Cr Alloy 3149-3154A
- Elastic constants**
- Application of the Generalized Method of Cells Principle to Particulate-Reinforced Metal Matrix Composites 1029-1039B
- Variability of Large-Crack Fatigue-Crack-Growth Thresholds in Structural Alloys 3721-3735A
- Elastic deformation**
- The Effect of Surface Deformation on Lubrication and Oxide-Scale Fracture in Cold Metal Rolling 919-928B
- Fatigue and Fracture Behavior of Bulk Metallic Glass 3489-3498A
- Elastic limit**
- Communications: Ultra-High-Speed Exploding Properties of Ti-6Al-4V Alloy Having Equiaxed and Bimodal Microstructures. 719-724A
- Nanoscale view of shock-wave splitting in diamond. 2647-2650A
- Elasticity**
- Deformation Behavior of Zr₃Al-Nb Alloys I: Room-Temperature and High-Temperature Deformation Study. 189-203A
- Elastoplasticity**
- Microstructure evolution and mechanical behavior of bulk copper obtained by consolidation of micro- and nanopowders using equal-channel angular extrusion. 2935-2949A
- Electric arc furnaces**
- Mathematical Modeling of a Direct Current Electric Arc: Part I. Analysis of the Characteristics of a Direct Current Arc. 363-372B
- Mathematical Modeling of a Direct Current Electric Arc: Part II. Dimensionless Representation of a Direct Current Arc. 373-380B
- Nanoparticle Recovery Using a Fume Collector Comprised of Carbonized Refuse-Derived Fuel 993-998B
- Electric devices**
- Two-Layered Zr-Base Amorphous Alloy/Metal Surface Composites Fabricated by High Energy Electron-Beam Irradiation 3455-3460A
- Electric discharge machining**
- Characteristics of the Rough-Cut Surface of Quenched and Tempered Martensitic Stainless Steel Using Wire Electrical Discharge Machining. 1351-1357A
- Electric fields**
- Effects of Simultaneous Displacive and Ionizing Radiations and of Electric Field on Radiation Damage in Ionic Crystals. 2257-2266A
- Electric furnaces**
- Nickel Droplet Settling Behavior in an Electric Furnace 839-845B
- Electric potential**
- Mathematical Modeling of a Direct Current Electric Arc: Part I. Analysis of the Characteristics of a Direct Current Arc. 363-372B
- Electric power generation**
- Effects of Heat Treatment and Testing Temperature on Fracture Mechanics Behavior of Low-Si CA-15 Stainless Steel. 471-480A
- Electric wire**
- Mechanism of Resistance Microwelding of Crossed Fine Nickel

| | | | |
|--|------------|--|--|
| Wires | 3165-3176A | | |
| Electrical steels, Powder technology | | | |
| Densification of a Powder-Metal Skeleton by Transient Liquid-Phase Infiltration. | 631-640A | | |
| Electrodes | | | |
| Mathematical Modeling of a Direct Current Electric Arc: Part II. Dimensionless Representation of a Direct Current Arc. | 373-380B | | |
| Electrolysis | | | |
| Direct Electrolytic Preparation of Chromium Powder. | 223-233B | | |
| Electrolytes | | | |
| Communication: Discussion of "Thermodynamics of Liquid Al-Na Alloys Determined by Using CaF ₂ Solid Electrolyte". | 393-398B | | |
| Communication: Authors' Reply. | 398-400B | | |
| Communication: Properties of MgOHCl. | 406-408B | | |
| Electrolytic cells | | | |
| Communication: Preparation of MgOHCl by Controlled Dehydration of MgCl ₂ ·6H ₂ O. | 405-406B | | |
| Electromagnetic fields | | | |
| Flow of Conducting Liquid around Two Nonconducting Particles in DC Electromagnetic Field and the Electromagnetic Migration Force | 847-855B | | |
| Effect of Low-Frequency Electromagnetic Casting on the Castability, Microstructure, and Tensile Properties of Direct-Chill Cast Al-Zn-Mg-Cu Alloy. | 2487-2494A | | |
| Electromagnetic forming | | | |
| Microstructure Development during High Velocity Deformation | 3091-3101A | | |
| Electromagnetic stirring | | | |
| Channel Segregation during Solidification and the Effects of an Alternating Traveling Magnetic Field. | 743-754B | | |
| Simulation of Flow Control in the Meniscus of a Continuous Casting Mold with Opposing Alternating Current Magnetic Fields | 1129-1137B | | |
| Grain Refinement Induced by Electromagnetic Stirring: A Dendrite Fragmentation Criterion | 3201-3210A | | |
| Electron beam melting | | | |
| Diffusion Models for Evaporation Losses during Electron-Beam Melting of Alpha/Beta-Titanium Alloys. | 235-245B | | |
| Electron beam welding | | | |
| Assessment of the Origin of Porosity in Electron-Beam-Welded TA6V Plates. | 879-889A | | |
| Evolution of Microstructure and Texture in Mg-Al-Zn Alloys during Electron-Beam and Gas Tungsten Arc Welding. | 2455-2469A | | |
| Electron beams | | | |
| Two-Layered Zr-Base Amorphous Alloy/Metal Surface Composites Fabricated by High Energy Electron-Beam Irradiation | 3455-3460A | | |
| Electron irradiation | | | |
| Experimental and Theoretical Evidence for Carbon-Vacancy Binding in Austenite. | 2239-2245A | | |
| Electronic devices | | | |
| Mechanism of Resistance Microwelding of Crossed Fine Nickel Wires | 3165-3176A | | |
| Elongated structure | | | |
| Microstructural Effects on Fatigue and Dwell-Fatigue Crack Growth in α/β Ti-6Al-2Sn-4Zr-2Mo-0.1Si. | 163-187A | | |
| Microstructural Characterization of Secondary-Phase Particles in a Hot-Deformed Al-Cu-Mg-Zr Alloy. | 293-300A | | |
| Plastic deformation behavior of aluminum casting alloys A356/357. | 2707-2718A | | |
| Effect of Initial Grain Size of Austenite on Hot-Deformed Structure of Ni-30Fe Alloy | 3399-3408A | | |
| Elongation | | | |
| Effect of Microstructure on Mechanical Properties of As-Cast Mg-Al Alloys. | 309-319A | | |
| Dispersion Strengthening in a Hypereutectic Al-Si Alloy Prepared by Extrusion of Rapidly Solidified Powder. | 333-339A | | |
| Correlation of the Microstructure and Mechanical Properties of Oxide-Dispersion-Strengthened Coppers Fabricated by Internal Oxidation. | 493-502A | | |
| Dynamic Phase Transformation during Superplastic Deformation of Nb/Nb ₂ Al In-Situ Composite. | 503-511A | | |
| Transition of Dominant Diffusion Process during Superplastic Deformation in AZ61 Magnesium Alloys. | 555-562A | | |
| High-Strain-Rate Superplastic Behavior of Equal-Channel Angular-Pressed 5083 Al-0.2 Wt Pct Sc. | 825-837A | | |
| The Tensile Response of a Fine-Grained AA5754 Alloy Produced by Asymmetric Rolling and Annealing. | 997-1006A | | |
| Fracture Behavior of Thixoformed 357-T5 Al Alloys. | 1017-1027A | | |
| Achieving Enhanced Ductility in a Dilute Magnesium Alloy through Severe Plastic Deformation. | 1735-1744A | | |
| Effects of Carbon Fiber/Al Interface on Mechanical Properties of Carbon-Fiber-Reinforced Aluminum-Matrix Composites. | 2153-2160A | | |
| Effect of Microstructure on the Stability of Retained Austenite in Transformation-Induced-Plasticity Steels. | 2331-2341A | | |
| Superplastic Behavior and Microstructure Evolution in a Commercial Al-Mg-Sc Alloy Subjected to Intense Plastic Straining. | 2383-2392A | | |
| Effect of Low-Frequency Electromagnetic Casting on the Castability, Microstructure, and Tensile Properties of Direct-Chill Cast Al-Zn-Mg-Cu Alloy. | 2487-2494A | | |
| Tensile properties and microstructure of Haynes 25 alloy after aging at elevated temperatures for extended times. | 2767-2781A | | |
| Tensile behavior of friction-stir-welded Al 6061-T651. | 2829-2835A | | |
| Quality Assessment of Artificially Aged A357 Aluminum Alloy Cast Ingots by Introducing Approximate Expressions of the Quality Index QD | 3079-3089A | | |
| Ductility Exhaustion Mechanisms in Thermally Exposed Thin Sheets of a Near- β Titanium Alloy | 3113-3127A | | |
| Effects of Temperature and Strain Rate on Tensile Properties and Activation Energy for Dynamic Strain Aging in Alloy 625 | 3129-3139A | | |
| Communication: Tensile Properties of Chromium Alloyed with Silver | 3329-3331A | | |
| Inclusion-Controlled Fatigue Properties of 1800 MPA-Class Spring Steels | 3737-3744A | | |
| Texture Evolution and Mechanical Anisotropy in Dual-Phase Ti3Al-Based Alloy Loaded at 700 °C to 1000 °C | 3803-3815A | | |
| Embedded atom method | | | |
| Molecular-dynamics study of mechanical deformation in nanocrystalline aluminum. | 2719-2723A | | |
| Embrittlement | | | |
| Quench Embrittlement of Hardened 5160 Steel as a Function of Austenitizing Temperature. | 153-162A | | |
| In-Situ Observations of Low-Cycle Fatigue Damage in Cast AM60B Magnesium in an Environmental Scanning Electron Microscope. | 321-331A | | |
| Ductility Exhaustion Mechanisms in Thermally Exposed Thin Sheets of a Near- β Titanium Alloy | 3113-3127A | | |
| The Microstructural, Mechanical, and Fracture Properties of Austenitic Stainless Steel Alloyed with Gallium | 3445-3454A | | |
| Effect of Sn on Microstructure and Mechanical Properties of Ti-Base Dendrite/Ultrafine-Structured Multicomponent Alloys | 3605-3612A | | |
| Empirical equations | | | |
| Time-dependent deformation in an enhanced SiC/SiC composite. | 2853-2859A | | |
| Energetic materials | | | |
| Atomic force microscopy studies of fracture surfaces of composition B energetic materials. | 2675-2079A | | |
| Energy absorption | | | |
| Evaluation of Mechanical Properties of Porous 6061 Alloys Fabricated by the Powder Compression and Induction Heating Process. | 2419-2426A | | |
| Energy of formation | | | |
| Standard Gibbs Energy of Formation of Mg48Zn52 Determined by Solution Calorimetry and Measurement of Heat Capacity from Near Absolute Zero Kelvin | 891-895B | | |
| Effect of strain reversal on the dynamic spheroidization of Ti-6Al-4V during hot deformation. | 2993-3001A | | |
| Thermodynamic Investigations of Cr3C2 and Reassessment of the Cr-C System | 3673-3680A | | |
| Energy use | | | |
| Thermodynamic Properties and Diffusion Thermodynamic Factors in B2-NiAl | 867-876B | | |
| Engine valves | | | |
| The Development and Experimental Validation of a Numerical Model of an Induction Skull Melting Furnace. | 785-803B | | |
| Enthalpy | | | |
| Partial Atomic Volume and Partial Molar Enthalpy of Formation of the 3d Metals in the Palladium-Based Solid Solutions. | 63-70A | | |
| The influence of chemical equilibrium on fluid-solid reaction rates and the falsification of activation energy. | 121-131B | | |
| Thermodynamic Properties and Diffusion Thermodynamic Factors in B2-NiAl | 867-876B | | |
| Standard Gibbs Energy of Formation of Mg48Zn52 Determined by Solution Calorimetry and Measurement of Heat Capacity from Near Absolute Zero Kelvin | 891-895B | | |
| Calorimetric Determination of the 5 Hydride Dissolution Enthalpy in ZIRCALOY-4. | 2343-2349A | | |
| Thermodynamic Aspects of the Constitution, Grain Refining, and Solidification Enthalpies of Al-Ce-Si Alloys | 3349-3362A | | |
| Thermodynamic Investigations of Cr3C2 and Reassessment of the Cr-C System | 3673-3680A | | |
| Entrainment | | | |
| Study of Inclusion Re-Entrainment in a Filter Bed | 999-1009B | | |
| Effects of the entrained surface film on the reliability of castings. | 2893-2902A | | |
| Entropy | | | |
| Thermodynamic Properties and Diffusion Thermodynamic Factors in B2-NiAl | 867-876B | | |
| Entropy of formation | | | |
| Standard Gibbs Energy of Formation of Mg48Zn52 Determined by Solution Calorimetry and Measurement of Heat Capacity from Near Absolute Zero Kelvin | 891-895B | | |
| Epitaxial growth | | | |
| Communication: The Observation and Identification of the Oxide Film on the Creep Cavity Wall of Type 316L Stainless Steel | 3331-3333A | | |
| Equal channel angular extrusion | | | |
| The Effect of Temperature and Extrusion Speed on The Consolidation of Zirconium-Based Metallic Glass Powder Using Equal-Channel Angular Extrusion. | 247-256A | | |
| Effect of Deformation Route on Microstructural Development in Aluminum Processed by Equal Channel Angular Extrusion. | 1359-1368A | | |
| Superplastic Behavior and Microstructure Evolution in a Commercial Al-Mg-Sc Alloy Subjected to Intense Plastic Straining. | 2383-2392A | | |
| Microstructure evolution and mechanical behavior of bulk copper obtained by consolidation of micro- and nanopowders using equal-channel angular extrusion. | 2935-2949A | | |
| Microindentation of Aluminum | 3323-3328A | | |
| Equal channel angular pressing | | | |
| Microstructure Transformation from Lamellar to Equiaxed Microduplex through Equal-Channel Angular Pressing in an Al-33 Pct Cu Eutectic Alloy. | 279-286A | | |
| Dislocation Structure and Deformation in Iron Processed by Equal-Channel-Angular Pressing. | 1343-1350A | | |
| Achieving Enhanced Ductility in a Dilute Magnesium Alloy | | | |

- through Severe Plastic Deformation. 1735-1744A
- Equiaxed structure**
- Microstructural Effects on Fatigue and Dwell-Fatigue Crack Growth in α/β Ti-6Al-2Sn-4Zr-2Mo-0.1Si. 163-187A
- Microstructure Transformation from Lamellar to Equiaxed Microduplex through Equal-Channel Angular Pressing in an Al-33 Pct Cu Eutectic Alloy. 279-286A
- Communications: Ultra-High-Speed Exploding Properties of Ti-6Al-4V Alloy Having Equiaxed and Bimodal Microstructures. 719-724A
- Communication: Effect of Thermomechanical Processing on Grain Structure Development in a Twin-Belt Strip Cast Automotive Aluminum Alloy. 949-952A
- Effect of Deformation Route on Microstructural Development in Aluminum Processed by Equal Channel Angular Extrusion. 1359-1368A
- Erratum: A Solutal Interaction mechanism for the Columnar-to-Equiaxed Transition in Alloy Solidification. 1915A
- Grain Refinement of Superalloy IN718C by the Addition of Inoculants. 2111-2114A
- Evolution of Microstructure and Texture in Mg-Al-Zn Alloys during Electron-Beam and Gas Tungsten Arc Welding. 2455-2469A
- Coarsening behavior of an alpha-beta titanium alloy. 2809-2819A
- Dynamic Deformation Behavior and Ballistic Impact Properties of Ti-6Al-4V Alloy Having Equiaxed and Bimodal Microstructures. 3103-3112A
- Effect of Initial Grain Size of Austenite on Hot-Deformed Structure of Ni-30Fe Alloy. 3399-3408A
- A Novel Experiment for the Study of Substrate-Induced Nucleation in Metallic Alloys: Application to Zn-Al. 3543-3550A
- Erosion rate**
- Solid Particle Erosion of Al Alloy and Al-Alloy Composites: Effect of Heat Treatment and Angle of Impingement. 1369-1379A
- Error analysis**
- Thermodynamic Investigations of Cr3C2 and Reassessment of the Cr-C System. 3673-3680A
- Eutectic composition**
- Effect of Microstructure on Mechanical Properties of As-Cast Mg-Al Alloys. 309-319A
- A Comparison between Growth Morphology of "Eutectic" Cells/Dendrites and Single-Phase Cells/Dendrites. 1632-1635A
- Eutectic temperature**
- Carbides in high-speed steels containing silicon. 2757-2766A
- Experimental and modeling studies of the thermal conditions and magnesium, iron, and copper content on the morphology of the aluminum silicon eutectic in hypoeutectic aluminum-silicon alloys. 2981-2991A
- Communication: A thousandfold creep strengthening by Ca addition in die-cast AM50 magnesium alloy. 3029-3032A
- Communication: Eutectic solidification of aluminum-silicon alloys. 3038-3043A
- Infrared Brazing Cu and Ti Using a 95Ag-5Al Braze Alloy. 3177-3186A
- Eutectics**
- Correction to Metallurgical and Materials Transactions A, November 2003, vol. 34A, pp. 2690-2693: "Authors Reply" to Discussion of "Eutectic Solidification of Al-Si Alloys". 959A
- Plastic deformation behavior of aluminum casting alloys A356/357. 2707-2718A
- The Influence of Strontium on Porosity Formation in Al-Si Alloys. 3531-3541A
- Effects of Alloy Composition and Casting Speed on Structure Formation and Hot Tearing during Direct-Chill Casting of Al-Cu Alloys. 3551-3561A
- Experimental Determination of Solid-Liquid Interfacial Energy for Zn Solid Solution in Equilibrium with the Zn-Al Eutectic Liquid. 3665-3672A
- Tensile Test Behavior of the Eutectic Sn-Ag Solder Joint in Ball Grid Array Assemblies. 3817-3821A
- Eutectics, Microstructure**
- Microstructure Transformation from Lamellar to Equiaxed Microduplex through Equal-Channel Angular Pressing in an Al-33 Pct Cu Eutectic Alloy. 279-286A
- Eutectoid composition**
- Effect of Ternary Additions on the Structure and Properties of Coatings Produced by a High Aluminum Galvanizing Bath. 3707-3720A
- Eutectoid reactions**
- Monosilicide-Disilicide-Silicon Phase Equilibria in the Nickel-Platinum-Silicon and Nickel-Palladium-Silicon Systems. 3053-3061A
- Eutectoid temperature**
- An Effect of a Strong Magnetic Field on the Phase Transformation in Plain Carbon Steels. 1663-1668A
- Microstructural modification of as-cast NiAl bronze by friction stir processing. 2951-2961A
- Monosilicide-Disilicide-Silicon Phase Equilibria in the Nickel-Platinum-Silicon and Nickel-Palladium-Silicon Systems. 3053-3061A
- Eutectoids**
- Synthesis of Nanocrystalline Zn-22 Pct Al Using Cryomilling. 573-581A
- Evaporation**
- Diffusion Models for Evaporation Losses during Electron-Beam Melting of Alpha/Beta-Titanium Alloys. 235-245B
- Excitation**
- Effects of Simultaneous Displacive and Ionizing Radiations and of Electric Field on Radiation Damage in Ionic Crystals. 2257-2266A
- Exothermic reactions**
- Nickel-Aluminides/Steel Clad Pipe Fabricated by Reactive Centrifugal Casting Method from Liquid Aluminum and Solid Nickel. 1517-1524A
- Explosive compacting**
- Hot Explosive Compaction of Aluminum-Nickel Composites. 1125-1131A
- Exposure**
- Electrochemical Evaluation of a Corrosion Fatigue Failure Mechanism in a Duplex Stainless Steel. 2427-2437A
- Ductility Exhaustion Mechanisms in Thermally Exposed Thin Sheets of a Near- β Titanium Alloy. 3113-3127A
- Extraction**
- Rare Earth Extraction from Bastnaesite Concentrate by Step-wise Carbochlorination-Chemical Vapor Transport-Oxidation. 217-221B
- Salt Roasting of Suncor Oil Sands Fly Ash. 1051-1058B
- Extreme values**
- Response of Primary Dendrite Spacing to Varying Temperature Gradient during Directional Solidification. 735-742B
- Extrusion**
- Co-Deformation Processing and Modeling of In-Situ Multiphase Composites. 1603-1611A
- Achieving Enhanced Ductility in a Dilute Magnesium Alloy through Severe Plastic Deformation. 1735-1744A
- Extrusion rate**
- Microstructure evolution and mechanical behavior of bulk copper obtained by consolidation of micro- and nanopowders using equal-channel angular extrusion. 2935-2949A
- Fabrication**
- Fabrication of Foamable Precursors by Powder Compression and Induction Heating Process. 769-776B
- Face centered cubic lattice**
- Single-Crystal Elastic Constants of Fe-15Ni-15Cr Alloy. 3149-3154A
- Face centered cubic lattices**
- Experimental and Theoretical Evidence for Carbon-Vacancy Binding in Austenite. 2239-2245A
- Temperature Effects on the Lattice Constants and Crystal Structure of a Co-27Cr-5Mo Low-Carbon Alloy. 2517-2523A
- Communication: Formation of Simple Crystal Structures in Cu-Co-Ni-Cr-Al-Fe-Ti-V Alloys with Multiprincipal Metallic Elements. 2533-2536A
- Dislocation structure behind a shock front in fcc perfect crystals: atomistic simulation results. 2609-2615A
- Tensile properties and microstructure of Haynes 25 alloy after aging at elevated temperatures for extended times. 2767-2781A
- Failure**
- A Hybrid Micromechanical-Macroscopic Model for the Analysis of the Tensile Behavior of Cavitating Materials. 1141-1149A
- Failure in Internally Pressurized Bent Tubes. 1151-1158A
- Superplastic Behavior and Microstructure Evolution in a Commercial Al-Mg-Sc Alloy Subjected to Intense Plastic Straining. 2383-2392A
- Effect of microstructural length scales on spall behavior of copper. 2663-2673A
- Atomic force microscopy studies of fracture surfaces of composition B energetic materials. 2675-2079A
- Deformation and Failure of Zr5Nb5Al10Cu15.4Ni12.6/W Particle Composites Under Quasi-Static and Dynamic Compression. 3439-3444A
- In-Situ Microfracture Observation of Strip-Cast Zr-Ti-Cu-Ni-Be Bulk Metallic Glass Alloys. 3753-3761A
- Failure mechanisms**
- Electrochemical Evaluation of a Corrosion Fatigue Failure Mechanism in a Duplex Stainless Steel. 2427-2437A
- On the Isotropy of the Dynamic Mechanical and Failure Properties of Swaged Tungsten Heavy Alloys. 3787-3795A
- Failure Mode Analysis and a Mechanism for Hot-Ductility Improvement in the Nb-Microalloyed Steel. 3823-3832A
- Failure modes**
- Understanding the Contributions of Normal-Fatigue and Static Loading to the Dwell Fatigue in a Near-Alpha Titanium Alloy. 3141-3148A
- Failure Mode Analysis and a Mechanism for Hot-Ductility Improvement in the Nb-Microalloyed Steel. 3823-3832A
- Fatigue (materials)**
- Thermomechanical Fatigue Behavior of the Third-Generation, Single-Crystal Superalloy TMS-75: Deformation Structure. 1779-1787A
- Understanding the Contributions of Normal-Fatigue and Static Loading to the Dwell Fatigue in a Near-Alpha Titanium Alloy. 3141-3148A
- Fatigue cracking**
- Electrochemical Evaluation of a Corrosion Fatigue Failure Mechanism in a Duplex Stainless Steel. 2427-2437A
- The Microstructural, Mechanical, and Fracture Properties of Austenitic Stainless Steel Alloyed with Gallium. 3445-3454A
- Effect of Boron on the Low-Cycle Fatigue Behavior and Deformation Structure of INCONEL 718 at 650°C. 3477-3487A
- Fatigue failure**
- Characterizing Small Fatigue Cracks in Metallic Alloys. 7-14A
- Thermal-Imaging Technologies for Detecting Damage during High-Cycle Fatigue. 15-23A
- Effects of Lamination and Changes in Layer Thickness on Fatigue-Crack Propagation of Lightweight Laminated Metal Composites. 45-52A
- Effect of Reinforcement-Particle-Oriented Anisotropy on the Tensile and Fatigue Behavior of Metal-Matrix Composites. 53-61A
- Microstructural Effects on Fatigue and Dwell-Fatigue Crack Growth in α/β Ti-6Al-2Sn-4Zr-2Mo-0.1Si. 163-187A
- In-Situ Observations of Low-Cycle Fatigue Damage in Cast AM60B Magnesium in an Environmental Scanning Electron Microscope. 321-331A
- Effects of Heat Treatment and Testing Temperature on Fracture Mechanics Behavior of Low-Si CA-15 Stainless Steel. 471-480A
- Damage Repair in CMSX-4 Alloy without Fatigue Life Reduction Penalty. 535-542A
- Effects of Partial Recrystallization on High-Cycle Fatigue Deformation and Crack Generation of a Nitrogen-Strength-

- ened 32Mn-7Cr Austenitic Steel at Liquid-Nitrogen Temperature. 543-553A
- Low-Cycle Fatigue Behavior of ULTIMET Alloy. 785-796A
- Fracture Behavior of Thixoformed 357-T5 Al Alloys. 1017-1027A
- Fatigue of Cold-Work Tool Steels: Effect of Heat Treatment and Carbide Morphology on Fatigue Crack Formation, Life, and Fracture Surface Observations. 1289-1300A
- Fatigue Fracture Mechanism Maps for a Type 304 Stainless Steel. 1311-1316A
- Hydrogen-Involving Tensile and Cyclic Deformation Behavior of Low-Alloy Pressure Vessel Steel. 1477-1486A
- The Effect of Lamellar Morphology on Tensile and High-Cycle Fatigue Behavior of Orthorhombic Ti-22Al-27Nb Alloy. 2161-2170A
- Effects of Changes in Test Temperature on Fatigue Crack Propagation of Al6090/SiCp-Al 6013 Laminated Metal Composites. 2291-2303A
- Electrochemical Evaluation of a Corrosion Fatigue Failure Mechanism in a Duplex Stainless Steel. 2427-2437A
- Communication: High-temperature fatigue crack growth behavior of 17-4 PH stainless steels. 3018-3024A
- Tensile and Fatigue Behavior of Al-Based Metal Matrix Composites Reinforced with Continuous Carbon or Alumina Fibers: Part II. Quasi-Unidirectional Composite Cross-Ply Laminates. 3307-3317A
- The Microstructural, Mechanical, and Fracture Properties of Austenitic Stainless Steel Alloyed with Gallium. 3445-3454A
- Fatigue and Fracture Behavior of Bulk Metallic Glass. 3489-3498A
- Variability of Large-Crack Fatigue-Crack-Growth Thresholds in Structural Alloys. 3721-3735A
- Fatigue life**
- Shear Force Effects on Fretting Fatigue Behavior of Ti-6Al-4V. 131-138A
- Damage Repair in CMSX-4 Alloy without Fatigue Life Reduction Penalty. 535-542A
- Temperature Evolution and Life Prediction in Fatigue of Superalloys. 839-848A
- Effects of Temperature and Shot Peening on S-N Behavior of a PM Ni-Ba Superalloy UDIMET 720. 1007-1016A
- Fatigue of Cold-Work Tool Steels: Effect of Heat Treatment and Carbide Morphology on Fatigue Crack Formation, Life, and Fracture Surface Observations. 1289-1300A
- Control of Residual Stresses Affecting Fatigue Life of Pulsed Current Gas-Metal-Arc Weld of High-Strength Aluminum Alloy. 2439-2444A
- A Through-Process Model of an A356 Brake Caliper for Fatigue Life Prediction. 3275-3288A
- Tensile and Fatigue Behavior of Al-Based Metal Matrix Composites Reinforced with Continuous Carbon or Alumina Fibers: Part II. Quasi-Unidirectional Composite Cross-Ply Laminates. 3307-3317A
- Communication: Comparisons of Experimental Measurements and a Theoretical Model for Specimen Self-Heating during Fatigue of Type 316 LN Stainless Steel. 3334-3339A
- Fatigue and Fracture Behavior of Bulk Metallic Glass. 3489-3498A
- Fatigue limit**
- Gigacycle Fatigue Properties of a Modified-Ausformed Si-Mn Steel and Effects of Microstructure. 1715-1723A
- Fatigue strength**
- Effect of Reinforcement-Particle-Orientation Anisotropy on the Tensile and Fatigue Behavior of Metal-Matrix Composites. 53-61A
- Damage Repair in CMSX-4 Alloy without Fatigue Life Reduction Penalty. 535-542A
- Effects of Partial Recrystallization on High-Cycle Fatigue Deformation and Crack Generation of a Nitrogen-Strengthened 32Mn-7Cr Austenitic Steel at Liquid-Nitrogen Temperature. 543-553A
- Fatigue of Cold-Work Tool Steels: Effect of Heat Treatment and Carbide Morphology on Fatigue Crack Formation, Life, and Fracture Surface Observations. 1289-1300A
- Tensile and Fatigue Behavior of Al-Based Metal Matrix Composites Reinforced with Continuous Carbon or Alumina Fibers: Part I. Quasi-Unidirectional Composites. 3289-3305A
- Inclusion-Controlled Fatigue Properties of 1800 MPA-Class Spring Steels. 3737-3744A
- Fatigue tests**
- Shear Force Effects on Fretting Fatigue Behavior of Ti-6Al-4V. 131-138A
- In-Situ Observations of Low-Cycle Fatigue Damage in Cast AM60B Magnesium in an Environmental Scanning Electron Microscope. 321-331A
- Damage Repair in CMSX-4 Alloy without Fatigue Life Reduction Penalty. 535-542A
- Effect of Broaching on High-Temperature Fatigue Behavior in Notched Specimens of INCONEL 718. 771-783A
- Low-Cycle Fatigue Behavior of ULTIMET Alloy. 785-796A
- Gigacycle Fatigue Properties of a Modified-Ausformed Si-Mn Steel and Effects of Microstructure. 1715-1723A
- Effects of Changes in Test Temperature on Fatigue Crack Propagation of Al6090/SiCp-Al 6013 Laminated Metal Composites. 2291-2303A
- The effect of grain size on low-cycle fatigue behavior of Al-2024 polycrystalline alloy. 2725-2728A
- Communication: Comparisons of Experimental Measurements and a Theoretical Model for Specimen Self-Heating during Fatigue of Type 316 LN Stainless Steel. 3334-3339A
- Inclusion-Controlled Fatigue Properties of 1800 MPA-Class Spring Steels. 3737-3744A
- Faults**
- Defect Structures in Cosputtered Thin Films of Transition Metal Disilicides with C11b, C40 and C54 Structures. 2229-2238A
- FCC metals**
- Dislocation mechanics-based constitutive equations. 2547-2555A
- Grain size dependence of the activation parameters for plastic deformation: influence of crystal structure, slip system, and rate-controlling dislocation mechanism. 2697-2705A
- Feedback control**
- Phase Transformations and Control of Residual Stresses in Thick Spray-Formed Steel Shells. 1113-1122B
- Fermi surface**
- Standard Gibbs Energy of Formation of Mg48Zn52 Determined by Solution Calorimetry and Measurement of Heat Capacity from Near Absolute Zero Kelvin. 891-895B
- Ferrite**
- Liquidus Temperatures in Calcium Ferrite Slags in Equilibrium with Molten Copper. 203-215B
- A Model for Ferrite/Pearlite Band Formation and Prevention in Steels. 425-433A
- Fiber Texture and Substructural Features in the Caliber-Rolled Low-Carbon Steels. 665-677A
- Measurement and Modeling of the Electromagnetic Response to Phase Transformation in Steels. 965-972A
- Effect of Simulated Thermal Cycles on the Microstructure of the Heat-Affected Zone in HSLA-80 and HSLA-100 Steel Plates. 985-996A
- Coupled-Solute Drag Effects on Ferrite Formation in Fe-C-X Systems. 1187-1210A
- Molybdenum Accumulation at Ferrite:Austenite Interfaces during Isothermal Transformation of an Fe-0.24 Pct C-0.93 Pct Mo Alloy. 1223-1235A
- Studies of the Influence of Alloying Elements on the Growth of Ferrite from Austenite under Decarburization Conditions: Fe-C-Ni Alloys. 1237-1242A
- Characteristics of the Rough-Cut Surface of Quenched and Tempered Martensitic Stainless Steel Using Wire Electrical Discharge Machining. 1351-1357A
- An Effect of a Strong Magnetic Field on the Phase Transformation in Plain Carbon Steels. 1663-1668A
- A Metallurgical Interpretation of the Static Recrystallization Kinetics of an Intercritically Deformed C-Mn Steel. 1889-1898A
- Microstructures of a Powder Metallurgy-Hot-Isostatically Pressed Super Duplex Stainless Steel Forming in Industrial Heat Treatments. 2103-2109A
- Characterization of the Nucleation and Growth Behavior of Copper Precipitates in Low-Carbon Steels. 2323-2329A
- Effect of Microstructure on the Stability of Retained Austenite in Transformation-Induced-Plasticity Steels. 2331-2341A
- Communication: Effect of texture and microstructure on resistance to cracking of high-strength hot-rolled Nb-Ti microalloyed steels. 3024-3029A
- Austenite Formation during Intercritical Annealing. 3363-3375A
- The Nitriding Kinetics of Iron-Chromium Alloys: The Role of Excess Nitrogen: Experiments and Modelling. 3387-3398A
- Effect of Different Cr Contents on Tensile and Corrosion Behaviors of 0.13 Pct N-Containing CD4MCU Cast Duplex Stainless Steels. 3431-3438A
- Double Loop Electrochemical Potentiokinetic Reactivation Test Optimization in Checking of Duplex Stainless Steel Intergranular Corrosion Susceptibility. 3499-3513A
- Communication: Ferrite Number as a Function of the Larson-Miller Parameter for Austenitic Stainless Weld Metals after Creep Testing. 3631-3633A
- Role of Carbon and Alloying Elements in the Formation of Bainitic Ferrite. 3693-3700A
- Widmanstätten Ferrite Plate Formation in Low-Carbon Steels. 3701-3706A
- Ferrite, Microstructure**
- Study of the Ferrite Grain Coarsening behind the Transformation Front by Electron Backscattered Diffraction Techniques. 93-102A
- Ferrites**
- Reaction Sequences in the Formation of Silico-Ferrites of Calcium and Aluminum in Iron Ore Sinter. 929-936B
- Ferritic stainless steels, Microstructure**
- Communication: Grain Boundary Engineering of Ferritic-Martensitic Alloy T91. 717-718A
- Ferritic transformations**
- Study of the Austempering Transformation Kinetics in Compacted Graphite Cast Irons. 103-110A
- The Diffusional Formation of Ferrite from Austenite in Fe-C-Ni Alloys. 1211-1221A
- Monte Carlo-Method Simulation of the Deformation-Induced Ferrite Transformation in the Fe-C System. 1565-1577A
- A novel observation of strain-induced ferrite-to-austenite retransformation after intercritical deformation of C-Mn steel. 2789-2797A
- Ferroelectric domains**
- Local Electromechanical Response at a Single Ferroelectric Domain Wall in Lithium Niobate. 2287-2290A
- Ferromagnetism**
- Single-Crystal Elastic Constants of Fe-15Ni-15Cr Alloy. 3149-3154A
- Ferromanganese**
- Multicomponent Diffusion in Molten Slags. 675-684B
- Ferrous alloys**
- The Diffusional Formation of Ferrite from Austenite in Fe-C-Ni Alloys. 1211-1221A
- Molybdenum Accumulation at Ferrite:Austenite Interfaces during Isothermal Transformation of an Fe-0.24 Pct C-0.93 Pct Mo Alloy. 1223-1235A
- Studies of the Influence of Alloying Elements on the Growth of Ferrite from Austenite under Decarburization Conditions: Fe-C-Ni Alloys. 1237-1242A
- The Role of Melt Pool Behavior in Free-Jet Melt Spinning. 1539-1553A
- Magnetic Contribution to the Interdiffusion Coefficients in Bcc (α) and Fcc (γ) Fe-Ni Alloys. 1681-1690A

- Microstructural Evolution in Iron Aluminide Fe-28Al-2C after High-Temperature Hydrogen Treatment. 1789-1798A
- A Quantitative Dendrite Growth Model and Analysis of Stability Concepts. 2471-2485A
- Shear localization-martensitic transformation interactions in Fe-Cr-Ni monocrystal. 2575-2586A
- Crystallographic textures in rolled and annealed Fe-Ga and Fe-Al alloys. 2963-2970A
- Single-Crystal Elastic Constants of Fe-15Ni-15Cr Alloy. 3149-3154A
- The Nitriding Kinetics of Iron-Chromium Alloys: The Role of Excess Nitrogen: Experiments and Modelling. 3387-3398A
- Ferrous alloys, Microstructure**
- Communication: Nature of Massive Transformation. 351-352A
- Fiber composites**
- Communication: Observed Dependencies of the Large Thermal-Compressive Response of a NiTi Shape-Memory Alloy Fiber Aluminum Metal Matrix Composite on Maximum Tensile Strain Imposed during a Preceding Room-Temperature Tensile Process. 1403-1406A
- Effects of Carbon Fiber/Al Interface on Mechanical Properties of Carbon-Fiber-Reinforced Aluminum-Matrix Composites. Study of the Porosity Produced in an Aluminum Alloy Matrix Composite Due to a T6 Heat Treatment. 2153-2160A
- 2503-2510A
- Fiber composites, Mechanical properties**
- Damage Evolution during Thermal Fatigue in Fiber-Reinforced Light-Metal-Matrix Composites. 37-43A
- Creep Behavior of Copper-Chromium In-Situ Composite. 695-705A
- Fiber pull out**
- Tensile and Fatigue Behavior of Al-Based Metal Matrix Composites Reinforced with Continuous Carbon or Alumina Fibers: Part II. Quasi-Unidirectional Composite Cross-Ply Laminates. 3307-3317A
- Fiber-matrix interfaces**
- Study of the Porosity Produced in an Aluminum Alloy Matrix Composite Due to a T6 Heat Treatment. 2503-2510A
- Tensile and Fatigue Behavior of Al-Based Metal Matrix Composites Reinforced with Continuous Carbon or Alumina Fibers: Part I. Quasi-Unidirectional Composites. 3289-3305A
- Fibrous structure**
- Fiber Texture and Substructural Features in the Caliber-Rolled Low-Carbon Steels. 665-677A
- Eutectic Grains in Unmodified and Strontium-Modified Hypoeutectic Aluminum-Silicon Alloys. 1829-1837A
- Field effects**
- An Effect of a Strong Magnetic Field on the Phase Transformation in Plain Carbon Steels. 1663-1668A
- Field theory**
- An Effect of a Strong Magnetic Field on the Phase Transformation in Plain Carbon Steels. 1663-1668A
- Characterization of Three-Dimensional Grain Structure in Polycrystalline Iron by Serial Sectioning. 1927-1933A
- Filtration**
- Study of Inclusion Re-Entrainment in a Filter Bed. 999-1009B
- Finite element method**
- Study on Notch Fracture of TiAl Alloys at Room Temperature. On the Development of a Three-Dimensional Transient Thermal Model to Predict Ingot Cooling Behavior during the Start-Up Phase of the Direct Chill-Casting Process for an AA5182 Aluminum Alloy Ingot. 439-456A
- 523-540B
- Analysis of Thin-Slab Casting by the Compact-Strip Process: Part II. Effect of Operating and Design Parameters on Solidification and Bulging. 561-573B
- Channel Segregation during Solidification and the Effects of an Alternating Traveling Magnetic Field. 743-754B
- Effect of Broaching on High-Temperature Fatigue Behavior in Notched Specimens of INCONEL 718. 771-783A
- The Effect of Surface Deformation on Lubrication and Oxide-Scale Fracture in Cold Metal Rolling. 919-928B
- Measurement and Modeling of the Electromagnetic Response to Phase Transformation in Steels. 965-972A
- Application of the Generalized Method of Cells Principle to Particulate-Reinforced Metal Matrix Composites. 1029-1039B
- The Cut-Groove Technique to Infer Interfacial Effects during Hot Rolling. 1087-1095A
- Thermomechanical Finite-Element Model of Shell Behavior in Continuous Casting of Steel. 1151-1172B
- A Numerical Analysis of Intergranular Penny-Shaped Microcrack Shrinkage Controlled by Coupled Surface and Interface Diffusion. 1301-1309A
- Characterization and Modeling of Quenching-Induced Residual Stresses in the Nickel-Based Superalloy IN718. 1703-1713A
- Void Nucleation by Inclusion Cracking. 1745-1755A
- Experimental and Numerical Study on the Relationship between Creep Crack Growth Properties and Fracture Mechanisms. 1757-1764A
- Effects of Loading Rate on Fracture Behavior of Low-Alloy Steel with Different Grain Sizes. 1765-1778A
- The Influence of a Martensitic Phase Transformation on Stress Development in Thermal Barrier Coating Systems. 2279-2286A
- An Eulerian Finite-Element Model for Determination of Deformation State of a Copper Subjected to Orthogonal Cutting. 2393-2400A
- Finite element method simulation of mushy zone behavior during direct-chill casting of an Al-4.5 pct Cu alloy. 2917-2926A
- Effects of Alloy Composition and Casting Speed on Structure Formation and Hot Tearing during Direct-Chill Casting of Al-Cu Alloys. 3551-3561A
- Modeling of Distortion after Densification during Liquid-Phase Sintering. 3833-3841A
- Development and Validation of a Thermal Model of the Direct Chill Casting of AZ31 Magnesium Billets. 3843-3854A
- Flame spraying**
- Residual Stresses in High Velocity Oxy-Fuel Metallic Coatings. 1807-1814A
- Flow**
- Simulation of Die Filling for the Wax Injection Process: Part II. Numerical Simulation. 761-768B
- Flow control**
- Physical and Mathematical Determination of the Influence of Input Temperature Changes on the Molten Steel Flow Characteristics in Slab Tundishes. 957-966B
- Simulation of Flow Control in the Meniscus of a Continuous Casting Mold with Opposing Alternating Current Magnetic Fields. 1129-1137B
- Flow rate**
- A Numerical Study of Oxidation Behavior during Reactive Atomization and Deposition. 1173-1185B
- Flow stability**
- Study of Inclusion Re-Entrainment in a Filter Bed. 999-1009B
- Fluid dynamics**
- Simulation of Flow in a Continuous Galvanizing Bath: Part I. Thermal Effects of Ingot Addition. 161-170B
- Mathematical Simulation and Physical Modeling of Unsteady Fluid Flows in a Water Model of a Slab Mold. 449-460B
- Diffusion-Coefficient Measurements in Liquid Metallic Alloys. 909-917B
- Fluid flow**
- Mathematical Modeling of a Direct Current Electric Arc: Part II. Dimensionless Representation of a Direct Current Arc. 373-380B
- Fluid Flows in Metallurgy - Friend or Foe? 417-437B
- Mathematical Simulation and Physical Modeling of Unsteady Fluid Flows in a Water Model of a Slab Mold. 449-460B
- Liquid Convection Effects on the Pushing-Engulfment Transition of Insoluble Particles by a Solidifying Interface: Part I. Analytical Calculation of the Lift Forces. 613-621A
- Liquid Convection Effects on the Pushing-Engulfment Transition of Insoluble Particles by a Solidifying Interface: Part II. Numerical Calculation of Drag and Lift Forces on a Particle in Parabolic Shear Flow. 623-629A
- Study of Transient Flow and Particle Transport in Continuous Steel Caster Molds: Part I. Fluid Flow. 685-702B
- Study of Transient Flow and Particle Transport in Continuous Steel Caster Molds: Part II. Particle Transport. 703-714B
- Diffusion-Coefficient Measurements in Liquid Metallic Alloys. 909-917B
- Computational and Experimental Study of Turbulent Flow in a 0.4-Scale Water Model of a Continuous Steel Caster. 967-982B
- Simulation of Flow Control in the Meniscus of a Continuous Casting Mold with Opposing Alternating Current Magnetic Fields. 1129-1137B
- Thermomechanical Finite-Element Model of Shell Behavior in Continuous Casting of Steel. 1151-1172B
- Influence of Convection on Feathered Grain Formation in Aluminum Alloys. 2495-2501A
- Marangoni convection in weld pool in CO₂-Ar-shielded gas thermal arc welding. 2861-2867A
- Fluxing**
- The Solidification of Undercooled Melts via Twinned Dendritic Growth. 3211-3220A
- Fly ash**
- Salt Roasting of Suncor Oil Sands Fly Ash. 1051-1058B
- Foamed metals**
- Fabrication of Foamable Precursors by Powder Compression and Induction Heating Process. 769-776B
- Evaluation of Mechanical Properties of Porous 6061 Alloys Fabricated by the Powder Compression and Induction Heating Process. 2419-2426A
- Foaming**
- Additions to Generate Foam in Stainless Steelmaking. 643-650B
- Forced convection**
- Flow of Conducting Liquid around Two Nonconducting Particles in DC Electromagnetic Field and the Electromagnetic Migration Force. 847-855B
- Formability**
- Cu Precipitation in a Prestrained Fe-1.5 Wt Pct Cu Alloy during Isothermal Aging. 1263-1272A
- Formability and Strength of Friction-Stir-Welded Aluminum Sheets. 3461-3468A
- Inclusion-Controlled Fatigue Properties of 1800 MPA-Class Spring Steels. 3737-3744A
- Formalism**
- Critical Thermodynamic Assessment and Modeling of the Fe-Ni-S System. 897-907B
- Foundry practice**
- Model-Based Melt Rate Control during Vacuum Arc Remelting of Alloy 718. 101-113B
- Diffusion Models for Evaporation Losses during Electron-Beam Melting of Alpha/Beta-Titanium Alloys. 235-245B
- Inertial and Buoyancy Driven Water Flows under Gas Bubbling and Thermal Stratification Conditions in a Tundish Model. 247-257B
- Determination of Interfacial Heat-Transfer Boundary Conditions in an Aluminum Low-Pressure Permanent Mold Test Casting. 299-311B
- Surface-Oriented Melt/Substrate Heat-Transfer Model in Aluminum Strip Casting. 351-361B
- On the Development of a Three-Dimensional Transient Thermal Model to Predict Ingot Cooling Behavior during the Start-Up Phase of the Direct Chill-Casting Process for an AA5182 Aluminum Alloy Ingot. 523-540B
- Analysis of Thin-Slab Casting by the Compact-Strip Process: Part I. Heat Extraction and Solidification. 541-560B
- Analysis of Thin-Slab Casting by the Compact-Strip Process:

- Part II. Effect of Operating and Design Parameters on Solidification and Bulging. 561-573B
Communication: Casting of Aluminum-Based Wrought Alloys Using Controlled Diffusion Solidification. 2174-2180A
- Fourier analysis**
Studies of Lattice Imperfections in Deformed Aluminum-Based Lithium Alloys by X-Ray Diffraction 3319-3322A
- Fractography**
Tensile behavior of friction-stir-welded A356-T6/Al 6061-T651 Bi-alloy plate. 2837-2843A
Understanding the Contributions of Normal-Fatigue and Static Loading to the Dwell Fatigue in a Near-Alpha Titanium Alloy 3141-3148A
Tensile and Fatigue Behavior of Al-Based Metal Matrix Composites Reinforced with Continuous Carbon or Alumina Fibers: Part II. Quasi-Unidirectional Composite Cross-Ply Laminates 3307-3317A
Effect of Boron on the Low-Cycle Fatigue Behavior and Deformation Structure of INCONEL 718 at 650°C 3477-3487A
- Fracture mechanics**
Microstructural Effects on Fatigue and Dwell-Fatigue Crack Growth in α/β Ti-6Al-2Sn-4Zr-2Mo-0.1Si. 163-187A
Effects of Heat Treatment and Testing Temperature on Fracture Mechanics Behavior of Low-Si CA-15 Stainless Steel. 471-480A
Deformation and Damage Mechanisms of Zinc Coatings on Hot-Dip Galvanized Steel Sheets: Part II. Damage Modes, Mechanisms and Modeling of Cleavage Fracture in Simulated Heat-Affected Zone Microstructures of a High-Strength Low Alloy Steel. 813-823A
Fatigue Fracture Mechanism Maps for a Type 304 Stainless Steel. 1039-1053A
Microstructure, Mechanical Properties, and Fracture Mechanism of As-Cast (Ti0.5Cu0.25Ni0.15Sn0.05Zr0.05)(100-x)Mo(x) Composites. 1311-1316A
Experimental and Numerical Study on the Relationship between Creep Crack Growth Properties and Fracture Mechanisms. 1591-1601A
Effects of Martensite Morphology and Tempering on Dynamic Deformation Behavior of Dual-Phase Steels. 1757-1764A
Superplastic Behavior and Microstructure Evolution in a Commercial Al-Mg-Sc Alloy Subjected to Intense Plastic Straining. 2371-2382A
Electrochemical Evaluation of a Corrosion Fatigue Failure Mechanism in a Duplex Stainless Steel. 2383-2392A
Communication: High-temperature fatigue crack growth behavior of 17-4 PH stainless steels. 2427-2437A
Communication: Effect of texture and microstructure on resistance to cracking of high-strength hot-rolled Nb-Ti microalloyed steels. 3018-3024A
Fatigue and Fracture Behavior of Bulk Metallic Glass 3024-3029A
Variability of Large-Crack Fatigue-Crack-Growth Thresholds in Structural Alloys 3489-3498A
Inclusion-Controlled Fatigue Properties of 1800 MPA-Class Spring Steels 3721-3735A
In-Situ Microfracture Observation of Strip-Cast Zr-Ti-Cu-Ni-Be Bulk Metallic Glass Alloys 3737-3744A
Fracture Behavior of Thick-Section Weldment in Fe-12Cr-12Ni-10Mn-0.24N Stainless Steel at Liquid Helium Temperature 3753-3761A
Tensile Test Behavior of the Eutectic Sn-Ag Solder Joint in Ball Grid Array Assemblies 3797-3802A
3817-3821A
- Fracture strength**
Communications: Ultra-High-Speed Exploding Properties of Ti-6Al-4V Alloy Having Equiaxed and Bimodal Microstructures. 719-724A
Microstructure, Mechanical Properties, and Fracture Mechanism of As-Cast (Ti0.5Cu0.25Ni0.15Sn0.05Zr0.05)(100-x)Mo(x) Composites. 1591-1601A
Effect of Low-Frequency Electromagnetic Casting on the Castability, Microstructure, and Tensile Properties of Direct-Chill Cast Al-Zn-Mg-Cu Alloy. 2487-2494A
- Fracture surfaces**
Atomic force microscopy studies of fracture surfaces of composition B energetic materials. 2675-2079A
Fatigue and Fracture Behavior of Bulk Metallic Glass 3489-3498A
- Fracture toughness**
Grain-Size Effect on Shape-Memory Behavior of $\text{Ti}_{50}\text{Ni}_{49}\text{Zr}_{15.4}$ Thin Films. 111-119A
A New Quality Index for Characterizing Aluminum Cast Alloys with Regard to Aircraft Structure Design Requirements. 301-308A
Effects of Heat Treatment and Testing Temperature on Fracture Mechanics Behavior of Low-Si CA-15 Stainless Steel. 471-480A
Communication: Resonant Vibration Behavior of an Al-3.8Cu-0.8Li-0.3Mg Alloy. 952-957A
Mechanisms and Modeling of Cleavage Fracture in Simulated Heat-Affected Zone Microstructures of a High-Strength Low Alloy Steel. 1039-1053A
Fine Carbide-Strengthened 3Cr-3WVTa Bainitic Steel. 1281-1288A
Fracture Toughness of Selectively Reinforced Al2124 Alloy: Pre-crack Tip in the Composite Side. 1393-1401A
The Influences of Multiscale-Sized Second-Phase Particles on Ductility of Aged Aluminum Alloys. 1725-1734A
Effects of Alloying Elements on Fracture Toughness in the Transition Temperature Region of Base Metals and Simulated Heat-Affected Zones of Mn-Mo-Ni Low-Alloy Steels. 2027-2037A
Microstructure and mechanical properties of a 2000 MPa Co-free maraging steel after aging at 753 K. 2747-2755A
Quality Assessment of Artificially Aged A357 Aluminum Alloy Cast Ingots by Introducing Approximate Expressions of the Quality Index QD 3079-3089A
The Microstructural, Mechanical, and Fracture Properties of Austenitic Stainless Steel Alloyed with Gallium 3445-3454A
Two-Layered Zr-Base Amorphous Alloy/Metal Surface Composites Fabricated by High Energy Electron-Beam Irradiation 3455-3460A
- Defect Structures and Room Temperature Mechanical Properties of C15 Laves Phases in Zr-Nb-Cr and Zr-Hf-Cr Alloy Systems** 3469-3476A
In-Situ Microfracture Observation of Strip-Cast Zr-Ti-Cu-Ni-Be Bulk Metallic Glass Alloys 3753-3761A
Fracture Behavior of Thick-Section Weldment in Fe-12Cr-12Ni-10Mn-0.24N Stainless Steel at Liquid Helium Temperature 3797-3802A
Communication: Room-Temperature Cleavage Fracture of FeMnAlC Steels 3863-3866A
- Fracturing**
Effect of Microstructure on Mechanical Properties of As-Cast Mg-Al Alloys. 309-319A
Oxide Defects in a Vacuum Investment-Cast Ni-Based Turbine Blade. 2063-2071A
- Fragmentation**
Undercooling and Solidification of Al-50 At. Pct Si Alloy by Electromagnetic Levitation. 607-612A
Erratum: A Solutal Interaction mechanism for the Columnar-to-Equiaxed Transition in Alloy Solidification. 1915A
Grain Refinement Induced by Electromagnetic Stirring: A Dendrite Fragmentation Criterion 3201-3210A
- Free electrons**
Standard Gibbs Energy of Formation of Mg48Zn52 Determined by Solution Calorimetry and Measurement of Heat Capacity from Near Absolute Zero Kelvin 891-895B
- Free energy**
The influence of chemical equilibrium on fluid-solid reaction rates and the falsification of activation energy. 121-131B
A Thermodynamic Model for Deoxidation Equilibria in Steel. 493-507B
Standard Gibbs Energy of Formation of Mg48Zn52 Determined by Solution Calorimetry and Measurement of Heat Capacity from Near Absolute Zero Kelvin 891-895B
An Effect of a Strong Magnetic Field on the Phase Transformation in Plain Carbon Steels. 1663-1668A
Magnetic Contribution to the Interdiffusion Coefficients in Bcc (α) and Fcc (γ) Fe-Ni Alloys. 1681-1690A
Coarsening Behavior of Ni3Ga Precipitates in Ni-Ga Alloys: Dependence of Microstructure and Kinetics on Volume Fraction 3063-3069A
Nucleation of Solid Aluminum on Inclusion Particles Injected into Al-Si-Fe Alloys 3233-3250A
Thermodynamic Investigations of Cr3C2 and Reassessment of the Cr-C System 3673-3680A
- Freezing**
Thermodynamic Aspects of the Constitution, Grain Refining, and Solidification Enthalpies of Al-Ce-Si Alloys 3349-3362A
- Fretting**
Shear Force Effects on Fretting Fatigue Behavior of Ti-6Al-4V. 131-138A
- Friction**
Shear Force Effects on Fretting Fatigue Behavior of Ti-6Al-4V. 131-138A
Effect of Aging and Deformation on the Microstructure and Properties of Fe-Ni-Ti Maraging Steel. 973-983A
The Cut-Groove Technique to Infer Interfacial Effects during Hot Rolling. 1087-1095A
Modeling of Distortion after Densification during Liquid-Phase Sintering 3833-3841A
- Friction stir welding**
Material Flow Patterns and Cavity Model in Friction-Stir Welding of Aluminum Alloys. 153-160B
Characterization of Plastic Flow and Resulting Microtextures in a Friction Stir Weld. 777-783B
Microstructural Evolution in the Heat-Affected Zone of a Friction Stir Weld. 1487-1499A
Tensile behavior of friction-stir-welded Al 6061-T651. 2829-2835A
Tensile behavior of friction-stir-welded A356-T6/Al 6061-T651 Bi-alloy plate. 2837-2843A
Formability and Strength of Friction-Stir-Welded Aluminum Sheets 3461-3468A
- Frictional wear**
Correlation of Microstructure and Abrasive and Sliding Wear Resistance of (TiC, SiC)/Ti-6Al-4V Surface Composites Fabricated by High-Energy Electron-Beam Irradiation. 139-151A
- Fuels**
Nanoparticle Recovery Using a Fume Collector Comprised of Carbonized Refuse-Derived Fuel 993-998B
- Functionally gradient materials**
Creep Behavior of a Rotating Functionally Graded Composite Disc Operating under Thermal Gradient. 1381-1391A
- Furans**
Study on Polychlorinated Dibenzo-p-Dioxin/Furan Formation in Iron Ore Sintering Process 983-991B
- Galena**
Dislocations in Milled Galena (PbS). 2223-2228A
- Gallium**
Phase Stability and Phase Transformations in Plutonium and Plutonium-Gallium Alloys. 2267-2278A
The Microstructural, Mechanical, and Fracture Properties of Austenitic Stainless Steel Alloyed with Gallium 3445-3454A
- Gallium, Thermal properties**
Partial Atomic Volume and Partial Molar Enthalpy of Formation of the 3d Metals in the Palladium-Based Solid Solutions. 63-70A
- Gallium compounds**
Coarsening Behavior of Ni3Ga Precipitates in Ni-Ga Alloys: Dependence of Microstructure and Kinetics on Volume Fraction 3063-3069A
- Galvanized steels**

- Vapor Pressure Measurement of Zn-Fe Intermetallic Compounds. 487-492B
- Galvanizing**
- Simulation of Flow in a Continuous Galvanizing Bath: Part I. Thermal Effects of Ingot Addition. 161-170B
- Simulation of Flow in a Continuous Galvanizing Bath: Part II. Transient Aluminum Distribution Resulting from Ingot Addition. 171-178B
- Vapor Pressure Measurement of Zn-Fe Intermetallic Compounds. 487-492B
- Communication: Persistence of Superficial Contamination of Rolled Steel during Successive Treatments up to the Formation of a Galvanneal Coating. 2185-2187A
- Effect of Ternary Additions on the Structure and Properties of Coatings Produced by a High Aluminum Galvanizing Bath. 3707-3720A
- Gas flow**
- Inertial and Buoyancy Driven Water Flows under Gas Bubbling and Thermal Stratification Conditions in a Tundish Model. 247-257B
- Blast Furnace Burden Softening and Melting Phenomena: Part I. Pellet Bulk Interaction Observation. 829-838B
- Spot Turbulence, Breakup, and Coalescence of Bubbles Released from a Porous Plug Injector into a Gas-Stirred Ladle. 949-956B
- Gas injection**
- Spot Turbulence, Breakup, and Coalescence of Bubbles Released from a Porous Plug Injector into a Gas-Stirred Ladle. 949-956B
- Gas metal arc welding**
- Numerical Analysis of Metal Transfer in Gas Metal Arc Welding under Modified Pulsed Current Conditions. 857-866B
- Precipitate Microstructures and Resulting Properties of Al-Zn-Mg Metal Inert Gas-Weld Heat-Affected Zones. 1437-1448A
- Control of Residual Stresses Affecting Fatigue Life of Pulsed Current Gas-Metal-Arc Weld of High-Strength Aluminum Alloy. 2439-2444A
- Marangoni convection in weld pool in CO₂-Ar-shielded gas thermal arc welding. 2861-2867A
- Gas phases**
- Dynamics of Coupled and Uncoupled Two-Phase Flows in a Slab Mold. 85-99B
- Gas temperature**
- Study on Polychlorinated Dibenzo-p-Dioxin/Furan Formation in Iron Ore Sintering Process. 983-991B
- Gas tungsten arc welding**
- Evolution of Microstructure and Texture in Mg-Al-Zn Alloys during Electron-Beam and Gas Tungsten Arc Welding. 2455-2469A
- Formability and Strength of Friction-Stir-Welded Aluminum Sheets. 3461-3468A
- Gas turbine engines**
- Mechanism of Primary MC Carbide Decomposition in Ni-Base Superalloys. 1669-1679A
- Gas turbine engines, Mechanical properties**
- Damage Repair in CMSX-4 Alloy without Fatigue Life Reduction Penalty. 535-542A
- Gating and riser**
- Computational and Experimental Study of Turbulent Flow in a 0.4-Scale Water Model of a Continuous Steel Caster. 967-982B
- Geometry**
- Calculation of Physicochemical Properties in a Ternary System with Miscibility Gap. 715-720B
- Analysis of intergranular impurity concentration and the effects on the ductility of copper-shaped charge jets. 2567-2573A
- Gibbsite**
- Reaction Sequences in the Formation of Silico-Ferrites of Calcium and Aluminum in Iron Ore Sinter. 929-936B
- Glass formation**
- Two-Layered Zr-Base Amorphous Alloy/Metal Surface Composites Fabricated by High Energy Electron-Beam Irradiation. 3455-3460A
- Glass transition temperature**
- The Effect of Temperature and Extrusion Speed on The Consolidation of Zirconium-Based Metallic Glass Powder Using Equal-Channel Angular Extrusion. 247-256A
- Gold base alloys**
- Partial Diffusion Reactions and the Associated Volume Changes in Thermally Exposed Au-Al Ball Bonds. 1273-1280A
- Gold compounds**
- Kinetics of Gold(III) Chloride Complex Reduction Using Sulfur(IV). 1071-1085B
- Grain boundaries**
- Study of the Ferrite Grain Coarsening behind the Transformation Front by Electron Backscattered Diffraction Techniques. Charpy-Impact-Toughness Prediction using an "Effective" Grain Size for Thermomechanically Controlled Rolled Microalloyed Steels. 93-102A
- Quench Embrittlement of Hardened 5160 Steel as a Function of Austenitizing Temperature. 121-130A
- Simulation of the Sintering Densification and Shrinkage Behavior of Powder-Injection-Molded 17-4 PH Stainless Steel. 153-162A
- Microstructural Characterization of Secondary-Phase Particles in a Hot-Deformed Al-Cu-Mg-Zr Alloy. 257-263A
- Communication: Nature of Massive Transformation. 293-300A
- Role of Temperature and Strain Rate on the Hydrogen-Induced Intergranular Rupture in Alloy 600. 351-352A
- Damage Repair in CMSX-4 Alloy without Fatigue Life Reduction Penalty. 457-464A
- Effects of Partial Recrystallization on High-Cycle Fatigue Deformation and Crack Generation of a Nitrogen-Strengthened 32Mn-7Cr Austenitic Steel at Liquid-Nitrogen Temperature. 535-542A
- ened 32Mn-7Cr Austenitic Steel at Liquid-Nitrogen Temperature. 543-553A
- Mechanisms of Strain Accumulation and Damage Development during Creep of Prestrained 316 Stainless Steels. 563-571A
- Synthesis of Nanocrystalline Zn-22 Pct Al Using Cryomilling. 573-581A
- Communication: Grain Boundary Engineering of Ferritic-Martensitic Alloy T91. 717-718A
- Hydrogen Trap States in Ultrahigh-Strength AERMET 100 Steel. 849-864A
- Coupled-Solute Drag Effects on Ferrite Formation in Fe-C-X Systems. 1187-1210A
- Fine Carbide-Strengthened 3Cr-3WV Ta Bainitic Steel. 1281-1288A
- Effect of Zr and B on Castability of Ni-Based Superalloy IN792. 1337-1342A
- Effect of Deformation Route on Microstructural Development in Aluminum Processed by Equal Channel Angular Extrusion. 1359-1368A
- Monte Carlo-Method Simulation of the Deformation-Induced Ferrite Transformation in the Fe-C System. 1565-1577A
- Quantitative Characterization of the Three-Dimensional Microstructure of Polycrystalline Al-Sn using X-Ray Microtomography. 1953-1961A
- Statistically Representative Three-Dimensional Microstructures Based on Orthogonal Observation Sections. 1969-1979A
- New Stereology for the Recovery of Grain-Boundary Plane Distributions in the Crystal Frame. 1991-1998A
- The Effect of Lamellar Morphology on Tensile and High-Cycle Fatigue Behavior of Orthorhombic Ti-22Al-27Nb Alloy. 2161-2170A
- Analysis of intergranular impurity concentration and the effects on the ductility of copper-shaped charge jets. 2567-2573A
- The effect of grain size on low-cycle fatigue behavior of Al-2024 polycrystalline alloy. 2725-2728A
- Communication: A thousandfold creep strengthening by Ca addition in die-cast AM50 magnesium alloy. 3029-3032A
- Effects of Temperature and Strain Rate on Tensile Properties and Activation Energy for Dynamic Strain Aging in Alloy 625. 3129-3139A
- Austenite Formation during Intercritical Annealing. 3363-3375A
- Effect of Initial Grain Size of Austenite on Hot-Deformed Structure of Ni-30Fe Alloy. 3399-3408A
- On Cells and Microbands Formed in an Interstitial-Free Steel during Cold Rolling at Low to Medium Reductions. 3423-3430A
- Mechanisms of Hf Dopant Incorporation during the Early Stage of Chemical Vapor Deposition Aluminide Coating Growth under Continuous Doping Conditions. 3581-3593A
- Experimental Determination of Solid-Liquid Interfacial Energy for Zn Solid Solution in Equilibrium with the Zn-Al Eutectic Liquid. 3665-3672A
- Widmanstätten Ferrite Plate Formation in Low-Carbon Steels. 3701-3706A
- Grain boundary migration**
- The Effect of Heat Treatment on Mg₂Si Coarsening in Aluminum 6105 Alloy. 435-438A
- A Numerical Analysis of Intergranular Penny-Shaped Microcrack Shrinkage Controlled by Coupled Surface and Interface Diffusion. 1301-1309A
- Grain boundary segregation**
- Effect of Low-Frequency Electromagnetic Casting on the Castability, Microstructure, and Tensile Properties of Direct-Chill Cast Al-Zn-Mg-Cu Alloy. 2487-2494A
- Grain boundary sliding**
- Dynamic Phase Transformation during Superplastic Deformation of Nb/Nb₃Al In-Situ Composite. 503-511A
- Failure Mode Analysis and a Mechanism for Hot-Ductility Improvement in the Nb-Microalloyed Steel. 3823-3832A
- Grain growth**
- Study of the Ferrite Grain Coarsening behind the Transformation Front by Electron Backscattered Diffraction Techniques. 93-102A
- Simulation of the Sintering Densification and Shrinkage Behavior of Powder-Injection-Molded 17-4 PH Stainless Steel. 257-263A
- Effects of an α -Al₂O₃ Thin Film on the Oxidation Behavior of a Single-Crystal Ni-Based Superalloy. 1055-1065A
- Effect of Clustering of Precipitates on Grain Growth. 1097-1103A
- Dislocation Structure and Deformation in Iron Processed by Equal-Channel-Angular Pressing. 1343-1350A
- Quantitative Characterization of Microstructures of Liquid-Phase-Sintered Two-Phase Materials. 1881-1888A
- Quantitative Characterization of the Three-Dimensional Microstructure of Polycrystalline Al-Sn using X-Ray Microtomography. 1953-1961A
- Oxide Dispersion Strengthening of Nickel Electrodeposits for Microsystem Applications. 2351-2360A
- Communication: Texture characterization of autogenous Nd:YAG laser welds in AA5182-O and AA6111-T4 aluminum alloys. 3032-3038A
- On the Influence of In-Situ Reactions on Grain Size during Reactive Atomization and Deposition. 3251-3263A
- Grain orientation**
- A Single-Grain Approach Applied to the Modeling of Recrystallization Kinetics for Cold-Rolled Single-Phase Metals. 741-749A
- Statistically Representative Three-Dimensional Microstructures Based on Orthogonal Observation Sections. 1969-1979A
- New Stereology for the Recovery of Grain-Boundary Plane Distributions in the Crystal Frame. 1991-1998A
- Texture Evolution and Mechanical Anisotropy in Dual-Phase Ti3Al-Based Alloy Loaded at 700 °C to 1000 °C. 3803-3815A
- Grain refinement**
- Study of the Ferrite Grain Coarsening behind the Transformation Front by Electron Backscattered Diffraction Techniques. 93-102A
- Effects of Partial Recrystallization on High-Cycle Fatigue Deformation and Crack Generation of a Nitrogen-Strengthened 32Mn-7Cr Austenitic Steel at Liquid-Nitrogen Temperature. 543-553A
- Synthesis of Nanocrystalline Zn-22 Pct Al Using Cryomilling. 573-581A
- Fiber Texture and Substructural Features in the Caliber-Rolled

- Low-Carbon Steels. 665-677A
- Deformation and Damage Mechanisms of Zinc Coatings on Hot-Dip Galvanized Steel Sheets: Part II. Damage Modes. 813-823A
- Yield Behavior of Commercial Al-Si Alloys in the Semisolid State 1187-1202B
- Grain Refinement of Superalloy IN718C by the Addition of Inoculants. 2111-2114A
- The Behavior and Effect of Rare Earth CeO₂ on In-Situ TiC/Al Composite. 2511-2515A
- Development of thermal strain in the coherent mushy zone during solidification of aluminum alloys. 2903-2915A
- Directional Solidification of Large Superalloy Castings with Radiation and Liquid-Metal Cooling: A Comparative Assessment. 3221-3231A
- Nucleation of Solid Aluminum on Inclusion Particles Injected into Al-Si-Fe Alloys. 3233-3250A
- Thermodynamic Aspects of the Constitution, Grain Refining, and Solidification Enthalpies of Al-Ce-Si Alloys. 3349-3362A
- Grain size**
- Zinc Recovery from Spent ZnO Catalyst by Carbon in the Presence of Calcium Carbonate. 55-63B
- Grain-Size Effect on Shape-Memory Behavior of Ti₃₅Ni₄₉Zr_{15.4} Thin Films. 111-119A
- Charpy-Impact-Toughness Prediction using an "Effective" Grain Size for Thermomechanically Controlled Rolled Microalloyed Steels. 121-130A
- Effect of Microstructure on Mechanical Properties of As-Cast Mg-Al Alloys. 309-319A
- Correlation of the Microstructure and Mechanical Properties of Oxide-Dispersion-Strengthened Coppers Fabricated by Internal Oxidation. 493-502A
- Transition of Dominant Diffusion Process during Superplastic Deformation in AZ61 Magnesium Alloys. 555-562A
- Synthesis of Nanocrystalline Zn-22 Pct Al Using Cryomilling. A Single-Grain Approach Applied to the Modeling of Recrystallization Kinetics for Cold-Rolled Single-Phase Metals. 573-581A
- Deformation and Damage Mechanisms of Zinc Coatings on Hot-Dip Galvanized Steel Sheets: Part I. Deformation Modes. Measurement and Modeling of the Electromagnetic Response to Phase Transformation in Steels. 741-749A
- Effect of Simulated Thermal Cycles on the Microstructure of the Heat-Affected Zone in HSLA-80 and HSLA-100 Steel Plates. 797-811A
- The Tensile Response of a Fine-Grained AA5754 Alloy Produced by Asymmetric Rolling and Annealing. 965-972A
- Morphologies of Silicon Crystals Solidified on a Chill Plate. Effect of Clustering of Precipitates on Grain Growth. 985-996A
- Modification-Related Porosity Formation in Hypoeutectic Aluminum-Silicon Alloys. 997-1006A
- Cr-Mo Solid Solutions Forced by High-Energy Ball Milling. Effect of Deformation Route on Microstructural Development in Aluminum Processed by Equal Channel Angular Extrusion. 1067-1073A
- Microstructure, Mechanical Properties, and Fracture Mechanism of As-Cast (Ti_{0.5}Cu_{0.25}Ni_{0.15}Sn_{0.05}Zr_{0.05})(100-x)Mo(x) Composites. 1097-1103A
- Mechanism of Primary MC Carbide Decomposition in Ni-Base Superalloys. 1097-1106B
- Achieving Enhanced Ductility in a Dilute Magnesium Alloy through Severe Plastic Deformation. 1105-1111A
- Effects of Loading Rate on Fracture Behavior of Low-Alloy Steel with Different Grain Sizes. 1359-1368A
- Eutectic Grains in Unmodified and Strontium-Modified Hypoeutectic Aluminum-Silicon Alloys. 1591-1601A
- Effect of Thermomechanical Treatment on the Evolution of Rolling and Recrystallization Textures in Twin-Belt Cast AA5754 Aluminum Alloy. 1669-1679A
- Quantitative Characterization of Microstructures of Liquid-Phase-Sintered Two-Phase Materials. 1735-1744A
- Characterization of Three-Dimensional Grain Structure in Polycrystalline Iron by Serial Sectioning. 1765-1778A
- Multiscale Structure and Properties of Cast and Deformation Processed Polycrystalline NiTi Shape-Memory Alloys. 1829-1837A
- Evolution of Microstructure and Texture in Mg-Al-Zn Alloys during Electron-Beam and Gas Tungsten Arc Welding. 1839-1851A
- Effect of Low-Frequency Electromagnetic Casting on the Castability, Microstructure, and Tensile Properties of Direct-Chill Cast Al-Zn-Mg-Cu Alloy. 1881-1888A
- Dislocation mechanics-based constitutive equations. 1927-1933A
- Shear localization-martensitic transformation interactions in Fe-Cr-Ni monocrystal. 2013-2025A
- High-pressure, laser-driven deformation of an aluminum alloy. Atomic force microscopy studies of fracture surfaces of composition B energetic materials. 2455-2469A
- Grain size dependence of the activation parameters for plastic deformation: influence of crystal structure, slip system, and rate-controlling dislocation mechanism. 2487-2494A
- Molecular-dynamics study of mechanical deformation in nanocrystalline aluminum. 2547-2555A
- The effect of grain size on low-cycle fatigue behavior of Al-2024 polycrystalline alloy. 2575-2586A
- Effect of low-temperature shock compression on the microstructure and strength of copper. 2625-2631A
- On the Influence of In-Situ Reactions on Grain Size during Reactive Atomization and Deposition. 2675-2079A
- Effect of Initial Grain Size of Austenite on Hot-Deformed Structure of Ni-30Fe Alloy. 2697-2705A
- Texture Evolution and Mechanical Anisotropy in Dual-Phase Ti3Al-Based Alloy Loaded at 700 °C to 1000 °C. 2719-2723A
- Microstructure Characterization and Creep Deformation of an Al-10 Wt Pct Ti-2 Wt Pct Cu Nanocomposite. 2725-2728A
- 3803-3815A
- 3855-3861A
- per obtained by consolidation of micro- and nanopowders using equal-channel angular extrusion. 2935-2949A
- Grain structure**
- Communication: Effect of Thermomechanical Processing on Grain Structure Development in a Twin-Belt Strip Cast Automotive Aluminum Alloy. 949-952A
- The Tensile Response of a Fine-Grained AA5754 Alloy Produced by Asymmetric Rolling and Annealing. 997-1006A
- Eutectic Grains in Unmodified and Strontium-Modified Hypoeutectic Aluminum-Silicon Alloys. 1829-1837A
- Characterization of Three-Dimensional Grain Structure in Polycrystalline Iron by Serial Sectioning. 1927-1933A
- Statistically Representative Three-Dimensional Microstructures Based on Orthogonal Observation Sections. 1969-1979A
- Superplastic Behavior and Microstructure Evolution in a Commercial Al-Mg-Sc Alloy Subjected to Intense Plastic Straining. 2383-2392A
- Effects of Alloy Composition and Casting Speed on Structure Formation and Hot Tearing during Direct-Chill Casting of Al-Cu Alloys. 3551-3561A
- Application of a Substructure-Based Hardening Model to Copper under Loading Path Changes. 3763-3774A
- Grain sub boundaries**
- Microstructural Characterization of Secondary-Phase Particles in a Hot-Deformed Al-Cu-Mg-Zr Alloy. 293-300A
- A Single-Grain Approach Applied to the Modeling of Recrystallization Kinetics for Cold-Rolled Single-Phase Metals. 741-749A
- Grains**
- Influence of Convection on Feathery Grain Formation in Aluminum Alloys. 2495-2501A
- Granular materials**
- The Rotary Kiln: An Investigation of Bed Heat Transfer in the Transverse Plane. 1059-1070B
- Graphite**
- Blast Furnace Burden Softening and Melting Phenomena: Part I. Pellet Bulk Interaction Observation. 829-838B
- Graphite, Reduction (chemical)**
- Influence of Chemical Compositions of Slag and Graphite on the Phenomena Occurring in the Graphite/Slag Interfacial Region. 75-83B
- Graphitic structure**
- From Flake to Nodular: A New Theory of Morphological Modification in Gray Cast Iron. 313-330B
- Gravitation**
- Channel Segregation during Solidification and the Effects of an Alternating Traveling Magnetic Field. 743-754B
- Modeling of Distortion after Densification during Liquid-Phase Sintering. 3833-3841A
- Gruneisen parameter**
- Single-Crystal Elastic Constants of Fe-15Ni-15Cr Alloy. 3149-3154A
- Guinier Preston zone**
- Surface Hardening of Nickel Alloys by Means of Plasma Nitriding. 227-238A
- Microstructural Evolution in the Heat-Affected Zone of a Friction Stir Weld. 1487-1499A
- Modeling the Age-Hardening Behavior of Al-Si-Cu Alloys. 2407-2418A
- Hafnium**
- The Influence of Texture, Strain Rate, Temperature, and Chemistry on the Mechanical Behavior of Hafnium. 1999-2011A
- Mechanisms of Hf Dopant Incorporation during the Early Stage of Chemical Vapor Deposition Aluminide Coating Growth under Continuous Doping Conditions. 3581-3593A
- Hafnium, Coatings**
- Effects of Prehardening on Morphological Development of a Chemical Vapor Deposition Aluminide Coating Formed on Single-Crystal Ni-Based Superalloy. 891-897A
- Hardenability**
- Gigacycle Fatigue Properties of a Modified-Ausformed Si-Mn Steel and Effects of Microstructure. 1715-1723A
- Effects of Alloying Elements on Fracture Toughness in the Transition Temperature Region of Base Metals and Simulated Heat-Affected Zones of Mn-Mo-Ni Low-Alloy Steels. 2027-2037A
- Hardening**
- Low-Cycle Fatigue Behavior of ULTIMET Alloy. 785-796A
- Effects of Temperature and Shot Peening on S-N Behavior of a PM Ni-Base Superalloy UDIMET 720. 1007-1016A
- Experimental and Theoretical Evidence for Carbon-Vacancy Binding in Austenite. 2239-2245A
- Second-Order Stresses and Strains in Heterogeneous Steels: Self-Consistent Modeling and X-Ray Diffraction Analysis. 2361-2369A
- Grain-size dependence of the flow stress of Cu from millimeters to nanometers. 2681-2696A
- Cyclic deformation behavior and dislocation structure of Ti-2 Al Pct Al single crystals oriented for double prism slip. 2845-2852A
- Microstructural modification of as-cast NiAl bronze by friction stir processing. 2951-2961A
- Ductility Exhaustion Mechanisms in Thermally Exposed Thin Sheets of a Near-β Titanium Alloy. 3113-3127A
- Effect of Boron on the Low-Cycle Fatigue Behavior and Deformation Structure of INCONEL 718 at 650 °C. 3477-3487A
- Application of a Substructure-Based Hardening Model to Copper under Loading Path Changes. 3763-3774A
- Hardening, Heating effects**
- Communication: Discussion of "Precipitation of Austenite Particles at Grain Boundaries during Aging of Fe-Mn-Ni Steel". 352-355A
- Communication: Authors' Reply. 355-356A
- Hardness**
- Grain size distribution**
- Microstructure evolution and mechanical behavior of bulk cop-

| | | | |
|---|------------|---|------------|
| Correlation of Microstructure and Abrasive and Sliding Wear Resistance of (TiC,SiC)/Ti-6Al-4V Surface Composites Fabricated by High-Energy Electron-Beam Irradiation. | 139-151A | tensitic Alloy T91. | 717-718A |
| Deformation Behavior of Zr ₃ Al-Nb Alloys I: Room-Temperature and High-Temperature Deformation Study. | 189-203A | Heat transfer | |
| Deformation Behavior of Zr ₃ Al-Nb Alloys II: Indentation Creep Studies. | 205-216A | Surface-Oriented Melt/Substrate Heat-Transfer Model in Aluminum Strip Casting. | 351-361B |
| The Effect of Temperature and Extrusion Speed on The Consolidation of Zirconium-Based Metallic Glass Powder Using Equal-Channel Angular Extrusion. | 247-256A | Mathematical Modeling of a Direct Current Electric Arc: Part II. Dimensionless Representation of a Direct Current Arc. | 373-380B |
| Effect of Microstructure on Mechanical Properties of As-Cast Mg-Al Alloys. | 309-319A | Thermal Diffusivity Measurements of Some Synthetic CaO-Al ₂ O ₃ -SiO ₂ Slags. | 461-469B |
| Correlation of Microstructure and Thermal-Fatigue Properties of Centrifugally Cast High-Speed Steel Rolls. | 481-492A | On the Development of a Three-Dimensional Transient Thermal Model to Predict Ingot Cooling Behavior during the Start-Up Phase of the Direct Chill-Casting Process for an AA5182 Aluminum Alloy Ingot. | 523-540B |
| Correlation of Microstructure with the Hardness and Wear Resistance of (TiC,SiC)/Ti-6Al-4V Surface Composites Fabricated by High-Energy Electron-Beam Irradiation. | 525-534A | The Development and Experimental Validation of a Numerical Model of an Induction Skull Melting Furnace. | 785-803B |
| Densification of a Powder-Metal Skeleton by Transient Liquid-Phase Infiltration. | 631-640A | The Rotary Kiln: An Investigation of Bed Heat Transfer in the Transverse Plane | 1059-1070B |
| Correlation of Microstructure with Hardness and Wear Resistance in (TiC,SiC)/Stainless Steel Surface Composites Fabricated by High-Energy Electron-Beam Irradiation. | 1029-1038A | The Cut-Groove Technique to Infer Interfacial Effects during Hot Rolling. | 1087-1095A |
| Preparation of Cu-Ni Alloys through a New Chemical Route Alteration in Hydrogen Absorption by and Hydrogen Permeation through a High-Strength Low-Alloy Steel due to Plasma Source Ion Implantation of Nitrogen | 1107-1112B | Thermomechanical Finite-Element Model of Shell Behavior in Continuous Casting of Steel | 1151-1172B |
| Fabrication of Carbide-Particle-Reinforced Titanium Aluminide-Matrix Composites by Laser-Engineered Net Shaping. | 1123-1128B | Development of thermal strain in the coherent mushy zone during solidification of aluminum alloys. | 2903-2915A |
| Wear Resistance and High-Temperature Compression Strength of Fcc CuCoNiCrAl _{0.5} Fe Alloy with Boron Addition. | 1133-1140A | Experimental Determination of Solid-Liquid Interfacial Energy for Zn Solid Solution in Equilibrium with the Zn-Al Eutectic Liquid | 3665-3672A |
| Wear Behavior, Microstructure, and Dimensional Stability of As-Cast Zinc-Aluminum/SiC (Metal Matrix Composites) Alloys. | 1465-1469A | Heat transfer coefficients | |
| Microstructural Evolution in Laser-Deposited Multilayer Ti-6Al-4V Builds: Part I. Microstructural Characterization. | 1579-1590A | A Model of the Interfacial Heat Transfer Coefficient for the Aluminum Gravity Die-Casting Process. | 721-733B |
| Comparison of Microstructural Evolution in Laser-Deposited and Arc-Melted In-Situ Ti-TiB Composites. | 1861-1867A | Heat transmission | |
| Communication: Quantification of Overaging Hardening Kinetics of Aluminum Alloys. | 2143-2152A | Estimation of Multiple Heat-Flux Components at the Metal/Mold Interface in Bar and Plate Aluminum Alloy Castings. | 575-585B |
| Characterization of the Nucleation and Growth Behavior of Copper Precipitates in Low-Carbon Steels. | 2172-2174A | Heat treatment | |
| Two-Layered Zr-Base Amorphous Alloy/Metal Surface Composites Fabricated by High Energy Electron-Beam Irradiation | 2323-2329A | Study of the Porosity Produced in an Aluminum Alloy Matrix Composite Due to a T6 Heat Treatment. | 2503-2510A |
| Characterization of Retrogression and Reaging Behavior of 8090 Al-Li-Cu-Mg-Zr Alloy | 3455-3460A | Communication: Transformation of mechanically alloyed Nb-Sn powder to Nb ₃ Sn. | 3009-3012A |
| Communication: Room-Temperature Cleavage Fracture of FeMnAl Steels | 3681-3691A | Communication: Diffusion coefficients for modeling the heat treatment of Ti-6Al-4V. | 3015-3018A |
| | 3863-3866A | Determination of Isothermal Transformation Diagrams for Sigma-Phase Formation in Cast Duplex Stainless Steels CD3MN and CD3MWCuN | 3377-3386A |
| HCP metals | | Heating | |
| Grain size dependence of the activation parameters for plastic deformation: influence of crystal structure, slip system, and rate-controlling dislocation mechanism. | 2697-2705A | The Rotary Kiln: An Investigation of Bed Heat Transfer in the Transverse Plane | 1059-1070B |
| Health | | Heating effects | |
| Nanotechnology: Scientific Challenges and Societal Benefits and Risks | 1021-1028B | Study of the Porosity Produced in an Aluminum Alloy Matrix Composite Due to a T6 Heat Treatment. | 2503-2510A |
| Nanotechnology: Scientific Challenges and Societal Benefits and Risks | 3641-3648A | Heating rate | |
| Heat affected zone | | Microstructural Evolution in Laser-Deposited Multilayer Ti-6Al-4V Builds: Part II. Thermal Modeling. | 1869-1879A |
| Precipitate Microstructures and Resulting Properties of Al-Zn-Mg Metal Inert Gas-Weld Heat-Affected Zones. | 1437-1448A | Heavy metals | |
| Microstructural Evolution in the Heat-Affected Zone of a Friction Stir Weld. | 1487-1499A | Modeling of Distortion after Densification during Liquid-Phase Sintering | 3833-3841A |
| Effects of Alloying Elements on Fracture Toughness in the Transition Temperature Region of Base Metals and Simulated Heat-Affected Zones of Mn-Mo-Ni Low-Alloy Steels. | 2027-2037A | Hematite | |
| Formability and Strength of Friction-Stir-Welded Aluminum Sheets | 3461-3468A | Experimental Study of Phase Equilibria in the Al-Fe-Zn-O System in Air. | 633-642B |
| Heat affected zone, Mechanical properties | | Reaction Sequences in the Formation of Silico-Ferrites of Calcium and Aluminum in Iron Ore Sinter | 929-936B |
| Mechanisms and Modeling of Cleavage Fracture in Simulated Heat-Affected Zone Microstructures of a High-Strength Low Alloy Steel. | 1039-1053A | Heterogeneity | |
| Heat affected zone, Microstructure | | A Metallurgical Interpretation of the Static Recrystallization Kinetics of an Intercritically Deformed C-Mn Steel. | 1889-1898A |
| Effect of Simulated Thermal Cycles on the Microstructure of the Heat-Affected Zone in HSLA-80 and HSLA-100 Steel Plates. | 985-996A | Hexagonal cells | |
| Heat capacity | | Temperature Effects on the Lattice Constants and Crystal Structure of a Co-27Cr-5Mo Low-Carbon Alloy. | 2517-2523A |
| Standard Gibbs Energy of Formation of Mg ₄₈ Zn ₅₂ Determined by Solution Calorimetry and Measurement of Heat Capacity from Near Absolute Zero Kelvin | 891-895B | A Micromechanical Analysis of the Yielding Behavior of Individual Widmanstätten Colonies of an $\alpha + \beta$ Titanium Alloy | 3409-3422A |
| Heat of formation | | Hexagonal lattice | |
| A Thermodynamic Model for Deoxidation Equilibria in Steel. Standard Gibbs Energy of Formation of Mg ₄₈ Zn ₅₂ Determined by Solution Calorimetry and Measurement of Heat Capacity from Near Absolute Zero Kelvin | 493-507B | Analysis of Diffusive Cellular Patterns in Directional Solidification of Bulk Samples. | 239-246A |
| Thermodynamic Investigations of Cr ₃ C ₂ and Reassessment of the Cr-C System | 891-895B | High alloy steels, Diffusion | |
| Heat of reaction | | Hydrogen Trap States in Ultrahigh-Strength AERMET 100 Steel. | 849-864A |
| The influence of chemical equilibrium on fluid-solid reaction rates and the falsification of activation energy. | 121-131B | High carbon steels, Mechanical properties | |
| Heat of transformation | | Quench Embrittlement of Hardened 5160 Steel as a Function of Austenitizing Temperature. | 153-162A |
| Characterization of the peritectic reaction in medium-alloy steel through microsegregation and heat-of-transformation studies. | 2869-2879A | High cycle fatigue | |
| Heat resistant steels | | Thermal-Imaging Technologies for Detecting Damage during High-Cycle Fatigue. | 15-23A |
| Effect of Carbon Concentration on Precipitation Behavior of M ₂₃ C ₆ Carbides and MX Carbonitrides in Martensitic 9Cr Steel during Heat Treatment. | 1255-1262A | Effects of Partial Recrystallization on High-Cycle Fatigue Deformation and Crack Generation of a Nitrogen-Strengthened 32Mn-7Cr Austenitic Steel at Liquid-Nitrogen Temperature. | 543-553A |
| Heat resistant steels, Microstructure | | Fracture Behavior of Thixoformed 357-T5 Al Alloys. | 1017-1027A |
| Communication: Grain Boundary Engineering of Ferritic-Martensitic Alloy T91. | | The Effect of Lamellar Morphology on Tensile and High-Cycle Fatigue Behavior of Orthorhombic Ti-22Al-27Nb Alloy. | 2161-2170A |
| | | Room-temperature tensile and high-cycle-fatigue strength of fine TiB particulate-reinforced Ti-22Al-27Nb composites. | 2971-2979A |
| | | High speed tool steels | |
| | | Carbides in high-speed steels containing silicon. | 2757-2766A |
| | | Residual Stress-Affected Diffusion during Plasma Nitriding of Tool Steels | 3523-3530A |
| | | High speed tool steels, Mechanical properties | |
| | | Correlation of Microstructure and Thermal-Fatigue Properties of Centrifugally Cast High-Speed Steel Rolls. | 481-492A |
| | | High strength low alloy steels | |
| | | Alteration in Hydrogen Absorption by and Hydrogen Perme- | |

- ation through a High-Strength Low-Alloy Steel due to Plasma Source Ion Implantation of Nitrogen 1123-1128B
- Hydrogen-Involved Tensile and Cyclic Deformation Behavior of Low-Alloy Pressure Vessel Steel. 1477-1486A
- Effects of Alloying Elements on Fracture Toughness in the Transition Temperature Region of Base Metals and Simulated Heat-Affected Zones of Mn-Mo-Ni Low-Alloy Steels. 2027-2037A
- Effects of Martensite Morphology and Tempering on Dynamic Deformation Behavior of Dual-Phase Steels. 2371-2382A
- Communication: Effect of texture and microstructure on resistance to cracking of high-strength hot-rolled Nb-Ti microalloyed steels. 3024-3029A
- Failure Mode Analysis and a Mechanism for Hot-Ductility Improvement in the Nb-Microalloyed Steel 3823-3832A
- High strength low alloy steels, Mechanical properties**
- Charpy-Impact-Toughness Prediction using an "Effective" Grain Size for Thermomechanically Controlled Rolled Microalloyed Steels. 121-130A
- High strength low alloy steels, Microstructure**
- Study of the Ferrite Grain Coarsening behind the Transformation Front by Electron Backscattered Diffraction Techniques. 93-102A
- High strength low alloy steels, Welding**
- Effect of Simulated Thermal Cycles on the Microstructure of the Heat-Affected Zone in HSLA-80 and HSLA-100 Steel Plates. 985-996A
- Mechanisms and Modeling of Cleavage Fracture in Simulated Heat-Affected Zone Microstructures of a High-Strength Low Alloy Steel. 1039-1053A
- High strength steels**
- Modeling Microbiologically Influenced Corrosion of N-80 Carbon Steel by Fuzzy Calculus. 2051-2056A
- High strength steels, Diffusion**
- Hydrogen Trap States in Ultrahigh-Strength AERMET 100 Steel. 849-864A
- High temperature superconductors**
- The Magic of Plutonium: 5f Electrons and Phase Instability. 2207-2222A
- Homogeneity**
- Preparation of Cu-Ni Alloys through a New Chemical Route Comparison of Microstructural Evolution in Laser-Deposited and Arc-Melted In-Situ Ti-TiB Composites. 1107-1112B 2143-2152A
- Homogenizing**
- The Effect of Heat Treatment on Mg₂Si Coarsening in Aluminum 6105 Alloy. 435-438A
- Hoop stress**
- Characterization and Modeling of Quenching-Induced Residual Stresses in the Nickel-Based Superalloy IN718. 1703-1713A
- Hot dip galvanizing**
- Deformation and Damage Mechanisms of Zinc Coatings on Hot-Dip Galvanized Steel Sheets: Part I. Deformation Modes. 797-811A
- Deformation and Damage Mechanisms of Zinc Coatings on Hot-Dip Galvanized Steel Sheets: Part II. Damage Modes. 813-823A
- Hot dipping**
- A Novel Experiment for the Study of Substrate-Induced Nucleation in Metallic Alloys: Application to Zn-Al 3543-3550A
- Hot extrusion**
- Transition of Dominant Diffusion Process during Superplastic Deformation in AZ61 Magnesium Alloy. 555-562A
- Neutron Diffraction Study of Texture Development during Hot Working of Different Gamma-Titanium Aluminide Alloys 3563-3570A
- Hot isostatic pressing**
- Copper-Zirconium Tungstate Composites Exhibiting Low and Negative Thermal Expansion Influenced by Reinforcement Phase Transformations. 1159-1165A
- Hot pressing**
- Deformation Behavior of Zr₃Al-Nb Alloys I: Room-Temperature and High-Temperature Deformation Study. 189-203A
- Hot rolling**
- Deformation Behavior of Zr₃Al-Nb Alloys I: Room-Temperature and High-Temperature Deformation Study. 189-203A
- The Tensile Response of a Fine-Grained AA5754 Alloy Produced by Asymmetric Rolling and Annealing. 997-1006A
- The Cut-Groove Technique to Infer Interfacial Effects during Hot Rolling. 1087-1095A
- Crystallographic textures in rolled and annealed Fe-Ga and Fe-Al alloys. 2963-2970A 3363-3375A
- Austenite Formation during Intercritical Annealing Inclusion-Controlled Fatigue Properties of 1800 MPA-Class Spring Steels 3737-3744A
- Hot work tool steels, Coating**
- Process Efficiency Measurements in the Laser Engineered Net Shaping Process. 143-152B
- Hot workability**
- Communication: The Dependence of Cavity-Growth Rate on Stress Triaxiality. 2187-2190A
- Hot working**
- Influence of Stress State on Cavitation during Hot Working of Ti-6Al-4V. 655-663A
- Deformation and Recrystallization Behavior during Hot Working of a Coarse-Grain, Nickel-Base Superalloy Ingot Material. 679-693A
- Neutron Diffraction Study of Texture Development during Hot Working of Different Gamma-Titanium Aluminide Alloys 3563-3570A
- HVOF spraying**
- Effect of Thermal Spray on the Microstructure and Adhesive Strength of High Velocity Oxy-Fuel-Sprayed Ni-Cr Coatings on 9Cr-1Mo Steel 3187-3199A
- Hybrid composites, Thermal properties**
- Some Studies on the Thermal-Expansion Behavior of C-Fiber, SiC_f, and In-Situ Mg₂Si-Reinforced AZ31 Mg Alloy-Based Hybrid Composites. 1167-1176A
- Hydraulic turbines, Mechanical properties**
- Communication: Cavitation Erosion Characteristics of a NiTi Alloy. 356-362A
- Hydrides**
- Calorimetric Determination of the 5 Hydride Dissolution Enthalpy in ZIRCALOY-4. 2343-2349A
- Hydrodynamics**
- Study of Inclusion Re-Entrainment in a Filter Bed 999-1009B
- Hydroforming**
- Failure in Internally Pressurized Bent Tubes. 1151-1158A
- Hydrogen embrittlement**
- Hydrogen Trap States in Ultrahigh-Strength AERMET 100 Steel. 849-864A
- Hydrogen reduction**
- Preparation of Cu-Ni Alloys through a New Chemical Route 1107-1112B
- Hydrogen storage**
- Quantification of Hydrogen Diffusion and Trapping in 2.25Cr-1Mo and 3Cr-1Mo-V Steels with the Electrochemical Permeation Technique and Melt Extractions. 1449-1464A
- Hydrogen Absorption of Incoherent TiC Particles in Iron from Environment at High Temperatures 3155-3163A
- Hydrolysis**
- Lubricant Pyrolysis during Sintering of Powder Metallurgy Compacts. 381-392B
- Communication: Preparation of MgOHCl by Controlled Dehydration of MgCl₂·6H₂O. 405-406B
- Hydrometallurgy**
- Communication: Structural Change of Mechanically Activated Molybdenite and the Effect of Mechanical Activation on Molybdenite 1203-1207B
- Hypereutectic structures**
- Effect of Sn on Microstructure and Mechanical Properties of Ti-Base Dendrite/Ultrafine-Structured Multicomponent Alloys 3605-3612A
- Hypoeutectic structures**
- Modification-Related Porosity Formation in Hypoeutectic Aluminum-Silicon Alloys 1097-1106B
- Experimental and modeling studies of the thermal conditions and magnesium, iron, and copper content on the morphology of the aluminum silicon eutectic in hypoeutectic aluminum silicon alloys. 2981-2991A
- Communication: Eutectic solidification of aluminum-silicon alloys. 3038-3043A
- Nucleation of Solid Aluminum on Inclusion Particles Injected into Al-Si-Fe Alloys 3233-3250A
- Hysteresis**
- Ferromagnetic Properties of Deformation-Induced Martensite Transformation in AISI 304 Stainless Steel. 599-605A
- Response of Primary Dendrite Spacing to Varying Temperature Gradient during Directional Solidification. 735-742B
- Temperature Evolution and Life Prediction in Fatigue of Superalloys. 839-848A
- Study of the Ni41.3Ti38.7Nb20 wide transformation hysteresis shape-memory alloy. 2783-2788A
- Effect of Boron on the Low-Cycle Fatigue Behavior and Deformation Structure of INCONEL 718 at 650°C 3477-3487A
- Immersion tests (corrosion)**
- The Role of Microstructure in Localized Corrosion of Magnesium Alloys. 2525-2531A
- Impact**
- Communication: Cavitation Erosion Characteristics of a NiTi Alloy. 356-362A
- Fracture Behavior of Thixoformed 357-T5 Al Alloys. 1017-1027A
- The Effects of Strain Rate and Welding Current Mode on the Dynamic Impact Behavior of Plasma-Arc-Welded 304L Stainless Steel Weldments. 1501-1515A
- Impact strength**
- Charpy-Impact-Toughness Prediction using an "Effective" Grain Size for Thermomechanically Controlled Rolled Microalloyed Steels. 121-130A
- Quench Embrittlement of Hardened 5160 Steel as a Function of Austenitizing Temperature. 153-162A
- Densification of a Powder-Metal Skeleton by Transient Liquid-Phase Infiltration. 631-640A
- Communications: Ultra-High-Speed Exploding Properties of Ti-6Al-4V Alloy Having Equiaxed and Bimodal Microstructures. 719-724A
- Effects of Alloying Elements on Fracture Toughness in the Transition Temperature Region of Base Metals and Simulated Heat-Affected Zones of Mn-Mo-Ni Low-Alloy Steels. 2027-2037A
- Communication: Effect of texture and microstructure on resistance to cracking of high-strength hot-rolled Nb-Ti microalloyed steels. 3024-3029A
- Impact tests**
- Mechanical Properties of Al-60 Pct SiCp Composites Alloyed with Mg. 2127-2141A
- Dynamic deformation and damage in cast γ-TiAl during Taylor cylinder impact: experiments and model validation. 2557-2566A
- A Semiautomated Electron Backscatter Diffraction Technique for Extracting Reliable Twin Statistics 3745-3751A
- Impingement**
- Solid Particle Erosion of Al Alloy and Al-Alloy Composites: Effect of Heat Treatment and Angle of Impingement. 1369-1379A
- Effect of Initial Grain Size of Austenite on Hot-Deformed Structure of Ni-30Fe Alloy 3399-3408A

| | | | |
|---|------------|--|------------|
| Impurities | | | |
| Communication: Diffusion coefficients for modeling the heat treatment of Ti-6Al-4V. | 3015-3018A | Liquid | 3665-3672A |
| Continuous Cooling β -to- α Transformation Behaviors of Extra-Pure and Commercially Pure Ti | 3071-3077A | Interfacial properties | |
| | | Development and Validation of a Thermal Model of the Direct Chill Casting of AZ31 Magnesium Billets | 3843-3854A |
| Incandescent lamps | | Interfacial shear strength | |
| Temperature-Dependent Variability in Lifetime Prediction of Thermally Activated Systems. | 1471-1476A | The Effect of Temperature, Matrix Alloying and Substrate Coatings on Wettability and Shear Strength of Al/Al ₂ O ₃ Couples. | 911-923A |
| Inclusions | | Interfacial stresses | |
| Communication: Nature of Massive Transformation. | 351-352A | Tensile and Fatigue Behavior of Al-Based Metal Matrix Composites Reinforced with Continuous Carbon or Alumina Fibers: Part II. Quasi-Unidirectional Composite Cross-Ply Laminates | 3307-3317A |
| Cr-Mo Solid Solutions Forced by High-Energy Ball Milling. | 1105-1111A | | |
| Void Nucleation by Inclusion Cracking. | 1745-1755A | Intergranular corrosion | |
| Oxide Defects in a Vacuum Investment-Cast Ni-Based Turbine Blade. | 2063-2071A | Double Loop Electrochemical Potentiokinetic Reactivation Test Optimization in Checking of Duplex Stainless Steel Intergranular Corrosion Susceptibility | 3499-3513A |
| Communication: The Influence of Cylindrical Inclusions on the Stability of a Directionally Solidified Interface. | 2181-2185A | Intergranular fracture | |
| Inclusion-Controlled Fatigue Properties of 1800 MPA-Class Spring Steels | 3737-3744A | Quench Embrittlement of Hardened 5160 Steel as a Function of Austenitizing Temperature. | 153-162A |
| Fracture Behavior of Thick-Section Weldment in Fe-12Cr-12Ni-10Mn-0.24N Stainless Steel at Liquid Helium Temperature | 3797-3802A | Role of Temperature and Strain Rate on the Hydrogen-Induced Intergranular Rupture in Alloy 600. | 457-464A |
| Indentation | | A Numerical Analysis of Intergranular Penny-Shaped Microcrack Shrinkage Controlled by Coupled Surface and Interface Diffusion. | 1301-1309A |
| Deformation Behavior of Zr ₃ Al-Nb Alloys II: Indentation Creep Studies. | 205-216A | Characteristics of the Rough-Cut Surface of Quenched and Tempered Martensitic Stainless Steel Using Wire Electrical Discharge Machining. | 1351-1357A |
| Microindentation of Aluminum | 3323-3328A | Molecular-dynamics study of mechanical deformation in nanocrystalline aluminum. | 2719-2723A |
| Induction coils | | Effect of Boron on the Low-Cycle Fatigue Behavior and Deformation Structure of INCONEL 718 at 650°C | 3477-3487A |
| The Development and Experimental Validation of a Numerical Model of an Induction Skull Melting Furnace. | 785-803B | Intergranular structure | |
| Induction heating | | Communication: Discussion of "Precipitation of Austenite Particles at Grain Boundaries during Aging of Fe-Mn-Ni Steel". | 352-355A |
| Fabrication of Foamable Precursors by Powder Compression and Induction Heating Process. | 769-776B | Communication: Authors' Reply. | 355-356A |
| Evaluation of Mechanical Properties of Porous 6061 Alloys Fabricated by the Powder Compression and Induction Heating Process. | 2419-2426A | Intermetallic phases | |
| Induction melting | | Deformation Behavior of Zr ₃ Al-Nb Alloys I: Room-Temperature and High-Temperature Deformation Study. | 189-203A |
| The Development and Experimental Validation of a Numerical Model of an Induction Skull Melting Furnace. | 785-803B | Vapor Pressure Measurement of Zn-Fe Intermetallic Compounds. | 487-492B |
| Infiltration | | The Microstructural Response of Delta-Stabilized Plutonium to Pulsed Laser Welding. | 2445-2454A |
| Densification of a Powder-Metal Skeleton by Transient Liquid-Phase Infiltration. | 631-640A | The Role of Microstructure in Localized Corrosion of Magnesium Alloys. | 2525-2531A |
| Freeze-Off Limits in Transient Liquid-Phase Infiltration. | 641-653A | Intermetallics | |
| Mg AZ80/SiC Composite Bars Fabricated by Infiltration of Porous Ceramic Preforms. | 707-715A | Vapor Pressure Measurement of Zn-Fe Intermetallic Compounds. | 487-492B |
| Ingot casting | | The Development and Experimental Validation of a Numerical Model of an Induction Skull Melting Furnace. | 785-803B |
| Model-Based Melt Rate Control during Vacuum Arc Remelting of Alloy 718. | 101-113B | Thermodynamic Properties and Diffusion Thermodynamic Factors in B2-NiAl | 867-876B |
| On the Development of a Three-Dimensional Transient Thermal Model to Predict Ingot Cooling Behavior during the Start-Up Phase of the Direct Chill-Casting Process for an AA5182 Aluminum Alloy Ingot. | 523-540B | Communication: Observed Dependencies of the Large Thermal-Compressive Response of a NiTi Shape-Memory Alloy Fiber Aluminum Metal Matrix Composite on Maximum Tensile Strain Imposed during a Preceding Room-Temperature Tensile Process. | 1403-1406A |
| Effect of Low-Frequency Electromagnetic Casting on the Castability, Microstructure, and Tensile Properties of Direct-Chill Cast Al-Zn-Mg-Cu Alloy. | 2487-2494A | The Solidification Characteristics of Fe-Rich Intermetallics in Al-11.5Si-0.4Mg Cast Alloys. | 1425-1435A |
| Ingot | | Nickel-Aluminides/Steel Clad Pipe Fabricated by Reactive Centrifugal Casting Method from Liquid Aluminum and Solid Nickel. | 1517-1524A |
| Quality Assessment of Artificially Aged A357 Aluminum Alloy Cast Ingots by Introducing Approximate Expressions of the Quality Index QD | 3079-3089A | Microstructural Evolution in Iron Aluminide Fe-28Al-2C after High-Temperature Hydrogen Treatment. | 1789-1798A |
| Injection | | Intermetallic Diffusion Coatings for Enhanced Hot-Salt Oxidation Resistance of Nitrogen-Containing Austenitic Stainless Steels. | 1799-1806A |
| Simulation of Die Filling for the Wax Injection Process: Part I. Models for Material Behavior. | 755-759B | A Study on the Microstructural Evolution of Al-25 At. Pct V-12.5 At. pct M (M = Cu, Ni, Mn) Powders by Planetary Ball Milling. | 1853-1860A |
| Simulation of Die Filling for the Wax Injection Process: Part II. Numerical Simulation. | 761-768B | Multiscale Structure and Properties of Cast and Deformation Processed Polycrystalline NiTi Shape-Memory Alloys. | 2013-2025A |
| Inlet temperature | | Crystallization of Co100-xPt ₁₀ Si ₁₂ Amorphous Metallic Alloys. | 2057-2061A |
| Physical and Mathematical Determination of the Influence of Input Temperature Changes on the Molten Steel Flow Characteristics in Slab Tundishes | 957-966B | Influence of Microstructure on Tensile and Creep Properties of a New Castable TiAl-Based Alloy. | 2087-2102A |
| Inoculation | | Communication: Determination of γ Phase Lattice Parameter Based on the Chemical Concentration of Its Sublattices in Ni-Base Superalloys. | 2171-2172A |
| Grain Refinement of Superalloy IN718C by the Addition of Inoculants. | 2111-2114A | The Magic of Plutonium: 5f Electrons and Phase Instability. Dynamic deformation and damage in cast γ -TiAl during Taylor cylinder impact: experiments and model validation. | 2207-2222A |
| Interface reactions | | Communication: Transformation of mechanically alloyed Nb-Sn powder to Nb ₃ Sn. | 2557-2566A |
| Damage Evolution during Thermal Fatigue in Fiber-Reinforced Light-Metal-Matrix Composites. | 37-43A | Coarsening Behavior of Ni ₃ Ga Precipitates in Ni-Ga Alloys: Dependence of Microstructure and Kinetics on Volume Fraction | 3009-3012A |
| Solid-State Reactions during Heating Mechanically Milled Al/TiO ₂ Composite Powders. | 2115-2125A | Neutron Diffraction Study of Texture Development during Hot Working of Different Gamma-Titanium Aluminide Alloys | 3063-3069A |
| Effects of Carbon Fiber/Al Interface on Mechanical Properties of Carbon-Fiber-Reinforced Aluminum-Matrix Composites. | 2153-2160A | Mechanisms of Hf Dopant Incorporation during the Early Stage of Chemical Vapor Deposition Aluminide Coating Growth under Continuous Doping Conditions | 3563-3570A |
| Infrared Brazing Cu and Ti Using a 95Ag-5Al Braze Alloy | 3177-3186A | Effect of Sn on Microstructure and Mechanical Properties of Ti-Base Dendrite/Ultrafine-Structured Multicomponent Alloys | 3581-3593A |
| Interfaces | | Texture Evolution and Mechanical Anisotropy in Dual-Phase Ti ₃ Al-Based Alloy Loaded at 700 °C to 1000 °C | 3605-3612A |
| Modeling of Laser Cladding with Powder Injection | 1139-1150B | Microstructure Characterization and Creep Deformation of an Al-10 Wt Pct Ti-2 Wt Pct Cu Nanocomposite | 3803-3815A |
| Communication: The Influence of Cylindrical Inclusions on the Stability of a Directionally Solidified Interface. | 2181-2185A | Intermetallics, Coatings | |
| Nonequilibrium molecular dynamics simulations of metallic friction at Ta/Al and Cu/Ag interfaces. | 2741-2745A | Effects of Preheating on Morphological Development of a Chemical Vapor Deposition Aluminide Coating Formed on | 3855-3861A |
| Effect of Thermal Spray on the Microstructure and Adhesive Strength of High Velocity Oxy-Fuel-Sprayed Ni-Cr Coatings on 9Cr-1Mo Steel | 3187-3199A | | |
| An Analytical Model for the Oxide Size in Al Alloys Synthesized by Reactive Atomization and Deposition | 3265-3273A | | |
| A Micromechanical Analysis of the Yielding Behavior of Individual Widmanstätten Colonies of an $\alpha + \beta$ Titanium Alloy | 3409-3422A | | |
| Interfacial energy | | | |
| Coarsening of Al ₃ Sc precipitates in an Al-0.28 Wt pct Sc alloy. | 3003-3008A | | |
| Coarsening Behavior of Ni ₃ Ga Precipitates in Ni-Ga Alloys: Dependence of Microstructure and Kinetics on Volume Fraction | 3063-3069A | | |
| Nucleation of Solid Aluminum on Inclusion Particles Injected into Al-Si-Fe Alloys | 3233-3250A | | |
| Experimental Determination of Solid-Liquid Interfacial Energy for Zn Solid Solution in Equilibrium with the Zn-Al Eutectic | | | |

| | | | |
|---|------------|------------|--|
| Single-Crystal Ni-Based Superalloy. | 891-897A | | |
| Intermetallics, Composite materials | | | |
| Fabrication of Carbide-Particle-Reinforced Titanium Aluminide-Matrix Composites by Laser-Engineered Net Shaping. | 1133-1140A | | |
| Intermetallics, Mechanical properties | | | |
| Deformation Behavior of Zr ₃ Al-Nb Alloys II: Indentation Creep Studies. | 205-216A | | |
| Communication: Cavitation Erosion Characteristics of a NiTi Alloy. | 356-362A | | |
| Study on Notch Fracture of TiAl Alloys at Room Temperature. | 439-456A | | |
| Intermetallics, Microstructure | | | |
| Recrystallization Behavior of a Heavily Cold-Rolled Ni ₃ Al (B,Zr) Alloy. | 71-81A | | |
| Intermetallics, Phase transformations | | | |
| Dynamic Phase Transformation during Superplastic Deformation of Nb/Nb ₃ Al In-Situ Composite. | 503-511A | | |
| Shape Memory Properties of Ni-Ti Based Melt-Spun Ribbons. | 761-770A | | |
| Intermetallics, Powder technology | | | |
| Hot Explosive Compaction of Aluminum-Nickel Composites. | 1125-1131A | | |
| Internal energy | | | |
| Advancing Towards Constitutive Equations for the Metal Industry via the LEDS Theory. | 5-54B | | |
| Advancing Towards Constitutive Equations for the Metal Industry via the LEDS Theory. | 369-418A | | |
| A novel observation of strain-induced ferrite-to-austenite retransformation after intercritical deformation of C-Mn steel. | 2789-2797A | | |
| Internal friction | | | |
| Damping Properties of Austenitic Stainless Steels Containing Strain-Induced Martensite. | 2401-2406A | | |
| Internal oxidation | | | |
| Correlation of the Microstructure and Mechanical Properties of Oxide-Dispersion-Strengthened Coppers Fabricated by Internal Oxidation. | 493-502A | | |
| Effects of an α -Al ₂ O ₃ Thin Film on the Oxidation Behavior of a Single-Crystal Ni-Based Superalloy. | 1055-1065A | | |
| Intersections | | | |
| Grain-size dependence of the flow stress of Cu from millimeters to nanometers. | 2681-2696A | | |
| Interstitial free steels | | | |
| Effect of the Presence of Alloying Elements in Interstitial-Free and Low-Carbon Steels on Their Surface Composition after Annealing in Reducing Atmospheres (Dew Point = -30 °C). | 2039-2050A | | |
| Communication: Persistence of Superficial Contamination of Rolled Steel during Successive Treatments up to the Formation of a Galvanneal Coating. | 2185-2187A | | |
| On Cells and Microbands Formed in an Interstitial-Free Steel during Cold Rolling at Low to Medium Reductions | 3423-3430A | | |
| Interstitial free steels, Coating | | | |
| Deformation and Damage Mechanisms of Zinc Coatings on Hot-Dip Galvanized Steel Sheets: Part I. Deformation Modes. | 797-811A | | |
| Deformation and Damage Mechanisms of Zinc Coatings on Hot-Dip Galvanized Steel Sheets: Part II. Damage Modes. | 813-823A | | |
| Interstitials | | | |
| Experimental and Theoretical Evidence for Carbon-Vacancy Binding in Austenite. | 2239-2245A | | |
| Investment casting | | | |
| Simulation of Die Filling for the Wax Injection Process: Part I. Models for Material Behavior. | 755-759B | | |
| Simulation of Die Filling for the Wax Injection Process: Part II. Numerical Simulation. | 761-768B | | |
| Investment castings | | | |
| Oxide Defects in a Vacuum Investment-Cast Ni-Based Turbine Blade. | 2063-2071A | | |
| Ion beams | | | |
| Focused Ion-Beam Tomography. | 1935-1943A | | |
| Solute diffusion in liquid nickel measured by pulsed ion beam melting. | 2803-2807A | | |
| Ion implantation | | | |
| Alteration in Hydrogen Absorption by and Hydrogen Permeation through a High-Strength Low-Alloy Steel due to Plasma Source Ion Implantation of Nitrogen | 1123-1128B | | |
| Ion nitriding | | | |
| Surface Hardening of Nickel Alloys by Means of Plasma Nitriding. | 227-238A | | |
| Residual Stress-Affected Diffusion during Plasma Nitriding of Tool Steels | 3523-3530A | | |
| Ionic crystals | | | |
| Effects of Simultaneous Displacive and Ionizing Radiations and of Electric Field on Radiation Damage in Ionic Crystals. | 2257-2266A | | |
| Ionizing radiation | | | |
| Effects of Simultaneous Displacive and Ionizing Radiations and of Electric Field on Radiation Damage in Ionic Crystals. | 2257-2266A | | |
| Iron | | | |
| Lubricant Pyrolysis during Sintering of Powder Metallurgy Compacts. | 381-392B | | |
| Vapor Pressure Measurement of Zn-Fe Intermetallic Compounds. | 487-492B | | |
| Experimental Study of Phase Equilibria in the Al-Fe-Zn-O System in Air. | 633-642B | | |
| Critical Thermodynamic Assessment and Modeling of the Fe-Ni-S System | 897-907B | | |
| The Role of Particle Size on the Laser Sintering of Iron Powder Nanoparticle Recovery Using a Fume Collector Comprised of Carbonized Refuse-Derived Fuel | 937-948B | | |
| Salt Roasting of Suncor Oil Sands Fly Ash | 993-998B | | |
| Coupled-Solute Drag Effects on Ferrite Formation in Fe-C-X Systems. | 1051-1058B | | |
| Dislocation Structure and Deformation in Iron Processed by Equal-Channel-Angular Pressing. | | 1187-1210A | |
| Monte Carlo-Method Simulation of the Deformation-Induced Ferrite Transformation in the Fe-C System. | | 1343-1350A | |
| Hydrogen Absorption of Incoherent TiC Particles in Iron from Environment at High Temperatures | | 1565-1577A | |
| An Experimental and Theoretical Analysis of the Phase Equilibria in the Fe-Cr-VC System | | 3155-3163A | |
| Iron, Binary systems | | | |
| Fcc/Hcp Martensitic Transformation in the Fe-Mn System: Part II. Driving Force and Thermodynamics of the Nucleation Process. | | 3649-3663A | |
| Iron, Crystal lattices | | | |
| Advancing Towards Constitutive Equations for the Metal Industry via the LEDS Theory. | | 83-91A | |
| Advancing Towards Constitutive Equations for the Metal Industry via the LEDS Theory. | | 5-54B | |
| Iron, Physical properties | | | |
| Communication: The Contact Angle between Liquid Iron and a Single-Crystal Magnesium Oxide Substrate at 1873 K. | | 369-418A | |
| Iron, Reactions (chemical) | | | |
| The Effect of CaF ₂ on Thermodynamics of CaO-CaF ₂ -SiO ₂ -(MgO) Slags. | | 179-181B | |
| Iron and steel making | | | |
| The Effect of CaF ₂ on Thermodynamics of CaO-CaF ₂ -SiO ₂ -(MgO) Slags. | | 115-120B | |
| Communication: Phase Equilibria of the Al ₂ O ₃ -CaF ₂ -FeO _n System. | | 115-120B | |
| Communication: A Model for Estimating Exposed Plume Eye Area in Steel Refining Ladles Covered with Thin Slag. | | 181-182B | |
| Fluid Flows in Metallurgy - Friend or Foe? | | 400-404B | |
| Additions to Generate Foam in Stainless Steelmaking. | | 417-437B | |
| Multicomponent Diffusion in Molten Slags. | | 643-650B | |
| Blast Furnace Burden Softening and Melting Phenomena: Part I. Pellet Bulk Interaction Observation | | 675-684B | |
| Critical Thermodynamic Evaluation and Optimization of the FeO-Fe ₂ O ₃ -MgO-SiO ₂ System | | 829-838B | |
| Spot Turbulence, Breakup, and Coalescence of Bubbles Released from a Porous Plug Injector into a Gas-Stirred Ladle | | 877-889B | |
| Physical and Mathematical Determination of the Influence of Input Temperature Changes on the Molten Steel Flow Characteristics in Slab Tundishes | | 949-956B | |
| Iron and steel plants | | | |
| Study on Polychlorinated Dibenzo-p-Dioxin/Furan Formation in Iron Ore Sintering Process | | 957-966B | |
| Iron compounds | | | |
| Critical Thermodynamic Evaluation and Optimization of the FeO-Fe ₂ O ₃ -MgO-SiO ₂ System | | 983-991B | |
| Microstructural Evolution in Iron Aluminide Fe-28Al-2C after High-Temperature Hydrogen Treatment. | | 877-889B | |
| Iron ores | | | |
| Reaction Sequences in the Formation of Silico-Ferrites of Calcium and Aluminum in Iron Ore Sinter | | 1789-1798A | |
| Study on Polychlorinated Dibenzo-p-Dioxin/Furan Formation in Iron Ore Sintering Process | | 929-936B | |
| Iron oxides | | | |
| Effect of the Presence of Alloying Elements in Interstitial-Free and Low-Carbon Steels on Their Surface Composition after Annealing in Reducing Atmospheres (Dew Point = -30 °C). | | 983-991B | |
| Irradiation | | | |
| Two-Layered Zr-Base Amorphous Alloy/Metal Surface Composites Fabricated by High Energy Electron-Beam Irradiation | | 2039-2050A | |
| Isothermal annealing | | | |
| Quantitative Analysis of Texture Evolution of Cold-Rolled Direct-Chill-Cast and Continuous-Cast AA5052 and AA5182 Aluminum Alloys during Isothermal Annealing | | 3455-3460A | |
| Isotropy | | | |
| Temperature Effects on the Lattice Constants and Crystal Structure of a Co-27Cr-5Mo Low-Carbon Alloy. | | 3613-3629A | |
| On the Isotropy of the Dynamic Mechanical and Failure Properties of Swaged Tungsten Heavy Alloys | | 2517-2523A | |
| Killed steels | | | |
| Thermodynamic Evaluation and Optimization of the MnO-Al ₂ O ₃ and MnO-Al ₂ O ₃ -SiO ₂ Systems and Applications to Inclusion Engineering. | | 3787-3795A | |
| Kilns | | | |
| The Rotary Kiln: An Investigation of Bed Heat Transfer in the Transverse Plane | | 259-268B | |
| Kinetics | | | |
| Coarsening behavior of an alpha-beta titanium alloy. | | 1059-1070B | |
| Communication: Evaluation of aging precipitation kinetics and potential in aluminum alloys using indiscriminately integrated peak areas in calorimetry curves. | | 2809-2819A | |
| Ladle metallurgy | | | |
| Communication: A Model for Estimating Exposed Plume Eye Area in Steel Refining Ladles Covered with Thin Slag. | | 3012-3015A | |
| Fluid Flows in Metallurgy - Friend or Foe? | | 400-404B | |
| Spot Turbulence, Breakup, and Coalescence of Bubbles Released from a Porous Plug Injector into a Gas-Stirred Ladle | | 417-437B | |
| The Effect of Carbon in Slag on Steel Reoxidation and Carbon Analysis by X-Ray Photoelectron Spectroscopy in the CaO-SiO ₂ -Al ₂ O ₃ -MgO-MnO-FeO System | | 949-956B | |
| Lamellar structure | | | |
| Microstructure Transformation from Lamellar to Equiaxed | | 1087-1095B | |

- Microduplex through Equal-Channel Angular Pressing in an Al-33 Pct Cu Eutectic Alloy. 279-286A
- Overstability of Lamellar Eutectic Growth below the Minimum-Undercooling Spacing. 1815-1828A
- The Effect of Lamellar Morphology on Tensile and High-Cycle Fatigue Behavior of Orthorhombic Ti-22Al-27Nb Alloy. 2161-2170A
- A Micromechanical Analysis of the Yielding Behavior of Individual Widmanstätten Colonies of an $\alpha + \beta$ Titanium Alloy. 3409-3422A
- Neutron Diffraction Study of Texture Development during Hot Working of Different Gamma-Titanium Aluminide Alloys. 3563-3570A
- Laminates**
- Effects of Changes in Test Temperature on Fatigue Crack Propagation of Al6090/SiCp-Al 6013 Laminated Metal Composites. 2291-2303A
- Tensile and Fatigue Behavior of Al-Based Metal Matrix Composites Reinforced with Continuous Carbon or Alumina Fibers: Part I. Quasi-Unidirectional Composites. 3289-3305A
- Tensile and Fatigue Behavior of Al-Based Metal Matrix Composites Reinforced with Continuous Carbon or Alumina Fibers: Part II. Quasi-Unidirectional Composite Cross-Ply Laminates. 3307-3317A
- Two-Layered Zr-Base Amorphous Alloy/Metal Surface Composites Fabricated by High Energy Electron-Beam Irradiation. 3455-3460A
- Laminates, Mechanical properties**
- Effects of Lamination and Changes in Layer Thickness on Fatigue-Crack Propagation of Lightweight Laminated Metal Composites. 45-52A
- Large eddy simulation**
- Computational and Experimental Study of Turbulent Flow in a 0.4-Scale Water Model of a Continuous Steel Caster. 967-982B
- Laser beam cladding**
- Modeling of Laser Cladding with Powder Injection. 1139-1150B
- Laser beam welding**
- Mechanism Governing Nitrogen Absorption by Steel Weld Metal during Laser Welding. 331-338B
- Computational Modeling of Laser Welding of Cu-Ni Dissimilar Couple. 339-350B
- The Microstructural Response of Delta-Stabilized Plutonium to Pulsed Laser Welding. 2445-2454A
- Communication: Texture characterization of autogenous Nd:YAG laser welds in AA5182-O and AA6111-T4 aluminum alloys. 3032-3038A
- Laser processing**
- Process Efficiency Measurements in the Laser Engineered Net Shaping Process. 143-152B
- Laser sintering**
- The Role of Particle Size on the Laser Sintering of Iron Powder. 937-948B
- Latent heat**
- Thermodynamic Aspects of the Constitution, Grain Refining, and Solidification Enthalpies of Al-Ce-Si Alloys. 3349-3362A
- Lattice parameters**
- Fcc/Hcp Martensitic Transformation in the Fe-Mn System: Part II. Driving Force and Thermodynamics of the Nucleation Process. 83-91A
- Cr-Mo Solid Solutions Forced by High-Energy Ball Milling. Communication: Determination of γ Phase Lattice Parameter Based on the Chemical Concentration of Its Sublattices in Ni-Base Superalloys. 1105-1111A
- Modeling of Lattice Parameter in the Ni-Al System. 2171-2172A
- Temperature Effects on the Lattice Constants and Crystal Structure of a Co-27Cr-5Mo Low-Carbon Alloy. 2313-2321A
- Communication: The Observation and Identification of the Oxide Film on the Creep Cavity Wall of Type 316L Stainless Steel. 2517-2523A
- Defect Structures and Room Temperature Mechanical Properties of C15 Laves Phases in Zr-Nb-Cr and Zr-Hf-Cr Alloy Systems. 3331-3333A
- 3469-3476A
- Lattice vacancies**
- Communication: Grain Boundary Engineering of Ferritic-Martensitic Alloy T91. 717-718A
- Magnetic Contribution to the Interdiffusion Coefficients in Bcc (α) and Fcc (γ) Fe-Ni Alloys. 1681-1690A
- Experimental and Theoretical Evidence for Carbon-Vacancy Binding in Austenite. 2239-2245A
- Effects of Simultaneous Displacive and Ionizing Radiations and of Electric Field on Radiation Damage in Ionic Crystals. 2257-2266A
- Characterization of the peritectic reaction in medium-alloy steel through microsegregation and heat-of-transformation studies. 2869-2879A
- Lattices**
- Characterization of Surface Deformation around Vickers Indents in Monocrystalline Materials. 2247-2255A
- Nanoscale view of shock-wave splitting in diamond. 2647-2650A
- Studies of Lattice Imperfections in Deformed Aluminum-Based Lithium Alloys by X-Ray Diffraction. 3319-3322A
- Brass Type Shear Bands and their Influence on Texture Formation. 3775-3786A
- Microstructure Characterization and Creep Deformation of an Al-10 Wt Pct Ti-2 Wt Pct Cu Nanocomposite. 3855-3861A
- Laves phase**
- Tensile properties and microstructure of Haynes 25 alloy after aging at elevated temperatures for extended times. 2767-2781A
- Defect Structures and Room Temperature Mechanical Properties of C15 Laves Phases in Zr-Nb-Cr and Zr-Hf-Cr Alloy Systems. 3469-3476A
- Leaching**
- Rare Earth Extraction from Bastnaesite Concentrate by Stepwise Carbochlorination-Chemical Vapor Transport-Oxidation. 217-221B
- Salt Roasting of Suncor Oil Sands Fly Ash. 1051-1058B
- Lead (metal)**
- Thermodynamic Study of the Effect of Calcium on Removal of Phosphorus from Silicon by Acid Leaching Treatment. 277-284B
- Grain Refinement Induced by Electromagnetic Stirring: A Dendrite Fragmentation Criterion. 3201-3210A
- Lead (metal), Binary systems**
- A Comparison of the Molecular Interaction Volume Model with the Subregular Solution Model in Multicomponent Liquid Alloys. 419-424A
- Lead base alloys**
- Channel Segregation during Solidification and the Effects of an Alternating Traveling Magnetic Field. 743-754B
- Mushy-zone Rayleigh number to describe macrosegregation and channel segregate formation during directional solidification of metallic alloys. 2927-2934A
- Grain Refinement Induced by Electromagnetic Stirring: A Dendrite Fragmentation Criterion. 3201-3210A
- Leading edges**
- Dislocation structure behind a shock front in fcc perfect crystals: atomistic simulation results. 2609-2615A
- Levitation casting**
- Effect of Low-Frequency Electromagnetic Casting on the Castability, Microstructure, and Tensile Properties of Direct-Chill Cast Al-Zn-Mg-Cu Alloy. 2487-2494A
- Lifetime**
- Temperature-Dependent Variability in Lifetime Prediction of Thermally Activated Systems. 1471-1476A
- LIGA process**
- Oxide Dispersion Strengthening of Nickel Electrodeposits for Microsystem Applications. 2351-2360A
- Limestone**
- Additions to Generate Foam in Stainless Steelmaking. 643-650B
- Linear analysis**
- Thermodynamic Investigations of Cr3C2 and Reassessment of the Cr-C System. 3673-3680A
- Liquid alloys**
- Diffusion-Coefficient Measurements in Liquid Metallic Alloys. 909-917B
- Liquid flow**
- Influence of Convection on Feathery Grain Formation in Aluminum Alloys. 2495-2501A
- Liquid metals**
- On Different Modifications of the Capillary Model of Penetration of Inert Liquid Metals into Porous Refractories and their Connection to the Pore Size Distribution of the Refractories. 471-486B
- Flow of Conducting Liquid around Two Nonconducting Particles in DC Electromagnetic Field and the Electromagnetic Migration Force. 847-855B
- Spot Turbulence, Breakup, and Coalescence of Bubbles Released from a Porous Plug Injector into a Gas-Stirred Ladle. 949-956B
- Liquid metals, Phases (state of matter)**
- A Comparison of the Molecular Interaction Volume Model with the Subregular Solution Model in Multicomponent Liquid Alloys. 419-424A
- Liquid phase sintering**
- Modeling of Distortion after Densification during Liquid-Phase Sintering. 3833-3841A
- Liquid phases**
- Dynamics of Coupled and Uncoupled Two-Phase Flows in a Slab Mold. 85-99B
- Thermodynamic Evaluation and Optimization of the MnO-Al2O3 and MnO-Al2O3-SiO2 Systems and Applications to Inclusion Engineering. 259-268B
- Formation of Core-Type Macroscopic Morphologies in Cu-Fe Base Alloys with Liquid Miscibility Gap. 1243-1253A
- Modeling of Irregular Eutectic Microstructures in Solidification of Al-Si Alloys. 1555-1563A
- Solute diffusion in liquid nickel measured by pulsed ion beam melting. 2803-2807A
- Experimental Determination of Solid-Liquid Interfacial Energy for Zn Solid Solution in Equilibrium with the Zn-Al Eutectic Liquid. 3665-3672A
- Liquid-solid interfaces**
- Experimental Determination of Solid-Liquid Interfacial Energy for Zn Solid Solution in Equilibrium with the Zn-Al Eutectic Liquid. 3665-3672A
- Liquidus**
- Liquidus Temperatures in Calcium Ferrite Slags in Equilibrium with Molten Copper. 203-215B
- Freeze-Off Limits in Transient Liquid-Phase Infiltration. 641-653A
- Critical Thermodynamic Evaluation and Optimization of the FeO-Fe2O3-MgO-SiO2 System. 877-889B
- Critical Thermodynamic Assessment and Modeling of the Fe-Ni-S System. 897-907B
- Diffusion-Coefficient Measurements in Liquid Metallic Alloys. 909-917B
- A Thermodynamic Description of the Al-Mn-Si System over the Entire Composition and Temperature Ranges. 1613-1628A
- Grain Refinement Induced by Electromagnetic Stirring: A Dendrite Fragmentation Criterion. 3201-3210A
- Lithium niobates**
- Local Electromechanical Response at a Single Ferroelectric Domain Wall in Lithium Niobate. 2287-2290A
- Localized corrosion**
- The Role of Microstructure in Localized Corrosion of Magnesium Alloys. 2525-2531A

- Low alloy steels**
Gigacycle Fatigue Properties of a Modified-Ausformed Si-Mn Steel and Effects of Microstructure. 1715-1723A
Void Nucleation by Inclusion Cracking. 1745-1755A
Effects of Loading Rate on Fracture Behavior of Low-Alloy Steel with Different Grain Sizes. 1765-1778A
- Low alloy steels, Phases (state of matter)**
Evolution of Secondary Phases in Cr-V Low-Alloy Steels during Aging. 751-759A
- Low carbon steels**
Analysis of Thin-Slab Casting, by the Compact-Strip Process: Part I. Heat Extraction and Solidification. 541-560B
Experimental Determination of the Carbon Solubility Limit in Ferritic Steels. 1655-1661A
Residual Stresses in High Velocity Oxy-Fuel Metallic Coatings. Effect of the Presence of Alloying Elements in Interstitial-Free and Low-Carbon Steels on Their Surface Composition after Annealing in Reducing Atmospheres (Dew Point = -30 °C). Characterization of the Nucleation and Growth Behavior of Copper Precipitates in Low-Carbon Steels. 1807-1814A
Austenite Formation during Intercritical Annealing of Widmanstätten Ferrite Plate Formation in Low-Carbon Steels. 2039-2050A
2323-2329A
3363-3375A
3701-3706A
- Low carbon steels, Microstructure**
Fiber Texture and Substructural Features in the Caliber-Rolled Low-Carbon Steels. 665-677A
- Low cycle fatigue**
In-Situ Observations of Low-Cycle Fatigue Damage in Cast AM60B Magnesium in an Environmental Scanning Electron Microscope. 321-331A
Low-Cycle Fatigue Behavior of ULTIMET Alloy. 785-796A
Temperature Evolution and Life Prediction in Fatigue of Super-alloys. 839-848A
The effect of grain size on low-cycle fatigue behavior of Al-2024 polycrystalline alloy. 2725-2728A
Effect of Boron on the Low-Cycle Fatigue Behavior and Deformation Structure of INCONEL 718 at 650°C. 3477-3487A
- Low expansion alloys**
Magnetic Contribution to the Interdiffusion Coefficients in Bcc (α) and Fcc (γ) Fe-Ni Alloys. 1681-1690A
- Lubrication**
The Effect of Surface Deformation on Lubrication and Oxide-Scale Fracture in Cold Metal Rolling. 919-928B
- Luders lines**
Thermal-Imaging Technologies for Detecting Damage during High-Cycle Fatigue. 15-23A
- Macrostructure**
Formation of Core-Type Macroscopic Morphologies in Cu-Fe Base Alloys with Liquid Miscibility Gap. 1243-1253A
Microstructural Evolution in Laser-Deposited Multilayer Ti-6Al-4V Builds: Part I. Microstructural Characterization. 1861-1867A
- Magnesite refractories**
The Solubility of Cr₂O₃ in Calcium Ferrite Slags at 1573 K. 197-202B
- Magnesium**
Communication: Preparation of MgOHCl by Controlled Dehydration of MgCl₂·6H₂O. 405-406B
Communication: Properties of MgOHCl. 406-408B
Development and Validation of a Thermal Model of the Direct Chill Casting of AZ31 Magnesium Billets. 3843-3854A
- Magnesium, Reduction (chemical)**
Mechanism of Titanium Sponge Formation in the Kroll Reduction Reactor. 65-74B
- Magnesium base alloys**
Standard Gibbs Energy of Formation of Mg₄₈Zn₅₂ Determined by Solution Calorimetry and Measurement of Heat Capacity from Near Absolute Zero Kelvin. 891-895B
Effect of Mg₂Si Particles on the Elevated Temperature Tensile Properties of Squeeze-Cast Mg-Al Alloys. 1629-1632A
Achieving Enhanced Ductility in a Dilute Magnesium Alloy through Severe Plastic Deformation. 1735-1744A
The Effect of Silicon Content on the Microstructure and Creep Behavior in Die-Cast Magnesium AS Alloys. 1905-1909A
Evolution of Microstructure and Texture in Mg-Al-Zn Alloys during Electron-Beam and Gas Tungsten Arc Welding. 2455-2469A
The Role of Microstructure in Localized Corrosion of Magnesium Alloys. 2525-2531A
Communication: A thousandfold creep strengthening by Ca addition in die-cast AM50 magnesium alloy. 3029-3032A
- Magnesium base alloys, Composite materials**
Quantifying Thermomechanical Fatigue of Light-Metal-Matrix Composites by Mechanical Spectroscopy. 25-35A
Damage Evolution during Thermal Fatigue in Fiber-Reinforced Light-Metal-Matrix Composites. 37-43A
Mg AZ80/SiC Composite Bars Fabricated by Infiltration of Porous Ceramic Preforms. 707-715A
Some Studies on the Thermal-Expansion Behavior of C-Fiber, SiC_p, and In-Situ Mg₂Si-Reinforced AZ31 Mg Alloy-Based Hybrid Composites. 1167-1176A
- Magnesium base alloys, Mechanical properties**
Eff. of Microstructure on Mechanical Properties of As-Cast Mg-Al Alloys. 309-319A
In-Situ Observations of Low-Cycle Fatigue Damage in Cast AM60B Magnesium in an Environmental Scanning Electron Microscope. 321-331A
Transition of Dominant Diffusion Process during Superplastic Deformation in AZ61 Magnesium Alloys. 555-562A
- Magnesium compounds**
Effects of Simultaneous Displacive and Ionizing Radiations and of Electric Field on Radiation Damage in Ionic Crystals. 2257-2266A
- Magnesium oxide**
Phase Equilibrium and Distribution of Minor Elements between Ni-S Melt and Al₂O₃-CaO-MgO Slag at 1873 K. 1041-1049B
- Magnetic anisotropy**
Crystallization of Co_{100-x}Pt_xB₁₀Si₁₂ Amorphous Metallic Alloys. 2057-2061A
- Magnetic fields**
Channel Segregation during Solidification and the Effects of an Alternating Traveling Magnetic Field. 743-754B
Simulation of Flow Control in the Meniscus of a Continuous Casting Mold with Opposing Alternating Current Magnetic Fields. 1129-1137B
An Effect of a Strong Magnetic Field on the Phase Transformation in Plain Carbon Steels. 1663-1668A
- Magnetic flux**
Mathematical Modeling of a Direct Current Electric Arc: Part I. Analysis of the Characteristics of a Direct Current Arc. 363-372B
- Magnetite**
Microreaction Mechanism in Reduction of Magnetite to Wustite. 517-522B
- Magnetization**
Ferromagnetic Properties of Deformation-Induced Martensite Transformation in AISI 304 Stainless Steel. 599-605A
An Effect of a Strong Magnetic Field on the Phase Transformation in Plain Carbon Steels. 1663-1668A
- Magnetostriiction**
Crystallographic textures in rolled and annealed Fe-Ga and Fe-Al alloys. 2963-2970A
- Manganese**
A Thermodynamic Description of the Al-Mn-Si System over the Entire Composition and Temperature Ranges. 1613-1628A
Experimental Investigation and Thermodynamic Calculation of the Phase Equilibria in the Cu-Sn and Cu-Sn-Mn Systems. 1641-1654A
- Manganese, Binary systems**
Fcc/Hcp Martensitic Transformation in the Fe-Mn System: Part II. Driving Force and Thermodynamics of the Nucleation Process. 83-91A
- Manganese steels, Heat treatment**
Communication: Discussion of "Precipitation of Austenite Particles at Grain Boundaries during Aging of Fe-Mn-Ni Steel". 352-355A
Communication: Authors' Reply. 355-356A
- Manganese steels, Mechanical properties**
Thermal-Imaging Technologies for Detecting Damage during High-Cycle Fatigue. 15-23A
- Maraging steels**
Microstructure and mechanical properties of a 2000 MPa Co-free maraging steel after aging at 753 K. 2747-2755A
- Maraging steels, Structural hardening**
Effect of Aging and Deformation on the Microstructure and Properties of Fe-Ni-Ti Maraging Steel. 973-983A
- Marangoni convection**
Marangoni convection in weld pool in CO₂-Ar-shielded gas thermal arc welding. 2861-2867A
- Martensite**
Fcc/Hcp Martensitic Transformation in the Fe-Mn System: Part II. Driving Force and Thermodynamics of the Nucleation Process. 83-91A
Effect of Aging and Deformation on the Microstructure and Properties of Fe-Ni-Ti Maraging Steel. 973-983A
Effect of Simulated Thermal Cycles on the Microstructure of the Heat-Affected Zone in HSLA-80 and HSLA-100 Steel Plates. 985-996A
Characteristics of the Rough-Cut Surface of Quenched and Tempered Martensitic Stainless Steel Using Wire Electrical Discharge Machining. 1351-1357A
Multiscale Structure and Properties of Cast and Deformation Processed Polycrystalline NiTi Shape-Memory Alloys. 2013-2025A
Effects of Martensite Morphology and Tempering on Dynamic Deformation Behavior of Dual-Phase Steels. 2371-2382A
Damping Properties of Austenitic Stainless Steels Containing Strain-Induced Martensite. 2401-2406A
The influence of explosive-driven 'Taylor-wave' shock pre-straining on the structure/property behavior of 304 stainless steel. 2617-2624A
Microstructure and mechanical properties of a 2000 MPa Co-free maraging steel after aging at 753 K. 2747-2755A
Study of the Ni₄₁.3Ti₃₈.7Nb₂₀ wide transformation hysteresis shape-memory alloy. 2783-2788A
Continuous Cooling β -to- α Transformation Behaviors of Extra-Pure and Commercially Pure Ti. 3071-3077A
- Martensitic stainless steels**
Characteristics of the Rough-Cut Surface of Quenched and Tempered Martensitic Stainless Steel Using Wire Electrical Discharge Machining. 1351-1357A
- Martensitic stainless steels, Mechanical properties**
Effects of Heat Treatment and Testing Temperature on Fracture Mechanics Behavior of Low-Si CA-15 Stainless Steel. 471-480A
- Martensitic transformation**
The Influence of a Martensitic Phase Transformation on Stress Development in Thermal Barrier Coating Systems. 2279-2286A
Continuous Cooling β -to- α Transformation Behaviors of Extra-Pure and Commercially Pure Ti. 3071-3077A
- Martensitic transformations**
Fcc/Hcp Martensitic Transformation in the Fe-Mn System: Part II. Driving Force and Thermodynamics of the Nucleation Process. 83-91A

- Ferromagnetic Properties of Deformation-Induced Martensite Transformation in AISI 304 Stainless Steel.** 599-605A
- Shape Memory Properties of Ni-Ti Based Melt-Spun Ribbons. Multiscale Structure and Properties of Cast and Deformation Processed Polycrystalline NiTi Shape-Memory Alloys.** 2013-2025A
- Shear localization-martensitic transformation interactions in Fe-Cr-Ni monocystal.** 2575-2586A
- Study of the Ni41.3Ti38.7Nb20 wide transformation hysteresis shape-memory alloy.** 2783-2788A
- Microstructural modification of as-cast NiAl bronze by friction stir processing.** 2951-2961A
- Microstructure Development during High Velocity Deformation** 3091-3101A
- Mass flow**
- Dynamics of Coupled and Uncoupled Two-Phase Flows in a Slab Mold.** 85-99B
- Mass transfer**
- The influence of chemical equilibrium on fluid-solid reaction rates and the falsification of activation energy.** 121-131B
- Simulation of Flow in a Continuous Galvanizing Bath: Part II. Transient Aluminum Distribution Resulting from Ingot Addition.** 171-178B
- Kinetics of As, Sb, Bi and Pb Volatilization from Industrial Copper Matte during Ar + O₂ Bubbling.** 651-661B
- Massive type transformation**
- Continuous Cooling β -to- α Transformation Behaviors of Extra-Pure and Commercially Pure Ti** 3071-3077A
- Materials processing**
- Infrared Brazing Cu and Ti Using a 95Ag-5Al Braze Alloy** 3177-3186A
- Mathematical analysis**
- Advancing Towards Constitutive Equations for the Metal Industry via the LEDS Theory.** 5-54B
- Fcc/Hcp Martensitic Transformation in the Fe-Mn System: Part II. Driving Force and Thermodynamics of the Nucleation Process.** 83-91A
- Study of the Austempering Transformation Kinetics in Compacted Graphite Cast Irons.** 103-110A
- Grain-Size Effect on Shape-Memory Behavior of $\text{Ti}_{49.7}\text{Ni}_{49.7}\text{Zr}_{1.4}$ Thin Films.** 111-119A
- The influence of chemical equilibrium on fluid-solid reaction rates and the falsification of activation energy.** 121-131B
- Deformation Behavior of $\text{Zr}_{50}\text{Al}_{50}$ Alloys II: Indentation Creep Studies.** 205-216A
- Quantitative Analysis of Texture Evolution in Cold-Rolled, Continuous-Cast AA 5xxx-Series Aluminum Alloys.** 265-277A
- Advancing Towards Constitutive Equations for the Metal Industry via the LEDS Theory.** 369-418A
- Study on Notch Fracture of TiAl Alloys at Room Temperature. A Model of the Interfacial Heat Transfer Coefficient for the Aluminum Gravity Die-Casting Process.** 439-456A
- Shape Memory Properties of Ni-Ti Based Melt-Spun Ribbons. Assessment of the Origin of Porosity in Electron-Beam-Welded TA6V Plates.** 721-733B
- Effect of Clustering of Precipitates on Grain Growth.** 761-770A
- Communication: Determination of γ Phase Lattice Parameter Based on the Chemical Concentration of Its Sublattices in Ni-Base Superalloys.** 879-889A
- Analysis of intergranular impurity concentration and the effects on the ductility of copper-shaped charge jets.** 1097-1103A
- Effect of microstructural length scales on spall behavior of copper.** 2171-2172A
- Effect of low-temperature shock compression on the microstructure and strength of copper.** 2567-2573A
- Characterization of the peritectic reaction in medium-alloy steel through microsegregation and heat-of-transformation studies.** 2663-2673A
- Coarsening of Al₃Sc precipitates in an Al-0.28 Wt pct Sc alloy.** 2729-2739A
- Mathematical models**
- Modeling of the Solubilities of NiO/NiAl₂O₄ and FeO/FeAl₂O₄ in Cryolite Melts at 1300 K.** 2869-2879A
- Process Efficiency Measurements in the Laser Engineered Net Shaping Process.** 3003-3008A
- Simulation of Flow in a Continuous Galvanizing Bath: Part I. Thermal Effects of Ingot Addition.** 133-141B
- Simulation of Flow in a Continuous Galvanizing Bath: Part II. Transient Aluminum Distribution Resulting from Ingot Addition.** 143-152B
- Analysis of Diffusive Cellular Patterns in Directional Solidification of Bulk Samples.** 161-170B
- Simulation of the Sintering Densification and Shrinkage Behavior of Powder-Injection-Molded 17-4 PH Stainless Steel.** 171-178B
- Analytical, Numerical, and Experimental Analysis of Inverse Macroscopic Segregation during Upward Unidirectional Solidification of Al-Cu Alloys.** 239-246A
- Determination of Interfacial Heat-Transfer Boundary Conditions in an Aluminum Low-Pressure Permanent Mold Test Casting.** 257-263A
- Mathematical Modeling of a Direct Current Electric Arc: Part I. Analysis of the Characteristics of a Direct Current Arc.** 285-297B
- Mathematical Modeling of a Direct Current Electric Arc: Part II. Dimensionless Representation of a Direct Current Arc.** 299-311B
- A Comparison of the Molecular Interaction Volume Model with the Subregular Solution Model in Multicomponent Liquid Alloys.** 363-372B
- On Different Modifications of the Capillary Model of Penetration of Inert Liquid Metals into Porous Refractories and their Connection to the Pore Size Distribution of the Refractories.** 373-380B
- A Thermodynamic Model for Deoxidation Equilibria in Steel. Modeling the Dependence of Alumina Solubility on Temperature and Melt Composition in Cryolite-Based Melts.** 419-424A
- Formation of Mesoscale Roughening in 6022-T4 Al Sheets Deformed in Plane-Strain Tension.** 471-486B
- Analysis of Thin-Slab Casting, by the Compact-Strip Process:** 493-507B
- Part I. Heat Extraction and Solidification.** 509-515B
- Precise Determination of the Activation Energy for Desorption of Hydrogen in Two Ti-Added Steels by a Single Thermal-Desorption Spectrum.** 513-524A
- Liquid Convection Effects on the Pushing-Engulfment Transition of Insoluble Particles by a Solidifying Interface: Part I. Analytical Calculation of the Lift Forces.** 541-560B
- Liquid Convection Effects on the Pushing-Engulfment Transition of Insoluble Particles by a Solidifying Interface: Part II. Numerical Calculation of Drag and Lift Forces on a Particle in Parabolic Shear Flow.** 587-597B
- Freeze-Off Limits in Transient Liquid-Phase Infiltration.** 613-621A
- Study of Transient Flow and Particle Transport in Continuous Steel Caster Molds: Part I. Fluid Flow.** 623-629A
- Study of Transient Flow and Particle Transport in Continuous Steel Caster Molds: Part II. Particle Transport.** 641-653A
- Calculation of Physicochemical Properties in a Ternary System with Miscibility Gap.** 685-702B
- A Model of the Interfacial Heat Transfer Coefficient for the Aluminum Gravity Die-Casting Process.** 703-714B
- Response of Primary Dendrite Spacing to Varying Temperature Gradient during Directional Solidification.** 715-720B
- Simulation of Die Filling for the Wax Injection Process: Part 1. Models for Material Behavior.** 721-733B
- Simulation of Die Filling for the Wax Injection Process: Part II. Numerical Simulation.** 735-742B
- The Development and Experimental Validation of a Numerical Model of an Induction Skull Melting Furnace.** 755-759B
- Communication: A Computational Assessment of Viscosity Measurement in Rotating Viscometers through Detailed Numerical Simulation.** 761-768B
- Nickel Droplet Settling Behavior in an Electric Furnace.** 785-803B
- Critical Thermodynamic Evaluation and Optimization of the FeO-Fe₂O₃-MgO-SiO₂ System.** 805-809B
- Physical and Mathematical Determination of the Influence of Input Temperature Changes on the Molten Steel Flow Characteristics in Slab Tundishes.** 839-845B
- Study of Inclusion Re-Entrainment in a Filter Bed.** 877-889B
- Mechanisms and Modeling of Cleavage Fracture in Simulated Heat-Affected Zone Microstructures of a High-Strength Low Alloy Steel.** 957-966B
- Modeling of Laser Cladding with Powder Injection.** 999-1009B
- Cu Precipitation in a Prestrained Fe-1.5 Wt pct Cu Alloy during Isothermal Aging.** 1039-1053A
- Communication: Constitutive Equation for Structural Steels.** 1139-1150B
- Temperature-Dependent Variability in Lifetime Prediction of Thermally Activated Systems.** 1263-1272A
- Interaction of Porosity with a Planar Solid/Liquid Interface.** 1410-1414A
- Experimental Investigation and Thermodynamic Calculation of the Phase Equilibria in the Cu-Sn and Cu-Sn-Mn Systems.** 1471-1476A
- The Influences of Multiscale-Sized Second-Phase Particles on Ductility of Aged Aluminum Alloys.** 1525-1538A
- Erratum: A Solutal Interaction mechanism for the Columnar-to-Equiaxed Transition in Alloy Solidification.** 1641-1654A
- Communication: A Brick-Wall Model for Calculating Young's Modulus of a Particulate Composite.** 1725-1734A
- Validation of Predicted Precipitate Compositions in Al-Si-Ge.** 1915A
- Modeling of Lattice Parameter in the Ni-Al System.** 2191-2192A
- Characterization of the Nucleation and Growth Behavior of Copper Precipitates in Low-Carbon Steels.** 2305-2311A
- Second-Order Stresses and Strains in Heterogeneous Steels: Self-Consistent Modeling and X-Ray Diffraction Analysis.** 2313-2321A
- Modeling the Age-Hardening Behavior of Al-Si-Cu Alloys.** 2323-2329A
- Laser-induced shock compression of copper: orientation and pressure decay effects.** 2361-2369A
- Grain size dependence of the activation parameters for plastic deformation: influence of crystal structure, slip system, and rate-controlling dislocation mechanism.** 2407-2418A
- Plastic deformation behavior of aluminum casting alloys A356/357.** 2633-2646A
- Communication: Diffusion coefficients for modeling the heat treatment of Ti-6Al-4V.** 2697-2705A
- Quality Assessment of Artificially Aged A357 Aluminum Alloy Cast Ingots by Introducing Approximate Expressions of the Quality Index QD.** 2707-2718A
- A Through-Process Model of an A356 Brake Caliper for Fatigue Life Prediction.** 3015-3018A
- Microindentation of Aluminum.** 3079-3089A
- Development and Validation of a Thermal Model of the Direct Chill Casting of AZ31 Magnesium Billets.** 3275-3288A
- Mechanical alloying** 3323-3328A
- Mechanochemical Processing of Nanocrystalline Ti-6Al-4V Alloy.** 3843-3854A
- Communication: Transformation of mechanically alloyed Nb-Sn powder to Nb₃Sn.** 1899-1903A
- Mechanical properties** 3009-3012A
- Effect of Microstructure on the Stability of Retained Austenite in Transformation-Induced-Plasticity Steels.** 2331-2341A
- Mechanical twinning**
- Deformation and Damage Mechanisms of Zinc Coatings on Hot-Dip Galvanized Steel Sheets: Part I. Deformation Modes.** 797-811A
- Medical equipment**
- Mechanism of Resistance Microwelding of Crossed Fine Nickel Wires.** 3165-3176A
- Medium carbon steels**
- Analysis of Thin-Slab Casting, by the Compact-Strip Process: Part I. Heat Extraction and Solidification.** 541-560B
- Modeling Microbiologically Influenced Corrosion of N-80 Carbon Steel by Fuzzy Calculus.** 2051-2056A
- Melt spinning**
- The Role of Melt Pool Behavior in Free-Jet Melt Spinning.** 1539-1553A

- Melting**
Blast Furnace Burden Softening and Melting Phenomena: Part I. Pellet Bulk Interaction Observation
Modeling of Laser Cladding with Powder Injection
Solute diffusion in liquid nickel measured by pulsed ion beam melting. 829-838B
1139-1150B
2803-2807A
- Melting furnaces**
The Development and Experimental Validation of a Numerical Model of an Induction Skull Melting Furnace. 785-803B
- Melts**
Amphoteric Behavior of Alumina in Viscous Flow and Structure of CaO-SiO_2 (MgO) Al_2O_3 Slags
Modeling the Dependence of Alumina Solubility on Temperature and Melt Composition in Cryolite-Based Melts.
Communication: The Influence of Cylindrical Inclusions on the Stability of a Directionally Solidified Interface. 269-275B
509-515B
2181-2185A
- Melts, Reactions (chemical)**
Modeling of the Solubilities of $\text{NiO/NiAl}_2\text{O}_4$ and $\text{FeO/FeAl}_2\text{O}_4$ in Cryolite Melts at 1300 K.
Communication: The Solubility of Titanium Dioxide in Cryolite-Alumina Melts at 1300 K. 133-141B
182-186B
- Mercury**
On Different Modifications of the Capillary Model of Penetration of Inert Liquid Metals into Porous Refractories and their Connection to the Pore Size Distribution of the Refractories.
Simulation of Flow Control in the Meniscus of a Continuous Casting Mold with Opposing Alternating Current Magnetic Fields 471-486B
1129-1137B
- Metal fibers**
Communication: Observed Dependencies of the Large Thermal-Compressive Response of a NiTi Shape-Memory Alloy Fiber Aluminum Metal Matrix Composite on Maximum Tensile Strain Imposed during a Preceding Room-Temperature Tensile Process. 1403-1406A
- Metal matrix composites**
Application of the Generalized Method of Cells Principle to Particle-Reinforced Metal Matrix Composites
Communication: Observed Dependencies of the Large Thermal-Compressive Response of a NiTi Shape-Memory Alloy Fiber Aluminum Metal Matrix Composite on Maximum Tensile Strain Imposed during a Preceding Room-Temperature Tensile Process. 1029-1039B
1403-1406A
Wear Behavior, Microstructure, and Dimensional Stability of As-Cast Zinc-Aluminum/SiC (Metal Matrix Composites) Alloys. 1579-1590A
Co-Deformation Processing and Modeling of In-Situ Multiphase Composites. 1603-1611A
Comparison of Microstructural Evolution in Laser-Deposited and Arc-Melted In-Situ Ti-TiB Composites. 2143-2152A
Effects of Carbon Fiber/Al Interface on Mechanical Properties of Carbon-Fiber-Reinforced Aluminum-Matrix Composites. Study of the Porosity Produced in an Aluminum Alloy Matrix Composite Due to a T6 Heat Treatment. 2153-2160A
2503-2510A
Tensile and Fatigue Behavior of Al-Based Metal Matrix Composites Reinforced with Continuous Carbon or Alumina Fibers: Part I. Quasi-Unidirectional Composites 3289-3305A
Tensile and Fatigue Behavior of Al-Based Metal Matrix Composites Reinforced with Continuous Carbon or Alumina Fibers: Part II. Quasi-Unidirectional Composite Cross-Ply Laminates 3307-3317A
- Metal matrix composites, Anisotropy**
Effect of Reinforcement-Particle-Oriented Anisotropy on the Tensile and Fatigue Behavior of Metal-Matrix Composites. 53-61A
- Metal matrix composites, Mechanical properties**
Quantifying Thermomechanical Fatigue of Light-Metal-Matrix Composites by Mechanical Spectroscopy. 25-35A
Damage Evolution during Thermal Fatigue in Fiber-Reinforced Light-Metal-Matrix Composites. 37-43A
Effects of Lamination and Changes in Layer Thickness on Fatigue-Crack Propagation of Lightweight Laminated Metal Composites. 45-52A
- Metal matrix composites, Microstructure**
Correlation of Microstructure with Hardness and Wear Resistance in (TiC,SiC)/Stainless Steel Surface Composites Fabricated by High-Energy Electron-Beam Irradiation. 1029-1038A
- Metal matrix composites, Powder technology**
Copper-Zirconium Tungstate Composites Exhibiting Low and Negative Thermal Expansion Influenced by Reinforcement Phase Transformations. 1159-1165A
- Metal matrix composites, Thermal properties**
Some Studies on the Thermal-Expansion Behavior of C-Fiber, SiC_p , and In-Situ Mg_2Si -Reinforced AZ31 Mg Alloy-Based Hybrid Composites. 1167-1176A
- Metal scrap**
Metal Vapor Treatment for Enhancing the Dissolution of Platinum Group Metals from Automotive Catalyst Scrap 817-824B
- Metal surfaces**
Two-Layered Zr-Base Amorphous Alloy/Metal Surface Composites Fabricated by High Energy Electron-Beam Irradiation 3455-3460A
- Metal vapors**
Metal Vapor Treatment for Enhancing the Dissolution of Platinum Group Metals from Automotive Catalyst Scrap 817-824B
- Metallic glasses**
The Role of Melt Pool Behavior in Free-Jet Melt Spinning. Crystallization of $\text{Co}_{100-x}\text{PxB}_{10}\text{Si}_{12}$ Amorphous Metallic Alloys. 1539-1553A
2057-2061A
Deformation and Failure of $\text{Zr}_{57}\text{Nb}_{5}\text{Al}_{10}\text{Cu}_{15.4}\text{Ni}_{12.6}\text{W}$ Particulate Composites Under Quasi-Static and Dynamic Compression 3439-3444A
3489-3498A
Fatigue and Fracture Behavior of Bulk Metallic Glass
In-Situ Microfracture Observation of Strip-Cast Zr-Ti-Cu-Ni-Be Bulk Metallic Glass Alloys 3753-3761A
- Metallic glasses, Mechanical properties**
The Effect of Temperature and Extrusion Speed on The Consolidation of Zirconium-Based Metallic Glass Powder Using Equal-Channel Angular Extrusion. 247-256A
- Metallurgical coke**
Mechanism and Rate of Reaction of Al_2O_3 , Al, and CO Vapors with Carbon. 617-623B
- Metallurgy**
Grain-size dependence of the flow stress of Cu from millimeters to nanometers. 2691-2696A
- Metastable phases**
Experimental Study of Phase Equilibria in the Al-Fe-Zn-O System in Air. 633-642B
- Methane**
Reduction of Cobalt Oxide With Methane 825-828B
- Microalloying**
Failure Mode Analysis and a Mechanism for Hot-Ductility Improvement in the Nb-Microalloyed Steel 3823-3832A
- Microcracks**
Advancing Towards Constitutive Equations for the Metal Industry via the LEDS Theory. 5-54B
Advancing Towards Constitutive Equations for the Metal Industry via the LEDS Theory. 369-418A
A Numerical Analysis of Intergranular Penny-Shaped Microcrack Shrinkage Controlled by Coupled Surface and Interface Diffusion. 1301-1309A
Local Electrochemical Studies after Heat Treatment of Stainless Steel: Role of Induced Metallurgical and Surface Modifications on Pitting Triggering 3515-3521A
- Microgravity**
Liquid Convection Effects on the Pushing-Engulfment Transition of Insoluble Particles by a Solidifying Interface: Part I. Analytical Calculation of the Lift Forces. 613-621A
- Microhardness**
Effect of Aging and Deformation on the Microstructure and Properties of Fe-Ni-Ti Maraging Steel. 973-983A
Hot Explosive Compaction of Aluminum-Nickel Composites. Microstructural Evolution in the Heat-Affected Zone of a Friction Stir Weld. 1125-1131A
1487-1499A
An Eulerian Finite-Element Model for Determination of Deformation State of a Copper Subjected to Orthogonal Cutting. Evolution of Microstructure and Texture in Mg-Al-Zn Alloys during Electron-Beam and Gas Tungsten Arc Welding. 2393-2400A
2455-2469A
A novel observation of strain-induced ferrite-to-austenite transformation after intercritical deformation of C-Mn steel. 2789-2797A
Microindentation of Aluminum 3323-3328A
- Microphysics**
Nonequilibrium molecular dynamics simulations of metallic friction at Ta/Al and Cu/Ag interfaces. 2741-2745A
- Microporosity**
In-Situ Observations of Low-Cycle Fatigue Damage in Cast AM60B Magnesium in an Environmental Scanning Electron Microscope. 321-331A
Synthesis of Nanocrystalline Zn-22 Pct Al Using Cryomilling. 573-581A
- Microstrain**
Surface Hardening of Nickel Alloys by Means of Plasma Nitriding. 227-238A
Studies of Lattice Imperfections in Deformed Aluminum-Based Lithium Alloys by X-Ray Diffraction 3319-3322A
- Microstructural analysis**
Effect of Deformation Route on Microstructural Development in Aluminum Processed by Equal Channel Angular Extrusion. The Effects of Strain Rate and Welding Current Mode on the Dynamic Impact Behavior of Plasma-Arc-Welded 304L Stainless Steel Weldments. 1359-1368A
1501-1515A
Microstructural Evolution in Iron Aluminide Fe-28Al-2C after High-Temperature Hydrogen Treatment. 1789-1798A
Characterization of Three-Dimensional Grain Structure in Polycrystalline Iron by Serial Sectioning. 1927-1933A
Focused Ion-Beam Tomography. 1935-1943A
- Microstructural effects**
Effect of Microstructure on Mechanical Properties of As-Cast Mg-Al Alloys. 309-319A
- Microstructure**
Modification-Related Porosity Formation in Hypoeutectic Aluminum-Silicon Alloys 1097-1106B
Yield Behavior of Commercial Al-Si Alloys in the Semisolid State 1187-1202B
Communication: Effect of Microstructure on Tensile Behavior of Thixoformed 357-T5 Semisolid Al Alloy. 1407-1410A
Microstructural Evolution in Laser-Deposited Multilayer Ti-6Al-4V Builds: Part II. Thermal Modeling. 1869-1879A
Dislocations in Milled Galena (PbS). 2223-2228A
Damping Properties of Austenitic Stainless Steels Containing Strain-Induced Martensite. 2401-2406A
Communication: Formation of Simple Crystal Structures in Cu-Co-Ni-Cr-Al-Fe-Ti-V Alloys with Multiprincipal Metallic Elements. 2533-2536A
Analysis of intergranular impurity concentration and the effects on the ductility of copper-shaped charge jets. 2567-2573A
Gas nitriding of high vanadium steels - experiments and simulations. 2799-2802A
Coarsening behavior of an alpha-beta titanium alloy. 2809-2819A

- Effect of Thermal Spray on the Microstructure and Adhesive Strength of High Velocity Oxy-Fuel-Sprayed Ni-Cr Coatings on 9Cr-1Mo Steel 3187-3199A
- On Cells and Microbands Formed in an Interstitial-Free Steel during Cold Rolling at Low to Medium Reductions 3423-3430A
- Characterization of Retrogression and Reaging Behavior of 8090 Al-Li-Cu-Mg-Zr Alloy 3681-3691A
- Variability of Large-Crack Fatigue-Crack-Growth Thresholds in Structural Alloys 3721-3735A
- A Semiautomated Electron Backscatter Diffraction Technique for Extracting Reliable Twin Statistics 3745-3751A
- On the Isotropy of the Dynamic Mechanical and Failure Properties of Swaged Tungsten Heavy Alloys 3787-3795A
- Modeling of Distortion after Densification during Liquid-Phase Sintering 3833-3841A
- Microstructure Characterization and Creep Deformation of an Al-10 Wt Pct Ti-2 Wt Pct Cu Nanocomposite 3855-3861A
- Microwelding**
Mechanism of Resistance Microwelding of Crossed Fine Nickel Wires 3165-3176A
- Migration**
Flow of Conducting Liquid around Two Nonconducting Particles in DC Electromagnetic Field and the Electromagnetic Migration Force 847-855B
- Milling**
Dislocations in Milled Galena (PbS). 2223-2228A
- Minimization**
Critical Thermodynamic Evaluation and Optimization of the FeO-Fe₂O₃-MgO-SiO₂ System 877-889B
- Miscibility**
Communication: Phase Equilibria of the Al₂O₃-CaF₂-FeO_n System. 181-182B
- Formation of Core-Type Macroscopic Morphologies in Cu-Fe Base Alloys with Liquid Miscibility Gap. 1243-1253A
- Miscibility gap**
Calculation of Physicochemical Properties in a Ternary System with Miscibility Gap. 715-720B
- Modification**
From Flake to Nodular: A New Theory of Morphological Modification in Gray Cast Iron. 313-330B
- Modulus of elasticity**
Effect of Reinforcement-Particle-Orientation Anisotropy on the Tensile and Fatigue Behavior of Metal-Matrix Composites. 53-61A
- Microstructure, Mechanical Properties, and Fracture Mechanism of As-Cast (Ti_{0.5}Cu_{0.25}Ni_{0.15}Sn_{0.05}Zr_{0.05})(100-x)Mo(x) Composites. 1591-1601A
- Multiscale Structure and Properties of Cast and Deformation Processed Polycrystalline NiTi Shape-Memory Alloys. 2013-2025A
- Communication: A Brick-Wall Model for Calculating Young's Modulus of a Particulate Composite. 2191-2192A
- Plastic deformation behavior of aluminum casting alloys A356/357. 2707-2718A
- Time-dependent deformation in an enhanced SiC/SiC composite. 2853-2859A
- Single-Crystal Elastic Constants of Fe-15Ni-15Cr Alloy 3149-3154A
- Effect of Sn on Microstructure and Mechanical Properties of Ti-Base Dendrite/Ultrathin-Structured Multicomponent Alloys 3605-3612A
- Molecular dynamics**
Dislocation structure behind a shock front in fcc perfect crystals: atomistic simulation results. 2609-2615A
- Nonequilibrium molecular dynamics simulations of metallic friction at Ta/Al and Cu/Ag interfaces. 2741-2745A
- Molecular structure**
Multicomponent Diffusion in Molten Slags. 675-684B
- Molybdenite**
Communication: Structural Change of Mechanically Activated Molybdenite and the Effect of Mechanical Activation on Molybdenite 1203-1207B
- Molybdenum**
Molybdenum Accumulation at Ferrite/Austenite Interfaces during Isothermal Transformation of an Fe-0.24 Pct C-0.93 Pct Mo Alloy. 1223-1235A
- Molybdenum base alloys**
Variability of Large-Crack Fatigue-Crack-Growth Thresholds in Structural Alloys 3721-3735A
- Molybdenum disilicide**
Characterization of Surface Deformation around Vickers Indents in Monocrystalline Materials. 2247-2255A
- Momentum transfer**
High-pressure, laser-driven deformation of an aluminum alloy. 2625-2631A
- Morphology**
Recrystallization Behavior of a Heavily Cold-Rolled Ni₃Al (B,Zr) Alloy. 71-81A
- Material Flow Patterns and Cavity Model in Friction-Stir Welding of Aluminum Alloys. 153-160B
- From Flake to Nodular: A New Theory of Morphological Modification in Gray Cast Iron. 313-330B
- A Study of Coarsening, Recrystallization, and Morphology of Microstructure in Al-Sc-(Zr)-(Mg) Alloys. 341-350A
- Communication: Cavitation Erosion Characteristics of a NiTi Alloy. 356-362A
- Formation of Mesoscale Roughening in 6022-T4 Al Sheets Deformed in Plane-Strain Tension. 513-524A
- Undercooling and Solidification of Al-50 At. Pct Si Alloy by Electromagnetic Levitation. 607-612A
- Measurement and Modeling of the Electromagnetic Response to Phase Transformation in Steels. 965-972A
- Morphologies of Silicon Crystals Solidified on a Chill Plate. 1067-1073A
- Coupled-Solute Drag Effects on Ferrite Formation in Fe-C-X Systems. 1187-1210A
- Formation of Core-Type Macroscopic Morphologies in Cu-Fe Base Alloys with Liquid Miscibility Gap. 1243-1253A
- Fatigue of Cold-Work Tool Steels: Effect of Heat Treatment and Carbide Morphology on Fatigue Crack Formation, Life, and Fracture Surface Observations. 1289-1300A
- Dislocation Structure and Deformation in Iron Processed by Equal-Channel-Angular Pressing. 1343-1350A
- Modeling of Irregular Eutectic Microstructures in Solidification of Al-Si Alloys. 1555-1563A
- Wear Behavior, Microstructure, and Dimensional Stability of As-Cast Zinc-Aluminum/SiC (Metal Matrix Composites) Alloys. 1579-1590A
- Co-Deformation Processing and Modeling of In-Situ Multiphase Composites. 1603-1611A
- A Comparison between Growth Morphology of "Eutectic" Cells/Dendrites and Single-Phase Cells/Dendrites. 1632-1635A
- Microstructural Evolution in Iron Aluminide Fe-28Al-2C after High-Temperature Hydrogen Treatment. 1789-1798A
- Eutectic Grains in Unmodified and Strontium-Modified Hypoeutectic Aluminum-Silicon Alloys. 1829-1837A
- Microstructural Evolution in Laser-Deposited Multilayer Ti-6Al-4V Builds: Part I. Microstructural Characterization. 1861-1867A
- The Effect of Silicon Content on the Microstructure and Creep Behavior in Die-Cast Magnesium AS Alloys. 1905-1909A
- The Effect of Lamellar Morphology on Tensile and High-Cycle Fatigue Behavior of Orthorhombic Ti-22Al-27Nb Alloy. 2161-2170A
- Effect of Microstructure on the Stability of Retained Austenite in Transformation-Induced-Plasticity Steels. 2331-2341A
- Effects of Martensite Morphology and Tempering on Dynamic Deformation Behavior of Dual-Phase Steels. 2371-2382A
- Modeling the Age-Hardening Behavior of Al-Si-Cu Alloys. 2407-2418A
- Evaluation of Mechanical Properties of Porous 6061 Alloys Fabricated by the Powder Compression and Induction Heating Process. 2419-2426A
- The Microstructural Response of Delta-Stabilized Plutonium to Pulsed Laser Welding. 2445-2454A
- A Quantitative Dendrite Growth Model and Analysis of Stability Concepts. 2471-2485A
- The Role of Microstructure in Localized Corrosion of Magnesium Alloys. 2525-2531A
- Morphology of fractured domains in brittle fracture. 2651-2661A
- Experimental and modeling studies of the thermal conditions and magnesium, iron, and copper content on the morphology of the aluminum silicon eutectic in hypoeutectic aluminum silicon alloys. 2981-2991A
- Communication: Eutectic solidification of aluminum-silicon alloys. 3038-3043A
- The Nitriding Kinetics of Iron-Chromium Alloys; The Role of Excess Nitrogen: Experiments and Modelling 3387-3398A
- The Influence of Strontium on Porosity Formation in Al-Si Alloys 3531-3541A
- Morphology, Heating effects**
Communication: Discussion of "Precipitation of Austenite Particles at Grain Boundaries during Aging of Fe-Mn-Ni Steel". 352-355A
- Communication: Authors' Reply. 355-356A
- Multilayers**
Intermetallic Diffusion Coatings for Enhanced Hot-Salt Oxidation Resistance of Nitrogen-Containing Austenitic Stainless Steels. 1799-1806A
- Microstructural Evolution in Laser-Deposited Multilayer Ti-6Al-4V Builds: Part II. Thermal Modeling. 1869-1879A
- Mushy zones**
Development of thermal strain in the coherent mushy zone during solidification of aluminum alloys. 2903-2915A
- Finite element method simulation of mushy zone behavior during direct-chill casting of an Al-4.5 pct Cu alloy. 2917-2926A
- Mushy-zone Rayleigh number to describe macrosegregation and channel segregate formation during directional solidification of metallic alloys. 2927-2934A
- Experimental and modeling studies of the thermal conditions and magnesium, iron, and copper content on the morphology of the aluminum silicon eutectic in hypoeutectic aluminum silicon alloys. 2981-2991A
- Grain Refinement Induced by Electromagnetic Stirring: A Dendrite Fragmentation Criterion 3201-3210A
- Nanocomposites**
Microstructure Characterization and Creep Deformation of an Al-10 Wt Pct Ti-2 Wt Pct Cu Nanocomposite 3855-3861A
- Nanoindentation**
Oxide Dispersion Strengthening of Nickel Electrodeposits for Microsystem Applications. 2351-2360A
- Nanomaterials**
The Three-Dimensional X-ray Crystal Microscope: A New Tool for Materials Characterization. 1963-1967A
- The Magic of Plutonium: 5f Electrons and Phase Instability. 2207-2222A
- Nanoparticles**
Nanoparticle Recovery Using a Fume Collector Comprised of Carbonized Refuse-Derived Fuel 993-998B
- Molecular-dynamics study of mechanical deformation in nanocrystalline aluminum. 2719-2723A
- Microstructure evolution and mechanical behavior of bulk copper obtained by consolidation of micro- and nanopowders using equal-channel angular extrusion. 2935-2949A
- Nanostructure**
Focused Ion-Beam Tomography. 1935-1943A
- The Three-Dimensional X-ray Crystal Microscope: A New Tool for Materials Characterization. 1963-1967A

- Nanotechnology**
Nanotechnology: Scientific Challenges and Societal Benefits and Risks 1021-1028B
Nanotechnology: Scientific Challenges and Societal Benefits and Risks 3641-3648A
- Necking**
Superplastic Behavior and Microstructure Evolution in a Commercial Al-Mg-Sc Alloy Subjected to Intense Plastic Straining 2383-2392A
Plastic deformation behavior of aluminum casting alloys A356/357 2707-2718A
- Neutron diffraction**
Neutron Diffraction Study of Texture Development during Hot Working of Different Gamma-Titanium Aluminide Alloys 3563-3570A
- Nickel**
Computational Modeling of Laser Welding of Cu-Ni Dissimilar Couple 339-350B
Critical Thermodynamic Assessment and Modeling of the Fe-Ni-S System 897-907B
Salt Roasting of Suncor Oil Sands Fly Ash 1051-1058B
Magnetic Contribution to the Interdiffusion Coefficients in Bcc (α) and Fcc (γ) Fe-Ni Alloys 1681-1690A
Modeling of Lattice Parameter in the Ni-Al System 2313-2321A
Oxide Dispersion Strengthening of Nickel Electrodeposits for Microsystem Applications 2351-2360A
Grain size dependence of the activation parameters for plastic deformation: influence of crystal structure, slip system, and rate-controlling dislocation mechanism 2697-2705A
Solute diffusion in liquid nickel measured by pulsed ion beam melting 2803-2807A
Characterization of the peritectic reaction in medium-alloy steel through microsegregation and heat-of-transformation studies 2869-2879A
Monosilicide-Disilicide-Silicon Phase Equilibria in the Nickel-Platinum-Silicon and Nickel-Palladium-Silicon Systems 3053-3061A
Mechanism of Resistance Microwelding of Crossed Fine Nickel Wires 3165-3176A
- Nickel, Crystal lattices**
Advancing Towards Constitutive Equations for the Metal Industry via the LEDS Theory 5-54B
Advancing Towards Constitutive Equations for the Metal Industry via the LEDS Theory 369-418A
- Nickel aluminides**
Thermodynamic Properties and Diffusion Thermodynamic Factors in B2-NiAl 867-876B
- Nickel base alloys**
Effect of Zr and B on Castability of Ni-Based Superalloy IN792. Communication: Observed Dependencies of the Large Thermal-Compressive Response of a NiTi Shape-Memory Alloy Fiber Aluminum Metal Matrix Composite on Maximum Tensile Strain Imposed during a Preceding Room-Temperature Tensile Process 1403-1406A
Nickel-Aluminides/Steel Clad Pipe Fabricated by Reactive Centrifugal Casting Method from Liquid Aluminum and Solid Nickel 1517-1524A
Mechanism of Primary MC Carbide Decomposition in Ni-Based Superalloys 1669-1679A
Characterization and Modeling of Quenching-Induced Residual Stresses in the Nickel-Based Superalloy IN718 1703-1713A
Thermomechanical Fatigue Behavior of the Third-Generation, Single-Crystal Superalloy TMS-75: Deformation Structure. Communication: Strengthening by γ/γ' Interfacial Dislocation Networks in TMS-162-Toward a Fifth-Generation Single-Crystal Superalloy 1779-1787A
Multiscale Structure and Properties of Cast and Deformation Processed Polycrystalline NiTi Shape-Memory Alloys 1911-1914A
Oxide Defects in a Vacuum Investment-Cast Ni-Based Turbine Blade 2013-2025A
Grain Refinement of Superalloy IN718C by the Addition of Inoculants 2063-2071A
Communication: Determination of γ' Phase Lattice Parameter Based on the Chemical Concentration of Its Sublattices in Ni-Based Superalloys 2111-2114A
The Influence of a Martensitic Phase Transformation on Stress Development in Thermal Barrier Coating Systems 2171-2172A
Study of the Ni41.3Ti38.7Nb20 wide transformation hysteresis shape-memory alloy 2279-2286A
Effect of dissolved tungsten on the deformation of 70Ni-30Fe alloys 2783-2788A
Coarsening Behavior of Ni3Ga Precipitates in Ni-Ga Alloys: Dependence of Microstructure and Kinetics on Volume Fraction 2821-2828A
Effects of Temperature and Strain Rate on Tensile Properties and Activation Energy for Dynamic Strain Aging in Alloy 625 3063-3069A
Effect of Thermal Spray on the Microstructure and Adhesive Strength of High Velocity Oxy-Fuel-Sprayed Ni-Cr Coatings on 9Cr-1Mo Steel 3129-3139A
Directional Solidification of Large Superalloy Castings with Radiation and Liquid-Metal Cooling: A Comparative Assessment 3187-3199A
Effect of Initial Grain Size of Austenite on Hot-Deformed Structure of Ni-30Fe Alloy 3221-3231A
Effect of Boron on the Low-Cycle Fatigue Behavior and Deformation Structure of INCONEL 718 at 650°C 3399-3408A
Mechanisms of Hf Dopant Incorporation during the Early Stage of Chemical Vapor Deposition Aluminide Coating Growth under Continuous Doping Conditions 3477-3487A
Variability of Large-Crack Fatigue-Crack-Growth Thresholds in Structural Alloys 3581-3593A
- Nickel base alloys, Coating**
Effects of Preheating on Morphological Development of a Chemical Vapor Deposition Aluminide Coating Formed on Single-Crystal Ni-Based Superalloy 3721-3735A
- Nickel base alloys, Directional solidification**
Effect of Grain-Boundary Characteristics on Castability of Nickel-Base Superalloys 891-897A
- Nickel base alloys, Heat treatment**
Surface Hardening of Nickel Alloys by Means of Plasma Nitriding 939-946A
- Nickel base alloys, Mechanical properties**
Characterizing Small Fatigue Cracks in Metallic Alloys. Communication: Cavitation Erosion Characteristics of a NiTi Alloy 7-14A
Role of Temperature and Strain Rate on the Hydrogen-Induced Intergranular Rupture in Alloy 600 356-362A
Damage Repair in CMSX-4 Alloy without Fatigue Life Reduction Penalty 457-464A
Effect of Broaching on High-Temperature Fatigue Behavior in Notched Specimens of INCONEL 718 535-542A
Temperature Evolution and Life Prediction in Fatigue of Superalloys 771-783A
Effects of Temperature and Shot Peening on S-N Behavior of a PM Ni-Base Superalloy UDIMET 720 839-848A
- Nickel base alloys, Melting**
Model-Based Melt Rate Control during Vacuum Arc Remelting of Alloy 718 1007-1016A
- Nickel base alloys, Microstructure**
Recrystallization Behavior of a Heavily Cold-Rolled Ni₃Al (B,Zr) Alloy 101-113B
Deformation and Recrystallization Behavior during Hot Working of a Coarse-Grain, Nickel-Base Superalloy Ingot Material. Interfacial Segregation and Influence of Antiphase Boundaries on Rafting in a γ/γ' Alloy 71-81A
679-693A
733-740A
- Nickel base alloys, Oxidation**
Effects of an α -Al₂O₃ Thin Film on the Oxidation Behavior of a Single-Crystal Ni-Based Superalloy 1055-1065A
Effects of Preoxidation on the Nucleation and Growth Behavior of Chemically Vapor-Deposited α -Al₂O₃ on a Single-Crystal Ni-Based Superalloy 1113-1124A
- Nickel base alloys, Phase transformations**
Shape Memory Properties of Ni-Ti Based Melt-Spun Ribbons 761-770A
- Nickel base alloys, Powder technology**
Densification of a Powder-Metal Skeleton by Transient Liquid-Phase Infiltration 631-640A
Freeze-Off Limits in Transient Liquid-Phase Infiltration 641-653A
- Nickel chromium molybdenum steels**
Hydrogen-Involved Tensile and Cyclic Deformation Behavior of Low-Alloy Pressure Vessel Steel 1477-1486A
Void Nucleation by Inclusion Cracking 1745-1755A
- Nickel compounds**
Communication: Observed Dependencies of the Large Thermal-Compressive Response of a NiTi Shape-Memory Alloy Fiber Aluminum Metal Matrix Composite on Maximum Tensile Strain Imposed during a Preceding Room-Temperature Tensile Process 1403-1406A
Nickel-Aluminides/Steel Clad Pipe Fabricated by Reactive Centrifugal Casting Method from Liquid Aluminum and Solid Nickel 1517-1524A
Multiscale Structure and Properties of Cast and Deformation Processed Polycrystalline NiTi Shape-Memory Alloys 2013-2025A
Communication: Determination of γ' Phase Lattice Parameter Based on the Chemical Concentration of Its Sublattices in Ni-Based Superalloys 2171-2172A
- Nickel compounds, Mechanical properties**
Communication: Cavitation Erosion Characteristics of a NiTi Alloy 356-362A
- Nickel compounds, Microstructure**
Recrystallization Behavior of a Heavily Cold-Rolled Ni₃Al (B,Zr) Alloy 71-81A
- Nickel compounds, Phase transformations**
Shape Memory Properties of Ni-Ti Based Melt-Spun Ribbons 761-770A
- Nickel compounds, Powder technology**
Hot Explosive Compaction of Aluminum-Nickel Composites 1125-1131A
- Nickel mattes**
Nickel Droplet Settling Behavior in an Electric Furnace 839-845B
- Nickel steels, Heat treatment**
Communication: Discussion of "Precipitation of Austenite Particles at Grain Boundaries during Aging of Fe-Mn-Ni Steel". Communication: Authors' Reply 352-355A
355-356A
- Niobium**
Failure Mode Analysis and a Mechanism for Hot-Ductility Improvement in the Nb-Microalloyed Steel 3823-3832A
- Niobium base alloys**
Dynamic Phase Transformation during Superplastic Deformation of Nb/Nb₃Al In-Situ Composite 503-511A
Communication: Transformation of mechanically alloyed Nb-Sn powder to Nb3Sn 3009-3012A
Variability of Large-Crack Fatigue-Crack-Growth Thresholds in Structural Alloys 3721-3735A
- Niobium base alloys, Oxidation**
Cyclic Oxidation Response of Multiphase Niobium-Based Alloys 589-597A
- Niobium compounds**
Communication: Transformation of mechanically alloyed Nb-Sn powder to Nb3Sn 3009-3012A
- Niobium compounds, Phase transformations**

- Dynamic Phase Transformation during Superplastic Deformation of Nb/Nb₃Al In-Situ Composite. 503-511A
- Nitrates**
Additions to Generate Foam in Stainless Steelmaking. 643-650B
- Nitriding**
Gas nitriding of high vanadium steels - experiments and simulations. 2799-2802A
The Nitriding Kinetics of Iron-Chromium Alloys; The Role of Excess Nitrogen: Experiments and Modelling 3387-3398A
- Nitrogen**
Alteration in Hydrogen Absorption by and Hydrogen Permeation through a High-Strength Low-Alloy Steel due to Plasma Source Ion Implantation of Nitrogen 1123-1128B
- Nodes**
Analysis of intergranular impurity concentration and the effects on the ductility of copper-shaped charge jets. 2567-2573A
- Nodular iron**
From Flake to Nodular: A New Theory of Morphological Modification in Gray Cast Iron. 313-330B
- Nodular iron, Microstructure**
Effect of Clustering of Precipitates on Grain Growth. 1097-1103A
- Nonlinear dynamics**
Nonequilibrium molecular dynamics simulations of metallic friction at Ta/Al and Cu/Ag interfaces. 2741-2745A
- Nonmetallic inclusions**
Flow of Conducting Liquid around Two Nonconducting Particles in DC Electromagnetic Field and the Electromagnetic Migration Force 847-855B
Study of Inclusion Re-Entrainment in a Filter Bed 999-1009B
Interaction of Porosity with a Planar Solid/Liquid Interface. 1525-1538A
Nucleation of Solid Aluminum on Inclusion Particles Injected into Al-Si-Fe Alloys 3233-3250A
- Normal distribution**
Determination of Volume Fractions of Texture Components with Standard Distributions in Euler Space. 1075-1086A
- Notch sensitivity**
Tensile and Fatigue Behavior of Al-Based Metal Matrix Composites Reinforced with Continuous Carbon or Alumina Fibers: Part II. Quasi-Unidirectional Composite Cross-Ply Laminates 3307-3317A
- Notch toughness**
Effects of Loading Rate on Fracture Behavior of Low-Alloy Steel with Different Grain Sizes. 1765-1778A
- Nuclear reactors**
Communication: Grain Boundary Engineering of Ferritic-Martensitic Alloy T91. 717-718A
- Nucleate boiling**
On the Development of a Three-Dimensional Transient Thermal Model to Predict Ingot Cooling Behavior during the Start-Up Phase of the Direct Chill-Casting Process for an AA5182 Aluminum Alloy Ingot. 523-540B
- Nucleation**
Fcc/Hcp Martensitic Transformation in the Fe-Mn System: Part II. Driving Force and Thermodynamics of the Nucleation Process. 83-91A
Communication: Nature of Massive Transformation. Mechanisms of Strain Accumulation and Damage Development during Creep of Prestrained 316 Stainless Steels. 563-571A
Deformation and Recrystallization Behavior during Hot Working of a Coarse-Grain, Nickel-Base Superalloy Ingot Material. 679-693A
Communication: Resonant Vibration Behavior of an Al-3.8Cu-0.8Li-0.3Mg Alloy. 952-957A
Effects of Temperature and Shot Peening on S-N Behavior of a PM Ni-Base Superalloy UDIMET 720. 1007-1016A
Effect of Clustering of Precipitates on Grain Growth. 1097-1103A
Effects of Preoxidation on the Nucleation and Growth Behavior of Chemically Vapor-Deposited α -Al₂O₃ on a Single-Crystal Ni-Based Superalloy. 1113-1124A
Coupled-Solute Drag Effects on Ferrite Formation in Fe-C-X Systems. 1187-1210A
Studies of the Influence of Alloying Elements on the Growth of Ferrite from Austenite under Decarburization Conditions: Fe-C-Ni Alloys. 1237-1242A
Cu Precipitation in a Prestrained Fe-1.5 Wt Pct Cu Alloy during Isothermal Aging. 1263-1272A
The Solidification Characteristics of Fe-Rich Intermetallics in Al-11.5Si-0.4Mg Cast Alloys. 1425-1435A
The Role of Melt Pool Behavior in Free-Jet Melt Spinning. 1539-1553A
Modeling of Irregular Eutectic Microstructures in Solidification of Al-Si Alloys. 1555-1563A
Monte Carlo-Method Simulation of the Deformation-Induced Ferrite Transformation in the Fe-C System. 1565-1577A
Void Nucleation by Inclusion Cracking. 1745-1755A
Effects of Loading Rate on Fracture Behavior of Low-Alloy Steel with Different Grain Sizes. 1765-1778A
Effect of Thermomechanical Treatment on the Evolution of Rolling and Recrystallization Textures in Twin-Belt Cast AA5754 Aluminum Alloy. 1839-1851A
Erratum: A Solubility Interaction mechanism for the Columnar-to-Equiaxed Transition in Alloy Solidification. 1915A
Crystallization of Co100-xPb10Si12 Amorphous Metallic Alloys. 2057-2061A
Microstructures of a Powder Metallurgy-Hot-Isostatically Pressed Super Duplex Stainless Steel Forming in Industrial Heat Treatments. 2103-2109A
Characterization of the Nucleation and Growth Behavior of Copper Precipitates in Low-Carbon Steels. 2323-2329A
Morphology of fractured domains in brittle fracture. 2651-2661A
- Tensile properties and microstructure of Haynes 25 alloy after aging at elevated temperatures for extended times. 2767-2781A
Communication: Eutectic solidification of aluminum-silicon alloys. 3038-3043A
Microstructure Development during High Velocity Deformation Nucleation of Solid Aluminum on Inclusion Particles Injected into Al-Si-Fe Alloys 3091-3101A
Communication: The Observation and Identification of the Oxide Film on the Creep Cavity Wall of Type 316L Stainless Steel 3233-3250A
Austenite Formation during Intercritical Annealing 3331-3333A
A Novel Experiment for the Study of Substrate-Induced Nucleation in Metallic Alloys: Application to Zn-Al 3363-3375A
Widmanstätten Ferrite Plate Formation in Low-Carbon Steels 3543-3550A
3701-3706A
- Nuclei**
Erratum: A Solubility Interaction mechanism for the Columnar-to-Equiaxed Transition in Alloy Solidification. 1915A
- Numerical analysis**
Simulation of Flow in a Continuous Galvanizing Bath: Part I. Thermal Effects of Ingot Addition. 161-170B
A Numerical Study of Oxidation Behavior during Reactive Atomization and Deposition 1173-1185B
Solute diffusion in liquid nickel measured by pulsed ion beam melting. 2803-2807A
- On-line systems**
Solid-State Reduction of Chromium Oxide by Methane-Containing Gas. 609-615B
- Optimization**
Critical Thermodynamic Evaluation and Optimization of the FeO-Fe₂O₃-MgO-SiO₂ System 877-889B
- Orientation**
Tensile Anisotropy in Cu-Ni-Mn-Sn-Al Alloys. 465-469A
Application of the Generalized Method of Cells Principle to Particulate-Reinforced Metal Matrix Composites 1029-1039B
A Micromechanical Analysis of the Yielding Behavior of Individual Widmanstätten Colonies of an α + β Titanium Alloy 3409-3422A
A Semiautomated Electron Backscatter Diffraction Technique for Extracting Reliable Twin Statistics 3745-3751A
On the Isotropy of the Dynamic Mechanical and Failure Properties of Swaged Tungsten Heavy Alloys 3787-3795A
- Orientation relationships**
Communication: Nature of Massive Transformation. Microstructure and mechanical properties of a 2000 MPa Co-free maraging steel after aging at 753 K. 351-352A
2747-2755A
- Oriented fiber composites**
Tensile and Fatigue Behavior of Al-Based Metal Matrix Composites Reinforced with Continuous Carbon or Alumina Fibers: Part I. Quasi-Unidirectional Composites 3289-3305A
Tensile and Fatigue Behavior of Al-Based Metal Matrix Composites Reinforced with Continuous Carbon or Alumina Fibers: Part II. Quasi-Unidirectional Composite Cross-Ply Laminates 3307-3317A
- Orthorhombic lattice**
Determination of Volume Fractions of Texture Components with Standard Distributions in Euler Space. 1075-1086A
Room-temperature tensile and high-cycle-fatigue strength of fine TiB particulate-reinforced Ti-22Al-27Nb composites. 2971-2979A
- Ostwald ripening**
Coarsening of Al₃Sc precipitates in an Al-0.28 Wt pct Sc alloy. 3003-3008A
- Overaging**
Effect of Aging and Deformation on the Microstructure and Properties of Fe-Ni-Ti Maraging Steel. 973-983A
Communication: Quantification of Overaging Hardening Kinetics of Aluminum Alloys. 2172-2174A
- Oxidation**
Kinetics of Chlorination of Tantalum Pentoxide in Mixture with Sucrose Carbon by Chlorine Gas. 439-448B
The Effect of Carbon in Slag on Steel Reoxidation and Carbon Analysis by X-Ray Photoelectron Spectroscopy in the CaO-SiO₂-Al₂O₃-MgO-MnO-FeO System 1067-1095B
Communication: Structural Change of Mechanically Activated Molybdenite and the Effect of Mechanical Activation on Molybdenite 1203-1207B
Hydrogen Absorption of Incoherent TiC Particles in Iron from Environment at High Temperatures 3155-3163A
- Oxidation rate**
Kinetics of As, Sb, Bi and Pb Volatilization from Industrial Copper Matte during Ar + O₂ Bubbling. 651-661B
Effects of an α -Al₂O₃ Thin Film on the Oxidation Behavior of a Single-Crystal Ni-Based Superalloy. 1055-1065A
Effects of Preoxidation on the Nucleation and Growth Behavior of Chemically Vapor-Deposited α -Al₂O₃ on a Single-Crystal Ni-Based Superalloy. 1113-1124A
A Numerical Study of Oxidation Behavior during Reactive Atomization and Deposition 1173-1185B
Effect of the Presence of Alloying Elements in Interstitial-Free and Low-Carbon Steels on Their Surface Composition after Annealing in Reducing Atmospheres (Dew Point = -30 °C). 2039-2050A
- Oxidation resistance**
Cyclic Oxidation Response of Multiphase Niobium-Based Alloys. 589-597A
Intermetallic Diffusion Coatings for Enhanced Hot-Salt Oxidation Resistance of Nitrogen-Containing Austenitic Stainless Steels. 1799-1806A
The Influence of a Martensitic Phase Transformation on Stress Development in Thermal Barrier Coating Systems. 2279-2286A
Effect of Thermal Spray on the Microstructure and Adhesive Strength of High Velocity Oxy-Fuel-Sprayed Ni-Cr Coatings

- on 9Cr-1Mo Steel 3187-3199A
- Oxidation tests**
- Cyclic Oxidation Response of Multiphase Niobium-Based Alloys. 589-597A
- Oxide coatings**
- Effects of an α -Al₂O₃ Thin Film on the Oxidation Behavior of a Single-Crystal Ni-Based Superalloy. 1055-1065A
- Effects of Preoxidation on the Nucleation and Growth Behavior of Chemically Vapor-Deposited α -Al₂O₃ on a Single-Crystal Ni-Based Superalloy. 1113-1124A
- The Solidification Characteristics of Fe-Rich Intermetallics in Al-11.5Si-0.4Mg Cast Alloys. 1425-1435A
- Oxide dispersion strengthening**
- Oxide Dispersion Strengthening of Nickel Electrodeposits for Microsystem Applications. 2351-2360A
- Oxide films**
- Communication: The Observation and Identification of the Oxide Film on the Creep Cavity Wall of Type 316L Stainless Steel 3331-3333A
- Oxides**
- Kinetics of Chlorination of Tantalum Pentoxide in Mixture with Sucrose Carbon by Chlorine Gas. 439-448B
- Critical Thermodynamic Evaluation and Optimization of the FeO-Fe₂O₃-MgO-SiO₂ System. 877-889B
- The Effect of Surface Deformation on Lubrication and Oxide-Scale Fracture in Cold Metal Rolling. 919-928B
- A Numerical Study of Oxidation Behavior during Reactive Atomization and Deposition. 1173-1185B
- Oxide Defects in a Vacuum Investment-Cast Ni-Based Turbine Blade. 2063-2071A
- An Analytical Model for the Oxide Size in Al Alloys Synthesized by Reactive Atomization and Deposition. 3265-3273A
- Oxides, Extraction**
- Zinc Recovery from Spent ZnO Catalyst by Carbon in the Presence of Calcium Carbonate. 55-63B
- Oxides, Impurities**
- Communication: Phase Equilibria of the Al₂O₃-CaF₂-FeO_n System. 181-182B
- Oxidizing atmospheres**
- The Effect of Carbon in Slag on Steel Reoxidation and Carbon Analysis by X-Ray Photoelectron Spectroscopy in the CaO-SiO₂-Al₂O₃-MgO-MnO-FeO System. 1087-1095B
- Oxygen**
- Experimental Study of Phase Equilibria in the Al-Fe-Zn-O System in Air. 633-642B
- Oxygen steel making**
- Continuous Oxygen Steelmaking with Copper-, Tin-, and Zinc-Contaminated Scrap. 663-674B
- Palladium**
- Monoisilicide-Disilicide-Silicon Phase Equilibria in the Nickel-Platinum-Silicon and Nickel-Palladium-Silicon Systems. 3053-3061A
- Palladium base alloys, Thermal properties**
- Partial Atomic Volume and Partial Molar Enthalpy of Formation of the 3d Metals in the Palladium-Based Solid Solutions. 63-70A
- Paper machines**
- Microstructures of a Powder Metallurgy--Hot-Isostatically Pressed Super Duplex Stainless Steel Forming in Industrial Heat Treatments. 2103-2109A
- Partial pressure**
- Thermodynamic Properties and Diffusion Thermodynamic Factors in B2-NiAl. 867-876B
- Phase Equilibrium and Distribution of Minor Elements between Ni-S Melt and Al₂O₃-CaO-MgO Slag at 1873 K. 1041-1049B
- Particle interactions**
- Flow of Conducting Liquid around Two Nonconducting Particles in DC Electromagnetic Field and the Electromagnetic Migration Force. 847-855B
- Particle shape**
- Application of the Generalized Method of Cells Principle to Particulate-Reinforced Metal Matrix Composites. 1029-1039B
- The Effect of Silicon Content on the Microstructure and Creep Behavior in Die-Cast Magnesium AS Alloys. 1905-1909A
- Particle size**
- Communication: Nature of Massive Transformation. 351-352A
- Reduction of Cobalt Oxide With Methane. 825-828B
- Study of Inclusion Re-Entrainment in a Filter Bed. 999-1009B
- Microstructures of a Powder Metallurgy--Hot-Isostatically Pressed Super Duplex Stainless Steel Forming in Industrial Heat Treatments. 2103-2109A
- Communication: The Influence of Cylindrical Inclusions on the Stability of a Directionally Solidified Interface. 2181-2185A
- Particle size distribution**
- The Role of Particle Size on the Laser Sintering of Iron Powder The Rotary Kiln: An Investigation of Bed Heat Transfer in the Transverse Plane. 937-948B
- Effect of Carbon Concentration on Precipitation Behavior of M23C6 Carbides and MX Carbonitrides in Martensitic 9Cr Steel during Heat Treatment. 1059-1070B
- Microstructural Evolution of Predeformed SiCp/ZA27 Composites during Partial Remelting. 1255-1262A
- 2073-2085A
- Particulate composites**
- Application of the Generalized Method of Cells Principle to Particulate-Reinforced Metal Matrix Composites. 1029-1039B
- Solid Particle Erosion of Al Alloy and Al-Alloy Composites: Effect of Heat Treatment and Angle of Impingement. 1369-1379A
- Creep Behavior of a Rotating Functionally Graded Composite Disc Operating under Thermal Gradient. 1381-1391A
- Fracture Toughness of Selectively Reinforced Al2124 Alloy: Precrack Tip in the Composite Side. 1393-1401A
- Co-Deformation Processing and Modeling of In-Situ Multiphase Composites. 1603-1611A
- A Comparison between Growth Morphology of "Eutectic" Cells/Dendrites and Single-Phase Cells/Dendrites. 1632-1635A
- Microstructural Evolution of Predeformed SiCp/ZA27 Composites during Partial Remelting. 2073-2085A
- Solid-State Reactions during Heating Mechanically Milled Al/TiO₂ Composite Powders. 2115-2125A
- Mechanical Properties of Al-60 Pct SiCp Composites Alloyed with Mg. 2127-2141A
- Comparison of Microstructural Evolution in Laser-Deposited and Arc-Melted In-Situ Ti-TiB Composites. 2143-2152A
- Communication: A Brick-Wall Model for Calculating Young's Modulus of a Particulate Composite. 2191-2192A
- The Behavior and Effect of Rare Earth CeO₂ on In-Situ TiC/Al Composite. 2511-2515A
- Room-temperature tensile and high-cycle-fatigue strength of fine TiB particulate-reinforced Ti-22Al-27Nb composites. 2971-2979A
- Deformation and Failure of Zr57Nb5Al10Cu15.4Ni12.6/W Particle Composites Under Quasi-Static and Dynamic Compression. 3439-3444A
- Particulate composites, Anisotropy**
- Effect of Reinforcement-Particle-Oriented Anisotropy on the Tensile and Fatigue Behavior of Metal-Matrix Composites. 53-61A
- Particulate composites, Mechanical properties**
- Correlation of Microstructure and Abrasive and Sliding Wear Resistance of (TiC,SiC)/Ti-6Al-4V Surface Composites Fabricated by High-Energy Electron-Beam Irradiation. 139-151A
- Effect of Temperature and Strain Rate on the Compressive Flow of Aluminum Composites Containing Submicron Alumina Particles. 287-292A
- Fabrication of Carbide-Particle-Reinforced Titanium Aluminide-Matrix Composites by Laser-Engineered Net Shaping. 1133-1140A
- Particulate composites, Physical properties**
- Reactive Wetting of SiO₂ Substrates by Molten Al. 583-588A
- Particulate composites, Powder technology**
- Mg AZ80/SiC Composite Bars Fabricated by Infiltration of Porous Ceramic Preforms. 707-715A
- Copper-Zirconium Tungstate Composites Exhibiting Low and Negative Thermal Expansion Influenced by Reinforcement Phase Transformations. 1159-1165A
- Pearlite**
- A Model for Ferrite/Pearlite Band Formation and Prevention in Steels. 425-433A
- Pellets**
- Blast Furnace Burden Softening and Melting Phenomena: Part I. Pellet Bulk Interaction Observation. 829-838B
- Penetration**
- On Different Modifications of the Capillary Model of Penetration of Inert Liquid Metals into Porous Refractories and their Connection to the Pore Size Distribution of the Refractories. 471-486B
- Reactive Wetting of SiO₂ Substrates by Molten Al. 583-588A
- Alteration in Hydrogen Absorption by and Hydrogen Permeation through a High-Strength Low-Alloy Steel due to Plasma Source Ion Implantation of Nitrogen. 1123-1128B
- Quantification of Hydrogen Diffusion and Trapping in 2.25Cr-1Mo and 3Cr-1Mo-V Steels with the Electrochemical Permeation Technique and Melt Extractions. 1449-1464A
- Pentlandite**
- Critical Thermodynamic Assessment and Modeling of the Fe-Ni-S System. 897-907B
- Periodic structures**
- Channel Segregation during Solidification and the Effects of an Alternating Traveling Magnetic Field. 743-754B
- Peritectic reactions**
- The Solidification Characteristics of Fe-Rich Intermetallics in Al-11.5Si-0.4Mg Cast Alloys. 1425-1435A
- Characterization of the peritectic reaction in medium-alloy steel through microsegregation and heat-of-transformation studies. 2869-2879A
- Permanent mold casting**
- Determination of Interfacial Heat-Transfer Boundary Conditions in an Aluminum Low-Pressure Permanent Mold Test Casting. 299-311B
- Permeability**
- Freeze-Off Limits in Transient Liquid-Phase Infiltration. 641-653A
- Channel Segregation during Solidification and the Effects of an Alternating Traveling Magnetic Field. 743-754B
- Modification-Related Porosity Formation in Hypoeutectic Aluminum-Silicon Alloys. 1097-1106B
- Communication: Casting of Aluminum-Based Wrought Alloys Using Controlled Diffusion Solidification. 2174-2180A
- Mushy-zone Rayleigh number to describe macrosegregation and channel segregate formation during directional solidification of metallic alloys. 2927-2934A
- pH**
- Communication: Properties of MgOHCl. 406-408B
- Phase boundary**
- The Effect of CaF₂ on Thermodynamics of CaO-CaF₂-SiO₂-(MgO) Slags. 115-120B
- Partial Diffusion Reactions and the Associated Volume Changes in Thermally Exposed Au-Al Ball Bonds. 1273-1280A
- Monte Carlo-Method Simulation of the Deformation-Induced Ferrite Transformation in the Fe-C System. 1565-1577A
- Microstructures of a Powder Metallurgy--Hot-Isostatically Pressed Super Duplex Stainless Steel Forming in Industrial

- Heat Treatments.** 2103-2109A
- Phase decomposition**
Mechanism of Primary MC Carbide Decomposition in Ni-Base Superalloys. 1669-1679A
- Phase diagrams**
Experimental Study of Phase Equilibria in the Al-Fe-Zn-O System in Air. 633-642B
Critical Thermodynamic Evaluation and Optimization of the FeO-Fe₂O₃-MgO-SiO₂ System. 877-889B
A Thermodynamic Description of the Al-Mn-Si System over the Entire Composition and Temperature Ranges. 1613-1628A
Experimental Investigation and Thermodynamic Calculation of the Phase Equilibria in the Cu-Sn and Cu-Sn-Mn Systems. An Effect of a Strong Magnetic Field on the Phase Transformation in Plain Carbon Steels. 1641-1654A
Phase Stability and Phase Transformations in Plutonium and Plutonium-Gallium Alloys. 1663-1668A
Modeling of Lattice Parameter in the Ni-Al System. 2267-2278A
Thermodynamic Aspects of the Constitution, Grain Refining, and Solidification Enthalpies of Al-Ce-Si Alloys. 2313-2321A
3349-3362A
- Phase separation**
Communication: Phase Equilibria of the Al₂O₃-CaF₂-FeO_n System. 181-182B
- Phase stability**
A Comparison of the Molecular Interaction Volume Model with the Subregular Solution Model in Multicomponent Liquid Alloys. 419-424A
The Magic of Plutonium: 5f Electrons and Phase Instability. Phase Stability and Phase Transformations in Plutonium and Plutonium-Gallium Alloys. 2207-2222A
Effect of Microstructure on the Stability of Retained Austenite in Transformation-Induced-Plasticity Steels. 2267-2278A
Thermodynamic Aspects of the Constitution, Grain Refining, and Solidification Enthalpies of Al-Ce-Si Alloys. 2331-2341A
3349-3362A
- Phase transformations**
Microrreaction Mechanism in Reduction of Magnetite to Wustite. 517-522B
Phase Stability and Phase Transformations in Plutonium and Plutonium-Gallium Alloys. 2267-2278A
Nanoscale view of shock-wave splitting in diamond. Communication: Transformation of mechanically alloyed Nb-Sn powder to Nb₃Sn. 2647-2650A
3009-3012A
Single-Crystal Elastic Constants of Fe-15Ni-15Cr Alloy. 3149-3154A
Thermodynamic Investigations of Cr₃C₂ and Reassessment of the Cr-C System. 3673-3680A
- Pinch rolls**
Analysis of Thin-Slab Casting, by the Compact-Strip Process: Part I. Heat Extraction and Solidification. 541-560B
- Pipe**
Nickel-Aluminides/Steel Clad Pipe Fabricated by Reactive Centrifugal Casting Method from Liquid Aluminum and Solid Nickel. 1517-1524A
- Pistons**
Study of the Porosity Produced in an Aluminum Alloy Matrix Composite Due to a T6 Heat Treatment. 2503-2510A
- Pitting (corrosion)**
Electrode Pitting in Resistance Spot Welding of Aluminum Alloy 5182. 217-226A
Electrochemical Evaluation of a Corrosion Fatigue Failure Mechanism in a Duplex Stainless Steel. 2427-2437A
Local Electrochemical Studies after Heat Treatment of Stainless Steel: Role of Induced Metallurgical and Surface Modifications on Pitting Triggering. 3515-3521A
- Plane strain**
Brass Type Shear Bands and their Influence on Texture Formation. 3775-3786A
- Planetary mills**
A Study on the Microstructural Evolution of Al-25 Al. Pct V-12.5 Al. pct M (M = Cu, Ni, Mn) Powders by Planetary Ball Milling. 1853-1860A
- Plasma arc welding**
The Effects of Strain Rate and Welding Current Mode on the Dynamic Impact Behavior of Plasma-Arc-Welded 304L Stainless Steel Weldments. 1501-1515A
- Plastic deformation**
Advancing Towards Constitutive Equations for the Metal Industry via the LEEDS Theory. 5-54B
Damage Evolution during Thermal Fatigue in Fiber-Reinforced Light-Metal-Matrix Composites. 37-43A
Advancing Towards Constitutive Equations for the Metal Industry via the LEEDS Theory. 369-418A
Study on Notch Fracture of TiAl Alloys at Room Temperature. Role of Temperature and Strain Rate on the Hydrogen-Induced Intergranular Rupture in Alloy 600. 439-456A
457-464A
Dynamic Phase Transformation during Superplastic Deformation of Nb/Nb₃Al In-Situ Composite. 503-511A
Damage Repair in CMSX-4 Alloy without Fatigue Life Reduction Penalty. 535-542A
Effects of Partial Recrystallization on High-Cycle Fatigue Deformation and Crack Generation of a Nitrogen-Strengthened 32Mn-7Cr Austenitic Steel at Liquid-Nitrogen Temperature. 543-553A
Transition of Dominant Diffusion Process during Superplastic Deformation in AZ61 Magnesium Alloys. 555-562A
Ferromagnetic Properties of Deformation-Induced Martensite Transformation in AISI 304 Stainless Steel. 599-605A
Deformation and Damage Mechanisms of Zinc Coatings on Hot-Dip Galvanized Steel Sheets: Part II. Damage Modes. High-Strain-Rate Superplastic Behavior of Equal-Channel Angular-Pressed 5083 Al-0.2 Wt Pct Sc. 825-837A
Quantification of Hydrogen Diffusion and Trapping in 2.25Cr-1Mo and 3Cr-1Mo-V Steels with the Electrochemical Permeation Technique and Melt Extractions. 1449-1464A
Wear Behavior, Microstructure, and Dimensional Stability of As-Cast Zinc-Aluminum/SiC (Metal Matrix Composites) Alloys. 1579-1590A
Characterization and Modeling of Quenching-Induced Residual Stresses in the Nickel-Based Superalloy IN718. 1703-1713A
Achieving Enhanced Ductility in a Dilute Magnesium Alloy through Severe Plastic Deformation. 1735-1744A
Effects of Loading Rate on Fracture Behavior of Low-Alloy Steel with Different Grain Sizes. 1765-1778A
A Metallurgical Interpretation of the Static Recrystallization Kinetics of an Intercritically Deformed C-Mn Steel. 1889-1898A
Dislocations in Milled Galena (PbS). 2223-2228A
Characterization of Surface Deformation around Vickers Indents in Monocrystalline Materials. 2247-2255A
Superplastic Behavior and Microstructure Evolution in a Commercial Al-Mg-Sc Alloy Subjected to Intense Plastic Straining. 2383-2392A
An Eulerian Finite-Element Model for Determination of Deformation State of a Copper Subjected to Orthogonal Cutting. 2393-2400A
Shear localization-martensitic transformation interactions in Fe-Cr-Ni monocrystal. 2575-2586A
The influence of explosive-driven 'Taylor-wave' shock pre-straining on the structure/property behavior of 304 stainless steel. 2617-2624A
Grain size dependence of the activation parameters for plastic deformation: influence of crystal structure, slip system, and rate-controlling dislocation mechanism. 2697-2705A
Plastic deformation behavior of aluminum casting alloys A356/357. 2707-2718A
The effect of grain size on low-cycle fatigue behavior of Al-2024 polycrystalline alloy. 2725-2728A
Effect of low-temperature shock compression on the microstructure and strength of copper. 2729-2739A
Understanding the Contributions of Normal-Fatigue and Static Loading to the Dwell Fatigue in a Near-Alpha Titanium Alloy Microindentation of Aluminum. 3141-3148A
Deformation and Failure of Zr57Nb5Al10Cu15.4Ni12.6W Particle Composites Under Quasi-Static and Dynamic Compression. 3323-3328A
3439-3444A
- Plastic flow**
Characterization of Plastic Flow and Resulting Microtextures in a Friction Stir Weld. 777-783B
Communication: Constitutive Equation for Structural Steels. Tensile behavior of friction-stir-welded Al 6061-T651. 1410-1414A
2829-2835A
Communication: A thousandfold creep strengthening by Ca addition in die-cast AM50 magnesium alloy. 3029-3032A
Dynamic Deformation Behavior and Ballistic Impact Properties of Ti-6Al-4V Alloy Having Equiaxed and Bimodal Microstructures. 3103-3112A
- Plasticity**
Quantifying Thermomechanical Fatigue of Light-Metal-Matrix Composites by Mechanical Spectroscopy. 25-35A
Deformation Behavior of Zr₃Al-Nb Alloys I: Room-Temperature and High-Temperature Deformation Study. 189-203A
Communication: Cavitation Erosion Characteristics of a NiTi Alloy. 356-362A
Formation of Mesoscale Roughening in 6022-T4 Al Sheets Deformed in Plane-Strain Tension. 513-524A
Void Nucleation by Inclusion Cracking. 1745-1755A
Characterization of Surface Deformation around Vickers Indents in Monocrystalline Materials. 2247-2255A
The Influence of a Martensitic Phase Transformation on Stress Development in Thermal Barrier Coating Systems. 2279-2286A
High-pressure, laser-driven deformation of an aluminum alloy. 2625-2631A
Austenite Formation during Intercritical Annealing. 3363-3375A
Fatigue and Fracture Behavior of Bulk Metallic Glass. 3489-3498A
Effect of Sn on Microstructure and Mechanical Properties of Ti-Base Dendrite/Ultrafine-Structured Multicomponent Alloys. 3605-3612A
Application of a Substructure-Based Hardening Model to Copper under Loading Path Changes. 3763-3774A
- Plating baths**
Simulation of Flow in a Continuous Galvanizing Bath: Part I. Thermal Effects of Ingot Addition. 161-170B
Simulation of Flow in a Continuous Galvanizing Bath: Part II. Transient Aluminum Distribution Resulting from Ingot Addition. 171-178B
Effect of Ternary Additions on the Structure and Properties of Coatings Produced by a High Aluminum Galvanizing Bath. 3707-3720A
- Platinum**
Monosilicide-Disilicide-Silicon Phase Equilibria in the Nickel-Platinum-Silicon and Nickel-Palladium-Silicon Systems. 3053-3061A
- Platinum compounds**
Crystallization of Co_{100-x}Pt_xB₁₀Si₁₂ Amorphous Metallic Alloys. 2057-2061A
- Platinum metals**
Metal Vapor Treatment for Enhancing the Dissolution of Platinum Group Metals from Automotive Catalyst Scrap. 817-824B
- Plutonium**
The Magic of Plutonium: 5f Electrons and Phase Instability. Phase Stability and Phase Transformations in Plutonium and Plutonium-Gallium Alloys. 2207-2222A
2267-2278A
The Microstructural Response of Delta-Stabilized Plutonium to Pulsed Laser Welding. 2445-2454A
- Plutonium alloys**
Phase Stability and Phase Transformations in Plutonium and Plutonium-Gallium Alloys. 2267-2278A

| | | |
|---|------------|--|
| Poissons ratio | | |
| Single-Crystal Elastic Constants of Fe-15Ni-15Cr Alloy | 3149-3154A | |
| Polarization | | |
| Effect of Different Cr Contents on Tensile and Corrosion Behaviors of 0.13 Pct N-Containing CD4MCU Cast Duplex Stainless Steels | 3431-3438A | |
| Characterization of Retrogression and Reaging Behavior of 8090 Al-Li-Cu-Mg-Zr Alloy | 3681-3691A | |
| Polycrystals | | |
| Statistically Representative Three-Dimensional Microstructures Based on Orthogonal Observation Sections | 1969-1979A | |
| Effect of microstructural length scales on spall behavior of copper | 2663-2673A | |
| Molecular-dynamics study of mechanical deformation in nanocrystalline aluminum | 2719-2723A | |
| Application of a Substructure-Based Hardening Model to Copper under Loading Path Changes | 3763-3774A | |
| Polyethylene, Joining | | |
| Effect of Surface Modification of High-Density Polyethylene by Direct Current and Radio Frequency Glow Discharge on Wetting and Adhesion Characteristics | 865-877A | |
| Polymers | | |
| Dislocation mechanics-based constitutive equations | 2547-2555A | |
| Polyvinyl chlorides | | |
| Study of Inclusion Re-Entrainment in a Filter Bed | 999-1009B | |
| Porosity | | |
| On Different Modifications of the Capillary Model of Penetration of Inert Liquid Metals into Porous Refractories and their Connection to the Pore Size Distribution of the Refractories | 471-486B | |
| Mg AZ80/SiC Composite Bars Fabricated by Infiltration of Porous Ceramic Preforms | 707-715A | |
| Fabrication of Foamable Precursors by Powder Compression and Induction Heating Process | 769-776B | |
| Assessment of the Origin of Porosity in Electron-Beam-Welded TA6V Plates | 879-889A | |
| The Role of Particle Size on the Laser Sintering of Iron Powder Communication: Effect of Thermomechanical Processing on Grain Structure Development in a Twin-Belt Strip Cast Automotive Aluminum Alloy | 937-948B | |
| Modification-Related Porosity Formation in Hypoeutectic Aluminum-Silicon Alloys | 949-952A | |
| Interaction of Porosity with a Planar Solid/Liquid Interface | 1097-1106B | |
| Grain Refinement of Superalloy IN718C by the Addition of Inoculants | 1525-1538A | |
| Mechanical Properties of Al-60 Pct SiCp Composites Alloyed with Mg | 2111-2114A | |
| Evaluation of Mechanical Properties of Porous 6061 Alloys Fabricated by the Powder Compression and Induction Heating Process | 2127-2141A | |
| Study of the Porosity Produced in an Aluminum Alloy Matrix Composite Due to a T6 Heat Treatment | 2419-2426A | |
| Segregation band formation in Al-Si die castings | 2503-2510A | |
| A Through-Process Model of an A356 Brake Caliper for Fatigue Life Prediction | 2881-2891A | |
| The Influence of Strontium on Porosity Formation in Al-Si Alloys | 3275-3288A | |
| The Selection of the Spray Deposition Rate during the Spray Rolling Process | 3531-3541A | |
| Effect of Ternary Additions on the Structure and Properties of Coatings Produced by a High Aluminum Galvanizing Bath | 3595-3603A | |
| Portevin-le Chatelier effect | | |
| Effects of Temperature and Strain Rate on Tensile Properties and Activation Energy for Dynamic Strain Aging in Alloy 625 | 3707-3720A | |
| Pouring | | |
| Estimation of Multiple Heat-Flux Components at the Metal/Mold Interface in Bar and Plate Aluminum Alloy Castings | 3129-3139A | |
| Effects of the entrained surface film on the reliability of castings | 575-585B | |
| Powder compacts | | |
| Fabrication of Foamable Precursors by Powder Compression and Induction Heating Process | 2893-2902A | |
| Evaluation of Mechanical Properties of Porous 6061 Alloys Fabricated by the Powder Compression and Induction Heating Process | 769-776B | |
| Precipitates | | |
| Effect of Simulated Thermal Cycles on the Microstructure of the Heat-Affected Zone in HSLA-80 and HSLA-100 Steel Plates | 2419-2426A | |
| Validation of Predicted Precipitate Compositions in Al-Si-Ge | 985-996A | |
| Characterization of the Nucleation and Growth Behavior of Copper Precipitates in Low-Carbon Steels | 2305-2311A | |
| Carbides in high-speed steels containing silicon | 2323-2329A | |
| Tensile behavior of friction-stir-welded Al 6061-T651 | 2757-2766A | |
| Coarsening of Al ₃ Sc precipitates in an Al-0.28 Wt pct Sc alloy | 2829-2835A | |
| Coarsening Behavior of Ni ₃ Ga Precipitates in Ni-Ga Alloys | 3003-3008A | |
| Dependence of Microstructure and Kinetics on Volume Fraction | 3063-3069A | |
| Precipitation | | |
| Recrystallization Behavior of a Heavily Cold-Rolled Ni ₃ Al (B,Zr) Alloy | 71-81A | |
| Grain-Size Effect on Shape-Memory Behavior of Ti ₃₅ Co ₄₉ Zr _{15.4} Thin Films | 111-119A | |
| Correlation of Microstructure and Abrasive and Sliding Wear Resistance of (TiC,SiC)/Ti-6Al-4V Surface Composites Fabricated by High-Energy Electron-Beam Irradiation | 139-151A | |
| A Study of Coarsening, Recrystallization, and Morphology of Microstructure in Al-Sc-(Zr)-(Mg) Alloys | 341-350A | |
| Communication: Nature of Massive Transformation | 351-352A | |
| Communication: Discussion of "Precipitation of Austenite Particles at Grain Boundaries during Aging of Fe-Mn-Ni Steel" | 352-355A | |
| Communication: Authors' Reply | 355-356A | |
| The Effect of Heat Treatment on Mg ₂ Si Coarsening in Aluminum 6105 Alloy | 435-438A | |
| Correlation of Microstructure with the Hardness and Wear Resistance of (TiC,SiC)/Ti-6Al-4V Surface Composites Fabricated by High-Energy Electron-Beam Irradiation | 525-534A | |
| Interfacial Segregation and Influence of Antiphase Boundaries on Raising in a γ/γ' Alloy | 733-740A | |
| Evolution of Secondary Phases in Cr-V Low-Alloy Steels during Aging | 751-759A | |
| Low-Cycle Fatigue Behavior of ULTIMET Alloy | 785-796A | |
| Hydrogen Trap States in Ultrahigh-Strength AEPMET 100 Steel | 849-864A | |
| Correlation of Microstructure with Hardness and Wear Resistance in (TiC,SiC)/Stainless Steel Surface Composites Fabricated by High-Energy Electron-Beam Irradiation | 1029-1038A | |
| Phase Equilibrium and Distribution of Minor Elements between Ni-S Melt and Al ₂ O ₃ -CaO-MgO Slag at 1873 K | 1041-1049B | |
| Effect of Clustering of Precipitates on Grain Growth | 1097-1103A | |
| Some Studies on the Thermal-Expansion Behavior of C-Fiber, SiC _p , and In-Situ Mg ₂ Si-Reinforced AZ31 Mg Alloy-Based Hybrid Composites | 1167-1176A | |
| Coupled-Solute Drag Effects on Ferrite Formation in Fe-C-X Systems | 1187-1210A | |
| Molybdenum Accumulation at Ferrite/Austenite Interfaces during Isothermal Transformation of an Fe-0.24 Pct C-0.93 Pct Mo Alloy | 1223-1235A | |
| Studies of the Influence of Alloying Elements on the Growth of Ferrite from Austenite under Decarburization Conditions: Fe-C-Ni Alloys | 1237-1242A | |
| Effect of Carbon Concentration on Precipitation Behavior of M23C6 Carbides and MX Carbonitrides in Martensitic 9Cr Steel during Heat Treatment | 1255-1262A | |
| Fine Carbide-Strengthened 3Cr-3WVtA Bainitic Steel | 1281-1288A | |
| Microstructural Banding and Failure of a Stainless Steel | 1317-1324A | |
| Microstructural Evolution in the Heat-Affected Zone of a Friction Stir Weld | 1487-1499A | |
| Mechanism of Primary MC Carbide Decomposition in Ni-Based Superalloys | 1669-1679A | |
| The Influences of Multiscale-Sized Second-Phase Particles on Ductility of Aged Aluminum Alloys | 1725-1734A | |
| Thermomechanical Fatigue Behavior of the Third-Generation, Single-Crystal Superalloy TMS-75: Deformation Structure | 1779-1787A | |
| Communication: Strengthening by γ/γ' Interfacial Dislocation Networks in TMS-162-Toward a Fifth-Generation Single-Crystal Superalloy | 1911-1914A | |
| Multiscale Structure and Properties of Cast and Deformation Processed Polycrystalline NiTi Shape-Memory Alloys | 2013-2025A | |
| Oxide Defects in a Vacuum Investment-Cast Ni-Based Turbine Blade | 2063-2071A | |
| Microstructures of a Powder Metallurgy--Hot-Isostatically Pressed Super Duplex Stainless Steel Forming in Industrial Heat Treatments | 2103-2109A | |
| Comparison of Microstructural Evolution in Laser-Deposited and Arc-Melted In-Situ Ti-TiB Composites | 2143-2152A | |
| Validation of Predicted Precipitate Compositions in Al-Si-Ge | 2305-2311A | |
| Characterization of the Nucleation and Growth Behavior of Copper Precipitates in Low-Carbon Steels | 2323-2329A | |
| Microstructure and mechanical properties of a 2000 MPa Co-fiber maraging steel after aging at 753 K | 2747-2755A | |
| Carbides in high-speed steels containing silicon | 2757-2766A | |
| Characterization of the peritectic reaction in medium-alloy steel through microsegregation and heat-of-transformation studies | 2869-2879A | |
| Communication: Evaluation of aging precipitation kinetics and potential in aluminum alloys using indiscriminately integrated peak areas in calorimetry curves | 3012-3015A | |
| Coarsening Behavior of Ni ₃ Ga Precipitates in Ni-Ga Alloys: Dependence of Microstructure and Kinetics on Volume Fraction | 3063-3069A | |
| Effects of Temperature and Strain Rate on Tensile Properties and Activation Energy for Dynamic Strain Aging in Alloy 625 | 3129-3139A | |
| The Nitriding Kinetics of Iron-Chromium Alloys; The Role of Excess Nitrogen: Experiments and Modelling | 3387-3398A | |
| Double Loop Electrochemical Potentiokinetic Reactivation Test Optimization in Checking of Duplex Stainless Steel Intergranular Corrosion Susceptibility | 3499-3513A | |
| Mechanisms of Hf Dopant Incorporation during the Early Stage of Chemical Vapor Deposition Aluminide Coating Growth under Continuous Doping Conditions | 3581-3593A | |
| Effect of Sn on Microstructure and Mechanical Properties of Ti-Base Dendrite/Ultrafine-Structured Multicomponent Alloys | 3605-3612A | |
| Characterization of Retrogression and Reaging Behavior of 8090 Al-Li-Cu-Mg-Zr Alloy | 3681-3691A | |
| Role of Carbon and Alloying Elements in the Formation of Bainitic Ferrite | 3693-3700A | |
| Microstructure Characterization and Creep Deformation of an Al-10 Wt Pct Ti-2 Wt Pct Cu Nanocomposite | 3855-3861A | |
| Precipitation hardening | | |
| Effect of Aging and Deformation on the Microstructure and Properties of Fe-Ni-Ti Maraging Steel | 973-983A | |
| Cu Precipitation in a Prestrained Fe-1.5 Wt Pct Cu Alloy during Isothermal Aging | 1263-1272A | |
| Precipitate Microstructures and Resulting Properties of Al-Zn-Mg Metal Inert Gas-Weld Heat-Affected Zones | 1437-1448A | |
| Influence of Microstructure on Tensile and Creep Properties of a New Castable TiAl-Based Alloy | 2087-2102A | |
| Communication: Quantification of Overaging Hardening Kinetics of Aluminum Alloys | 2172-2174A | |
| Modeling the Age-Hardening Behavior of Al-Si-Cu Alloys | 2407-2418A | |
| Ductility Exhaustion Mechanisms in Thermally Exposed Thin | | |

- Sheets of a Near- β Titanium Alloy 3113-3127A
- Precipitation hardening alloys**
Theoretical and Practical Implications of Creep Curve Shape Analyses for 2124 and 2419. 1691-1701A
- Precipitation hardening steels**
Communication: High-temperature fatigue crack growth behavior of 17-4 PH stainless steels. 3018-3024A
- Precipitation hardening steels, Powder technology**
Simulation of the Sintering Densification and Shrinkage Behavior of Powder-Injection-Molded 17-4 PH Stainless Steel. 257-263A
- Precursors**
Fabrication of Foamable Precursors by Powder Compression and Induction Heating Process. 769-776B
- Preferred orientation**
Effect of Reinforcement-Particle-Orientation Anisotropy on the Tensile and Fatigue Behavior of Metal-Matrix Composites. 53-61A
Effects of Heat Treatment and Testing Temperature on Fracture Mechanics Behavior of Low-Si CA-15 Stainless Steel. 471-480A
Deformation and Damage Mechanisms of Zinc Coatings on Hot-Dip Galvanized Steel Sheets: Part II. Damage Modes. 813-823A
Tensile behavior of friction-stir-welded A356-T6/Al 6061-T651 Bi-alloy plate. 2837-2843A
Crystallographic textures in rolled and annealed Fe-Ga and Fe-Al alloys. 2963-2970A
The Solidification of Undercooled Melts via Twinned Dendritic Growth. 3211-3220A
Neutron Diffraction Study of Texture Development during Hot Working of Different Gamma-Titanium Aluminide Alloys. 3563-3570A
- Pressure vessels**
Hydrogen-Involved Tensile and Cyclic Deformation Behavior of Low-Alloy Pressure Vessel Steel. 1477-1486A
- Pressurized water reactors**
Role of Temperature and Strain Rate on the Hydrogen-Induced Intergranular Rupture in Alloy 600. 457-464A
- Prestraining**
Mechanisms of Strain Accumulation and Damage Development during Creep of Prestrained 316 Stainless Steels. 563-571A
Cu Precipitation in a Prestrained Fe-1.5 Wt Pct Cu Alloy during Isothermal Aging. 1263-1272A
The influence of explosive-driven 'Taylor-wave' shock prestraining on the structure/property behavior of 304 stainless steel. 2617-2624A
- Process control**
Model-Based Melt Rate Control during Vacuum Arc Remelting of Alloy 718. 101-113B
- Process parameters**
Mechanism of Titanium Sponge Formation in the Kroll Reduction Reactor. 65-74B
Process Efficiency Measurements in the Laser Engineered Net Shaping Process. 143-152B
Determination of Interfacial Heat-Transfer Boundary Conditions in an Aluminum Low-Pressure Permanent Mold Test Casting. 299-311B
Freeze-Off Limits in Transient Liquid-Phase Infiltration. 641-653A
Simulation of Die Filling for the Wax Injection Process: Part 1. Models for Material Behavior. 755-759B
Effect of Surface Modification of High-Density Polyethylene by Direct Current and Radio Frequency Glow Discharge on Wetting and Adhesion Characteristics. 865-877A
The Cut-Groove Technique to Infer Interfacial Effects during Hot Rolling. 1087-1095A
Finite element method simulation of mushy zone behavior during direct-chill casting of an Al-4.5 pct Cu alloy. 2917-2926A
Effects of Alloy Composition and Casting Speed on Structure Formation and Hot Tearing during Direct-Chill Casting of Al-Cu Alloys. 3551-3561A
Development and Validation of a Thermal Model of the Direct Chill Casting of AZ31 Magnesium Billets. 3843-3854A
- Propellers, Mechanical properties**
Communication: Cavitation Erosion Characteristics of a NiTi Alloy. 356-362A
- Protective coatings**
Intermetallic Diffusion Coatings for Enhanced Hot-Salt Oxidation Resistance of Nitrogen-Containing Austenitic Stainless Steels. 1799-1806A
Effect of Thermal Spray on the Microstructure and Adhesive Strength of High Velocity Oxy-Fuel-Sprayed Ni-Cr Coatings on 9Cr-1Mo Steel. 3187-3199A
Effect of Ternary Additions on the Structure and Properties of Coatings Produced by a High Aluminum Galvanizing Bath. 3707-3720A
- Pseudoelasticity**
Communication: Cavitation Erosion Characteristics of a NiTi Alloy. 356-362A
- Pulsed arc welding**
Control of Residual Stresses Affecting Fatigue Life of Pulsed Current Gas-Metal-Arc Weld of High-Strength Aluminum Alloy. 2439-2444A
The Microstructural Response of Delta-Stabilized Plutonium to Pulsed Laser Welding. 2445-2454A
- Pulsed current**
Numerical Analysis of Metal Transfer in Gas Metal Arc Welding under Modified Pulsed Current Conditions. 857-866B
- Pyrite**
Critical Thermodynamic Assessment and Modeling of the Fe-Ni-S System. 897-907B
- Pyrolysis**
Lubricant Pyrolysis during Sintering of Powder Metallurgy Compacts. 381-392B
- Pyrrhotite**
Critical Thermodynamic Assessment and Modeling of the Fe-Ni-S System. 897-907B
- Quantitative analysis**
Thermal-Imaging Technologies for Detecting Damage during High-Cycle Fatigue. 15-23A
Formation of Mesoscale Roughening in 6022-T4 Al Sheets Deformed in Plane-Strain Tension. 513-524A
- Quantitative metallography**
Determination of Isothermal Transformation Diagrams for Sigma-Phase Formation in Cast Duplex Stainless Steels CD3MN and CD3MWCuN. 3377-3386A
- Quartz**
Reaction Sequences in the Formation of Silico-Ferrites of Calcium and Aluminum in Iron Ore Sinter. 929-936B
- Quaternary systems**
Experimental Study of Phase Equilibria in the Al-Fe-Zn-O System in Air. 633-642B
An Experimental and Theoretical Analysis of the Phase Equilibria in the Fe-Cr-VC System. 3649-3663A
- Quenching**
Communication: Room-Temperature Cleavage Fracture of FeMnAlC Steels. 3863-3866A
- Quenching (cooling)**
Freeze-Off Limits in Transient Liquid-Phase Infiltration. 641-653A
- Quenching and tempering**
Quench Embrittlement of Hardened 5160 Steel as a Function of Austenitizing Temperature. 153-162A
Characteristics of the Rough-Cut Surface of Quenched and Tempered Martensitic Stainless Steel Using Wire Electrical Discharge Machining. 1351-1357A
- Radiation damage**
Communication: Grain Boundary Engineering of Ferritic-Martensitic Alloy T91. 717-718A
Experimental and Theoretical Evidence for Carbon-Vacancy Binding in Austenite. 2239-2245A
Effects of Simultaneous Displacive and Ionizing Radiations and of Electric Field on Radiation Damage in Ionic Crystals. 2257-2266A
- Rapid quenching (metallurgy)**
Experimental Determination of Solid-Liquid Interfacial Energy for Zn Solid Solution in Equilibrium with the Zn-Al Eutectic Liquid. 3665-3672A
- Rapid solidification**
Dispersion Strengthening in a Hypereutectic Al-Si Alloy Prepared by Extrusion of Rapidly Solidified Powder. 333-339A
Room-temperature tensile and high-cycle-fatigue strength of fine TiB particulate-reinforced Ti-22Al-27Nb composites. 2971-2979A
- Rare earth metals**
Rare Earth Extraction from Bastnaesite Concentrate by Stepwise Carbochlorination-Chemical Vapor Transport-Oxidation. 217-221B
- Raw materials**
Communication: Structural Change of Mechanically Activated Molybdenite and the Effect of Mechanical Activation on Molybdenite. 1203-1207B
- Rayleigh number**
Mushy-zone Rayleigh number to describe macrosegregation and channel segregate formation during directional solidification of metallic alloys. 2927-2934A
- Reaction kinetics**
Recrystallization Behavior of a Heavily Cold-Rolled Ni₃Al (B,Zr) Alloy. 71-81A
Study of the Austempering Transformation Kinetics in Compacted Graphite Cast Irons. 103-110A
Continuous Oxygen Steelmaking with Copper-, Tin-, and Zinc-Contaminated Scrap. 663-674B
Reduction of Cobalt Oxide With Methane. 825-828B
Study on Polychlorinated Dibenzo-p-Dioxin/Furan Formation in Iron Ore Sintering Process. 983-991B
Kinetics of Gold(III) Chloride Complex Reduction Using Sulfur(IV). 1071-1085B
Preparation of Cu-Ni Alloys through a New Chemical Route. 1107-1112B
Intermetallic Diffusion Coatings for Enhanced Hot-Salt Oxidation Resistance of Nitrogen-Containing Austenitic Stainless Steels. 1799-1806A
Infrared Brazing Cu and Ti Using a 95Ag-5Al Braze Alloy. 3177-3186A
The Nitriding Kinetics of Iron-Chromium Alloys: The Role of Excess Nitrogen: Experiments and Modelling. 3387-3398A
- Reaction mechanisms**
Mechanism of Titanium Sponge Formation in the Kroll Reduction Reactor. 65-74B
Lubricant Pyrolysis during Sintering of Powder Metallurgy Compacts. 381-392B
Microreaction Mechanism in Reduction of Magnetite to Wustite. 517-522B
Mechanism and Rate of Reaction of Al₂O₃, Al, and CO Vapors with Carbon. 617-623B
Reaction Sequences in the Formation of Silico-Ferrites of Calcium and Aluminum in Iron Ore Sinter. 929-936B
Kinetics of Gold(III) Chloride Complex Reduction Using Sulfur(IV). 1071-1085B
- Reactivity**
Communication: Phase Equilibria of the Al₂O₃-CaF₂-FeO_n System. 181-182B
- Reactors**
Fluid Flows in Metallurgy - Friend or Foe? 417-437B
- Recovering**
Condensation of Zinc Vapor on Solid Media in Zn (g)-CO-CO₂.

- Ar Mixtures.**
Metal Vapor Treatment for Enhancing the Dissolution of Platinum Group Metals from Automotive Catalyst Scrap
Nanoparticle Recovery Using a Furnace Collector Comprised of Carbonized Refuse-Derived Fuel
Salt Roasting of Suncor Oil Sands Fly Ash
- Recrystallization**
Deformation Behavior of Zr_3Al-Nb Alloys I: Room-Temperature and High-Temperature Deformation Study.
Damage Repair in CMSX-4 Alloy without Fatigue Life Reduction Penalty.
The Tensile Response of a Fine-Grained AA5754 Alloy Produced by Asymmetric Rolling and Annealing.
Monte Carlo-Method Simulation of the Deformation-Induced Ferrite Transformation in the Fe-C System.
Multiscale Structure and Properties of Cast and Deformation Processed Polycrystalline NiTi Shape-Memory Alloys.
Study of the Ni41.3Ti38.7Nb20 wide transformation hysteresis shape-memory alloy.
Microstructure evolution and mechanical behavior of bulk copper obtained by consolidation of micro- and nanopowders using equal-channel angular extrusion.
Microindentation of Aluminum
Effect of Initial Grain Size of Austenite on Hot-Deformed Structure of Ni-30Fe Alloy
- Recrystallization**
Recrystallization Behavior of a Heavily Cold-Rolled Ni₃Al (B,Zr) Alloy.
Microstructure Transformation from Lamellar to Equiaxed Microduplex through Equal-Channel Angular Pressing in an Al-33 Pct Cu Eutectic Alloy.
Microstructural Characterization of Secondary-Phase Particles in a Hot-Deformed Al-Cu-Mg-Zr Alloy.
A Study of Coarsening, Recrystallization, and Morphology of Microstructure in Al-Sc-(Zr)-(Mg) Alloys.
Kinetics of Chlorination of Tantalum Pentoxide in Mixture with Sucrose Carbon by Chlorine Gas.
Effects of Partial Recrystallization on High-Cycle Fatigue Deformation and Crack Generation of a Nitrogen-Strengthened 32Mn-7Cr Austenitic Steel at Liquid-Nitrogen Temperature.
Fiber Texture and Substructural Features in the Caliber-Rolled Low-Carbon Steels.
A Single-Grain Approach Applied to the Modeling of Recrystallization Kinetics for Cold-Rolled Single-Phase Metals.
Deformation and Damage Mechanisms of Zinc Coatings on Hot-Dip Galvanized Steel Sheets: Part II. Damage Modes.
High-Strain-Rate Superplastic Behavior of Equal-Channel Angular-Pressed 5083 Al-0.2 Wt Pct Sc.
Monte Carlo-Method Simulation of the Deformation-Induced Ferrite Transformation in the Fe-C System.
Effect of Thermomechanical Treatment on the Evolution of Rolling and Recrystallization Textures in Twin-Belt Cast AA5754 Aluminum Alloy.
A Metallurgical Interpretation of the Static Recrystallization Kinetics of an Intercritically Deformed C-Mn Steel.
Multiscale Structure and Properties of Cast and Deformation Processed Polycrystalline NiTi Shape-Memory Alloys.
Shear localization-martensitic transformation interactions in Fe-Cr-Ni monocrystal.
Effect of low-temperature shock compression on the microstructure and strength of copper.
Communication: Effect of texture and microstructure on resistance to cracking of high-strength hot-rolled Nb-Ti microalloyed steels.
Austenite Formation during Intercritical Annealing
Quantitative Analysis of Texture Evolution of Cold-Rolled Direct-Chill-Cast and Continuous-Cast AA5052 and AA5182 Aluminum Alloys during Isothermal Annealing
- Reducing atmospheres**
Effect of the Presence of Alloying Elements in Interstitial-Free and Low-Carbon Steels on Their Surface Composition after Annealing in Reducing Atmospheres (Dew Point = -30 °C).
- Reduction**
Reduction of Cobalt Oxide With Methane
Blast Furnace Burden Softening and Melting Phenomena: Part I. Pellet Bulk Interaction Observation
Kinetics of Gold(III) Chloride Complex Reduction Using Sulfur(IV)
- Reduction (chemical)**
Solid-State Reduction of Chromium Oxide by Methane-Containing Gas.
Mechanism and Rate of Reaction of Al₂O₃, Al, and CO Vapors with Carbon.
- Refining**
Communication: A Model for Estimating Exposed Plume Eye Area in Steel Refining Ladles Covered with Thin Slag.
Spot Turbulence, Breakup, and Coalescence of Bubbles Released from a Porous Plug Injector into a Gas-Stirred Ladle
The Effect of Carbon in Slag on Steel Reoxidation and Carbon Analysis by X-Ray Photoelectron Spectroscopy in the CaO-SiO₂-Al₂O₃-MgO-MnO-FeO System
- Refractories**
Continuous Oxygen Steelmaking with Copper-, Tin-, and Zinc-Contaminated Scrap.
- Remanence**
Ferromagnetic Properties of Deformation-Induced Martensite Transformation in AISI 304 Stainless Steel.
- Residual stress**
Phase Transformations and Control of Residual Stresses in Thick Spray-Formed Steel Shells
Fracture Toughness of Selectively Reinforced Al2124 Alloy: Precrack Tip in the Composite Side.
Characterization and Modeling of Quenching-Induced Residual Stresses in the Nickel-Based Superalloy IN718.
Residual Stresses in High Velocity Oxy-Fuel Metallic Coatings. The Influence of a Martensitic Phase Transformation on Stress Development in Thermal Barrier Coating Systems.
Effects of Changes in Test Temperature on Fatigue Crack Propagation of Al6090/SiCp-Al 6013 Laminated Metal Composites.
Control of Residual Stresses Affecting Fatigue Life of Pulsed Current Gas-Metal-Arc Weld of High-Strength Aluminum Alloy.
Plastic deformation behavior of aluminum casting alloys A356/357.
A Through-Process Model of an A356 Brake Caliper for Fatigue Life Prediction
Residual Stress-Affected Diffusion during Plasma Nitriding of Tool Steels
- Resistance spot welding**
Electrode Pitting in Resistance Spot Welding of Aluminum Alloy 5182.
- Resistance welding**
Mechanism of Resistance Microwelding of Crossed Fine Nickel Wires
- Retained austenite**
Effect of Microstructure on the Stability of Retained Austenite in Transformation-Induced-Plasticity Steels.
- Rheocasting**
Yield Behavior of Commercial Al-Si Alloys in the Semisolid State
- Rheological properties**
Segregation band formation in Al-Si die castings.
- Rheology**
Simulation of Die Filling for the Wax Injection Process: Part 1. Models for Material Behavior.
- Roasting**
Salt Roasting of Suncor Oil Sands Fly Ash
- Robots**
Phase Transformations and Control of Residual Stresses in Thick Spray-Formed Steel Shells
- Rockwell hardness**
Quality Assessment of Artificially Aged A357 Aluminum Alloy Cast Ingots by Introducing Approximate Expressions of the Quality Index QD
- Rolling**
The Selection of the Spray Deposition Rate during the Spray Rolling Process
Communication: The Transient to Steady-State Transition during the Spray-Rolling Process
- Rolling direction**
Tensile Anisotropy in Cu-Ni-Mn-Sn-Al Alloys.
Formation of Mesoscale Roughening in 6022-T4 Al Sheets Deformed in Plane-Strain Tension.
Fiber Texture and Substructural Features in the Caliber-Rolled Low-Carbon Steels.
Crystallographic textures in rolled and annealed Fe-Ga and Fe-Al alloys.
Inclusion-Controlled Fatigue Properties of 1800 MPA-Class Spring Steels
- Rolling texture**
Quantitative Analysis of Texture Evolution in Cold-Rolled, Continuous-Cast AA 5xxx-Series Aluminum Alloys.
Ferromagnetic Properties of Deformation-Induced Martensite Transformation in AISI 304 Stainless Steel.
Effect of Thermomechanical Treatment on the Evolution of Rolling and Recrystallization Textures in Twin-Belt Cast AA5754 Aluminum Alloy.
- Roughness**
Communication: The Contact Angle between Liquid Iron and a Single-Crystal Magnesium Oxide Substrate at 1873 K.
Effect of Broaching on High-Temperature Fatigue Behavior in Notched Specimens of INCONEL 718.
Assessment of the Origin of Porosity in Electron-Beam-Welded TA6V Plates.
Residual Stress-Affected Diffusion during Plasma Nitriding of Tool Steels
- Rupturing**
Theoretical and Practical Implications of Creep Curve Shape Analyses for 2124 and 2419.
- S-N diagrams**
Effects of Temperature and Shot Peening on S-N Behavior of a PM Ni-Base Superalloy UDIMET 720.
Fatigue of Cold-Work Tool Steels: Effect of Heat Treatment and Carbide Morphology on Fatigue Crack Formation, Life, and Fracture Surface Observations.
- Sands**
Salt Roasting of Suncor Oil Sands Fly Ash
- Scale (corrosion)**
The Effect of Surface Deformation on Lubrication and Oxide-Scale Fracture in Cold Metal Rolling
Effects of an α -Al₂O₃ Thin Film on the Oxidation Behavior of a Single-Crystal Ni-Based Superalloy.
Intermetallic Diffusion Coatings for Enhanced Hot-Salt Oxida-

- tion Resistance of Nitrogen-Containing Austenitic Stainless Steels. 1799-1806A
- Effect of Thermal Spray on the Microstructure and Adhesive Strength of High Velocity Oxy-Fuel-Sprayed Ni-Cr Coatings on 9Cr-1Mo Steel. 3187-3199A
- Scandium, Alloying additive**
A Study of Coarsening, Recrystallization, and Morphology of Microstructure in Al-Sc-(Zr)-(Mg) Alloys. 341-350A
- Scandium, Thermal properties**
Partial Atomic Volume and Partial Molar Enthalpy of Formation of the 3d Metals in the Palladium-Based Solid Solutions. 63-70A
- Scrap**
Fluid Flows in Metallurgy - Friend or Foe? 417-437B
- Secondary hardening**
Effect of Aging and Deformation on the Microstructure and Properties of Fe-Ni-Ti Maraging Steel. 973-983A
- Sedimentation**
The Solidification Characteristics of Fe-Rich Intermetallics in Al-11.5Si-0.4Mg Cast Alloys. 1425-1435A
- Segregations**
Analytical, Numerical, and Experimental Analysis of Inverse Macrosegregation during Upward Unidirectional Solidification of Al-Cu Alloys. 285-297B
Communication: Discussion of "Precipitation of Austenite Particles at Grain Boundaries during Aging of Fe-Mn-Ni Steel". Communication: Authors' Reply. 352-355A
A Model for Ferrite/Pearlite Band Formation and Prevention in Steels. 355-356A
Role of Temperature and Strain Rate on the Hydrogen-Induced Intergranular Rupture in Alloy 600. 425-433A
Interfacial Segregation and Influence of Antiphase Boundaries on Rafting in a γ/γ' Alloy. 457-464A
Channel Segregation during Solidification and the Effects of an Alternating Traveling Magnetic Field. 733-740A
The Role of Particle Size on the Laser Sintering of Iron Powder Effect of Grain-Boundary Characteristics on Castability of Nickel-Base Superalloys. 743-754B
The Rotary Kiln: An Investigation of Bed Heat Transfer in the Transverse Plane. 937-948B
Molybdenum Accumulation at Ferrite/Austenite Interfaces during Isothermal Transformation of an Fe-0.24 Pct C-0.93 Pct Mo Alloy. 939-946A
Interaction of Porosity with a Planar Solid/Liquid Interface. Microstructural Evolution in Laser-Deposited Multilayer Ti-6Al-4V Builds: Part I. Microstructural Characterization. 1059-1070B
Quantitative Characterization of the Three-Dimensional Microstructure of Polycrystalline Al-Sn using X-Ray Microtomography. 1223-1235A
Effect of the Presence of Alloying Elements in Interstitial-Free and Low-Carbon Steels on Their Surface Composition after Annealing in Reducing Atmospheres (Dew Point = -30 °C). 1525-1538A
Characterization of the peritectic reaction in medium-alloy steel through microsegregation and heat-of-transformation studies. 1861-1867A
Segregation band formation in Al-Si die castings. 1953-1961A
Mushy-zone Rayleigh number to describe macrosegregation and channel segregate formation during directional solidification of metallic alloys. 2039-2050A
Self-propagating synthesis. 2869-2879A
Nickel-Aluminides/Steel Clad Pipe Fabricated by Reactive Centrifugal Casting Method from Liquid Aluminum and Solid Nickel. 2881-2891A
Semiconductors. 2927-2934A
Defect Structures in Cosputtered Thin Films of Transition Metal Disilicides with C11b, C40 and C54 Structures. 1517-1524A
Semipermanent mold casting. 2229-2238A
Determination of Interfacial Heat-Transfer Boundary Conditions in an Aluminum Low-Pressure Permanent Mold Test Casting. 299-311B
Semisolids. 1187-1202B
Yield Behavior of Commercial Al-Si Alloys in the Semisolid State
Sensitizing. 3499-3513A
Double Loop Electrochemical Potentiokinetic Reactivation Test Optimization in Checking of Duplex Stainless Steel Intergranular Corrosion Susceptibility
Serrated yielding. 25-35A
Quantifying Thermomechanical Fatigue of Light-Metal-Matrix Composites by Mechanical Spectroscopy.
Settling. 839-845B
Nickel Droplet Settling Behavior in an Electric Furnace
Shape memory. 111-119A
Grain-Size Effect on Shape-Memory Behavior of $Ti_{35}Ni_{49}Zr_{15.4}$ Thin Films. 761-770A
Shape Memory Properties of Ni-Ti Based Melt-Spun Ribbons.
Shape memory alloys. 1403-1406A
Communication: Observed Dependencies of the Large Thermal-Compressive Response of a NiTi Shape-Memory Alloy Fiber Aluminum Metal Matrix Composite on Maximum Tensile Strain Imposed during a Preceding Room-Temperature Tensile Process.
Multiscale Structure and Properties of Cast and Deformation Processed Polycrystalline NiTi Shape-Memory Alloys. 2013-2025A
Study of the Ni_{41.3}Ti_{38.7}Nb₂₀ wide transformation hysteresis shape-memory alloy. 2783-2788A
Shape memory alloys, Mechanical properties. 356-362A
Communication: Cavitation Erosion Characteristics of a NiTi Alloy.
- Shaped charges**
Analysis of intergranular impurity concentration and the effects on the ductility of copper-shaped charge jets. 2567-2573A
- Shaping**
Process Efficiency Measurements in the Laser Engineered Net Shaping Process. 143-152B
Fabrication of Carbide-Particle-Reinforced Titanium Aluminide-Matrix Composites by Laser-Engineered Net Shaping. 1133-1140A
- Shear**
Grain-size dependence of the flow stress of Cu from millimeters to nanometers. 2681-2696A
- Shear deformation**
Shear localization-martensitic transformation interactions in Fe-Cr-Ni monocrystal. 2575-2586A
Defect Structures and Room Temperature Mechanical Properties of C15 Laves Phases in Zr-Nb-Cr and Zr-Hf-Cr Alloy Systems. 3469-3476A
- Shear modulus**
Quantifying Thermomechanical Fatigue of Light-Metal-Matrix Composites by Mechanical Spectroscopy. 25-35A
- Shear properties**
Semi-Solid Rapid Compression Testing of Spray-Formed Hypereutectic Al-Si Alloys. 899-910A
- Shear strength**
Atomic force microscopy studies of fracture surfaces of composition B energetic materials. 2675-2079A
Infrared Brazing Cu and Ti Using a 95Ag-5Al Braze Alloy. 3177-3186A
- Shear stress**
Fiber Texture and Substructural Features in the Caliber-Rolled Low-Carbon Steels. 665-677A
Modeling of Laser Cladding with Powder Injection. 1139-1150B
Laser-induced shock compression of copper: orientation and pressure decay effects. 2633-2646A
Dynamic Deformation Behavior and Ballistic Impact Properties of Ti-6Al-4V Alloy Having Equiaxed and Bimodal Microstructures. 3103-3112A
- Shear tests**
The Effect of Temperature, Matrix Alloying and Substrate Coatings on Wettability and Shear Strength of Al/Al₂O₃ Couples. On the Isotropy of the Dynamic Mechanical and Failure Properties of Swaged Tungsten Heavy Alloys. 911-923A
3787-3795A
- Shearing**
Influence of Convection on Feathery Grain Formation in Aluminum Alloys. 2495-2501A
Grain-size dependence of the flow stress of Cu from millimeters to nanometers. 2681-2696A
- Sheet metal**
Ductility Exhaustion Mechanisms in Thermally Exposed Thin Sheets of a Near- β Titanium Alloy. 3113-3127A
Formability and Strength of Friction-Stir-Welded Aluminum Sheets. 3461-3468A
- Shells**
Phase Transformations and Control of Residual Stresses in Thick Spray-Formed Steel Shells. 1113-1122B
- Shock loading**
Effect of microstructural length scales on spall behavior of copper. 2663-2673A
Effect of low-temperature shock compression on the microstructure and strength of copper. 2729-2739A
- Shock wave propagation**
Nanoscale view of shock-wave splitting in diamond. 2647-2650A
- Shock waves**
The influence of explosive-driven 'Taylor-wave' shock pre-straining on the structure/property behavior of 304 stainless steel. 2617-2624A
- Short fibers**
Study of the Porosity Produced in an Aluminum Alloy Matrix Composite Due to a T6 Heat Treatment. 2503-2510A
- Short range order**
The Effect of Temperature and Extrusion Speed on The Consolidation of Zirconium-Based Metallic Glass Powder Using Equal-Channel Angular Extrusion. 247-256A
Interfacial Segregation and Influence of Antiphase Boundaries on Rafting in a γ/γ' Alloy. 733-740A
Critical Thermodynamic Assessment and Modeling of the Fe-Ni-S System. 897-907B
- Shot peening**
Effects of Temperature and Shot Peening on S-N Behavior of a PM Ni-Base Superalloy UDIMET 720. 1007-1016A
- Shrinkage**
Simulation of the Sintering Densification and Shrinkage Behavior of Powder-Injection-Molded 17-4 PH Stainless Steel. 257-263A
A Numerical Analysis of Intergranular Penny-Shaped Microcrack Shrinkage Controlled by Coupled Surface and Interface Diffusion. 1301-1309A
Grain Refinement of Superalloy IN718C by the Addition of Inoculants. 2111-2114A
- Sigma phase**
Microstructures of a Powder Metallurgy--Hot-Isostatically Pressed Super Duplex Stainless Steel Forming in Industrial Heat Treatments. 2103-2109A
Determination of Isothermal Transformation Diagrams for Sigma-Phase Formation in Cast Duplex Stainless Steels CD3MN and CD3MWCuN. 3377-3386A
Communication: Ferrite Number as a Function of the Larson-Miller Parameter for Austenitic Stainless Steel Weld Metals after

| | | | |
|--|------------|--|------------|
| Creep Testing | 3631-3633A | Single-Crystal Elastic Constants of Fe-15Ni-15Cr Alloy | 3149-3154A |
| Silicon | | Directional Solidification of Large Superalloy Castings with Radiation and Liquid-Metal Cooling: A Comparative Assessment | 3221-3231A |
| Thermodynamic Study of the Effect of Calcium on Removal of Phosphorus from Silicon by Acid Leaching Treatment | 277-284B | Mechanisms of Hf Dopant Incorporation during the Early Stage of Chemical Vapor Deposition Aluminide Coating Growth under Continuous Doping Conditions | 3581-3593A |
| A Thermodynamic Description of the Al-Mn-Si System over the Entire Composition and Temperature Ranges | 1613-1628A | Brass Type Shear Bands and their Influence on Texture Formation | 3775-3786A |
| Carbides in high-speed steels containing silicon | 2757-2766A | | |
| Monosilicide-Disilicide-Silicon Phase Equilibria in the Nickel-Platinum-Silicon and Nickel-Palladium-Silicon Systems | 3053-3061A | | |
| Silicon, Binary systems | | Single crystals, Coating | |
| Correction to Metallurgical and Materials Transactions A, November 2003, vol. 34A, pp. 2690-2693: "Authors Reply" to Discussion of "Eutectic Solidification of Al-Si Alloys" | 959A | Effects of Preheating on Morphological Development of a Chemical Vapor Deposition Aluminide Coating Formed on Single-Crystal Ni-Based Superalloy | 891-897A |
| Erratum: A Solubility Interaction Mechanism for the Columnar-to-Equiaxed Transition in Alloy Solidification | 1915A | Single crystals, Directional solidification | |
| Silicon base alloys, Crystal growth | | Effect of Grain-Boundary Characteristics on Castability of Nickel-Base Superalloys | 939-946A |
| Morphologies of Silicon Crystals Solidified on a Chill Plate | 1067-1073A | Single crystals, Mechanical properties | |
| Silicon carbide | | Damage Repair in CMSX-4 Alloy without Fatigue Life Reduction Penalty | 535-542A |
| Application of the Generalized Method of Cells Principle to Particulate-Reinforced Metal Matrix Composites | 1029-1039B | Single crystals, Oxidation | |
| Solid Particle Erosion of Al Alloy and Al-Alloy Composites: Effect of Heat Treatment and Angle of Impingement | 1369-1379A | Effects of an α -Al ₂ O ₃ Thin Film on the Oxidation Behavior of a Single-Crystal Ni-Based Superalloy | 1055-1065A |
| Creep Behavior of a Rotating Functionally Graded Composite Disc Operating under Thermal Gradient | 1381-1391A | Single crystals, Physical properties | |
| Fracture Toughness of Selectively Reinforced Al2124 Alloy: Precrack Tip in the Composite Side | 1393-1401A | Communication: The Contact Angle between Liquid Iron and a Single-Crystal Magnesium Oxide Substrate at 1873 K | 179-181B |
| Wear Behavior, Microstructure, and Dimensional Stability of As-Cast Zinc-Aluminum/SiC (Metal Matrix Composites) Alloys | 1579-1590A | Sinter (material) | |
| Microstructural Evolution of Preformed SiCp/ZA27 Composites during Partial Remelting | 2073-2085A | Reaction Sequences in the Formation of Silico-Ferrites of Calcium and Aluminum in Iron Ore Sinter | 929-936B |
| Mechanical Properties of Al-60 Pct SiCp Composites Alloyed with Mg | 2127-2141A | Sintered compacts | |
| Communication: A Brick-Wall Model for Calculating Young's Modulus of a Particulate Composite | 2191-2192A | Quantitative Characterization of Microstructures of Liquid-Phase-Sintered Two-Phase Materials | 1881-1888A |
| Effects of Changes in Test Temperature on Fatigue Crack Propagation of Al6090/SiCp-Al 6013 Laminated Metal Composites | 2291-2303A | Sintering | |
| Time-dependent deformation in an enhanced SiC/SiC composite | 2853-2859A | Direct Electrolytic Preparation of Chromium Powder | 223-233B |
| Silicon carbide, Composite materials | | Study on Polychlorinated Dibenzo-p-Dioxin/Furan Formation in Iron Ore Sintering Process | 983-991B |
| Effects of Lamination and Changes in Layer Thickness on Fatigue-Crack Propagation of Lightweight Laminated Metal Composites | 45-52A | Preparation of Cu-Ni Alloys through a New Chemical Route | 1107-1112B |
| Effect of Reinforcement-Particle-Orientation Anisotropy on the Tensile and Fatigue Behavior of Metal-Matrix Composites | 53-61A | Sintering (powder metallurgy) | |
| Correlation of Microstructure and Abrasive and Sliding Wear Resistance of (TiC,SiC)/Ti-6Al-4V Surface Composites Fabricated by High-Energy Electron-Beam Irradiation | 139-151A | Simulation of the Sintering Densification and Shrinkage Behavior of Powder-Injection-Molded 17-4 PH Stainless Steel | 257-263A |
| Correlation of Microstructure with the Hardness and Wear Resistance of (TiC,SiC)/Ti-6Al-4V Surface Composites Fabricated by High-Energy Electron-Beam Irradiation | 525-534A | Lubricant Pyrolysis during Sintering of Powder Metallurgy Compacts | 381-392B |
| Mg AZ80/SiC Composite Bars Fabricated by Infiltration of Porous Ceramic Preforms | 707-715A | Size effects | |
| Correlation of Microstructure with Hardness and Wear Resistance in (TiC,SiC)/Stainless Steel Surface Composites Fabricated by High-Energy Electron-Beam Irradiation | 1029-1038A | The effect of grain size on low-cycle fatigue behavior of Al-2024 polycrystalline alloy | 2725-2728A |
| Some Studies on the Thermal-Expansion Behavior of C-Fiber, SiCp, and In-Situ Mg ₂ Si-Reinforced AZ31 Mg Alloy-Based Hybrid Composites | 1167-1176A | Skull melting | |
| Silicon dioxide, Composite materials | | The Development and Experimental Validation of a Numerical Model of an Induction Skull Melting Furnace | 785-803B |
| Reactive Wetting of SiO ₂ Substrates by Molten Al | 583-588A | Slab casting | |
| Silicon steels, Powder technology | | Dynamics of Coupled and Uncoupled Two-Phase Flows in a Slab Mold | 85-99B |
| Densification of a Powder-Metal Skeleton by Transient Liquid-Phase Infiltration | 631-640A | Mathematical Simulation and Physical Modeling of Unsteady Fluid Flows in a Water Model of a Slab Mold | 449-460B |
| Silver | | Analysis of Thin-Slab Casting, by the Compact-Strip Process: Part I. Heat Extraction and Solidification | 541-560B |
| Nonequilibrium molecular dynamics simulations of metallic friction at Ta/Al and Cu/Ag interfaces | 2741-2745A | Analysis of Thin-Slab Casting by the Compact-Strip Process: Part II. Effect of Operating and Design Parameters on Solidification and Bulging | 561-573B |
| Infrared Brazing Cu and Ti Using a 95Ag-5Al Braze Alloy | 3177-3186A | Study of Transient Flow and Particle Transport in Continuous Steel Caster Molds: Part I. Fluid Flow | 685-702B |
| Communication: Tensile Properties of Chromium Alloyed with Silver | 3329-3331A | Study of Transient Flow and Particle Transport in Continuous Steel Caster Molds: Part II. Particle Transport | 703-714B |
| Simulation | | Slabs | |
| Nickel Droplet Settling Behavior in an Electric Furnace | 839-845B | Physical and Mathematical Determination of the Influence of Input Temperature Changes on the Molten Steel Flow Characteristics in Slab Tundishes | 957-966B |
| Numerical Analysis of Metal Transfer in Gas Metal Arc Welding under Modified Pulsed Current Conditions | 857-866B | Slags | |
| Nanoscale view of shock-wave splitting in diamond | 2647-2650A | The Solubility of Cr ₂ O ₃ in Calcium Ferrite Slags at 1573 K | 197-202B |
| Solute diffusion in liquid nickel measured by pulsed ion beam melting | 2803-2807A | Liquidus Temperatures in Calcium Ferrite Slags in Equilibrium with Molten Copper | 203-215B |
| Single crystals | | Thermodynamic Evaluation and Optimization of the MnO-Al ₂ O ₃ and MnO-Al ₂ O ₃ -SiO ₂ Systems and Applications to Inclusion Engineering | 259-268B |
| Thermomechanical Fatigue Behavior of the Third-Generation, Single-Crystal Superalloy TMS-75: Deformation Structure | 1779-1787A | Amphoteric Behavior of Alumina in Viscous Flow and Structure of CaO-SiO ₂ -(MgO)-Al ₂ O ₃ Slags | 269-275B |
| Communication: Strengthening by γ/γ' Interfacial Dislocation Networks in TMS-162-Toward a Fifth-Generation Single-Crystal Superalloy | 1911-1914A | Communication: A Model for Estimating Exposed Plume Eye Area in Steel Refining Ladles Covered with Thin Slag | 400-404B |
| A Tribute to Terence E. Mitchell | 2203-2205A | Thermal Diffusivity Measurements of Some Synthetic CaO-Al ₂ O ₃ -SiO ₂ Slags | 461-469B |
| Characterization of Surface Deformation around Vickers Indents in Monocrystalline Materials | 2247-2255A | Mechanism and Rate of Reaction of Al ₂ O ₃ , Al, and CO Vapors with Carbon | 617-623B |
| Second-Order Stresses and Strains in Heterogeneous Steels: Self-Consistent Modeling and X-Ray Diffraction Analysis | 2361-2369A | Multicomponent Diffusion in Molten Slags | 675-684B |
| Shear localization-martensitic transformation interactions in Fe-Cr-Ni monocrystal | 2575-2586A | Communication: A Computational Assessment of Viscosity Measurement in Rotating Viscometers through Detailed Numerical Simulation | 805-809B |
| Materials science under extreme conditions of pressure and strain rate | 2587-2607A | Blast Furnace Burden Softening and Melting Phenomena: Part I. Pellet Bulk Interaction Observation | 829-838B |
| Laser-induced shock compression of copper: orientation and pressure decay effects | 2633-2646A | Critical Thermodynamic Evaluation and Optimization of the FeO-Fe ₂ O ₃ -MgO-SiO ₂ System | 877-889B |
| Effect of microstructural length scales on spall behavior of copper | 2663-2673A | Communication: The Pressure of Al ₂ O ₃ and Al in Equilibrium with a Al ₂ O ₃ -Al ₄ C ₃ (Saturated) Slag at 1950°C to 2020°C | 1011-1013B |
| Cyclic deformation behavior and dislocation structure of Ti-2 At. Pct Al single crystals oriented for double prism slip | 2845-2852A | Phase Equilibrium and Distribution of Minor Elements between Ni-S Melt and Al ₂ O ₃ -CaO-MgO Slag at 1873 K | 1041-1049B |
| | | The Effect of Carbon in Slag on Steel Reoxidation and Carbon Analysis by X-Ray Photoelectron Spectroscopy in the CaO-SiO ₂ -Al ₂ O ₃ -MgO-MnO-FeO System | 1087-1095B |
| | | Slags, Reactions (chemical) | |
| | | The Effect of CaF ₂ on Thermodynamics of CaO-CaF ₂ -SiO ₂ (- | |

- MgO Slags.**
Communication: Phase Equilibria of the $\text{Al}_2\text{O}_3\text{-CaF}_2\text{-FeO}_n$ System. 115-120B
- Sliding friction**
Correlation of Microstructure and Abrasive and Sliding Wear Resistance of (TiC,SiC)/Ti-6Al-4V Surface Composites Fabricated by High-Energy Electron-Beam Irradiation. 181-182B
- Nonequilibrium molecular dynamics simulations of metallic friction at Ta/Al and Cu/Ag interfaces. 139-151A
- Slip**
Shear Force Effects on Fretting Fatigue Behavior of Ti-6Al-4V. Effects of Partial Recrystallization on High-Cycle Fatigue Deformation and Crack Generation of a Nitrogen-Strengthened 32Mn-7Cr Austenitic Steel at Liquid-Nitrogen Temperature. 2741-2745A
- Fiber Texture and Substructural Features in the Caliber-Rolled Low-Carbon Steels. 131-138A
- Deformation and Damage Mechanisms of Zinc Coatings on Hot-Dip Galvanized Steel Sheets: Part I. Deformation Modes. 543-553A
- Deformation and Damage Mechanisms of Zinc Coatings on Hot-Dip Galvanized Steel Sheets: Part II. Damage Modes. 665-677A
- The Influence of Texture, Strain Rate, Temperature, and Chemistry on the Mechanical Behavior of Hafnium. 797-811A
- A Tribute to Terence E. Mitchell. 813-823A
- Characterization of Surface Deformation around Vickers Indents in Monocrystalline Materials. 1999-2011A
- Second-Order Stresses and Strains in Heterogeneous Steels: Self-Consistent Modeling and X-Ray Diffraction Analysis. 2203-2205A
- Laser-induced shock compression of copper: orientation and pressure decay effects. 2247-2255A
- A Micromechanical Analysis of the Yielding Behavior of Individual Widmanstätten Colonies of an $\alpha + \beta$ Titanium Alloy. 2361-2369A
- Variability of Large-Crack Fatigue-Crack-Growth Thresholds in Structural Alloys. 2633-2646A
- Microstructure Characterization and Creep Deformation of an Al-10 Wt Pct Ti-2 Wt Pct Cu Nanocomposite. 3409-3422A
- Slip bands**
Recrystallization Behavior of a Heavily Cold-Rolled Ni_3Al (B,Zr) Alloy. 3721-3735A
- In-Situ Observations of Low-Cycle Fatigue Damage in Cast AM60B Magnesium in an Environmental Scanning Electron Microscope. 3855-3861A
- Formation of Mesoscale Roughening in 6022-T4 Al Sheets Deformed in Plane-Strain Tension. 71-81A
- Communications: Ultra-High-Speed Exploding Properties of Ti-6Al-4V Alloy Having Equiaxed and Bimodal Microstructures. 321-331A
- Communication: Resonant Vibration Behavior of an Al-3.8Cu-0.8Li-0.3Mg Alloy. 513-524A
- The Effects of Strain Rate and Welding Current Mode on the Dynamic Impact Behavior of Plasma-Arc-Welded 304L Stainless Steel Weldments. 719-724A
- Effect of Thermomechanical Treatment on the Evolution of Rolling and Recrystallization Textures in Twin-Belt Cast AA5754 Aluminum Alloy. 952-957A
- Shear localization-martensitic transformation interactions in Fe-Cr-Ni monocrystal. 1501-1515A
- High-pressure, laser-driven deformation of an aluminum alloy. The effect of grain size on low-cycle fatigue behavior of Al-2024 polycrystalline alloy. 2575-2586A
- Dynamic Deformation Behavior and Ballistic Impact Properties of Ti-6Al-4V Alloy Having Equiaxed and Bimodal Microstructures. 2625-2631A
- Deformation and Failure of Zr57Nb5Al10Cu15.4Ni12.6/W Particle Composites Under Quasi-Static and Dynamic Compression. 2725-2728A
- In-Situ Microfracture Observation of Strip-Cast Zr-Ti-Cu-Ni-Be Bulk Metallic Glass Alloys. 3103-3112A
- Brass Type Shear Bands and their Influence on Texture Formation. 3439-3444A
- Slip casting**
Direct Electrolytic Preparation of Chromium Powder. 3753-3761A
- Slip planes**
Grain-size dependence of the flow stress of Cu from millimeters to nanometers. 3775-3786A
- Cyclic deformation behavior and dislocation structure of Ti-2 At. Pct Al single crystals oriented for double prism slip. 2681-2696A
- A Micromechanical Analysis of the Yielding Behavior of Individual Widmanstätten Colonies of an $\alpha + \beta$ Titanium Alloy. 2845-2852A
- Effect of Boron on the Low-Cycle Fatigue Behavior and Deformation Structure of INCONEL 718 at 650°C. 3409-3422A
- Brass Type Shear Bands and their Influence on Texture Formation. 3477-3487A
- Slurries**
Yield Behavior of Commercial Al-Si Alloys in the Semisolid State. 3775-3786A
- Smelting**
The Solubility of Cr_2O_3 in Calcium Ferrite Slags at 1573 K. 1187-1202B
- Sotening**
Deformation and Recrystallization Behavior during Hot Working of a Coarse-Grain, Nickel-Base Superalloy Ingot Material. Blast Furnace Burden Softening and Melting Phenomena: Part I. Pellet Bulk Interaction Observation. 679-693A
- Effects of Temperature and Shot Peening on S-N Behavior of a PM Ni-Base Superalloy UDIMET 720. 829-838B
- Hydrogen-Involved Tensile and Cyclic Deformation Behavior of Low-Alloy Pressure Vessel Steel. 1007-1016A
- Microstructural Evolution in the Heat-Affected Zone of a Friction Stir Weld. 1477-1486A
- Effects of Martensite Morphology and Tempering on Dynamic Deformation Behavior of Dual-Phase Steels. 1487-1499A
- 2371-2382A
- Grain-size dependence of the flow stress of Cu from millimeters to nanometers. 2681-2696A
- A novel observation of strain-induced ferrite-to-austenite retransformation after intercritical deformation of C-Mn steel. Cyclic deformation behavior and dislocation structure of Ti-2 At. Pct Al single crystals oriented for double prism slip. 2789-2797A
- Microstructure evolution and mechanical behavior of bulk copper obtained by consolidation of micro- and nanopowders using equal-channel angular extrusion. 2845-2852A
- Deformation and Failure of Zr57Nb5Al10Cu15.4Ni12.6/W Particle Composites Under Quasi-Static and Dynamic Compression. 2935-2949A
- Formability and Strength of Friction-Stir-Welded Aluminum Sheets. 3439-3444A
- Effect of Boron on the Low-Cycle Fatigue Behavior and Deformation Structure of INCONEL 718 at 650°C. 3461-3468A
- Application of a Substructure-Based Hardening Model to Copper under Loading Path Changes. 3477-3487A
- Software packages**
Determination of Isothermal Transformation Diagrams for Sigma-Phase Formation in Cast Duplex Stainless Steels CD3MN and CD3MWCuN. 3763-3774A
- Solders**
Tensile Test Behavior of the Eutectic Sn-Ag Solder Joint in Ball Grid Array Assemblies. 3377-3386A
- Solid phases**
Thermodynamic Evaluation and Optimization of the MnO- Al_2O_3 and MnO- Al_2O_3 - SiO_2 Systems and Applications to Inclusion Engineering. 3817-3821A
- Communication: Nature of Massive Transformation. 259-268B
- Communication: Discussion of "Thermodynamics of Liquid Al-Na Alloys Determined by Using CaF_2 Solid Electrolyte". 351-352A
- Communication: Authors' Reply. 393-398B
- Textural Changes during $\beta \rightarrow \alpha$ and $\alpha \rightarrow \beta \rightarrow \alpha$ Transformations in a Near- α Titanium Alloy. 398-400B
- Modeling of Irregular Eutectic Microstructures in Solidification of Al-Si Alloys. 925-938A
- On the Influence of In-Situ Reactions on Grain Size during Reactive Atomization and Deposition. 1555-1563A
- Solid solutions**
Cyclic Oxidation Response of Multiphase Niobium-Based Alloys. 3251-3263A
- Experimental Study of Phase Equilibria in the Al-Fe-Zn-O System in Air. 589-597A
- Critical Thermodynamic Assessment and Modeling of the Fe-Ni-S System. 633-642B
- Cr-Mo Solid Solutions Forced by High-Energy Ball Milling. Alteration in Hydrogen Absorption by and Hydrogen Permeation through a High-Strength Low-Alloy Steel due to Plasma Source Ion Implantation of Nitrogen. 897-907B
- Communication: Formation of Simple Crystal Structures in Cu-Co-Ni-Cr-Al-Fe-Ti-V Alloys with Multiprincipal Metallic Elements. 1105-1111A
- Coarsening behavior of an alpha-beta titanium alloy. 1123-1128B
- Effect of dissolved tungsten on the deformation of 70Ni-30Fe alloys. 2533-2536A
- Communication: Transformation of mechanically alloyed Nb-Sn powder to Nb3Sn. 2809-2819A
- Monosilicide-Disilicide-Silicon Phase Equilibria in the Nickel-Platinum-Silicon and Nickel-Palladium-Silicon Systems. 2821-2828A
- Solid state**
Solid-State Reduction of Chromium Oxide by Methane-Containing Gas. 3009-3012A
- Reaction Sequences in the Formation of Silico-Ferrites of Calcium and Aluminum in Iron Ore Sinter. 609-615B
- Solid-State Reactions during Heating Mechanically Milled Al/TiO2 Composite Powders. 929-936B
- Modeling of Lattice Parameter in the Ni-Al System. Materials science under extreme conditions of pressure and strain rate. 2115-2125A
- High-pressure, laser-driven deformation of an aluminum alloy. 2313-2321A
- Solidification**
Process Efficiency Measurements in the Laser Engineered Net Shaping Process. 2587-2607A
- Determination of Interfacial Heat-Transfer Boundary Conditions in an Aluminum Low-Pressure Permanent Mold Test Casting. 2625-2631A
- Correlation of Microstructure and Thermal-Fatigue Properties of Centrifugally Cast High-Speed Steel Rolls. 143-152B
- Analysis of Thin-Slab Casting, by the Compact-Strip Process: Part I. Heat Extraction and Solidification. 299-311B
- Analysis of Thin-Slab Casting by the Compact-Strip Process: Part II. Effect of Operating and Design Parameters on Solidification and Bulging. 481-492A
- Estimation of Multiple Heat-Flux Components at the Metal/Mold Interface in Bar and Plate Aluminum Alloy Castings. 541-560B
- Undercooling and Solidification of Al-50 At. Pct Si Alloy by Electromagnetic Levitation. 561-573B
- Liquid Convection Effects on the Pushing-Engulfment Transition of Insoluble Particles by a Solidifying Interface: Part I. Analytical Calculation of the Lift Forces. 575-585B
- Freeze-Off Limits in Transient Liquid-Phase Infiltration. Deformation and Recrystallization Behavior during Hot Working of a Coarse-Grain, Nickel-Base Superalloy Ingot Material. 607-612A
- A Model of the Interfacial Heat Transfer Coefficient for the Aluminum Gravity Die-Casting Process. 613-621A
- Response of Primary Dendrite Spacing to Varying Temperature Gradient during Directional Solidification. 641-653A
- Channel Segregation during Solidification and the Effects of an Alternating Traveling Magnetic Field. 679-693A
- Correction to Metallurgical and Materials Transactions A, November 2003, vol. 34A, pp. 2690-2693: "Authors Reply" to 721-733B
- 735-742B
- 743-754B

- Discussion of "Eutectic Solidification of Al-Si Alloys" 959A
Correlation of Microstructure with Hardness and Wear Resistance in (TiC,SiC)/Stainless Steel Surface Composites Fabricated by High-Energy Electron-Beam Irradiation. 1029-1038A
Morphologies of Silicon Crystals Solidified on a Chill Plate. 1067-1073A
Modeling of Laser Cladding with Powder Injection. 1139-1150B
Contraction of Aluminum Alloys during and after Solidification. 1325-1335A
The Solidification Characteristics of Fe-Rich Intermetallics in Al-11.5Si-0.4Mg Cast Alloys. 1425-1435A
Interaction of Porosity with a Planar Solid/Liquid Interface. 1525-1538A
The Role of Melt Pool Behavior in Free-Jet Melt Spinning. 1539-1553A
Modeling of Irregular Eutectic Microstructures in Solidification of Al-Si Alloys. 1555-1563A
Wear Behavior, Microstructure, and Dimensional Stability of As-Cast Zinc-Aluminum/SiC (Metal Matrix Composites) Alloys. 1579-1590A
Microstructure, Mechanical Properties, and Fracture Mechanism of As-Cast (Ti0.5Cu0.25Ni0.15Sn0.05Zr0.05)(100-x)Mo(x) Composites. 1591-1601A
Eutectic Grains in Unmodified and Strontium-Modified Hypoeutectic Aluminum-Silicon Alloys. 1829-1837A
Erratum: A Solutal Interaction mechanism for the Columnar-to-Equiaxed Transition in Alloy Solidification. 1915A
Communication: Casting of Aluminum-Based Wrought Alloys Using Controlled Diffusion Solidification. 2174-2180A
Development of thermal strain in the coherent mushy zone during solidification of aluminum alloys. 2903-2915A
Communication: Eutectic solidification of aluminum-silicon alloys. 3038-3043A
Grain Refinement Induced by Electromagnetic Stirring: A Dendrite Fragmentation Criterion. 3201-3210A
The Solidification of Undercooled Melts via Twinned Dendritic Growth. 3211-3220A
On the Influence of In-Situ Reactions on Grain Size during Reactive Atomization and Deposition. 3251-3263A
Thermodynamic Aspects of the Constitution, Grain Refining, and Solidification Enthalpies of Al-Ce-Si Alloys. 3349-3362A
The Influence of Strontium on Porosity Formation in Al-Si Alloys. 3531-3541A
Effects of Alloy Composition and Casting Speed on Structure Formation and Hot Tearing during Direct-Chill Casting of Al-Cu Alloys. 3551-3561A
- Solidus**
Liquidus Temperatures in Calcium Ferrite Slags in Equilibrium with Molten Copper. 203-215B
Freeze-Off Limits in Transient Liquid-Phase Infiltration. 641-653A
- Solubility**
Modeling of the Solubilities of NiO/NiAl₂O₄ and FeO/FeAl₂O₄ in Cryolite Melts at 1300 K. 133-141B
Communication: The Solubility of Titanium Dioxide in Cryolite-Alumina Melts at 1300 K. 182-186B
Communication: Discussion of "Thermodynamics of Liquid Al-Na Alloys Determined by Using CaF₂ Solid Electrolyte". 393-398B
Communication: Authors' Reply. 398-400B
Modeling the Dependence of Alumina Solubility on Temperature and Melt Composition in Cryolite-Based Melts. 509-515B
Alteration in Hydrogen Absorption by and Hydrogen Permeation through a High-Strength Low-Alloy Steel due to Plasma Source Ion Implantation of Nitrogen. 1123-1128B
Experimental Determination of the Carbon Solubility Limit in Ferritic Steels. 1655-1661A
Calorimetric Determination of the 5 Hydride Dissolution Enthalpy in ZIRCALOY-4. 2343-2349A
Effect of dissolved tungsten on the deformation of 70Ni-30Fe alloys. 2821-2828A
The Nitriding Kinetics of Iron-Chromium Alloys; The Role of Excess Nitrogen: Experiments and Modelling. 3387-3398A
Mechanisms of Hf Dopant Incorporation during the Early Stage of Chemical Vapor Deposition Aluminide Coating Growth under Continuous Doping Conditions. 3581-3593A
- Solution annealing**
Effects of Temperature and Strain Rate on Tensile Properties and Activation Energy for Dynamic Strain Aging in Alloy 625. 3129-3139A
- Solution strengthening**
Influence of Microstructure on Tensile and Creep Properties of a New Castable TiAl-Based Alloy. 2087-2102A
Experimental and Theoretical Evidence for Carbon-Vacancy Binding in Austenite. 2239-2245A
Effect of dissolved tungsten on the deformation of 70Ni-30Fe alloys. 2821-2828A
- Spacing**
Overstability of Lamellar Eutectic Growth below the Minimum Undercooling Spacing. 1815-1828A
Grain-size dependence of the flow stress of Cu from millimeters to nanometers. 2681-2696A
- Spallation**
The Influence of a Martensitic Phase Transformation on Stress Development in Thermal Barrier Coating Systems. 2279-2286A
Effect of microstructural length scales on spall behavior of copper. 2663-2673A
- Spalling**
Cyclic Oxidation Response of Multiphase Niobium-Based Alloys. 589-597A
Deformation and Damage Mechanisms of Zinc Coatings on Hot-Dip Galvanized Steel Sheets: Part II. Damage Modes. 813-823A
- Speciation**
Communication: Properties of Mg(OHCl). 406-408B
- Specific heat**
Standard Gibbs Energy of Formation of Mg48Zn52 Determined by Solution Calorimetry and Measurement of Heat Capacity from Near Absolute Zero Kelvin. 891-895B
- Spheroidizing**
Effect of strain reversal on the dynamic spheroidization of Ti-6Al-4V during hot deformation. 2993-3001A
- Spinel**
Experimental Study of Phase Equilibria in the Al-Fe-Zn-O System in Air. 633-642B
Application of the Generalized Method of Cells Principle to Particulate-Reinforced Metal Matrix Composites. 1029-1039B
Effects of Simultaneous Displacive and Ionizing Radiations and of Electric Field on Radiation Damage in Ionic Crystals. 2257-2266A
- Splitting**
Deformation Behavior of Zr₃Al-Nb Alloys I: Room-Temperature and High-Temperature Deformation Study. 189-203A
Microstructural Banding and Failure of a Stainless Steel. 1317-1324A
- Sporting goods**
Two-Layered Zr-Base Amorphous Alloy/Metal Surface Composites Fabricated by High Energy Electron-Beam Irradiation. 3455-3460A
- Spray casting**
Analysis of Thin-Slab Casting, by the Compact-Strip Process: Part I. Heat Extraction and Solidification. 541-560B
Analysis of Thin-Slab Casting by the Compact-Strip Process: Part II. Effect of Operating and Design Parameters on Solidification and Bulging. 561-573B
- Spray forming**
Phase Transformations and Control of Residual Stresses in Thick Spray-Formed Steel Shells. 1113-1122B
- Spraying**
The Selection of the Spray Deposition Rate during the Spray Rolling Process. 3595-3603A
Communication: The Transient to Steady-State Transition during the Spray-Rolling Process. 3633-3635A
- Spring steels**
Inclusion-Controlled Fatigue Properties of 1800 MPA-Class Spring Steels. 3737-3744A
- Spring steels, Mechanical properties**
Quench Embrittlement of Hardened 5160 Steel as a Function of Austenitizing Temperature. 153-162A
- Sputtered films**
Defect Structures in Cosputtered Thin Films of Transition Metal Disilicides with C11b, C40 and C54 Structures. 2229-2238A
- Stacking fault energy**
Tensile Anisotropy in Cu-Ni-Mn-Sn-Al Alloys. 465-469A
- Stacking faults**
Deformation Behavior of Zr₃Al-Nb Alloys I: Room-Temperature and High-Temperature Deformation Study. 189-203A
Thermomechanical Fatigue Behavior of the Third-Generation, Single-Crystal Superalloy TMS-75: Deformation Structure, Damping Properties of Austenitic Stainless Steels Containing Strain-Induced Martensite. 1779-1787A
Dislocation structure behind a shock front in fcc perfect crystals: atomistic simulation results. 2401-2406A
Microstructure Development during High Velocity Deformation Studies of Lattice Imperfections in Deformed Aluminum-Based Lithium Alloys by X-Ray Diffraction. 2609-2615A
3091-3101A
3319-3322A
- Stainless steels**
Additions to Generate Foam in Stainless Steelmaking. 643-650B
Communication: High-temperature fatigue crack growth behavior of 17-4 PH stainless steels. 3018-3024A
- Stainless steels, Powder technology**
Simulation of the Sintering Densification and Shrinkage Behavior of Powder-Injection-Molded 17-4 PH Stainless Steel. 257-263A
- Stamping**
Failure in Internally Pressurized Bent Tubes. 1151-1158A
- Statistical analysis**
The Effect of Heat Treatment on Mg₂Si Coarsening in Aluminum 6105 Alloy. 435-438A
- Statistical methods**
A Semiautomated Electron Backscatter Diffraction Technique for Extracting Reliable Twin Statistics. 3745-3751A
- Steady state**
A Numerical Study of Oxidation Behavior during Reactive Atomization and Deposition. 1173-1185B
Communication: The Transient to Steady-State Transition during the Spray-Rolling Process. 3633-3635A
- Steam**
Effect of Thermal Spray on the Microstructure and Adhesive Strength of High Velocity Oxy-Fuel-Sprayed Ni-Cr Coatings on 9Cr-1Mo Steel. 3187-3199A
- Steel scrap**
Continuous Oxygen Steelmaking with Copper-, Tin-, and Zinc-Contaminated Scrap. 663-674B
- Steels**
Inertial and Buoyancy Driven Water Flows under Gas Bubbling and Thermal Stratification Conditions in a Tundish Model. 247-257B
Mechanism Governing Nitrogen Absorption by Steel Weld Metal during Laser Welding. 331-338B
Communication: A Model for Estimating Exposed Plume Eye Area in Steel Refining Ladles Covered with Thin Slag. 400-404B
A Thermodynamic Model for Deoxidation Equilibria in Steel. 493-507B
Analysis of Thin-Slab Casting by the Compact-Strip Process: Part II. Effect of Operating and Design Parameters on Solidification and Bulging. 561-573B
Study of Transient Flow and Particle Transport in Continuous Steel Caster Molds: Part II. Particle Transport. 703-714B
Flow of Conducting Liquid around Two Nonconducting Parti-

- cles in DC Electromagnetic Field and the Electromagnetic Migration Force 847-855B
- Computational and Experimental Study of Turbulent Flow in a 0.4-Scale Water Model of a Continuous Steel Caster 967-982B
- The Effect of Carbon in Slag on Steel Reoxidation and Carbon Analysis by X-Ray Photoelectron Spectroscopy in the CaO-SiO₂-Al₂O₃-MgO-MnO-FeO System 1087-1095B
- Phase Transformations and Control of Residual Stresses in Thick Spray-Formed Steel Shells 1113-1122B
- Thermomechanical Finite-Element Model of Shell Behavior in Continuous Casting of Steel 1151-1172B
- Fine Carbide-Strengthened 3Cr-3WVTA Bainitic Steel. 1281-1288A
- Nickel-Aluminides/Steel Clad Pipe Fabricated by Reactive Centrifugal Casting Method from Liquid Aluminum and Solid Nickel. 1517-1524A
- A Novel Experiment for the Study of Substrate-Induced Nucleation in Metallic Alloys: Application to Zn-Al 3543-3550A
- Application of a Substructure-Based Hardening Model to Copper under Loading Path Changes 3763-3774A
- Communication: Room-Temperature Cleavage Fracture of FeMnAl Steels 3863-3866A
- Steels, Phases (state of matter)**
- A Model for Ferrite/Pearlite Band Formation and Prevention in Steels. 425-433A
- Steels, Rolling**
- The Cut-Groove Technique to Infer Interfacial Effects during Hot Rolling. 1087-1095A
- Stiffness**
- Single-Crystal Elastic Constants of Fe-15Ni-15Cr Alloy 3149-3154A
- Two-Layered Zr-Base Amorphous Alloy/Metal Surface Composites Fabricated by High Energy Electron-Beam Irradiation 3455-3460A
- Stirring**
- Yield Behavior of Commercial Al-Si Alloys in the Semisolid State 1187-1202B
- Storage containers**
- The Microstructural, Mechanical, and Fracture Properties of Austenitic Stainless Steel Alloyed with Gallium 3445-3454A
- Straightening**
- Failure Mode Analysis and a Mechanism for Hot-Ductility Improvement in the Nb-Microalloyed Steel 3823-3832A
- Strain**
- Effect of Boron on the Low-Cycle Fatigue Behavior and Deformation Structure of INCONEL 718 at 650°C 3477-3487A
- In-Situ Microfracture Observation of Strip-Cast Zr-Ti-Cu-Ni-Be Bulk Metallic Glass Alloys 3753-3761A
- Strain aging**
- Hydrogen-Involving Tensile and Cyclic Deformation Behavior of Low-Alloy Pressure Vessel Steel. 1477-1486A
- Damping Properties of Austenitic Stainless Steels Containing Strain-Induced Martensite. 2401-2406A
- Strain distribution**
- Second-Order Stresses and Strains in Heterogeneous Steels: Self-Consistent Modeling and X-Ray Diffraction Analysis. 2361-2369A
- An Eulerian Finite-Element Model for Determination of Deformation State of a Copper Subjected to Orthogonal Cutting. 2393-2400A
- A novel observation of strain-induced ferrite-to-austenite transformation after intercritical deformation of C-Mn steel. 2789-2797A
- Strain hardening**
- Advancing Towards Constitutive Equations for the Metal Industry via the LEDS Theory. 5-54B
- Quantifying Thermomechanical Fatigue of Light-Metal-Matrix Composites by Mechanical Spectroscopy. 25-35A
- Advancing Towards Constitutive Equations for the Metal Industry via the LEDS Theory. 369-418A
- Effect of Broaching on High-Temperature Fatigue Behavior in Notched Specimens of INCONEL 718. 771-783A
- Dislocation Structure and Deformation in Iron Processed by Equal-Channel-Angular Pressing. 1343-1350A
- The Influence of Texture, Strain Rate, Temperature, and Chemistry on the Mechanical Behavior of Hafnium. 1999-2011A
- Dislocation mechanics-based constitutive equations. 2547-2555A
- Microstructure evolution and mechanical behavior of bulk copper obtained by consolidation of micro- and nanopowders using equal-channel angular extrusion. 2935-2949A
- A Micromechanical Analysis of the Yielding Behavior of Individual Widmanstätten Colonies of an $\alpha + \beta$ Titanium Alloy 3409-3422A
- Strain rate**
- Effect of Temperature and Strain Rate on the Compressive Flow of Aluminum Composites Containing Submicron Alumina Particles. 287-292A
- Role of Temperature and Strain Rate on the Hydrogen-Induced Intergranular Rupture in Alloy 600. 457-464A
- Dynamic Phase Transformation during Superplastic Deformation of Nb/Nb₃Al In-Situ Composite. 503-511A
- Transition of Dominant Diffusion Process during Superplastic Deformation in AZ61 Magnesium Alloys. 555-562A
- Deformation and Recrystallization Behavior during Hot Working of a Coarse-Grain, Nickel-Base Superalloy Ingot Material. 679-693A
- Communications: Ultra-High-Speed Exploding Properties of Ti-6Al-4V Alloy Having Equiaxed and Bimodal Microstructures. 719-724A
- Low-Cycle Fatigue Behavior of ULTIMET Alloy. 785-796A
- High-Strain-Rate Superplastic Behavior of Equal-Channel Angular-Pressed 5083 Al-0.2 Wt Pct Sc. 825-837A
- Fracture Behavior of Thixoformed 357-T5 Al Alloys. 1017-1027A
- Creep Behavior of a Rotating Functionally Graded Composite Disc Operating under Thermal Gradient. 1381-1391A
- Communication: Constitutive Equation for Structural Steels. 1410-1414A
- The Effects of Strain Rate and Welding Current Mode on the Dynamic Impact Behavior of Plasma-Arc-Welded 304L Stainless Steel Weldments. 1501-1515A
- Monte Carlo-Method Simulation of the Deformation-Induced Ferrite Transformation in the Fe-C System. 1565-1577A
- The Influence of Texture, Strain Rate, Temperature, and Chemistry on the Mechanical Behavior of Hafnium. 1999-2011A
- Communication: The Dependence of Cavity-Growth Rate on Stress Triaxiality. 2187-2190A
- Superplastic Behavior and Microstructure Evolution in a Commercial Al-Mg-Sc Alloy Subjected to Intense Plastic Straining. 2383-2392A
- Electrochemical Evaluation of a Corrosion Fatigue Failure Mechanism in a Duplex Stainless Steel. 2427-2437A
- Dislocation mechanics-based constitutive equations. 2547-2555A
- Dynamic deformation and damage in cast γ -TiAl during Taylor cylinder impact: experiments and model validation. 2557-2566A
- Analysis of intergranular impurity concentration and the effects on the ductility of copper-shaped charge jets. 2567-2573A
- Shear localization-martensitic transformation interactions in Fe-Cr-Ni monocrystal. 2575-2586A
- Materials science under extreme conditions of pressure and strain rate. 2587-2607A
- High-pressure, laser-driven deformation of an aluminum alloy. 2625-2631A
- The effect of grain size on low-cycle fatigue behavior of Al-2024 polycrystalline alloy. 2725-2728A
- Effect of low-temperature shock compression on the microstructure and strength of copper. 2729-2739A
- Time-dependent deformation in an enhanced SiC/SiC composite. 2853-2859A
- Effect of strain reversal on the dynamic spheroidization of Ti-6Al-4V during hot deformation. 2993-3001A
- Microstructure Development during High Velocity Deformation Effects of Temperature and Strain Rate on Tensile Properties and Activation Energy for Dynamic Strain Aging in Alloy 625 3129-3139A
- Effect of Different Cr Contents on Tensile and Corrosion Behaviors of 0.13 Pct N-Containing CD4MCU Cast Duplex Stainless Steels 3431-3438A
- Deformation and Failure of Zr57Nb5Al10Cu15.4Ni12.6/W Particle Composites Under Quasi-Static and Dynamic Compression 3439-3444A
- Effects of Alloy Composition and Casting Speed on Structure Formation and Hot Tearing during Direct-Chill Casting of Al-Cu Alloys 3551-3561A
- Tensile Test Behavior of the Eutectic Sn-Ag Solder Joint in Ball Grid Array Assemblies 3817-3821A
- Microstructure Characterization and Creep Deformation of an Al-10 Wt Pct Ti-2 Wt Pct Cu Nanocomposite 3855-3861A
- Strain rate sensitivity**
- Effect of dissolved tungsten on the deformation of 70Ni-30Fe alloys. 2821-2828A
- Strength to weight ratio**
- Communication: Casting of Aluminum-Based Wrought Alloys Using Controlled Diffusion Solidification. 2174-2180A
- A Through-Process Model of an A356 Brake Caliper for Fatigue Life Prediction 3275-3288A
- Stress concentration**
- Effects of Partial Recrystallization on High-Cycle Fatigue Deformation and Crack Generation of a Nitrogen-Strengthened 32Mn-7Cr Austenitic Steel at Liquid-Nitrogen Temperature. 543-553A
- Numerical Analysis of Metal Transfer in Gas Metal Arc Welding under Modified Pulsed Current Conditions 857-866B
- Fracture Behavior of Thixoformed 357-T5 Al Alloys. 1017-1027A
- Phase Equilibrium and Distribution of Minor Elements between Ni-S Melt and Al₂O₃-CaO-MgO Slag at 1873 K 1041-1049B
- Monte Carlo-Method Simulation of the Deformation-Induced Ferrite Transformation in the Fe-C System. 1565-1577A
- An Eulerian Finite-Element Model for Determination of Deformation State of a Copper Subjected to Orthogonal Cutting. 2393-2400A
- Morphology of fractured domains in brittle fracture. 2651-2661A
- Effect of low-temperature shock compression on the microstructure and strength of copper. 2729-2739A
- Tensile and Fatigue Behavior of Al-Based Metal Matrix Composites Reinforced with Continuous Carbon or Alumina Fibers: Part II. Quasi-Unidirectional Composite Cross-Ply Laminates 3307-3317A
- Effect of Boron on the Low-Cycle Fatigue Behavior and Deformation Structure of INCONEL 718 at 650°C 3477-3487A
- Stress corrosion cracking**
- Role of Temperature and Strain Rate on the Hydrogen-Induced Intergranular Rupture in Alloy 600. 457-464A
- Fracture Behavior of Thixoformed 357-T5 Al Alloys. 1017-1027A
- Effect of Different Cr Contents on Tensile and Corrosion Behaviors of 0.13 Pct N-Containing CD4MCU Cast Duplex Stainless Steels 3431-3438A
- Characterization of Retrogression and Reaging Behavior of 8090 Al-Li-Cu-Mg-Zr Alloy 3681-3691A
- Stress intensity**
- Characterizing Small Fatigue Cracks in Metallic Alloys. 7-14A
- Stress intensity factors**
- Variability of Large-Crack Fatigue-Crack-Growth Thresholds in Structural Alloys 3721-3735A
- Stress ratio**
- Influence of Stress State on Cavitation during Hot Working of Ti-6Al-4V. 655-663A
- Fatigue and Fracture Behavior of Bulk Metallic Glass 3489-3498A
- Variability of Large-Crack Fatigue-Crack-Growth Thresholds in Structural Alloys 3721-3735A
- Stress relaxation tests**
- A Metallurgical Interpretation of the Static Recrystallization Kinetics of an Intercritically Deformed C-Mn Steel. 1889-1898A

Stress strain curves

- Deformation and Recrystallization Behavior during Hot Working of a Coarse-Grain, Nickel-Base Superalloy Ingot Material. The Effects of Strain Rate and Welding Current Mode on the Dynamic Impact Behavior of Plasma-Arc-Welded 304L Stainless Steel Weldments. 679-693A
- Cyclic deformation behavior and dislocation structure of Ti-2 Al. Pct Al single crystals oriented for double prism slip. 1501-1515A
- Application of a Substructure-Based Hardening Model to Copper under Loading Path Changes 2845-2852A
- 3763-3774A
- Stresses**
- A Tribute to Terence E. Mitchell. 2203-2205A
- Grain-size dependence of the flow stress of Cu from millimeters to nanometers. 2681-2696A
- Striations**
- Fatigue Fracture Mechanism Maps for a Type 304 Stainless Steel. 1311-1316A
- Strip casting**
- Surface-Oriented Melt/Substrate Heat-Transfer Model in Aluminum Strip Casting. 351-361B
- Communication: Effect of Thermomechanical Processing on Grain Structure Development in a Twin-Belt Strip Cast Automotive Aluminum Alloy. 949-952A
- In-Situ Microfracture Observation of Strip-Cast Zr-Ti-Cu-Ni-Be Bulk Metallic Glass Alloys 3753-3761A
- Strip steel, Coating**
- Simulation of Flow in a Continuous Galvanizing Bath: Part I. Thermal Effects of Ingot Addition. 161-170B
- Simulation of Flow in a Continuous Galvanizing Bath: Part II. Transient Aluminum Distribution Resulting from Ingot Addition. 171-178B
- Strontium**
- Eutectic Grains in Unmodified and Strontium-Modified Hypoeutectic Aluminum-Silicon Alloys. 1829-1837A
- The Influence of Strontium on Porosity Formation in Al-Si Alloys 3531-3541A
- Structural steels**
- Study of Transient Flow and Particle Transport in Continuous Steel Caster Molds: Part I. Fluid Flow. 685-702B
- Fatigue of Cold-Work Tool Steels: Effect of Heat Treatment and Carbide Morphology on Fatigue Crack Formation, Life, and Fracture Surface Observations. 1289-1300A
- Communication: Constitutive Equation for Structural Steels. 1410-1414A
- Substructures**
- Critical Thermodynamic Evaluation and Optimization of the FeO-Fe₂O₃-MgO-SiO₂ System. 877-889B
- The influence of explosive-driven 'Taylor-wave' shock prestraining on the structure/property behavior of 304 stainless steel. 2617-2624A
- Application of a Substructure-Based Hardening Model to Copper under Loading Path Changes 3763-3774A
- Succinonitrile**
- Response of Primary Dendrite Spacing to Varying Temperature Gradient during Directional Solidification. 735-742B
- Sulfur**
- Critical Thermodynamic Assessment and Modeling of the Fe-Ni-S System. 897-907B
- Superalloys**
- Effect of Zr and B on Castability of Ni-Based Superalloy IN792. Mechanism of Primary MC Carbide Decomposition in Ni-Base Superalloys. 1337-1342A
- Characterization and Modeling of Quenching-Induced Residual Stresses in the Nickel-Based Superalloy IN718. 1669-1679A
- Experimental and Numerical Study on the Relationship between Creep Crack Growth Properties and Fracture Mechanisms. 1703-1713A
- Thermomechanical Fatigue Behavior of the Third-Generation, Single-Crystal Superalloy TMS-75: Deformation Structure. Communication: Strengthening by γ/γ' Interfacial Dislocation Networks in TMS-162-Toward a Fifth-Generation Single-Crystal Superalloy. 1757-1764A
- Oxide Defects in a Vacuum Investment-Cast Ni-Based Turbine Blade. 1779-1787A
- Grain Refinement of Superalloy IN718C by the Addition of Inoculants. 1911-1914A
- Communication: Determination of γ' Phase Lattice Parameter Based on the Chemical Concentration of Its Sublattices in Ni-Base Superalloys. 2063-2071A
- The Influence of a Martensitic Phase Transformation on Stress Development in Thermal Barrier Coating Systems. 2111-2114A
- Effects of Temperature and Strain Rate on Tensile Properties and Activation Energy for Dynamic Strain Aging in Alloy 625 Directional Solidification of Large Superalloy Castings with Radiation and Liquid-Metal Cooling: A Comparative Assessment. 2171-2172A
- Effect of Boron on the Low-Cycle Fatigue Behavior and Deformation Structure of INCONEL 718 at 650°C. 2279-2286A
- Superalloys, Coating**
- Effects of Preheating on Morphological Development of a Chemical Vapor Deposition Aluminate Coating Formed on Single-Crystal Ni-Based Superalloy. 3129-3139A
- Superalloys, Directional solidification**
- Effect of Grain-Boundary Characteristics on Castability of Nickel-Base Superalloys. 3221-3231A
- Superalloys, Heat treatment**
- Surface Hardening of Nickel Alloys by Means of Plasma Nitriding. 3477-3487A
- Superalloys, Mechanical properties**
- Characterizing Small Fatigue Cracks in Metallic Alloys. Thermal-Imaging Technologies for Detecting Damage during High-Cycle Fatigue. 7-14A
- Role of Temperature and Strain Rate on the Hydrogen-Induced Intergranular Rupture in Alloy 600. 15-23A
- Damage Repair in CMSX-4 Alloy without Fatigue Life Reduction Penalty. 457-464A
- Effect of Broaching on High-Temperature Fatigue Behavior in Notched Specimens of INCONEL 718. 535-542A
- Low-Cycle Fatigue Behavior of ULTIMET Alloy. 771-783A
- Temperature Evolution and Life Prediction in Fatigue of Superalloys. 785-796A
- Effects of Temperature and Shot Peening on S-N Behavior of a PM Ni-Base Superalloy UDIMET 720. 839-848A
- Superalloys, Melting**
- Model-Based Melt Rate Control during Vacuum Arc Remelting of Alloy 718. 1007-1016A
- Superalloys, Microstructure**
- Deformation and Recrystallization Behavior during Hot Working of a Coarse-Grain, Nickel-Base Superalloy Ingot Material. Interfacial Segregation and Influence of Antiphase Boundaries on Rafting in a γ/γ' Alloy. 101-113B
- Superalloys, Oxidation**
- Effects of an α -Al₂O₃ Thin Film on the Oxidation Behavior of a Single-Crystal Ni-Based Superalloy. 679-693A
- Effects of Preoxidation on the Nucleation and Growth Behavior of Chemically Vapor-Deposited α -Al₂O₃ on a Single-Crystal Ni-Based Superalloy. 733-740A
- Superconducting magnets**
- Fracture Behavior of Thick-Section Weldment in Fe-12Cr-12Ni-10Mn-0.24N Stainless Steel at Liquid Helium Temperature. 1055-1065A
- Superconductors**
- Communication: Transformation of mechanically alloyed Nb-Sn powder to Nb₃Sn. 1113-1124A
- Supercooling**
- The Solidification of Undercooled Melts via Twinned Dendritic Growth. 3797-3802A
- Superlattices**
- Deformation Behavior of Zr₂Al-Nb Alloys I: Room-Temperature and High-Temperature Deformation Study. 3009-3012A
- The Magic of Plutonium: 5f Electrons and Phase Instability. 3211-3220A
- Superplasticity**
- Dynamic Phase Transformation during Superplastic Deformation of Nb/Nb₃Al In-Situ Composite. 189-203A
- Transition of Dominant Diffusion Process during Superplastic Deformation in AZ61 Magnesium Alloys. 2207-2222A
- High-Strain-Rate Superplastic Behavior of Equal-Channel Angular-Pressed 5083 Al-0.2 Wt Pct Sc. 503-511A
- Superplastic Behavior and Microstructure Evolution in a Commercial Al-Mg-Sc Alloy Subjected to Intense Plastic Straining. 555-562A
- Texture Evolution and Mechanical Anisotropy in Dual-Phase Ti3Al-Based Alloy Loaded at 700 °C to 1000 °C. 825-837A
- Surface area**
- The Effect of Temperature and Extrusion Speed on The Consolidation of Zirconium-Based Metallic Glass Powder Using Equal-Channel Angular Extrusion. 2383-2392A
- Characterization of Three-Dimensional Grain Structure in Polycrystalline Iron by Serial Sectioning. 3803-3815A
- Effects of the entrained surface film on the reliability of castings. 247-256A
- Surface chemistry**
- Evaluation of Mechanical Properties of Porous 6061 Alloys Fabricated by the Powder Compression and Induction Heating Process. 1927-1933A
- Surface energy**
- Fcc/Hcp Martensitic Transformation in the Fe-Mn System: Part II. Driving Force and Thermodynamics of the Nucleation Process. 2893-2902A
- Communication: The Observation and Identification of the Oxide Film on the Creep Cavity Wall of Type 316L Stainless Steel. 2419-2426A
- Surface hardness**
- Surface Hardening of Nickel Alloys by Means of Plasma Nitriding. 83-91A
- Surface temperature**
- Analysis of Thin-Slab Casting, by the Compact-Strip Process: Part I. Heat Extraction and Solidification. 3331-3333A
- Surface tension**
- Freeze-Off Limits in Transient Liquid-Phase Infiltration. Modeling of Distortion after Densification during Liquid-Phase Sintering. 227-238A
- Swaging**
- On the Isotropy of the Dynamic Mechanical and Failure Properties of Swaged Tungsten Heavy Alloys. 541-560B
- Tailored blanks**
- Formability and Strength of Friction-Stir-Welded Aluminum Sheets. 641-653A
- Tantalum**
- Nonequilibrium molecular dynamics simulations of metallic friction at Ta/Al and Cu/Ag interfaces. 3833-3841A
- Tantalum compounds**
- Kinetics of Chlorination of Tantalum Pentoxide in Mixture with Sucrose Carbon by Chlorine Gas. 3787-3795A
- Tearing**
- Effect of Grain-Boundary Characteristics on Castability of

- Nickel-Base Superalloys.
Contraction of Aluminum Alloys during and after Solidification.
Effect of Zr and B on Castability of Ni-Based Superalloy IN792.
Communication: Casting of Aluminum-Based Wrought Alloys Using Controlled Diffusion Solidification.
The Microstructural, Mechanical, and Fracture Properties of Austenitic Stainless Steel Alloyed with Gallium
Effects of Alloy Composition and Casting Speed on Structure Formation and Hot Tearing during Direct-Chill Casting of Al-Cu Alloys
- Temperature dependence**
Modeling of Lattice Parameter in the Ni-Al System.
- Temperature distribution**
Simulation of Flow in a Continuous Galvanizing Bath: Part I. Thermal Effects of Ingot Addition.
Simulation of Flow in a Continuous Galvanizing Bath: Part II. Transient Aluminum Distribution Resulting from Ingot Addition.
Modeling of Laser Cladding with Powder Injection
- Temperature effects**
Temperature Effects on the Lattice Constants and Crystal Structure of a Co-27Cr-5Mo Low-Carbon Alloy.
- Temperature gradient**
Response of Primary Dendrite Spacing to Varying Temperature Gradient during Directional Solidification.
Overstability of Lamellar Eutectic Growth below the Minimum-Undercooling Spacing.
- Temperature measurement**
Microstructural modification of as-cast NiAl bronze by friction stir processing.
- Tempering**
Gigacycle Fatigue Properties of a Modified-Ausformed Si-Mn Steel and Effects of Microstructure.
Effects of Alloying Elements on Fracture Toughness in the Transition Temperature Region of Base Metals and Simulated Heat-Affected Zones of Mn-Mo-Ni Low-Alloy Steels.
Effects of Martensite Morphology and Tempering on Dynamic Deformation Behavior of Dual-Phase Steels.
Hydrogen Absorption of Incoherent TiC Particles in Iron from Environment at High Temperatures
- Tensile properties**
Effect of Reinforcement-Particle-Orientation Anisotropy on the Tensile and Fatigue Behavior of Metal-Matrix Composites.
Communication: Effect of Microstructure on Tensile Behavior of Thixoformed 357-T5 Semi-solid Al Alloy.
Effect of Mg₂Si Particles on the Elevated Temperature Tensile Properties of Squeeze-Cast Mg-Al Alloys.
Effects of Alloying Elements on Fracture Toughness in the Transition Temperature Region of Base Metals and Simulated Heat-Affected Zones of Mn-Mo-Ni Low-Alloy Steels.
Influence of Microstructure on Tensile and Creep Properties of a New Castable TiAl-Based Alloy.
Effects of Martensite Morphology and Tempering on Dynamic Deformation Behavior of Dual-Phase Steels.
Effect of Low-Frequency Electromagnetic Casting on the Castability, Microstructure, and Tensile Properties of Direct-Chill Cast Al-Zn-Mg-Cu Alloy.
Effects of the entrained surface film on the reliability of castings.
Dynamic Deformation Behavior and Ballistic Impact Properties of Ti-6Al-4V Alloy Having Equiaxed and Bimodal Microstructures
Tensile and Fatigue Behavior of Al-Based Metal Matrix Composites Reinforced with Continuous Carbon or Alumina Fibers: Part I. Quasi-Unidirectional Composites
Tensile and Fatigue Behavior of Al-Based Metal Matrix Composites Reinforced with Continuous Carbon or Alumina Fibers: Part II. Quasi-Unidirectional Composite Cross-Ply Laminates
Effect of Different Cr Contents on Tensile and Corrosion Behaviors of 0.13 Pct N-Containing CD4MCU Cast Duplex Stainless Steels
- Tensile strength**
Effect of Reinforcement-Particle-Orientation Anisotropy on the Tensile and Fatigue Behavior of Metal-Matrix Composites.
Effect of Microstructure on Mechanical Properties of As-Cast Mg-Al Alloys.
Dispersion Strengthening in a Hypereutectic Al-Si Alloy Prepared by Extrusion of Rapidly Solidified Powder.
Communication: Discussion of "Precipitation of Austenite Particles at Grain Boundaries during Aging of Fe-Mn-Ni Steel".
Communication: Authors' Reply.
Tensile Anisotropy in Cu-Ni-Mn-Sn-Al Alloys.
Correlation of Microstructure and Thermal-Fatigue Properties of Centrifugally Cast High-Speed Steel Rolls.
Correlation of the Microstructure and Mechanical Properties of Oxide-Dispersion-Strengthened Coppers Fabricated by Internal Oxidation.
Densification of a Powder-Metal Skeleton by Transient Liquid-Phase Infiltration.
Hydrogen-Involved Tensile and Cyclic Deformation Behavior of Low-Alloy Pressure Vessel Steel.
Effects of Carbon Fiber/Al Interface on Mechanical Properties of Carbon-Fiber-Reinforced Aluminum-Matrix Composites.
The Effect of Lamellar Morphology on Tensile and High-Cycle Fatigue Behavior of Orthorhombic Ti-22Al-27Nb Alloy.
Evolution of Microstructure and Texture in Mg-Al-Zn Alloys during Electron-Beam and Gas Tungsten Arc Welding.
Atomic force microscopy studies of fracture surfaces of composition B energetic materials.
- 939-946A
1325-1335A
1337-1342A
2174-2180A
3445-3454A
3551-3561A
2313-2321A
161-170B
171-178B
1139-1150B
2517-2523A
735-742B
1815-1828A
2951-2961A
1715-1723A
2027-2037A
2371-2382A
3155-3163A
53-61A
1407-1410A
1629-1632A
2027-2037A
2087-2102A
2371-2382A
2487-2494A
2893-2902A
3103-3112A
3289-3305A
3307-3317A
3431-3438A
53-61A
309-319A
333-339A
352-355A
355-356A
465-469A
481-492A
493-502A
631-640A
1477-1486A
2153-2160A
2161-2170A
2455-2469A
2675-2079A
- Effect of dissolved tungsten on the deformation of 70Ni-30Fe alloys.
Room-temperature tensile and high-cycle-fatigue strength of fine TiB particulate-reinforced Ti-22Al-27Nb composites.
Characterization of Retrogression and Reaging Behavior of 8090 Al-Li-Cu-Mg-Zr Alloy
- Tensile stress**
Study on Notch Fracture of TiAl Alloys at Room Temperature.
Correlation of Microstructure and Thermal-Fatigue Properties of Centrifugally Cast High-Speed Steel Rolls.
Hydrogen Trap States in Ultrahigh-Strength AERMET 100 Steel.
Phase Transformations and Control of Residual Stresses in Thick Spray-Formed Steel Shells
Communication: Observed Dependencies of the Large Thermal-Compressive Response of a NiTi Shape-Memory Alloy Fiber Aluminum Metal Matrix Composite on Maximum Tensile Strain Imposed during a Preceding Room-Temperature Tensile Process.
- Tensile tests**
Electrochemical Evaluation of a Corrosion Fatigue Failure Mechanism in a Duplex Stainless Steel.
Plastic deformation behavior of aluminum casting alloys A356/357.
Study of the Ni41.3Ti38.7Nb20 wide transformation hysteresis shape-memory alloy.
Ductility Exhaustion Mechanisms in Thermally Exposed Thin Sheets of a Near- β Titanium Alloy
Tensile Test Behavior of the Eutectic Sn-Ag Solder Joint in Ball Grid Array Assemblies
- Tension tests**
A New Quality Index for Characterizing Aluminum Cast Alloys with Regard to Aircraft Structure Design Requirements.
Role of Temperature and Strain Rate on the Hydrogen-Induced Intergranular Rupture in Alloy 600.
Dynamic Phase Transformation during Superplastic Deformation of Nb/Nb₃Al In-Situ Composite.
Influence of Stress State on Cavitation during Hot Working of Ti-6Al-4V.
Deformation and Damage Mechanisms of Zinc Coatings on Hot-Dip Galvanized Steel Sheets: Part II. Damage Modes.
High-Strain-Rate Superplastic Behavior of Equal-Channel Angular-Pressed 5083 Al-0.2 Wt Pct Sc.
Effect of Surface Modification of High-Density Polyethylene by Direct Current and Radio Frequency Glow Discharge on Wetting and Adhesion Characteristics.
Communication: Mechanical Behavior of a Cryomilled Nanostructured Al-7.5 pct Mg Alloy.
Mechanisms and Modeling of Cleavage Fracture in Simulated Heat-Affected Zone Microstructures of a High-Strength Low Alloy Steel.
A Hybrid Micromechanical-Macroscopic Model for the Analysis of the Tensile Behavior of Cavitating Materials.
Fine Carbide-Strengthened 3Cr-3WV Ta Bainitic Steel.
Void Nucleation by Inclusion Cracking.
Influence of Microstructure on Tensile and Creep Properties of a New Castable TiAl-Based Alloy.
Communication: The Dependence of Cavity-Growth Rate on Stress Triaxiality.
The influence of explosive-driven 'Taylor-wave' shock pre-straining on the structure/property behavior of 304 stainless steel.
- Ternary alloys**
Communication: Diffusion coefficients for modeling the heat treatment of Ti-6Al-4V.
Thermodynamic Aspects of the Constitution, Grain Refining, and Solidification Enthalpies of Al-Ce-Si Alloys
- Ternary systems**
Calculation of Physicochemical Properties in a Ternary System with Miscibility Gap.
Critical Thermodynamic Assessment and Modeling of the Fe-Ni-S System
A Thermodynamic Description of the Al-Mn-Si System over the Entire Composition and Temperature Ranges.
Experimental Investigation and Thermodynamic Calculation of the Phase Equilibria in the Cu-Sn and Cu-Sn-Mn Systems.
Monosilicide-Disilicide-Silicon Phase Equilibria in the Nickel-Platinum-Silicon and Nickel-Palladium-Silicon Systems
- Texture**
Fiber Texture and Substructural Features in the Caliber-Rolled Low-Carbon Steels.
Deformation and Recrystallization Behavior during Hot Working of a Coarse-Grain, Nickel-Base Superalloy Ingot Material.
Shape Memory Properties of Ni-Ti Based Melt-Spun Ribbons.
Characterization of Plastic Flow and Resulting Microtextures in a Friction Stir Weld.
Deformation and Damage Mechanisms of Zinc Coatings on Hot-Dip Galvanized Steel Sheets: Part I. Deformation Modes.
Textural Changes during $\beta \rightarrow \alpha$ and $\alpha \rightarrow \beta \rightarrow \alpha$ Transformations in a Near- α Titanium Alloy.
Determination of Volume Fractions of Texture Components with Standard Distributions in Euler Space.
Microstructural Evolution in the Heat-Affected Zone of a Friction Stir Weld.
New Stereology for the Recovery of Grain-Boundary Plane Distributions in the Crystal Frame.
The Influence of Texture, Strain Rate, Temperature, and Chemistry on the Mechanical Behavior of Hafnium.
Multiscale Structure and Properties of Cast and Deformation Processed Polycrystalline NiTi Shape-Memory Alloys.
Microstructural Evolution of Predeformed SiCp/ZA27 Compos-
- 2821-2828A
2971-2979A
3681-3691A
439-456A
481-492A
849-864A
1113-1122B
1403-1406A
2427-2437A
2707-2718A
2783-2788A
3113-3127A
3817-3821A
301-308A
457-464A
503-511A
655-663A
813-823A
825-837A
865-877A
947-949A
1039-1053A
1141-1149A
1281-1288A
1745-1755A
2087-2102A
2187-2190A
2617-2624A
3015-3018A
3349-3362A
715-720B
897-907B
1613-1628A
1641-1654A
3053-3061A
665-677A
679-693A
761-770A
777-783B
797-811A
925-938A
1075-1086A
1487-1499A
1991-1998A
1999-2011A
2013-2025A

- ites during Partial Remelting. 2073-2085A
- Second-Order Stresses and Strains in Heterogeneous Steels: Self-Consistent Modeling and X-Ray Diffraction Analysis. 2361-2369A
- Evolution of Microstructure and Texture in Mg-Al-Zn Alloys during Electron-Beam and Gas Tungsten Arc Welding. 2455-2469A
- High-pressure, laser-driven deformation of an aluminum alloy. Communication: Effect of texture and microstructure on resistance to cracking of high-strength hot-rolled Nb-Ti microalloyed steels. 2625-2631A
- Communication: Texture characterization of autogenous Nd:YAG laser welds in AA5182-O and AA6111-T4 aluminum alloys. 3024-3029A
- Neutron Diffraction Study of Texture Development during Hot Working of Different Gamma-Titanium Aluminide Alloys. 3032-3038A
- Quantitative Analysis of Texture Evolution of Cold-Rolled Direct-Chill-Cast and Continuous-Cast AA5052 and AA5182 Aluminum Alloys during Isothermal Annealing. 3563-3570A
- Variability of Large-Crack Fatigue-Crack-Growth Thresholds in Structural Alloys. 3613-3629A
- Application of a Substructure-Based Hardening Model to Copper under Loading Path Changes. 3721-3735A
- Brass Type Shear Bands and their Influence on Texture Formation. 3763-3774A
- Texture Evolution and Mechanical Anisotropy in Dual-Phase Ti3Al-Based Alloy Loaded at 700 °C to 1000 °C. 3775-3786A
- 3803-3815A
- Textures**
- Crystallographic textures in rolled and annealed Fe-Ga and Fe-Al alloys. 2963-2970A
- Thermal analysis**
- Eutectic Grains in Unmodified and Strontium-Modified Hypoeutectic Aluminum-Silicon Alloys. 1829-1837A
- Thermal barrier coatings**
- The Influence of a Martensitic Phase Transformation on Stress Development in Thermal Barrier Coating Systems. 2279-2286A
- Thermal conductivity**
- A Model of the Interfacial Heat Transfer Coefficient for the Aluminum Gravity Die-Casting Process. 721-733B
- Experimental Determination of Solid-Liquid Interfacial Energy for Zn Solid Solution in Equilibrium with the Zn-Al Eutectic Liquid. 3665-3672A
- Thermal cycling**
- Damage Evolution during Thermal Fatigue in Fiber-Reinforced Light-Metal-Matrix Composites. 37-43A
- Cyclic Oxidation Response of Multiphase Niobium-Based Alloys. 589-597A
- Some Studies on the Thermal-Expansion Behavior of C-Fiber, SiC_p and In-Situ Mg₂Si-Reinforced AZ31 Mg Alloy-Based Hybrid Composites. 1167-1176A
- Microstructural Evolution in Laser-Deposited Multilayer Ti-6Al-4V Builds: Part II. Thermal Modeling. 1869-1879A
- The Influence of a Martensitic Phase Transformation on Stress Development in Thermal Barrier Coating Systems. 2279-2286A
- Thermal diffusivity**
- Thermal Diffusivity Measurements of Some Synthetic CaO-Al₂O₃-SiO₂ Slags. 461-469B
- Thermal expansion**
- Damage Evolution during Thermal Fatigue in Fiber-Reinforced Light-Metal-Matrix Composites. 37-43A
- Copper-Zirconium Tungstate Composites Exhibiting Low and Negative Thermal Expansion Influenced by Reinforcement Phase Transformations. 1159-1165A
- Some Studies on the Thermal-Expansion Behavior of C-Fiber, SiC_p and In-Situ Mg₂Si-Reinforced AZ31 Mg Alloy-Based Hybrid Composites. 1167-1176A
- Residual Stresses in High Velocity Oxy-Fuel Metallic Coatings. Modeling of Lattice Parameter in the Ni-Al System. 1807-1814A
- Temperature Effects on the Lattice Constants and Crystal Structure of a Co-27Cr-5Mo Low-Carbon Alloy. 2313-2321A
- 2517-2523A
- Thermal fatigue**
- Quantifying Thermomechanical Fatigue of Light-Metal-Matrix Composites by Mechanical Spectroscopy. 25-35A
- Damage Evolution during Thermal Fatigue in Fiber-Reinforced Light-Metal-Matrix Composites. 37-43A
- Correlation of Microstructure and Thermal-Fatigue Properties of Centrifugally Cast High-Speed Steel Rolls. 481-492A
- Thermal insulation**
- The Influence of a Martensitic Phase Transformation on Stress Development in Thermal Barrier Coating Systems. 2279-2286A
- Thermal stability**
- The Effect of Temperature and Extrusion Speed on The Consolidation of Zirconium-Based Metallic Glass Powder Using Equal-Channel Angular Extrusion. 247-256A
- Synthesis of Nanocrystalline Zn-22 Pct Al Using Cryomilling. Some Studies on the Thermal-Expansion Behavior of C-Fiber, SiC_p and In-Situ Mg₂Si-Reinforced AZ31 Mg Alloy-Based Hybrid Composites. 573-581A
- A Study on the Microstructural Evolution of Al-25 At. Pct V-12.5 At. pct M (M = Cu, Ni, Mn) Powders by Planetary Ball Milling. 1167-1176A
- 1853-1860A
- Thermal stresses**
- Damage Evolution during Thermal Fatigue in Fiber-Reinforced Light-Metal-Matrix Composites. 37-43A
- Fabrication of Carbide-Particle-Reinforced Titanium Aluminide-Matrix Composites by Laser-Engineered Net Shaping. 1133-1140A
- Development of thermal strain in the coherent mushy zone during solidification of aluminum alloys. 2903-2915A
- Continuous Cooling β -to- α Transformation Behaviors of Extra-Pure and Commercially Pure Ti. 3071-3077A
- Thermocouples**
- Experimental and modeling studies of the thermal conditions and magnesium, iron, and copper content on the morphology of the aluminum silicon eutectic in hypoeutectic aluminum silicon alloys. 2981-2991A
- Thermodynamic properties**
- Calculation of Physicochemical Properties in a Ternary System with Miscibility Gap. 715-720B
- Thermodynamics**
- Advancing Towards Constitutive Equations for the Metal Industry via the LEDS Theory. 5-54B
- Fcc/Hcp Martensitic Transformation in the Fe-Mn System: Part II. Driving Force and Thermodynamics of the Nucleation Process. 83-91A
- The Effect of CaF₂ on Thermodynamics of CaO-CaF₂-SiO₂ (-MgO) Slags. 115-120B
- Modeling of the Solubilities of NiO/NiAl₂O₄ and FeO/FeAl₂O₄ in Cryolite Melts at 1300 K. 133-141B
- Communication: The Solubility of Titanium Dioxide in Cryolite-Alumina Melts at 1300 K. 182-186B
- Thermodynamic Evaluation and Optimization of the MnO-Al₂O₃ and MnO-Al₂O₃-SiO₂ Systems and Applications to Inclusion Engineering. 259-268B
- Thermodynamic Study of the Effect of Calcium on Removal of Phosphorus from Silicon by Acid Leaching Treatment. 277-284B
- Advancing Towards Constitutive Equations for the Metal Industry via the LEDS Theory. 369-418A
- Communication: Discussion of "Thermodynamics of Liquid Al-Na Alloys Determined by Using CaF₂ Solid Electrolyte". 393-398B
- Communication: Authors' Reply. 398-400B
- A Comparison of the Molecular Interaction Volume Model with the Subregular Solution Model in Multicomponent Liquid Alloys. 419-424A
- Vapor Pressure Measurement of Zn-Fe Intermetallic Compounds. 487-492B
- A Thermodynamic Model for Deoxidation Equilibria in Steel. Evolution of Secondary Phases in Cr-V Low-Alloy Steels during Aging. 493-507B
- 751-759A
- Critical Thermodynamic Evaluation and Optimization of the FeO-Fe₂O₃-MgO-SiO₂ System. 877-889B
- Critical Thermodynamic Assessment and Modeling of the Fe-Ni-S System. 897-907B
- Study on Polychlorinated Dibenzo-p-Dioxin/Furan Formation in Iron Ore Sintering Process. 983-991B
- Communication: The Pressure of Al₂O and Al in Equilibrium with a Al₂O₃-Al₄C₃ (Saturated) Slag at 1950 °C to 2020 °C. 1011-1013B
- The Effect of Carbon in Slag on Steel Reoxidation and Carbon Analysis by X-Ray Photoelectron Spectroscopy in the CaO-SiO₂-Al₂O₃-MgO-MnO-FeO System. 1087-1095B
- A Numerical Study of Oxidation Behavior during Reactive Atomization and Deposition. 1173-1185B
- A Thermodynamic Description of the Al-Mn-Si System over the Entire Composition and Temperature Ranges. 1613-1628A
- Experimental Investigation and Thermodynamic Calculation of the Phase Equilibria in the Cu-Sn and Cu-Sn-Mn Systems. 1641-1654A
- Characterization of the Nucleation and Growth Behavior of Copper Precipitates in Low-Carbon Steels. 2323-2329A
- The Behavior and Effect of Rare Earth CeO₂ on In-Situ TiC/Al Composite. 2511-2515A
- Temperature Effects on the Lattice Constants and Crystal Structure of a Co-27Cr-5Mo Low-Carbon Alloy. 2517-2523A
- Morphology of fractured domains in brittle fracture. 2651-2661A
- Effect of low-temperature shock compression on the microstructure and strength of copper. 2729-2739A
- Communication: Diffusion coefficients for modeling the heat treatment of Ti-6Al-4V. 3015-3018A
- Determination of Isothermal Transformation Diagrams for Sigma-Phase Formation in Cast Duplex Stainless Steels CD3MN and CD3MWCuN. 3377-3386A
- On Cells and Microbands Formed in an Interstitial-Free Steel during Cold Rolling at Low to Medium Reductions. 3423-3430A
- An Experimental and Theoretical Analysis of the Phase Equilibria in the Fe-Cr-VC System. 3649-3663A
- Thermoelectric properties**
- Thermomechanical Fatigue Behavior of the Third-Generation, Single-Crystal Superalloy TMS-75: Deformation Structure. 1779-1787A
- Thermomechanical treatment**
- Study of the Ferrite Grain Coarsening behind the Transformation Front by Electron Backscattered Diffraction Techniques. Charpy-Impact-Toughness Prediction using an "Effective" Grain Size for Thermomechanically Controlled Rolled Microalloyed Steels. 93-102A
- Effect of Thermomechanical Treatment on the Evolution of Rolling and Recrystallization Textures in Twin-Belt Cast AA5754 Aluminum Alloy. 121-130A
- 1839-1851A
- Failure Mode Analysis and a Mechanism for Hot-Ductility Improvement in the Nb-Microalloyed Steel. 3823-3832A
- Thermophysical properties**
- Phase Stability and Phase Transformations in Plutonium and Plutonium-Gallium Alloys. 2267-2278A
- Thin films**
- Effect of the Presence of Alloying Elements in Interstitial-Free and Low-Carbon Steels on Their Surface Composition after Annealing in Reducing Atmospheres (Dew Point = -30 °C). Defect Structures in Sputtered Thin Films of Transition Metal Disilicides with C11b, C40 and C54 Structures. 2039-2050A
- 2229-2238A
- Thin films. Mechanical properties**
- Grain-Size Effect on Shape-Memory Behavior of Ti_{35.0}Ni_{49.7}Zr_{15.4} Thin Films. 111-119A
- Tin**
- Experimental Investigation and Thermodynamic Calculation of

- the Phase Equilibria in the Cu-Sn and Cu-Sn-Mn Systems. Effect of Sn on Microstructure and Mechanical Properties of Ti-Base Dendrite/Ultrafine-Structured Multicomponent Alloys 1641-1654A
- Tin, Binary systems**
A Comparison of the Molecular Interaction Volume Model with the Subregular Solution Model in Multicomponent Liquid Alloys. 3605-3612A
- Tin base alloys**
Tensile Test Behavior of the Eutectic Sn-Ag Solder Joint in Ball Grid Array Assemblies 419-424A
- Tin compounds**
Communication: Transformation of mechanically alloyed Nb-Sn powder to Nb₃Sn. 3817-3821A
- Titanium**
Comparison of Microstructural Evolution in Laser-Deposited and Arc-Melted In-Situ Ti-TiB Composites. 3009-3012A
Grain size dependence of the activation parameters for plastic deformation: influence of crystal structure, slip system, and rate-controlling dislocation mechanism. 2143-2152A
Continuous Cooling β -to- α Transformation Behaviors of Extra-Pure and Commercially Pure Ti. 2697-2705A
3071-3077A
- Titanium, Reduction (chemical)**
Mechanism of Titanium Sponge Formation in the Kroll Reduction Reactor. 65-74B
- Titanium, Thermal properties**
Partial Atomic Volume and Partial Molar Enthalpy of Formation of the 3d Metals in the Palladium-Based Solid Solutions. 63-70A
- Titanium aluminides**
Dynamic deformation and damage in cast γ -TiAl during Taylor cylinder impact: experiments and model validation. 2557-2566A
Neutron Diffraction Study of Texture Development during Hot Working of Different Gamma-Titanium Aluminide Alloys. 3563-3570A
Texture Evolution and Mechanical Anisotropy in Dual-Phase Ti3Al-Based Alloy Loaded at 700 °C to 1000 °C. 3803-3815A
- Titanium base alloys**
Diffusion Models for Evaporation Losses during Electron-Beam Melting of Alpha/Beta-Titanium Alloys. 235-245B
The Development and Experimental Validation of a Numerical Model of an Induction Skull Melting Furnace. 785-803B
Microstructure, Mechanical Properties, and Fracture Mechanism of As-Cast (Ti_{0.5}Cu_{0.25}Ni_{0.15}Sn_{0.05}Zr_{0.05})(100-x)Mo(x) Composites. 1591-1601A
Co-Deformation Processing and Modeling of In-Situ Multiphase Composites. 1603-1611A
Microstructural Evolution in Laser-Deposited Multilayer Ti-6Al-4V Builds: Part I. Microstructural Characterization. 1861-1867A
Microstructural Evolution in Laser-Deposited Multilayer Ti-6Al-4V Builds: Part II. Thermal Modeling. 1869-1879A
Mechanochemical Processing of Nanocrystalline Ti-6Al-4V Alloy. 1899-1903A
Influence of Microstructure on Tensile and Creep Properties of a New Castable TiAl-Based Alloy. 2087-2102A
The Effect of Lamellar Morphology on Tensile and High-Cycle Fatigue Behavior of Orthorhombic Ti-22Al-27Nb Alloy. 2161-2170A
Coarsening behavior of an alpha-beta titanium alloy. 2809-2819A
Cyclic deformation behavior and dislocation structure of Ti-2 Al. Pct Al single crystals oriented for double prism slip. 2845-2852A
Room-temperature tensile and high-cycle-fatigue strength of fine TiB particulate-reinforced Ti-22Al-27Nb composites. 2971-2979A
Effect of strain reversal on the dynamic spheroidization of Ti-6Al-4V during hot deformation. 2993-3001A
Communication: Diffusion coefficients for modeling the heat treatment of Ti-6Al-4V. 3015-3018A
Dynamic Deformation Behavior and Ballistic Impact Properties of Ti-6Al-4V Alloy Having Equiaxed and Bimodal Microstructures. 3103-3112A
Ductility Exhaustion Mechanisms in Thermally Exposed Thin Sheets of a Near- β Titanium Alloy. 3113-3127A
Understanding the Contributions of Normal-Fatigue and Static Loading to the Dwell Fatigue in a Near-Alpha Titanium Alloy. 3141-3148A
Infrared Brazing Cu and Ti Using a 95Ag-5Al Braze Alloy. 3177-3186A
A Micromechanical Analysis of the Yielding Behavior of Individual Widmanstätten Colonies of an $\alpha + \beta$ Titanium Alloy. 3409-3422A
Effect of Sn on Microstructure and Mechanical Properties of Ti-Base Dendrite/Ultrafine-Structured Multicomponent Alloys. 3605-3612A
- Titanium base alloys, Composite materials**
Correlation of Microstructure and Abrasive and Sliding Wear Resistance of (TiC,SiC)/Ti-6Al-4V Surface Composites Fabricated by High-Energy Electron-Beam Irradiation. 139-151A
Correlation of Microstructure with the Hardness and Wear Resistance of (TiC,SiC)/Ti-6Al-4V Surface Composites Fabricated by High-Energy Electron-Beam Irradiation. 525-534A
Fabrication of Carbide-Particle-Reinforced Titanium Aluminide-Matrix Composites by Laser-Engineered Net Shaping. 1133-1140A
- Titanium base alloys, Mechanical properties**
Characterizing Small Fatigue Cracks in Metallic Alloys. 7-14A
Grain-Size Effect on Shape-Memory Behavior of Ti₅₀Ni₄₈Zr_{1.5} Thin Films. 111-119A
Shear Force Effects on Fatigue Behavior of Ti-6Al-4V. 131-138A
Microstructural Effects on Fatigue and Dwell-Fatigue Crack Growth in α/β Ti-6Al-2Sn-4Zr-2Mo-0.1Si. 163-187A
Study on Notch Fracture of TiAl Alloys at Room Temperature. 439-456A
Influence of Stress State on Cavitation during Hot Working of Ti-6Al-4V. 655-663A
Communications: Ultra-High-Speed Exploding Properties of Ti-6Al-4V Alloy Having Equiaxed and Bimodal Microstructures. 719-724A
- Titanium base alloys, Phase transformations**
Textural Changes during $\beta \rightarrow \alpha$ and $\alpha \rightarrow \beta \rightarrow \alpha$ Transformations in a Near- α Titanium Alloy. 925-938A
- Titanium base alloys, Welding**
Assessment of the Origin of Porosity in Electron-Beam-Welded TA6V Plates. 879-889A
- Titanium borides**
Room-temperature tensile and high-cycle-fatigue strength of fine TiB particulate-reinforced Ti-22Al-27Nb composites. 2971-2979A
- Titanium carbide**
The Behavior and Effect of Rare Earth CeO₂ on In-Situ TiC/Al Composite. 2511-2515A
Hydrogen Absorption of Incoherent TiC Particles in Iron from Environment at High Temperatures. 3155-3163A
- Titanium carbide, Composite materials**
Correlation of Microstructure and Abrasive and Sliding Wear Resistance of (TiC,SiC)/Ti-6Al-4V Surface Composites Fabricated by High-Energy Electron-Beam Irradiation. 139-151A
Correlation of Microstructure with the Hardness and Wear Resistance of (TiC,SiC)/Ti-6Al-4V Surface Composites Fabricated by High-Energy Electron-Beam Irradiation. 525-534A
Correlation of Microstructure with Hardness and Wear Resistance in (TiC,SiC)/Stainless Steel Surface Composites Fabricated by High-Energy Electron-Beam Irradiation. 1029-1038A
Fabrication of Carbide-Particle-Reinforced Titanium Aluminide-Matrix Composites by Laser-Engineered Net Shaping. 1133-1140A
- Titanium compounds**
The Development and Experimental Validation of a Numerical Model of an Induction Skull Melting Furnace. 785-803B
Communication: Observed Dependencies of the Large Thermal-Compressive Response of a NiTi Shape-Memory Alloy Fiber Aluminum Metal Matrix Composite on Maximum Tensile Strain Imposed during a Preceding Room-Temperature Tensile Process. 1403-1406A
Multiscale Structure and Properties of Cast and Deformation Processed Polycrystalline NiTi Shape-Memory Alloys. 2013-2025A
Influence of Microstructure on Tensile and Creep Properties of a New Castable TiAl-Based Alloy. 2087-2102A
Comparison of Microstructural Evolution in Laser-Deposited and Arc-Melted In-Situ Ti-TiB Composites. 2143-2152A
- Titanium compounds, Composite materials**
Fabrication of Carbide-Particle-Reinforced Titanium Aluminide-Matrix Composites by Laser-Engineered Net Shaping. 1133-1140A
- Titanium compounds, Mechanical properties**
Communication: Cavitation Erosion Characteristics of a NiTi Alloy. 356-362A
Study on Notch Fracture of TiAl Alloys at Room Temperature. 439-456A
- Titanium compounds, Phase transformations**
Shape Memory Properties of Ni-Ti Based Melt-Spun Ribbons. 761-770A
- Titanium diboride**
Co-Deformation Processing and Modeling of In-Situ Multiphase Composites. 1603-1611A
- Titanium dioxide**
Solid-State Reactions during Heating Mechanically Milled Al/TiO₂ Composite Powders. 2115-2125A
- Titanium dioxide, Reactions (chemical)**
Communication: The Solubility of Titanium Dioxide in Cryolite-Alumina Melts at 1300 K. 182-186B
- Titanium steels**
Precise Determination of the Activation Energy for Desorption of Hydrogen in Two Ti-Added Steels by a Single Thermal-Desorption Spectrum. 587-597B
- Tomography**
Focused Ion-Beam Tomography. 1935-1943A
- Tool steels**
Wear Resistance and High-Temperature Compression Strength of Fcc CuCoNiCrAl_{0.5}Fe Alloy with Boron Addition. 1465-1469A
- Tool wear**
Residual Stress-Affected Diffusion during Plasma Nitriding of Tool Steels. 3523-3530A
- Topography**
Characterization of Surface Deformation around Vickers Indents in Monocrystalline Materials. 2247-2255A
Atomic force microscopy studies of fracture surfaces of composition B energetic materials. 2675-2079A
- Topology**
Quantitative Characterization of the Three-Dimensional Microstructure of Polycrystalline Al-Sn using X-Ray Microtomography. 1953-1961A
- Torque**
Communication: A Computational Assessment of Viscosity Measurement in Rotating Viscometers through Detailed Numerical Simulation. 805-809B
- Torsion tests**
Microstructural Characterization of Secondary-Phase Particles in a Hot-Deformed Al-Cu-Mg-Zr Alloy. 293-300A
Effects of Martensite Morphology and Tempering on Dynamic Deformation Behavior of Dual-Phase Steels. 2371-2382A
Effect of strain reversal on the dynamic spheroidization of Ti-6Al-4V during hot deformation. 2993-3001A
Dynamic Deformation Behavior and Ballistic Impact Properties of Ti-6Al-4V Alloy Having Equiaxed and Bimodal Microstructures. 3103-3112A
- Toughness**
Quench Embrittlement of Hardened 5160 Steel as a Function of Austenitizing Temperature. 153-162A
Effect of Mg₂Si Particles on the Elevated Temperature Tensile Properties of Squeeze-Cast Mg-Al Alloys. 1629-1632A
A Comparison between Growth Morphology of "Eutectic" Cells/

| | | | |
|---|--|--|---|
| Dendrites and Single-Phase Cells/Dendrites. Mechanical Properties of Al-60 Pct SiCp Composites Alloyed with Mg. | 1632-1635A 2127-2141A | Superalloys. Oxide Defects in a Vacuum Investment-Cast Ni-Based Turbine Blade. Influence of Microstructure on Tensile and Creep Properties of a New Castable TiAl-Based Alloy. | 1669-1679A 2063-2071A 2087-2102A |
| Trajectories Nickel Droplet Settling Behavior in an Electric Furnace | 839-845B | Turbine blades, Mechanical properties Effects of Heat Treatment and Testing Temperature on Fracture Mechanics Behavior of Low-Si CA-15 Stainless Steel. | 471-480A |
| Transformation temperature Effect of Simulated Thermal Cycles on the Microstructure of the Heat-Affected Zone in HSLA-80 and HSLA-100 Steel Plates. Shear localization-martensitic transformation interactions in Fe-Cr-Ni monocrystal. Study of the Ni41.3Ti38.7Nb20 wide transformation hysteresis shape-memory alloy. | 985-996A 2575-2586A 2783-2788A | Turbine disks Characterization and Modeling of Quenching-Induced Residual Stresses in the Nickel-Based Superalloy IN718. | 1703-1713A |
| Transgranular fracture Effect of Boron on the Low-Cycle Fatigue Behavior and Deformation Structure of INCONEL 718 at 650°C Tensile Test Behavior of the Eutectic Sn-Ag Solder Joint in Ball Grid Array Assemblies | 3477-3487A 3817-3821A | Turbines The Influence of a Martensitic Phase Transformation on Stress Development in Thermal Barrier Coating Systems. | 2279-2286A |
| Transition metals Defect Structures in Cosputtered Thin Films of Transition Metal Disilicides with C11b, C40 and C54 Structures. | 2229-2238A | Turbochargers The Development and Experimental Validation of a Numerical Model of an Induction Skull Melting Furnace. | 785-803B |
| Trapping Hydrogen Absorption of Incoherent TiC Particles in Iron from Environment at High Temperatures | 3155-3163A | Turbulence Nickel Droplet Settling Behavior in an Electric Furnace Spot Turbulence, Breakup, and Coalescence of Bubbles Released from a Porous Plug Injector into a Gas-Stirred Ladle | 839-845B 949-956B |
| Triaxiality Influence of Stress State on Cavitation during Hot Working of Ti-6Al-4V. Microstructural Banding and Failure of a Stainless Steel. Void Nucleation by Inclusion Cracking. Communication: The Dependence of Cavity-Growth Rate on Stress Triaxiality. | 655-663A 1317-1324A 1745-1755A 2187-2190A | Turbulent flow Simulation of Flow in a Continuous Galvanizing Bath: Part I. Thermal Effects of Ingot Addition. Study of Transient Flow and Particle Transport in Continuous Steel Caster Molds: Part I. Fluid Flow. Study of Transient Flow and Particle Transport in Continuous Steel Caster Molds: Part II. Particle Transport. The Development and Experimental Validation of a Numerical Model of an Induction Skull Melting Furnace. Physical and Mathematical Determination of the Influence of Input Temperature Changes on the Molten Steel Flow Characteristics in Slab Tundishes Computational and Experimental Study of Turbulent Flow in a 0.4-Scale Water Model of a Continuous Steel Caster Thermomechanical Finite-Element Model of Shell Behavior in Continuous Casting of Steel Effects of the entrained surface film on the reliability of castings. | 161-170B 685-702B 703-714B 785-803B 957-966B 967-982B 1151-1172B 2893-2902A |
| Trinitrotoluene Atomic force microscopy studies of fracture surfaces of composition B energetic materials. | 2675-2079A | Twinning Advancing Towards Constitutive Equations for the Metal Industry via the LEDS Theory. Advancing Towards Constitutive Equations for the Metal Industry via the LEDS Theory. Low-Cycle Fatigue Behavior of ULTIMET Alloy. Deformation and Damage Mechanisms of Zinc Coatings on Hot-Dip Galvanized Steel Sheets: Part II. Damage Modes. Communication: Mechanical Behavior of a Cryomilled Nanostructured Al-7.5 pct Mg Alloy. The Influence of Texture, Strain Rate, Temperature, and Chemistry on the Mechanical Behavior of Hafnium. Defect Structures in Cosputtered Thin Films of Transition Metal Disilicides with C11b, C40 and C54 Structures. Dislocation mechanics-based constitutive equations. Laser-induced shock compression of copper: orientation and pressure decay effects. Effect of low-temperature shock compression on the microstructure and strength of copper. Microstructure Development during High Velocity Deformation A Semiautomated Electron Backscatter Diffraction Technique for Extracting Reliable Twin Statistics Brass Type Shear Bands and their Influence on Texture Formation | 5-54B 369-418A 785-796A 813-823A 947-949A 1999-2011A 2229-2238A 2547-2555A 2633-2646A 2729-2739A 3091-3101A 3745-3751A 3775-3786A |
| TRIP steels Effect of Microstructure on the Stability of Retained Austenite in Transformation-Induced-Plasticity Steels. Austenite Formation during Intercritical Annealing | 2331-2341A 3363-3375A | Ultimate tensile strength Oxide Dispersion Strengthening of Nickel Electrodeposits for Microsystem Applications. Tensile properties and microstructure of Haynes 25 alloy after aging at elevated temperatures for extended times. Tensile behavior of friction-stir-welded Al 6061-T651. Quality Assessment of Artificially Aged A357 Aluminum Alloy Cast Ingots by Introducing Approximate Expressions of the Quality Index QD Effects of Temperature and Strain Rate on Tensile Properties and Activation Energy for Dynamic Strain Aging in Alloy 625 | 265-277A 279-286A 825-837A 555-562A 825-837A 1187-1210A 1223-1235A 3377-3386A 1151-1158A |
| True strain Quantitative Analysis of Texture Evolution in Cold-Rolled, Continuous-Cast AA 5xxx-Series Aluminum Alloys. Microstructure Transformation from Lamellar to Equiaxed Microduplex through Equal-Channel Angular Pressing in an Al-33 Pct Cu Eutectic Alloy. High-Strain-Rate Superplastic Behavior of Equal-Channel Angular-Pressed 5083 Al-0.2 Wt Pct Sc. | 265-277A 279-286A 825-837A | Ultrafines Effect of Sn on Microstructure and Mechanical Properties of Ti-Base Dendrite/Ultrafine-Structured Multicomponent Alloys | 2351-2360A 2767-2781A 2829-2835A 3079-3089A 3129-3139A |
| True stress Transition of Dominant Diffusion Process during Superplastic Deformation in AZ61 Magnesium Alloys. High-Strain-Rate Superplastic Behavior of Equal-Channel Angular-Pressed 5083 Al-0.2 Wt Pct Sc. | 555-562A 825-837A | Ultrahigh vacuum Hydrogen Absorption of Incoherent TiC Particles in Iron from Environment at High Temperatures | 3155-3163A |
| TTT curves Coupled-Solute Drag Effects on Ferrite Formation in Fe-C-X Systems. Molybdenum Accumulation at Ferrite:Austenite Interfaces during Isothermal Transformation of an Fe-0.24 Pct C-0.93 Pct Mo Alloy. Determination of Isothermal Transformation Diagrams for Sigma-Phase Formation in Cast Duplex Stainless Steels CD3MN and CD3MWCuN | 1187-1210A 1223-1235A 3377-3386A | Uniform attack (corrosion) Effect of Different Cr Contents on Tensile and Corrosion Behaviors of 0.13 Pct N-Containing CD4MCU Cast Duplex Stainless Steels | 3431-3438A |
| Tubes, Metal working Failure in Internally Pressurized Bent Tubes. | 1151-1158A | Unit cell Communication: Determination of γ Phase Lattice Parameter Based on the Chemical Concentration of Its Sublattices in Ni-Base Superalloys. | 2171-2172A |
| Tundishes Inertial and Buoyancy Driven Water Flows under Gas Bubbling and Thermal Stratification Conditions in a Tundish Model. Fluid Flows in Metallurgy - Friend or Foe? Physical and Mathematical Determination of the Influence of Input Temperature Changes on the Molten Steel Flow Characteristics in Slab Tundishes Computational and Experimental Study of Turbulent Flow in a 0.4-Scale Water Model of a Continuous Steel Caster | 247-257B 417-437B 957-966B 967-982B | Unit cell, Mechanical properties A Hybrid Micromechanical-Macroscopic Model for the Analysis of the Tensile Behavior of Cavitating Materials. | 1141-1149A |
| Tungstates, Composite materials Copper-Zirconium Tungstate Composites Exhibiting Low and Negative Thermal Expansion Influenced by Reinforcement Phase Transformations. | 1159-1165A | Vacuum arc melting Model-Based Melt Rate Control during Vacuum Arc Remelting of Alloy 718. | 101-113B |
| Tungsten Temperature-Dependent Variability in Lifetime Prediction of Thermally Activated Systems. Effect of dissolved tungsten on the deformation of 70Ni-30Fe alloys. Deformation and Failure of Zr57Nb5Al10Cu15.4Ni12.6/W Particle Composites Under Quasi-Static and Dynamic Compression | 1471-1476A 2821-2828A 3439-3444A | Vacuum degassing Continuous Oxygen Steelmaking with Copper-, Tin-, and Zinc-Contaminated Scrap. | 663-674B |
| Tungsten base alloys Quantitative Characterization of Microstructures of Liquid-Phase-Sintered Two-Phase Materials. On the Isotropy of the Dynamic Mechanical and Failure Properties of Swaged Tungsten Heavy Alloys Modeling of Distortion after Densification during Liquid-Phase Sintering | 1881-1888A 3787-3795A 3833-3841A | | |
| Tungsten carbide Communication: A Brick-Wall Model for Calculating Young's Modulus of a Particulate Composite. | 2191-2192A | | |
| Turbine blades The Development and Experimental Validation of a Numerical Model of an Induction Skull Melting Furnace. Mechanism of Primary MC Carbide Decomposition in Ni-Base | 785-803B | | |

| | | |
|--|------------|--|
| Vanadium | | |
| Salt Roasting of Suncor Oil Sands Fly Ash | 1051-1058B | |
| Communication: Diffusion coefficients for modeling the heat treatment of Ti-6Al-4V. | 3015-3018A | |
| An Experimental and Theoretical Analysis of the Phase Equilibria in the Fe-Cr-VC System | 3649-3663A | |
| Vanadium, Thermal properties | | |
| Partial Atomic Volume and Partial Molar Enthalpy of Formation of the 3d Metals in the Palladium-Based Solid Solutions. | 63-70A | |
| Vanadium steels | | |
| Gas nitriding of high vanadium steels - experiments and simulations. | 2799-2802A | |
| Vapor | | |
| Condensation of Zinc Vapor on Solid Media in Zn (g)-CO-CO ₂ -Ar Mixtures. | 625-631B | |
| Vapor phases | | |
| Communication: Discussion of "Thermodynamics of Liquid Al-Na Alloys Determined by Using CaF ₂ Solid Electrolyte". | 393-398B | |
| Communication: Authors' Reply. | 398-400B | |
| Vapor pressure | | |
| Vapor Pressure Measurement of Zn-Fe Intermetallic Compounds. | 487-492B | |
| Communication: The Pressure of Al ₂ O ₃ and Al in Equilibrium with a Al ₂ O ₃ -Al ₂ C ₃ (Saturated) Slag at 1950°C to 2020°C | 1011-1013B | |
| Vaporizing | | |
| Thermodynamic Properties and Diffusion Thermodynamic Factors in B ₂ -NiAl | 867-876B | |
| Vibration | | |
| Communication: Resonant Vibration Behavior of an Al-3.8Cu-0.8Li-0.3Mg Alloy. | 952-957A | |
| Vickers indentation | | |
| Defect Structures and Room Temperature Mechanical Properties of C15 Laves Phases in Zr-Nb-Cr and Zr-Hf-Cr Alloy Systems | 3469-3476A | |
| Viscometers | | |
| Communication: A Computational Assessment of Viscosity Measurement in Rotating Viscometers through Detailed Numerical Simulation. | 805-809B | |
| Viscosity | | |
| Amphoteric Behavior of Alumina in Viscous Flow and Structure of CaO-SiO ₂ (-MgO)-Al ₂ O ₃ Slags. | 269-275B | |
| Freeze-Off Limits in Transient Liquid-Phase Infiltration. | 641-653A | |
| Communication: A Computational Assessment of Viscosity Measurement in Rotating Viscometers through Detailed Numerical Simulation. | 805-809B | |
| Semi-Solid Rapid Compression Testing of Spray-Formed Hypereutectic Al-Si Alloys. | 899-910A | |
| Modeling of Distortion after Densification during Liquid-Phase Sintering | 3833-3841A | |
| Viscous flow | | |
| Amphoteric Behavior of Alumina in Viscous Flow and Structure of CaO-SiO ₂ (-MgO)-Al ₂ O ₃ Slags. | 269-275B | |
| Voids | | |
| Mechanisms of Strain Accumulation and Damage Development during Creep of Prestrained 316 Stainless Steels. | 563-571A | |
| Void Nucleation by Inclusion Cracking. | 1745-1755A | |
| Tensile Test Behavior of the Eutectic Sn-Ag Solder Joint in Ball Grid Array Assemblies | 3817-3821A | |
| Volatilization | | |
| Kinetics of As, Sb, Bi and Pb Volatilization from Industrial Copper Matte during Ar + O ₂ Bubbling. | 651-661B | |
| Volume fraction | | |
| Quantitative Analysis of Texture Evolution in Cold-Rolled, Continuous-Cast AA 5xxx-Series Aluminum Alloys. | 265-277A | |
| Fiber Texture and Substructural Features in the Caliber-Rolled Low-Carbon Steels. | 665-677A | |
| Determination of Volume Fractions of Texture Components with Standard Distributions in Euler Space. | 1075-1086A | |
| Effect of Clustering of Precipitates on Grain Growth. | 1097-1103A | |
| A Hybrid Micromechanical-Macroscale Model for the Analysis of the Tensile Behavior of Cavitating Materials. | 1141-1149A | |
| A Numerical Study of Oxidation Behavior during Reactive Atomization and Deposition | 1173-1185B | |
| Microstructural Banding and Failure of a Stainless Steel. | 1317-1324A | |
| Quantitative Characterization of Microstructures of Liquid-Phase-Sintered Two-Phase Materials. | 1881-1888A | |
| Modeling the Age-Hardening Behavior of Al-Si-Cu Alloys. | 2407-2418A | |
| The effect of grain size on low-cycle fatigue behavior of Al-2024 polycrystalline alloy. | 2725-2728A | |
| Coarsening behavior of an alpha-beta titanium alloy. | 2809-2819A | |
| Effect of dissolved tungsten on the deformation of 70Ni-30Fe alloys. | 2821-2828A | |
| Coarsening Behavior of Ni ₃ Ga Precipitates in Ni-Ga Alloys: Dependence of Microstructure and Kinetics on Volume Fraction | 3063-3069A | |
| The Influence of Strontium on Porosity Formation in Al-Si Alloys | 3531-3541A | |
| Quantitative Analysis of Texture Evolution of Cold-Rolled Direct-Chill-Cast and Continuous-Cast AA5052 and AA5182 Aluminum Alloys during Isothermal Annealing | 3613-3629A | |
| Volumetric analysis | | |
| Communication: Properties of MgOHCl. | 406-408B | |
| Vortices | | |
| Grain Refinement Induced by Electromagnetic Stirring: A Dendrite Fragmentation Criterion | 3201-3210A | |
| Warm rolling | | |
| Crystallographic textures in rolled and annealed Fe-Ga and Fe- | | |
| Al alloys. | 2963-2970A | |
| Water quenching | | |
| Coarsening behavior of an alpha-beta titanium alloy. | 2809-2819A | |
| Waxes | | |
| Simulation of Die Filling for the Wax Injection Process: Part 1. Models for Material Behavior. | 755-759B | |
| Simulation of Die Filling for the Wax Injection Process: Part II. Numerical Simulation. | 761-768B | |
| Wear mechanisms | | |
| Correlation of Microstructure and Abrasive and Sliding Wear Resistance of (TiC,SiC)/Ti-6Al-4V Surface Composites Fabricated by High-Energy Electron-Beam Irradiation. | 139-151A | |
| Solid Particle Erosion of Al Alloy and Al-Alloy Composites: Effect of Heat Treatment and Angle of Impingement. | 1369-1379A | |
| Wear Behavior, Microstructure, and Dimensional Stability of As-Cast Zinc-Aluminum/SiC (Metal Matrix Composites) Alloys. | 1579-1590A | |
| Wear rate | | |
| Solid Particle Erosion of Al Alloy and Al-Alloy Composites: Effect of Heat Treatment and Angle of Impingement. | 1369-1379A | |
| Wear Behavior, Microstructure, and Dimensional Stability of As-Cast Zinc-Aluminum/SiC (Metal Matrix Composites) Alloys. | 1579-1590A | |
| Wear resistance | | |
| Correlation of Microstructure and Abrasive and Sliding Wear Resistance of (TiC,SiC)/Ti-6Al-4V Surface Composites Fabricated by High-Energy Electron-Beam Irradiation. | 139-151A | |
| Correlation of Microstructure with the Hardness and Wear Resistance of (TiC,SiC)/Ti-6Al-4V Surface Composites Fabricated by High-Energy Electron-Beam Irradiation. | 525-534A | |
| Correlation of Microstructure with Hardness and Wear Resistance in (TiC,SiC)/Stainless Steel Surface Composites Fabricated by High-Energy Electron-Beam Irradiation. | 1029-1038A | |
| Wear Resistance and High-Temperature Compression Strength of Fcc CuCoNiCrAl _{0.5} Fe Alloy with Boron Addition. | 1465-1469A | |
| Mechanical Properties of Al-60 Pct SiCp Composites Alloyed with Mg. | 2127-2141A | |
| Residual Stress-Affected Diffusion during Plasma Nitriding of Tool Steels | 3523-3530A | |
| Wear tests | | |
| Wear Behavior, Microstructure, and Dimensional Stability of As-Cast Zinc-Aluminum/SiC (Metal Matrix Composites) Alloys. | 1579-1590A | |
| Mechanical Properties of Al-60 Pct SiCp Composites Alloyed with Mg. | 2127-2141A | |
| Weight reduction | | |
| Formability and Strength of Friction-Stir-Welded Aluminum Sheets | 3461-3468A | |
| Weld defects | | |
| Material Flow Patterns and Cavity Model in Friction-Stir Welding of Aluminum Alloys. | 153-160B | |
| Weld metal | | |
| Control of Residual Stresses Affecting Fatigue Life of Pulsed Current Gas-Metal-Arc Weld of High-Strength Aluminum Alloy. | 2439-2444A | |
| Communication: Ferrite Number as a Function of the Larson-Miller Parameter for Austenitic Stainless Steel Metals after Creep Testing | 3631-3633A | |
| Weld metal pool | | |
| Computational Modeling of Laser Welding of Cu-Ni Dissimilar Couple. | 339-350B | |
| The Microstructural Response of Delta-Stabilized Plutonium to Pulsed Laser Welding. | 2445-2454A | |
| Marangoni convection in weld pool in CO ₂ -Ar-shielded gas thermal arc welding. | 2861-2867A | |
| Welded joints | | |
| Material Flow Patterns and Cavity Model in Friction-Stir Welding of Aluminum Alloys. | 153-160B | |
| Characterization of Plastic Flow and Resulting Microtextures in a Friction Stir Weld. | 777-783B | |
| Microstructural Evolution in the Heat-Affected Zone of a Friction Stir Weld. | 1487-1499A | |
| Control of Residual Stresses Affecting Fatigue Life of Pulsed Current Gas-Metal-Arc Weld of High-Strength Aluminum Alloy. | 2439-2444A | |
| The Microstructural Response of Delta-Stabilized Plutonium to Pulsed Laser Welding. | 2445-2454A | |
| Evolution of Microstructure and Texture in Mg-Al-Zn Alloys during Electron-Beam and Gas Tungsten Arc Welding. | 2455-2469A | |
| Tensile behavior of friction-stir-welded Al 6061-T651. | 2829-2835A | |
| Tensile behavior of friction-stir-welded A356-T6/Al 6061-T651 Bi-alloy plate. | 2837-2843A | |
| Marangoni convection in weld pool in CO ₂ -Ar-shielded gas thermal arc welding. | 2861-2867A | |
| Communication: Texture characterization of autogenous Nd:YAG laser welds in AA5182-O and AA6111-T4 aluminum alloys. | 3032-3038A | |
| Mechanism of Resistance Microwelding of Crossed Fine Nickel Wires | 3165-3176A | |
| Welded joints, Microstructure | | |
| Effect of Simulated Thermal Cycles on the Microstructure of the Heat-Affected Zone in HSLA-80 and HSLA-100 Steel Plates. | 985-996A | |
| Welded joints, Physical properties | | |
| Assessment of the Origin of Porosity in Electron-Beam-Welded TA6V Plates. | 879-889A | |
| Welding current | | |
| The Effects of Strain Rate and Welding Current Mode on the | | |

- Dynamic Impact Behavior of Plasma-Arc-Welded 304L Stainless Steel Weldments. 1501-1515A
- Mechanism of Resistance Microwelding of Crossed Fine Nickel Wires 3165-3176A
- Welding electrodes, Corrosion**
- Electrode Pitting in Resistance Spot Welding of Aluminum Alloy 5182. 217-226A
- Welding parameters**
- Material Flow Patterns and Cavity Model in Friction-Stir Welding of Aluminum Alloys. 153-160B
- Mechanism Governing Nitrogen Absorption by Steel Weld Metal during Laser Welding. 331-338B
- Assessment of the Origin of Porosity in Electron-Beam-Welded TA6V Plates. 879-889A
- The Effects of Strain Rate and Welding Current Mode on the Dynamic Impact Behavior of Plasma-Arc-Welded 304L Stainless Steel Weldments. 1501-1515A
- The Microstructural Response of Delta-Stabilized Plutonium to Pulsed Laser Welding. 2445-2454A
- Tensile behavior of friction-stir-welded Al 6061-T651. 2829-2835A
- Mechanism of Resistance Microwelding of Crossed Fine Nickel Wires 3165-3176A
- Weldments**
- The Effects of Strain Rate and Welding Current Mode on the Dynamic Impact Behavior of Plasma-Arc-Welded 304L Stainless Steel Weldments. 1501-1515A
- Fracture Behavior of Thick-Section Weldment in Fe-12Cr-12Ni-10Mn-0.24N Stainless Steel at Liquid Helium Temperature 3797-3802A
- Wettability**
- Influence of Chemical Compositions of Slag and Graphite on the Phenomena Occurring in the Graphite/Slag Interfacial Region. 75-83B
- The Effect of Temperature, Matrix Alloying and Substrate Coatings on Wettability and Shear Strength of Al/Al₂O₃ Couples. 911-923A
- The Behavior and Effect of Rare Earth CeO₂ on In-Situ TiC/Al Composite. 2511-2515A
- Nucleation of Solid Aluminum on Inclusion Particles Injected into Al-Si-Fe Alloys 3233-3250A
- Wetting**
- Influence of Chemical Compositions of Slag and Graphite on the Phenomena Occurring in the Graphite/Slag Interfacial Region. 75-83B
- Reactive Wetting of SiO₂ Substrates by Molten Al. 583-588A
- Effect of Surface Modification of High-Density Polyethylene by Direct Current and Radio Frequency Glow Discharge on Wetting and Adhesion Characteristics. 865-877A
- The Effect of Temperature, Matrix Alloying and Substrate Coatings on Wettability and Shear Strength of Al/Al₂O₃ Couples. 911-923A
- Infrared Brazing Cu and Ti Using a 95Ag-5Al Braze Alloy 3177-3186A
- Widmanstatten structure**
- Microstructural Evolution in Laser-Deposited Multilayer Ti-6Al-4V Builds: Part I. Microstructural Characterization. 1861-1867A
- Microstructural modification of as-cast NiAl bronze by friction stir processing. 2951-2961A
- A Micromechanical Analysis of the Yielding Behavior of Individual Widmanstatten Colonies of an $\alpha + \beta$ Titanium Alloy 3409-3422A
- Role of Carbon and Alloying Elements in the Formation of Bainitic Ferrite 3693-3700A
- Widmanstatten Ferrite Plate Formation in Low-Carbon Steels 3701-3706A
- Wire, Mechanical properties**
- Communications: Ultra-High-Speed Exploding Properties of Ti-6Al-4V Alloy Having Equiaxed and Bimodal Microstructures. 719-724A
- Work hardening**
- A Tribute to Terence E. Mitchell. 2203-2205A
- Effects of Temperature and Strain Rate on Tensile Properties and Activation Energy for Dynamic Strain Aging in Alloy 625 3129-3139A
- Work softening**
- Effect of low-temperature shock compression on the microstructure and strength of copper. 2729-2739A
- Wustite**
- Microrreaction Mechanism in Reduction of Magnetite to Wustite. 517-522B
- Communication: The Observation and Identification of the Oxide Film on the Creep Cavity Wall of Type 316L Stainless Steel 3331-3333A
- X ray diffraction**
- Studies of Lattice Imperfections in Deformed Aluminum-Based Lithium Alloys by X-Ray Diffraction 3319-3322A
- X ray microscopy**
- The Three-Dimensional X-ray Crystal Microscope: A New Tool for Materials Characterization. 1963-1967A
- Yield strength**
- Advancing Towards Constitutive Equations for the Metal Industry via the LEDS Theory. 5-54B
- Grain-Size Effect on Shape-Memory Behavior of Ti₃₅Ni₄₉Zr_{15.4} Thin Films. 111-119A
- Effect of Temperature and Strain Rate on the Compressive Flow of Aluminum Composites Containing Submicron Alumina Particles. 287-292A
- A New Quality Index for Characterizing Aluminum Cast Alloys with Regard to Aircraft Structure Design Requirements. 301-308A
- Effect of Microstructure on Mechanical Properties of As-Cast Mg-Al Alloys. 309-319A
- Advancing Towards Constitutive Equations for the Metal Industry via the LEDS Theory. 369-418A
- Correlation of the Microstructure and Mechanical Properties of Oxide-Dispersion-Strengthened Coppers Fabricated by Internal Oxidation. 493-502A
- Deformation and Recrystallization Behavior during Hot Working of a Coarse-Grain, Nickel-Base Superalloy Ingot Material. 679-693A
- Communication: Resonant Vibration Behavior of an Al-3.8Cu-0.8Li-0.3Mg Alloy. 952-957A
- The Tensile Response of a Fine-Grained AA5754 Alloy Produced by Asymmetric Rolling and Annealing. 997-1006A
- Fine Carbide-Strengthened 3Cr-3WV Ta Bainitic Steel. 1281-1288A
- Communication: Constitutive Equation for Structural Steels. 1410-1414A
- The Effects of Strain Rate and Welding Current Mode on the Dynamic Impact Behavior of Plasma-Arc-Welded 304L Stainless Steel Weldments. 1501-1515A
- Microstructure, Mechanical Properties, and Fracture Mechanism of As-Cast (Ti_{0.5}Cu_{0.25}Ni_{0.15}Sn_{0.05}Zr_{0.05})(100-x)Mo(x) Composites. 1591-1601A
- Co-Deformation Processing and Modeling of In-Situ Multiphase Composites. 1603-1611A
- The Influence of Texture, Strain Rate, Temperature, and Chemistry on the Mechanical Behavior of Hafnium. 1999-2011A
- The Effect of Lamellar Morphology on Tensile and High-Cycle Fatigue Behavior of Orthorhombic Ti-22Al-27Nb Alloy. 2161-2170A
- Oxide Dispersion Strengthening of Nickel Electrodeposits for Microsystem Applications. 2351-2360A
- An Eulerian Finite-Element Model for Determination of Deformation State of a Copper Subjected to Orthogonal Cutting. 2393-2400A
- Modeling the Age-Hardening Behavior of Al-Si-Cu Alloys. 2407-2418A
- High-pressure, laser-driven deformation of an aluminum alloy. Grain size dependence of the activation parameters for plastic deformation: influence of crystal structure, slip system, and rate-controlling dislocation mechanism. 2625-2631A
- Molecular-dynamics study of mechanical deformation in nanocrystalline aluminum. 2697-2705A
- Microstructure and mechanical properties of a 2000 MPa Co-free maraging steel after aging at 753 K. 2719-2723A
- Tensile properties and microstructure of Haynes 25 alloy after aging at elevated temperatures for extended times. 2747-2755A
- Effect of dissolved tungsten on the deformation of 70Ni-30Fe alloys. 2767-2781A
- Tensile behavior of friction-stir-welded Al 6061-T651. 2821-2828A
- Microstructure evolution and mechanical behavior of bulk copper obtained by consolidation of micro- and nanopowders using equal-channel angular extrusion. 2829-2835A
- Communication: A thousandfold creep strengthening by Ca addition in die-cast AM50 magnesium alloy. 2935-2949A
- Quality Assessment of Artificially Aged A357 Aluminum Alloy Cast Ingots by Introducing Approximate Expressions of the Quality Index QD. 3029-3032A
- Effects of Temperature and Strain Rate on Tensile Properties and Activation Energy for Dynamic Strain Aging in Alloy 625 3079-3089A
- Effect of Sn on Microstructure and Mechanical Properties of Ti-Base Dendrite/Ultrafine-Structured Multicomponent Alloys 3129-3139A
- Application of a Substructure-Based Hardening Model to Copper under Loading Path Changes. 3605-3612A
- Texture Evolution and Mechanical Anisotropy in Dual-Phase Ti3Al-Based Alloy Loaded at 700 °C to 1000 °C. 3763-3774A
- 3803-3815A
- Yield stress**
- Yield Behavior of Commercial Al-Si Alloys in the Semisolid State. 1187-1202B
- Second-Order Stresses and Strains in Heterogeneous Steels: Self-Consistent Modeling and X-Ray Diffraction Analysis. 2361-2369A
- Dislocation mechanics-based constitutive equations. 2547-2555A
- The influence of explosive-driven 'Taylor-wave' shock prestraining on the structure/property behavior of 304 stainless steel. 2617-2624A
- Tensile and Fatigue Behavior of Al-Based Metal Matrix Composites Reinforced with Continuous Carbon or Alumina Fibers: Part II. Quasi-Unidirectional Composite Cross-Ply Laminates. 3307-3317A
- A Micromechanical Analysis of the Yielding Behavior of Individual Widmanstatten Colonies of an $\alpha + \beta$ Titanium Alloy 3409-3422A
- Variability of Large-Crack Fatigue-Crack-Growth Thresholds in Structural Alloys 3721-3735A
- Zinc**
- Vapor Pressure Measurement of Zn-Fe Intermetallic Compounds. 487-492B
- Condensation of Zinc Vapor on Solid Media in Zn (g)-CO-CO₂-Ar Mixtures. 625-631B
- Experimental Study of Phase Equilibria in the Al-Fe-Zn-O System in Air. 633-642B
- Zinc, Binary systems**
- A Comparison of the Molecular Interaction Volume Model with the Subregular Solution Model in Multicomponent Liquid Alloys. 419-424A
- Zinc, Mechanical properties**
- Deformation and Damage Mechanisms of Zinc Coatings on Hot-Dip Galvanized Steel Sheets: Part II. Damage Modes. 813-823A
- Zinc, Microstructure**
- Deformation and Damage Mechanisms of Zinc Coatings on Hot-Dip Galvanized Steel Sheets: Part I. Deformation Modes. 797-811A
- Zinc, Recovering**
- Zinc Recovery from Spent ZnO Catalyst by Carbon in the Presence of Calcium Carbonate. 55-63B
- Zinc base alloys**
- Wear Behavior, Microstructure, and Dimensional Stability of As-Cast Zinc-Aluminum/SiC (Metal Matrix Composites) Alloys. 1579-1590A
- Microstructural Evolution of Predeformed SiCp/ZA27 Composites during Partial Remelting. 2073-2085A
- A Novel Experiment for the Study of Substrate-Induced Nucleation in Metallic Alloys: Application to Zn-Al. 3543-3550A
- Experimental Determination of Solid-Liquid Interfacial Energy

| | | | |
|--|------------|--|--------------------------|
| for Zn Solid Solution in Equilibrium with the Zn-Al Eutectic Liquid | 3665-3672A | sion | 3439-3444A |
| Zinc base alloys, Microstructure | | Two-Layered Zr-Base Amorphous Alloy/Metal Surface Composites Fabricated by High Energy Electron-Beam Irradiation | 3455-3460A |
| Synthesis of Nanocrystalline Zn-22 Pct Al Using Cryomilling. | 573-581A | Defect Structures and Room Temperature Mechanical Properties of C15 Laves Phases in Zr-Nb-Cr and Zr-Hf-Cr Alloy Systems | 3469-3476A 3489-3498A |
| Zinc coatings | | Fatigue and Fracture Behavior of Bulk Metallic Glass | |
| Effect of Ternary Additions on the Structure and Properties of Coatings Produced by a High Aluminum Galvanizing Bath | 3707-3720A | In-Situ Microfracture Observation of Strip-Cast Zr-Ti-Cu-Ni-Be Bulk Metallic Glass Alloys | 3753-3761A |
| Zirconium | | Zirconium base alloys, Mechanical properties | |
| The Development and Experimental Validation of a Numerical Model of an Induction Skull Melting Furnace. | 785-803B | Thermal-Imaging Technologies for Detecting Damage during High-Cycle Fatigue. | 15-23A |
| Effect of Zr and B on Castability of Ni-Based Superalloy IN792. | 1337-1342A | Deformation Behavior of Zr ₃ Al-Nb Alloys II: Indentation Creep Studies. | 205-216A |
| Grain size dependence of the activation parameters for plastic deformation: influence of crystal structure, slip system, and rate-controlling dislocation mechanism. | 2697-2705A | The Effect of Temperature and Extrusion Speed on The Consolidation of Zirconium-Based Metallic Glass Powder Using Equal-Channel Angular Extrusion. | 247-256A |
| A Semiautomated Electron Backscatter Diffraction Technique for Extracting Reliable Twin Statistics | 3745-3751A | Zirconium base alloys, Microstructure | |
| Zirconium, Alloying additive | | Deformation Behavior of Zr ₃ Al-Nb Alloys I: Room-Temperature and High-Temperature Deformation Study. | 189-203A |
| Microstructural Characterization of Secondary-Phase Particles in a Hot-Deformed Al-Cu-Mg-Zr Alloy. | 293-300A | Zirconium compounds, Composite materials | |
| Zirconium base alloys | | Copper-Zirconium Tungstate Composites Exhibiting Low and Negative Thermal Expansion Influenced by Reinforcement Phase Transformations. | 1159-1165A |
| Calorimetric Determination of the 5 Hydride Dissolution Enthalpy in ZIRCALOY-4. | 2343-2349A | | |
| Deformation and Failure of Zr57Nb5Al10Cu15.4Ni12.6/W Particle Composites Under Quasi-Static and Dynamic Compression | | | |